

**MEASUREMENT AND MODELLING OF  
STRUCTURE AND PORE LEVEL  
PROCESSES IN FILTERS AND WICKS**

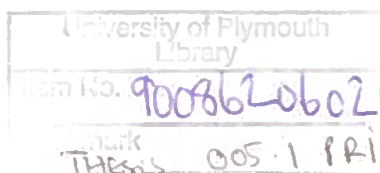
A thesis submitted to the University of Plymouth in partial fulfilment for the degree of

**DOCTOR OF PHILOSOPHY**

**John Charles Price B.Sc. (Hons)**

Environmental and Fluid Modelling Group  
School of Earth, Ocean and Environmental Sciences  
University of Plymouth

This research has been funded by Porvair Filtration Group Ltd..



## **SUPERVISORY TEAM**

### **Professor G. Peter Matthews**

Environmental and Fluid Modelling Group  
School of Earth, Ocean and Environmental Sciences

University of Plymouth

Plymouth

Devon

PL4 8AA

UK

Tel: 01752 233021

[pmatthews@plymouth.ac.uk](mailto:pmatthews@plymouth.ac.uk)

### **Dr John Maskall**

School of Earth, Ocean and Environmental Sciences

University of Plymouth

Plymouth

Devon

PL4 8AA

UK

Tel: 01752 584563

[j.maskall@plymouth.ac.uk](mailto:j.maskall@plymouth.ac.uk)

**Dr John Sexton**

Porvair Filtration Group Ltd.

Segensworth

Fareham

Hampshire

PO15 5RT

UK

Tel: 01489 864330

**Dr Kevin Quinlan**

Porvair Filtration Group Ltd.

Segensworth

Fareham

Hampshire

PO15 5RT

UK

Tel: 01489 864330

[Kevin.Quinlan@porvairfiltration.com](mailto:Kevin.Quinlan@porvairfiltration.com)

## ABSTRACT

Characterisation of new filtration and wicking materials through a “wet-bench” testing process is a requirement for many filtration companies before new products can be released to market. A reduction in this testing commitment through the application of successful computational based models, requiring minimal empirical input, would undoubtedly result in huge financial savings and reductions in testing lead times. Such models could offer total media characterisation and could also aid further insights into many filtration and wicking processes which before would have required an expensive combination of different testing procedures.

In this research, a depth filtration model has been developed, based on the three-dimensional void network model Pore-Cor. The geometry of the void network is fitted, by means of an 8-dimensional Boltzmann annealed amoeboid simplex, to the porosity and percolation characteristics of stainless steel sintered filters measured by mercury intrusion porosimetry (MIP). Preferential and critical flow paths through the network are calculated via a newly developed algorithm which allows a representation of net flow within individual pore/throat clusters. Particles from an experimental size distribution are fed along these flow-biased paths, using a newly developed random-particle-selection algorithm and, when straining occurs, the flow paths are re-calculated. The model is shown usefully to reproduce experimental filtration efficiencies as a function of pressure drop, measured by single pass tests. A critique of filtration efficiency measurements is given, suggesting use of a new ‘alpha efficiency’ rather than standard beta efficiency. The model is currently being adapted to accept porometry as well as porosimetry data, hence avoiding the use of mercury in future testing.

Further to development of the filtration model the research associated with this thesis has also investigated two related areas. One is an investigation of a hydrophilic treatment of a series of polymeric sinters using oxidizing plasma. The investigation shows an improved method of data analysis of capillary rise measurements. An optimization process for determining the correct hydrophilic treatment parameters is proposed based on the variance across sample sets, and results are interpreted with respect to the Vyon® samples analysed. Secondly an investigation of anomalous compression characteristics found in the MIP of stainless steel Sinterflo® media is presented. Hypotheses were proposed for the observed increase in media compressibility and these were investigated using the Pore-Cor void network model for comparison with other investigations of porosity and compression analysis. Preliminary results suggest increased compressibility arises from microscopic material deformities and micro-fractures found in the media.

# LIST OF CONTENTS

<b>COPYRIGHT STATEMENT</b> .....	<b>I</b>
<b>ABSTRACT</b> .....	<b>V</b>
<b>LIST OF CONTENTS</b> .....	<b>VI</b>
<b>LIST OF FIGURES</b> .....	<b>IX</b>
<b>LIST OF TABLES</b> .....	<b>XVII</b>
<b>DEDICATION</b> .....	<b>XVIII</b>
<b>ACKNOWLEDGEMENTS</b> .....	<b>XX</b>
<b>AUTHOR'S DECLARATION</b> .....	<b>XXII</b>
<b>CONFERENCES AND PRESENTATIONS</b> .....	<b>XXIII</b>
<b>OTHER ASSOCIATED PRESENTATIONS</b> .....	<b>XXIV</b>
<b>PUBLICATIONS</b> .....	<b>XXV</b>
<b>NOMENCLATURE</b> .....	<b>XXVI</b>
<b>1. INTRODUCTION</b> .....	<b>1</b>
1.1. <b>STRUCTURE OF THE THESIS</b> .....	<b>1</b>
1.2. <b>THE COLLABORATIVE BASIS AND AIM OF THIS RESEARCH PROJECT</b> .....	<b>2</b>
1.2.1. <b>Porvair Plc. and the filtration industry</b> .....	<b>4</b>
1.3. <b>THEORY AND LITERATURE REVIEW</b> .....	<b>5</b>
1.3.1. <b>Porous media</b> .....	<b>5</b>
1.3.2. <b>Filtration</b> .....	<b>8</b>
1.3.2.1. <b>Filtration in the context of this thesis</b> .....	<b>8</b>
1.3.3. <b>Fluid flow in porous media</b> .....	<b>13</b>
1.3.3.1. <b>Hydrodynamics of fluid flows</b> .....	<b>14</b>
1.3.3.1.1. <b>Saturated flow</b> .....	<b>14</b>
1.3.3.1.2. <b>Unsaturated flow</b> .....	<b>20</b>
1.3.4. <b>Modelling of Porous media and filtration processes</b> .....	<b>23</b>
1.3.4.1. <b>Model types associated with filter-medium filtration</b> .....	<b>27</b>
1.3.4.1.1. <b>Empirical models</b> .....	<b>28</b>
1.3.4.1.2. <b>Stochastic models</b> .....	<b>29</b>
1.3.4.1.3. <b>Trajectory analysis models</b> .....	<b>30</b>
1.3.4.1.4. <b>Network models</b> .....	<b>31</b>
1.3.5. <b>Pore-Cor</b> .....	<b>35</b>
1.3.5.1. <b>Structural characteristics and construction of the model unit cell</b> .....	<b>35</b>
1.3.5.2. <b>Percolation simulation in Pore-Cor</b> .....	<b>41</b>
1.3.5.3. <b>Compressibility Correction</b> .....	<b>42</b>
1.3.5.4. <b>Model Permeability and Flow Characteristics</b> .....	<b>43</b>
<b>2. SAMPLE SETS AND METHODOLOGY</b> .....	<b>47</b>
2.1. <b>FILTER MEDIA TESTING IN INDUSTRY</b> .....	<b>47</b>
2.1.1. <b>Existing techniques applied in industry</b> .....	<b>47</b>
2.1.1.1. <b>Scanning electron microscopy (SEM)</b> .....	<b>48</b>
2.1.1.2. <b>Mercury intrusion porosimetry (MIP)</b> .....	<b>49</b>
2.1.1.3. <b>Porometry</b> .....	<b>53</b>
2.1.1.4. <b>Pass tests</b> .....	<b>55</b>

2.2.	SAMPLE SELECTION AND RATIONALE .....	59
2.2.1.	Sinterflo® media.....	59
2.2.2.	Vyon® media.....	62
<b>3.</b>	<b>POROSIMETRY, MODELLING AND VALIDATION OF MODELLED STRUCTURES .....</b>	<b>66</b>
3.1.	MERCURY POROSIMETRY – MEASUREMENT AND DATA MANIPULATION.....	66
3.1.1.	Sinterflo® results discussion .....	72
3.1.2.	Vyon® results discussion.....	74
3.2.	MODELLING OF REPRESENTATIVE NETWORK REPRESENTATIONS .....	77
3.3.	ASSESSING VALIDITY OF MODELLED DATA.....	83
3.3.1.	Validation using modelled parameters and experimental data .....	83
3.3.2.	Breakthrough pore/throat size.....	84
3.3.3.	Validation of void networks using formation damage simulations .....	88
3.4.	CONCLUSIONS .....	93
<b>4.</b>	<b>DEVELOPMENT OF A FILTRATION MODEL IN PORE-COR.....</b>	<b>95</b>
4.1.	APPROACHING THE PROBLEM.....	95
4.2.	PROGRAMMING OF THE ACTIVE FLOW FIELD IN THE PORE-COR MODEL.....	100
4.2.1.	Testing and demonstration of the Colour Flow algorithm .....	102
4.3.	ADDITION OF CONTAMINANT PARTICLES TO THE PORE-COR MODEL .....	111
4.3.1.	Testing of the particle capture mechanisms .....	116
4.4.	AUTOMATION OF THE MODEL AND INTRODUCTION OF THE USER INTERFACE.....	119
4.4.1.	The Final Product.....	124
4.5.	OTHER PROGRAMMING ASPECTS .....	126
4.6.	CONCLUSIONS .....	126
<b>5.</b>	<b>MODELLING THE REAL FILTRATION ENVIRONMENT.....</b>	<b>128</b>
5.1.	SINGLE PASS TEST METHODOLOGY USED IN THIS STUDY .....	128
5.1.1.	Standard characterisation of filters .....	130
5.1.2.	Problems with the characterisation of filters in the context of this study ..	133
5.2.	RESULTS AND DISCUSSION .....	136
5.2.1.	Experimental pass tests .....	136
5.2.2.	Model simulations of single pass tests and filter characteristics.....	141
5.2.2.1.	Assessing blockage rates of simulated structures .....	142
5.2.2.2.	Discussion of the blockage rate assessment in simulated structures..	148
5.2.2.3.	Capture efficiency profiles of simulated filters.....	149
5.2.2.3.1.	Initial comparison of simulated capture efficiency profiles.....	149
5.2.2.3.2.	Discussion of the initial simulated capture efficiency profiles .....	150
5.2.2.3.3.	3-Dimensional simulated capture efficiency profiles .....	151
5.2.2.3.4.	Discussion of 3-Dimensional simulated capture efficiency profiles	155
5.2.2.4.	Comparison of efficiency calculations.....	157
5.2.2.5.	Permeability data from “clean” simulated filters.....	160
5.2.2.6.	Discussion of permeability results .....	162
5.3.	CONCLUSIONS .....	162

<b>6. WICKING PROPERTIES OF VYON® MEDIA.....</b>	<b>164</b>
6.1. BACKGROUND OF THE STUDY.....	164
6.1.1. The improved data analysis of wicking phenomena.....	166
6.1.2. Treatment of Vyon® media to enhance hydrophilicity.....	169
6.2. EXPERIMENTAL APPARATUS AND METHOD FOR WICKING ANALYSIS.....	170
6.3. RESULTS OF WICKING ANALYSIS.....	173
6.3.1. Initial sample set.....	173
6.3.2. Optimised second sample set.....	176
6.4. DISCUSSION OF WICKING PROPERTIES OF VYON® MEDIA.....	184
<b>7. COMPRESSIBILITY AND POROSITY LOSS IN SINTERFLO® MEDIA.....</b>	<b>187</b>
7.1. INTRODUCTION TO THE INVESTIGATION.....	187
7.1.1. Bulk Modulus and the apparent anomaly within Sinterflo Samples.....	187
7.1.2. Manufacturing procedure and its proposed relation with closed pores.....	189
7.2. METHOD OF INVESTIGATION.....	192
7.3. RESULTS.....	194
<b>8. OVERVIEW.....</b>	<b>211</b>
8.1. DEVELOPMENT OF A WORKING FILTRATION MODEL.....	211
8.2. INVESTIGATION OF HYDROPHILIC I-VYON® MEDIA.....	215
8.3. INVESTIGATION OF ANOMALOUS MATERIAL COMPRESSIBILITY IN SINTERFLO® MEDIA.....	216
8.4. FUTURE WORK.....	217
8.5. CONCLUSION.....	219
<b>REFERENCES.....</b>	<b>220</b>

## LIST OF FIGURES

Figure 1.1 Representation of a porous medium showing isolated pores, pores and interconnecting throats (Laudone, 2005) .....	6
Figure 1.2 Schematic of various porous media types (Schoelkopf, 2002).....	7
Figure 1.3 Graph showing relationship between particle size ( $d_p$ ) and capture efficiency ( $\eta$ ) for the four main particle capture mechanisms. ....	13
Figure 1.4 Parabolic velocity profile for laminar flow in a cylindrical tube. $V_{\max}$ shows the point of maximum fluid velocity and at the container walls $V = 0$ . ....	16
Figure 1.5 A classical representation of a porous medium using a bundle of straight cylindrical tubes as the porosity fraction of a solid.....	17
Figure 1.6 Schematic overview of the of the influences dictating unsaturated flow in porous media from a reservoir (left) into an evacuated capillary tube (Schoelkopf et al., 2000). ....	22
Figure 1.7 A conventional capillary bundle type model of porous media using capillary worm holes as a simplification of the true connectivity and tortuosity of a real sample. ....	24
Figure 1.8 A Monte-Carlo type generation of an advanced packed sphere pore network utilised in determining pore structures of some advanced models. ....	25
Figure 1.9 Visualisation of some constructed 2-dimensional networks used in filtration modeling. A = Hexagonal network, B = Triangular network, C = Voroni network and D = Double Hexagonal network. ....	32
Figure 1.10 Simulated Pore-Cor network representation showing cylindrical throat and cubic pore representation arranged in a 3-dimensional cartesian array. ....	36
Figure 1.11 Schematic of a non-wetting fluid entering a cylindrical tube and showing some of the variables found in the laplace equation. ....	42
Figure 1.12 Schematic representation of an 'arc' as defined by the Pore-Cor software. Annotation refers to values found in Equation 1.29. ....	44
Figure 2.1 A scanning electron micrograph of a resin impregnated sample of Vyon T filtration media showing magnification factor and scale bar. ....	48
Figure 2.2 Mercury in contact with a porous solid at the opening of a pore and under insufficient applied pressure to undergo intrusion. ....	50
Figure 2.3 Exploded diagram of a MIP penetrometer showing the volume calibrated sample cup, capillary stem and closure components used to seal the sample within the assembly (Webb & Orr, 1997). ....	50
Figure 2.4 Penetrometer containing a sample of porous media after mercury has been forced into pores. The diameter of the capillary is exaggerated for clarity. (Webb & Orr, 1997).....	51



Figure 2.5 A mercury intrusion curve derived from collected porosimetry data. Curve is plotted as an intrusion volume per unit weight of sample as a function of respective pore diameter as found by way of the Washburn equation.....	52
Figure 2.6 Porometry sample intrusion showing the acting capillary pressure against the intruding gas phase (Xonics data sheet).....	53
Figure 2.7 Graphical representation of porometry data showing gas flow rate as a function of pressure for a standard test sinter. The plot shows both the wet and dry runs of the analysis which are used to calculate pore size distributions of the media.....	55
Figure 2.8 Schematic of a multipass test system showing the cycled nature of contaminant fluid and particle counters $N_U$ and $N_D$ as upstream and downstream respectively.....	56
Figure 2.9 Schematic of a single pass test system showing the cycled nature of contaminant fluid and particle counters $N_U$ and $N_D$ as upstream and downstream respectively.....	58
Figure 2.10 Examples of flat sheet and cylinder forms of Sinterflo® media produced by green form sintering.....	60
Figure 2.11 Sample plug dimensions for stainless steel Sinterflo® media as used in mercury porosimetry experiments (MIP).....	61
Figure 2.12 Examples of Vyon® media in both sheet, roll and moulded formats. (change for PV ref show sheet and moulds).....	63
Figure 3.1 Picture of the Auto-Pore III Micromeritics porosimeter showing the four low pressure ports at the top of the instrument (grey cylindrical covers) and the two high pressure oil filled ports (black vertical closure units on the horizontal base).....	67
Figure 3.2 Microsoft Excel plot of MIP data for a S26 Sinterflo® plug as delivered by execution of the principle pressure table constructed for all sample sets (sample is corrected for compression effects).....	68
Figure 3.3 Mercury intrusion porosimetry curves for Sinterflow® samples S16, S21, S26, S36 and S41. Results shown are scaled by the 90% 10% trim method as stated above.....	71
Figure 3.4 Mercury intrusion porosimetry curves for Vyon® samples F, T and HP. Results shown are scaled by the 90% 10% trim method as stated above.....	72
Figure 3.5 Diagram and graph showing the comparison between pore size measurements as found by various techniques. The largest pore size determined in bubble point methodology is equivalent to $D_1$ , where the pore is most constricted. (Gupta and Jena, 1999).....	74
Figure 3.6 Results from the quick screening MIP of Vyon® samples for reproducibility, showing repeat intrusion curves of duplicate samples and relative porosity values.....	76

Figure 3.7 Stochastic realisation of an S16 Sinterflo® sample showing the representative cubic pores and cylindrical throat features that are fitted to the experimental intrusion curve by way of the Pore-Cor simplex. Note the 1mm scale bar at the underside of the unit cell. ....	78
Figure 3.8 Stochastic realisation of an S21 Sinterflo® sample. ....	78
Figure 3.9 Stochastic realisation of an S26 Sinterflo® sample. ....	79
Figure 3.10 Stochastic realisation of an S36 Sinterflo® sample. It may be seen in this structure that a lower value of pore skew has given a greater range of pore sizes. ....	79
Figure 3.11 Stochastic realisation of an S41 Sinterflo® sample. Note that in the S36 and S41 samples the scale bar is proportionally smaller, indicating the higher pore sizes in these media. This is also evident directly from the intrusion curves (Figure 3.3). ....	80
Figure 3.12 Stochastic realisation of a Vyon® T sample. ....	80
Figure 3.13 Stochastic realisation of a Vyon® F sample. Note the apparent loss of the pore structures but apparent increase in throat sizes compared to the higher porosity Vyon® T (Figure 3.4 and Figure 3.6). ....	81
Figure 3.14 Stochastic realisation of a Vyon® HP sample. Note the increased size in scale bar due to Vyon® HP media having a much larger experimental pore size. ....	81
Figure 3.15 Graph showing the trend in Sinterflo® media between maximum experimental pore size and modelled breakthrough pore size. Data points are labelled to corresponding media grade. ....	86
Figure 3.16 Graph showing how the division of the experimentally derived maximum pore size by half correlates with the modelled breakthrough pore size of the simulated Sinterflo® structures. ....	87
Figure 3.17 Results of formation damage simulations on Sinterflo samples. Permeability values have been normalised and represented as relative permeability's for ease of sample comparison. ....	89
Figure 3.18 Results of formation damage simulations on Vyon samples. Permeability values have been normalised and represented as relative permeability's for ease of sample comparison. ....	89
Figure 3.19 Comparison of the simulated formation damage results with the experimentally stated 98 and 99.9 % capture efficiencies. Formation damage results are presented as the particle size at which permeability = 0. ....	90
Figure 3.20 Effect of formation damage graph for 10 stochastic realizations of the Sinterflo® S26 media. The uncertainty of the particle size at which the permeability tends to zero is averaged for the 10 generations and represented by the average value. ....	92
Figure 4.1 Systematic flow diagram of the filtration model developed in the Pore-Cor software package. ....	99

Figure 4.2 Screen shot of the colour gradients as seen on the user interface. Red to blue representing flow in the positive direction and red to yellow for flow in the negative direction. Also indicated is the sensitivity control bar so that results may be expressed in a log or linear scale. ....	101
Figure 4.3 Diagram showing structure types available in Pore-Cor simulations. Bold numbers 1 – 7 refer to the structures used for testing the Colour Flow algorithm within this section.....	103
Figure 4.4 Pore and throat size distribution for vertically banded structure.....	103
Figure 4.5 Negative-direction flow (-x, -y, -z) through vertically banded structure (1 in Figure 4.3), correlation level = 1.....	104
Figure 4.6 Positive-direction flow (+x +y +z) through vertically banded structure (1 in Figure 4.3), correlation level = 1.....	105
Figure 4.7 Net flow through vertically banded structure (1 in Figure 4.3), correlation level = 0.95.....	106
Figure 4.8 Net flow through vertically banded structure (2 in Figure 4.3) with correlation level 0.5. The increased randomness of structure has caused an increased randomness of flow relative to Figure 4.6. ....	106
Figure 4.9 Net flow through structure with large surface throats (3 in Figure 4.3), correlation level = 1 .....	108
Figure 4.10 Net flow through small central pore type structure (4 in Figure 4.3), correlation level = 0.95 .....	108
Figure 4.11 Net flow through small central pore type structure (5 in Figure 4.3), correlation level = 0.5. The increased randomness of structure has caused an increased randomness of flow relative to Figure 4.9. ....	109
Figure 4.12 Net flow through large centred structure (6 in Figure 4.3), correlation level = 1 .....	110
Figure 4.13 Net flow through large centred structure (7 in Figure 4.3) , correlation level = 0.5. The increased randomness of structure has caused an increased randomness of flow relative to Figure 4.11.....	110
Figure 4.14 Diagram showing where parameter values for the Stein relationship equation (Eqn 3.1) arise from in a standard throat feature. Note that any changes in fluid chemistry or velocity will either decrease or increase the effective value of $\theta_a$ thus decreasing or increasing the probability of deposition respectively. ....	114
Figure 4.15 Pore-Cor Network simulation of S41 stainless steel filtration media prior to any filtration events, and showing calculated flow regimes by way of the “colourflow” algorithm. Areas within green circles are for comparison with Figure 4.16 to show flow affected by critical velocity deposition. ....	117

Figure 4.16 Pore-Cor Network simulation of S41 stainless steel filtration media as above, but after a series of critical velocity deposition events by manually controlled 10 micron contaminant particles set to deposit where $v^* = 0.25 \times v_{max}$ . Note areas in green circles have decreased flow intensity when compared with Figure 4.15. Changes in flow regime for such deposition events are found to be subtle over time due to small particle size and the associated gradual fouling of throat features.....	118
Figure 4.17 Pore-Cor Network simulation of S41 stainless steel filtration media as above, but after the application of straining simulations using a 20 micron particle size. Note the large changes in the flow regime when compared with figure 3.4. It is found that the instant plugging of such straining events has an instant effect on the structure of flow through the unit cell.....	118
Figure 4.18 Comparison between a challenge particle profile returned by way of the Gaussian consideration of a distribution size range and a realistic distribution profile of particles.....	121
Figure 4.19 Simplistic example distribution to explain weighted selection of integers in the random biased number selection of challenge particle. Size fractions are, 30 microns = 10 particles, 20 microns = 20 particle and 10 microns = 70 particles. ....	123
Figure 4.20 Screen shot of the programmed user interface for the final filtration module. Numbers in parentheses relate to descriptions in text.....	125
Figure 5.1 Schematic of the experimental single pass test apparatus.....	129
Figure 5.2 Graphical representation of the simulated particle size distributions used in simulations of pass tests on the Sinterflo® media. Note that all distributions are proportional to the experimental distribution exhibited by the betaratiometer.....	136
Figure 5.3 Sinterflo® S36 capture efficiency profiles for the 6-10 $\mu\text{m}$ contaminant particulate, as measured by betaratiometer. Results are normalized on the time axis to the 5 L $\text{min}^{-1}$ flow rate.....	137
Figure 5.4 Capture efficiency graphs for S36 Sinterflo® media at 5 & 7 L $\text{min}^{-1}$ flow rates against the normalized pressure drop data.....	139
Figure 5.5 Capture efficiency graphs for S41 Sinterflo® media at 5 & 7 L $\text{min}^{-1}$ flow rates against the normalized pressure drop data.....	140
Figure 5.6 Graph showing blockage rate of simulated S16 Sinterflo® media against selected particle size distributions outlined in Figure 5.2.....	143
Figure 5.7 Graph showing blockage rate of simulated S21 Sinterflo® media against selected particle size distributions outlined in Figure 5.2.....	144
Figure 5.8 Graph showing blockage rate of simulated S26 Sinterflo® media against selected particle size distributions outlined in Figure 5.2.....	144
Figure 5.9 Graph showing blockage rate of simulated S36 Sinterflo® media against selected particle size distributions outlined in Figure 5.2.....	145

Figure 5.10 Graph showing blockage rate of simulated S41 Sinterflo® media against selected particle size distributions outlined in Figure 5.2.....	145
Figure 5.11 Colour Flow representation of a clean S41 filter sample prior to any filtration events.....	147
Figure 5.12 Colour Flow representation of 50 % blocked S41 filter. Comparison with Figure 5.11 shows that there are many areas within the structure that have a reduced flow volume due to deposition events in the void structure. Reduction in flow is represented by the changes in the colour gradient as described in Section 4.2. ....	147
Figure 5.13 Graph comparing capture efficiencies of simulated filters at the applied particle sizes found in the filtration of the default distribution.....	150
Figure 5.14 3-dimensional plot of a simulated single pass test on S16 Sinterflo® media using the Div2 contaminant particle distribution highlighted in Figure 5.2. ....	152
Figure 5.15 3-dimensional plot of a simulated single pass test on S21 Sinterflo® media using the Div2 contaminant particle distribution highlighted in Figure 5.2. ....	153
Figure 5.16 3-dimensional plot of a simulated single pass test on S26 Sinterflo® media using the Div2 contaminant particle distribution highlighted in Figure 5.2. ....	153
Figure 5.17 3-dimensional plot of a simulated single pass test on S36 Sinterflo® media using the Default contaminant particle distribution highlighted in Figure 5.2. ....	154
Figure 5.18 3-dimensional plot of a simulated single pass test on S41 Sinterflo® media using the Default contaminant particle distribution highlighted in Figure 5.2. ....	154
Figure 5.19 Comparison of filter efficiency interpretations upon the same data set from an S41 Sinterflo® filter under pass test conditions. Different interpretations of data show the associated problems highlighted in Section 5.1.2.....	158
Figure 5.20 Comparison of filter efficiency between that derived from $\beta$ -ratios, $E$ , shown in (a) and the two derivations of alpha efficiency, $\alpha$ and $\alpha'$ , shown in (b) and (c) respectively. As may be seen although each method of efficiency interpretation holds consistency over the 40 $\mu\text{m}$ particle size their differing effect on the interpretation of capture efficiency at the lower particle sizes of the test are very different.....	159
Figure 5.21 Plot of $\log_{10}$ experimental permeability against $\log_{10}$ mean simulated permeability for all grades of Sinterflo® media tested. Error bars represent $\pm 1$ standard deviation.....	161
Figure 6.1 Schematic of the plasma chamber used in the oxidization of polymer pore surfaces to enhance media hydrophilicity. Oxygen is fed into the chamber under vacuum through the sample inlet point direct to the electrode set-up.....	170
Figure 6.2 Wetting apparatus showing detail of sample holder assembly, balance read out and wetting liquid reservoir. Note that in this diagram a soil sample holder is shown (numbered 3 in centre of diagram) rather than a sample of the Vyon® or i-Vyon® media.....	171

Figure 6.3 Graphical representation of a non-wicking hydrophobic sample of standard non-treated Vyon® (blue) and a hydrophilicly treated i-Vyon® sample showing inconsistent wicking performance (pink), as shown by the un-smooth wetting curve. ....	174
Figure 6.4 Photos of the patchy wicking performance of the hydrophilic treated i-Vyon® samples. All samples in the originally supplied sample set exhibited the same behaviour with large areas remaining hydrophobic in behaviour. The darker areas are those which have wicked wetting fluid effectively and the light patches those which are exhibiting varying degrees of hydrophobicity through the samples depth profile.....	175
Figure 6.5 Photo showing an example of the brown tide marks that were apparent in the inconsistently treated i-Vyon® samples after oven drying at 40 °C. Marks such as this were apparent around all areas that were observed not to wick water in the initial tests. .	176
Figure 6.6 Graph depicting a typical wetting profile of the same media (i-Vyon® T) in both water and hexane wetting liquids. Symbols $\Delta$ and $\square$ represent the start and finish points used in each curve for the calculation of the linear relationship between fluid wicking and the square root of time determined from the solution to Equation 6.4 for $\beta \Rightarrow 0.5$ . ....	177
Figure 6.7 Examples of wetting curves for each sample using water as the wetting liquid. ....	178
Figure 6.8 Examples of wetting curves for each sample using hexane as the wetting liquid. ....	179
Figure 6.9 $\ln cK$ values for all tested grades in hexane. Results show the mean of three replicates and $\pm 1$ standard deviation to show the degree of variance. ....	180
Figure 6.10 $\ln cK$ values for all tested grades in water. Results show the mean of three replicates and $\pm 1$ standard deviation to show the degree of variance. ....	180
Figure 6.11 Calculated apparent contact angles of water with the tested grades of Vyon® media used in the current wicking analysis. ....	182
Figure 6.12 Calculated values of $r_h$ for tested Vyon® sample grades. ....	184
Figure 7.1 2-dimensional representation of (A) an ideal sinter where sintering has left flow paths (represented by red arrows) between the sintered particles and (B) where the sintering process has induced particles to melt together to form a closed pore space (represented by green shaded area) inaccessible to intruding mercury and where flow can not enter during.....	190
Figure 7.2 Examples of sintered stainless steel media in various moulded configurations.....	191
Figure 7.3 Graphical representation of expected porosity in relation to nominal green form density that should exist in provided sintered samples. Note the expected decreasing porosity with increasing green form density.....	195

Figure 7.4 Comparison of expected porosity with true measured porosity by way of the weigh/measure technique and the ISO 2738 open porosity method. ....	197
Figure 7.5 Raw porosimetry curves for all nominal densities of sample sinters tested in the compression study. Nominal densities are highlighted in the legend as grams per cubic centimetre (g/cc) and cover the analysed sample range. ....	198
Figure 7.6 Screen shot of the Pore-Comp compression correction on high pressure data points in analysis of a nominal density = 5.9 g cm <sup>-3</sup> sample plug. This shows the presence of the pseudo intrusion effects that are used in the calculation of sample bulk modulus. They are represented by the rising values of the intrusion and extrusion data points (those represented by the circled series). The lower un-circled data series are those that are corrected for mercury and penetrometer compression effects (blue), and additionally for sample compression effects (red) to leave a true intrusion curve (Section 1.3.5.3). ....	199
Figure 7.7 Corrected porosimetry curves after compressibility correction and corrective trimming process as described in Section 3.1. ....	200
Figure 7.8 Comparison of the returned % porosity values for all nominal densities of samples tested via all analysis methods. ....	201
Figure 7.9 Bulk modulus values from compressibility corrections of porosimetry curves. Results are reported as the median value of the acceptable range as determined by manual processing of the compressibility correction. ....	202
Figure 7.10 Connectivity analysis for a sinter of nominal density 4.2 g cm <sup>-3</sup> . Results show that the percentage fraction of ink bottle pores, those where connectivity = 1, is ca. 2%. This indicates a low inclusion of the ink bottle phenomena in the tested sinter. .	204
Figure 7.11 Size distribution of ink bottle pores within the tested 4.2 g cm <sup>-3</sup> nominal density sample plug. Results are expressed as a percentage fraction of total pore number within the sample. ....	204
Figure 7.12 Connectivity analysis for a sinter of nominal density 5.9 g cm <sup>-3</sup> . Results show that the percentage fraction of ink bottle pores, those where connectivity = 1, is ca. 2%. This indicates a low inclusion of the ink bottle phenomena in the tested sinter. .	205
Figure 7.13 Size distribution of ink bottle pores within the tested 5.9 g cm <sup>-3</sup> nominal density sample plug. Results are expressed as a percentage fraction of total pore number within the sample. ....	205
Figure 7.14 Screen shot of PTSD analysis for a 4.2 g cm <sup>-3</sup> nominal density Sinterflo® sample plug. Note centre of the Gaussian throat size distribution ca. 30 µm. ....	207
Figure 7.15 Screen shot of PTSD analysis for a 5.9 g cm <sup>-3</sup> nominal density Sinterflo® sample plug. Note centre of the Gaussian throat size distribution ca. 3 µm. ....	208
Figure 7.16 Compressive load test results for the stainless steel Sinterflo® media. Samples 4.2 – 5.9 g cm <sup>-3</sup> nominal densities and solid stainless steel were all run under the same conditions of analysis. ....	210

## LIST OF TABLES

Table 2. 1 Physical properties of Sinterflow® stainless steel media PTL Ltd. ....	61
Table 2. 2 Physical properties of Vyon® polymeric media as measured by porometry (PTL) .....	64
Table 3.1 Table highlighting the fitting parameters used in the Pore-Cor stochastic realisations (Figure 3. 7 - Figure 3. 14). Feature diameters are governed by the experimental data file and all other values are derived by the software in obtaining a closest fit approximation of the experimental values.....	82
Table 3.2 Showing modelled breakthrough pore size, in relation to experimentally derived maximum pore size and comparison of experimental and modelled porosity.....	85
Table 3.3 Results for Sinterflo® formation damage simulations shown against 98 % and 99.9 % experimental capture efficiencies. Note the closeness of simulated results to experimental values.....	90
Table 5.1 Results of experimental permeability tests for each Sinterflo® grade tested. ...	141
Table 5.2 Comparison of experimental and simulated permeabilities. Values of permeability are expressed in milli Darcies (mD) . 1 milli Darcy = $0.987 \times 10^{-15} \text{ m}^2$ .....	160
Table 6.1 Summary of experimental data from wicking experiments undertaken in both water and hexane wetting fluids. Results expressed as a mean $\ln Ck$ value from three replicates of each experimental set. ....	181
Table 7.1 Modelled values of bulk modulus as found by Pore-Comp software in initial porosimetry experiments associated with this research. ....	188
Table 7.2 Tabulated results for the expected porosity (%) exhibited by differing nominal densities of green form sinters for comparison point of further investigations. ...	194
Table 7. 3 Table of measurements and results for both the standard weigh and measure porosity analysis and also the ISO 2738 open porosity analysis. The table shows results for all samples produced for this study. ....	196
Table 7.4 Comparison of sample porosities derived by all analysis methods. ....	201



## DEDICATION

*Dedicated to my father*

*Wish you were here!!*

*“True wisdom is less presuming than folly. The wise man doubteth often,  
and changeth his mind; the fool is obstinate, and doubteth not; he knoweth  
all things but his own ignorance.”*

**Akhenaton**

## ACKNOWLEDGEMENTS

I would firstly like to thank my academic supervisor Professor Peter Matthews. You have been amazing through my time under your wing and I thank you for your support through the hard times, and your continued encouragement and interest throughout the research. You have been a rock; congratulations on your Professorship. From someone who has witnessed your dedication first hand I must say you truly deserve it.

I would also like to thank John Sexton and Kevin Quinlan of Porvair Filtration Group. Without them this research would not have been possible. I thank you both for, your encouragement, support, opening my eyes to reality and sticking by the project throughout. I consider you both wise mentors not only in this work but also for the path of my future; your company on this journey has been much appreciated and I look forward to repaying your kindness someday. I would also like to thank all other employees of Porvair that I have had the pleasure to meet, especially Richard Morgan, Chris Lilley and Andy Bevis for their provision of sample sets, manufacturing data, training on the required test methods and huge overall knowledge of the subject. You have all been fantastic in giving up your time for the sometimes silly questions and ideas born from folly. I hope I can repay you those promised beers soon.

At the University of Plymouth I would like to offer huge thanks to all those I have had the pleasure of working and associating with. A special thanks to Debbie Petherick. As many have said before me, and many will without doubt say in future, you are "The Oracle"; thank you for everything you have done for me. I would also like to thank all members of my research group past and present especially Maurizio for his help with all things computer and for providing that unique laid back advice over a lunch or two when it was most needed. Although no longer at Plymouth, I would also like to thank Pat Gane and Cathy Ridgway of Omya AG for agreeing to, and undertaking mercury porosimetry of samples whilst our instrument in Plymouth was not in service.

Outside of the university I would like to thank Pete, Ju, Ty and Mel for their great friendship and support in all things outside of my research. Big thanks must also go to all members of the Hyde Park Social club who have accepted me as their own. Thank you for teaching me Euchre and being there when I have needed a break from academic overload. I also must thank three very special friends in Benny, Pully McAuley and

Bexy. You are all top of the heap, your friendship has meant the world to me and has never faltered even in the times I have probably not deserved it! Give me a few months of paid work and I may even cook you all dinner just to prove I can.

Beyond my life here in Plymouth I would like to thank all my long standing friends from back home, rugby, fishing and all other aspects of my life. Without you all I would not be who I am today. Also I must say thank you to Ruth and Bill you have been wonderful in keeping me going on this path that was partly born through your encouragement. Thanks to you all for many years of friendship and support.

Last and so far from least, I want to thank my mother, brother and family. Mum you have been the best. How on earth you have put up with me for this long I shall never know but I am truly grateful for your unconditional support through everything. Bro, the same goes out to you and Soph and thanks for the visits and the phone calls. To the rest of my wonderful family I thank you all for your support and also for keeping my mother sane through the tough times I have given her.

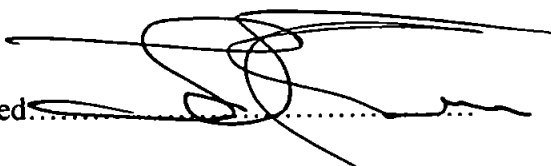
## AUTHOR'S DECLARATION

At no time during the registration for the degree of Doctor of Philosophy has the author been registered for any other University award.

This study was financed with the aid of a studentship from both Porvair Filtration Group Ltd. and the University of Plymouth.

Seminars and conferences were regularly attended throughout the period of study at which research was regularly presented. Consultation with other institutions occurred and several publications are to be prepared.

Word count: 42,954

Signed.....

John C. Price

## CONFERENCES AND PRESENTATIONS

South West Modelling Group Meeting, *Environmental interests in the South West in all Three Media – Water, Land and Air*. 15 October 2003, University of Plymouth, U.K.

University of Plymouth, School of Earth, Ocean and Environmental Sciences Research Seminars. March 2004, Plymouth, UK. Oral Presentation.

University of Plymouth Modelling seminars. Plymouth University Modelling Group Research Presentations July 2005, Plymouth, UK. Oral Presentation.

FILTECH 2005, International Conference and Exhibition for Filtration and Separation Technology. 11 – 13 October 2005, Wiesbaden, Germany. Oral Presentation.

The Filtration Society. One day conference, New Developments in Filtration Technology, 28 February 2006, Loughborough University, Loughborough, U.K. Oral Presentation.

## OTHER ASSOCIATED PRESENTATIONS

International Pore-Cor Training Course, University of Plymouth, 6-7 October 2004.  
Oral presentations and demonstrations of software.

International Pore-Cor Training Course, University of Plymouth, 6-8 April 2005. Oral presentations and demonstrations of software.

International Pore-Cor Training Course, University of Plymouth, 5-7 October 2005.  
Oral presentations and demonstrations of software.

International Pore-Cor Training Course, Interscience Belgium, 13-14 June 2006. Oral presentations and demonstrations of software.

Bonsai Technology. One Day Pore-Cor Training Course, 17 April 2007, University of Madrid, Madrid, Spain. Individually presented a one day training course on Pore-Cor through oral presentations and demonstrations of the software.

France Scientifique. One day Pore-Cor training course, 5 July 2007, BRGM Service Environnement and Procedes, Orleans, France. Individually presented a one day training course on Pore-Cor through oral presentations and demonstrations of the software.

## PUBLICATIONS

Price, J.C., Matthews, G.P., Quinlan, K., Sexton, J. and Matthews, A. G de G. (2008) A Depth filtration model of straining within the void networks of stainless steel filters. *A.I.Ch.E. Journal*, first submitted July 2008. Accepted for publication, subject to minor modifications.

Matthews, G.P., Watts, C.W., Price, J.C., Powlson, D.S. and Whalley, W.R. (2008) Wetting of agricultural soil measured by a simplified capillary rise technique. *European Journal of Soil Science*, 59, 4, 817 – 823.

Matthews, G.P.; Bodurtha, P.A.; Price, J.C.; Ridgway, C.J.; Johnson, A.; Roy, I.M.; Laudone, G.M. (2004) *Pore-Cor Research Suite User's Guide*. University of Plymouth Enterprise Ltd. U.K. ISBN: 18-84102-123-7

Other publications in preparation.



## NOMENCLATURE

$A$	Cross-sectional area
$A_{cell}$	Cross-sectional area of the unit cell
$a$	Radius of simulated particle
$B$	Percentage blockage of filter
$B_{model}$	Simulated percentage blockage of modelled unit cell
$C$	Capture efficiency
$C_{cum}$	Cumulative capture efficiency
$c$	Permeability coefficient also referred to as the 'Kozeny constant'
$d$	Diameter of a cylindrical tube or throat
$dp/dx$	Pressure gradient along a capillary
$E$	Filter efficiency
$E_x$	Filtration efficiency at size $x$
$F$	Volumetric flow capacity
$F_{arc}$	Flow capacity of an arc
$h$	Measurement of height
$K$	Permeability of a certain medium to a particular fluid
$K_s$	Saturated permeability of a material
$k$	Intrinsic (specific) permeability of a material, independent of the fluid used to measure it
$k_f$	Absolute permeability of working filter
$k_c$	Absolute permeability of clean filter
$L, l$	Measurement of length
$l_{cell}$	Length of the unit cell
$M_{ss}$	Bulk modulus of the solid sample

$N$	Number of particles deposited
$N_{ux}$	Number of particles upstream, where $x$ = representative group integer value
$N_{dx}$	Number of particles downstream, where $x$ = representative group integer value
$n$	Number of capillaries per unit area of cross section
$P_e$	External pressure
$P$	Pressure potential equivalent to the hydrostatic head
$P$	Pressure difference generated across the fluid meniscus
$P_{ue}$	Upstream pressure
$P_{de}$	Downstream pressure
$P_{uc}$	Upstream pressure corrected for housing loss
$P_{dc}$	Downstream pressure corrected for housing loss
$\Delta P_h$	Housing loss
$P^1$	Atmospheric pressure
$p$	pressure
$\Delta p$	Hydrostatic pressure difference
$\Delta P$	Difference between the capillary pressure and the externally applied pressure
$Q$	Volumetric flow rate
$q$	Flow rate
$\mathbf{q}$	Vector flow velocity
$R$	Inner radius of throat feature
$R_o$	Radius of associated network throat feature
$r$	measurement of a radius
$r_h$	Effective hydraulic radius

$r_{eff}$	Effective radius
$S$	Average specific surface area
$S_x$	Spherical equivalent particle size group where $x$ = group integer
$T$	Tortuosity
$t$	measurement of time
$t_0$	Time at the start of the experimental data acquisition
$t_{obs}$	Time elapsed until consequent experimental measurement
$V$	Measurement of Volume
$V_{int}$	Volume intrusion into the sample
$V_{obs}$	Intruded mercury volume reading
$\delta V_{blank}$	Change in the blank run volume reading
$V_{bulk}^I$	Sample bulk volume at atmospheric pressure
$V_{bulk}$	bulk or envelope volume of the unit cell
$V_{pore}$	Volume of pore
$V_{throat}$	Volume of throat
$\mathbf{v}$	Local velocity-vector of a point of the fluid
$v$	Average flow velocity in a tube
$v^*$	Critical velocity
$W$	Width of sample
$w$	Weight of water taken up due to capillary action
$w_{obs}$	Observed weight of water taken up from reservoir due to capillary action
$x$	distance travelled by the wetting front
$\alpha$	Alpha efficiency
$\beta$	Beta ratio
$\beta_x$	Beta Ratio at specified size $x$
$\lambda$	Mean free path

$\varepsilon$	Sample porosity
$C_{cum}$	Normalised cumulative efficiency
$\phi$	Porosity
$\gamma$	Interfacial tension
$\pi$	Mathematical constant, $\pi = 3.141592654$
$\eta$	Viscosity
$\theta$	contact angle of the meniscus surface with the solid surface (Eqn. 1.12) and lumped parameter in Equation 4.1
$\rho$	Density of the liquid
$\Delta \mathcal{R}_{rel}$	Normalised relative pressure drop
$\Omega_{cell}$	Averaging operator over the whole unit cell

# **1. Introduction**

## **1.1. Structure of the thesis**

This thesis is divided into eight chapters. This introductory chapter gives an insight into the rationale behind the associated research and, through the theory and literature review in Section 1.3, gives insight to relevant scientific literature and theory that will aid the reader's understanding of the work undertaken in further chapters. Chapter 2 gives a description of current methods used in the characterisation of filter media and also outlays the reasoning behind the selection of samples for this research. Chapters 3 – 5 cover the experimental, results and testing processes involved in the development and realisation of a working filtration model and its attachment to the existing void network software, namely Pore-Cor. Chapter 3 highlights the experimental analysis of the original sample sets and the associated modelling of void network representations that may be included as the basis for constructing a filtration model. Chapter 4 explains the development and construction of the filtration model and the algorithms that are included to allow realistic approximations in the model environment. In Chapter 5, the combination of the void networks validated in Chapter 3 and the model outlaid in Chapter 4 is then tested and compared to experimental wet bench data, and the model's success discussed.

Chapters 6 and 7 describe two satellite studies that have arisen from the initial study. The first, described in Chapter 6, is a study of enhanced wicking performance in sintered polymer media, previously prepared using a plasma oxidation process to induce hydrophilic behaviour of the material. This study also highlights an advanced method of data manipulation that should allow quick and efficient industrial optimisation of such samples. The second study presented in Chapter 7 is concerned with an analysis of an apparent

increase in the compressibility of stainless steel media when it is sintered to form filtration media. The study highlights the investigatory process that was undertaken after the samples analysed in Chapter 3 were found, by mercury porosimetry, to show anomalous compressibility characteristics.

Chapter 8 is an overview chapter which concludes the research carried out in the previous chapters. The successes and failures are discussed with respect to the specific aims highlighted in Section 1.2 and the objectives highlighted at the start of each subsequent chapter. It also includes a description of suggested future work, particularly to enable its further application to industrial use.

## **1.2. The collaborative basis and aim of this research project**

It has been noted that universities should make a stronger effort to bridge the gap between academic research and the requirement of the industrial end user so that advances in academic understanding can be easily applied to industrial requirement (Purchas, 2004). This thesis investigates the application and adaption of a highly sophisticated void network model, namely Pore-Cor, to the measurement and modelling of structural and pore-level processes in filters and wicks. The basis of the Pore-Cor model is the result of around £1.5 m research funding and twelve Ph D projects. The model itself has already effectively been applied to modelling the behaviour of fluids in many porous materials such as calcium carbonate blocks (Ridgway et al., 2001), soils (Holtham, 2006. Peat et al., 2000), oil reservoir sandstone characterisation and even nappy linings (Pore-Cor Application Notes, 2007). A description of the Pore-Cor model can be found in section 1.3.5.

The research within this thesis has, as its overall aim, the reduction in the requirement for wet bench testing methods so that temporal and financial reductions can be made in research and development programs within the filtration industry. This is to be achieved by the development of a sufficiently accurate filtration model which may be utilized at desk top computer level by trained operatives. The production of this model has three specific aims:

- (i) to increase understanding of filtration processes,
- (ii) to reduce the amount of testing required, e.g. increase filtration efficiency and lifespan, by using the model to interpolate and extrapolate existing measurements,
- (iii) to provide insights to aid in the development of new filters.

There are also wider aims to the research. With the ever increasing drive towards higher levels of environmental protection and legislation, there is an ever increasing demand for the extrapolation and prediction of environmental data. Many of the modelling aspects associated with filtration phenomena are directly applicable to modelling various environmental situations, particularly the migration of colloidal pollutants through soil matrices and the ageing and blocking of sub-terranean permeable reactive barriers. On a less direct level, there is the possibility of modelling the interactions of environmental components with instrumental columns in high performance liquid chromatography (HPLC) or gas chromatography (GC) instruments.

The work in this research project has as its foundations the technical and manufacturing expertise of Porvair Filtration Group Ltd (Fareham, UK), and the porous media and fluid modelling expertise already developed within the Environmental and Fluids Modelling Group at The University of Plymouth (Plymouth, UK).

### **1.2.1. Porvair Plc. and the filtration industry**

Porvair Filtration Group Limited (PFG) is a specialist filtration and separations company. It consists of four divisions; Microfiltrex, Porvair Technology, Filters for Industry and MF&T. These divisions design and manufacture filtration and separation systems for technically demanding environments in industries including aerospace, biosciences, chemical process, power generation, pharmaceutical, environmental and food & beverage. Continuous development of products & materials are vital to allow PFG to offer new and better solutions to applications. Between 20 & 30% of annual sales are made with products that are less than three years old, with a significant proportion of the workforce dedicated to product and process development. Development plays a fundamental part in PFG's operations and as a result, the company has developed a number of new bespoke products based on its established porous polymeric materials (known as Vyon®) and sintered metal media (known as Sinterflo®).

The company is increasingly dedicated to developing strong industrial and academic links so that they may invest in projects which offer the prospect of attractive market growth whilst continuing a sustainable benefit to its shareholders, staff and other stakeholders. Such commitment to investing in the future of the industry can only benefit the future of filtration technologies on the whole and has led to many project successes, many of which



are now included into current manufacturing and development processes within the company.

The total world sales of filtration and separation equipment were estimated at \$29.5 billion in 2003. It has also been forecast that overall growth of the industry is set to exceed 34% between 2004 through to 2009. This large predicted increase has many drivers, such as the ever increasing demands of government legislations on environmental and health issues, and increasing geographical markets such as China and South America (Sutherland, 2004).

### **1.3. Theory and literature review**

The following review of theory and literature aims to highlight how the study of transport and flow through porous media may be directly applied to the development of filtration models, and also gives an overview of the types and context of models which are already in existence.

#### **1.3.1. Porous media**

A porous medium can be described as a solid body containing many holes/voids and tortuous passages. The term Porosity is used to describe the volume fraction of the media which is applicable to the total void space. If fluid is then flowed through the medium, the fraction of this porosity that contributes to the flow transfer is termed the effective porosity (Cheremisinoff, 1983). Extremely small voids may be termed molecular interstices and extremely large ones caverns (Scheidegger, 1974). Laudone (2005) states that pores have an intermediate size, between molecular interstices and caverns, and that they may be

interconnected or isolated, as shown (figure 1.1.) Traditionally the smaller interconnecting pores have been called throats. Pores are found to exist in nearly every body. These pores range in size from those visible with the human eye, such as holes in sponges or soil, to those which may only be visible with the aid of microscopy such as the pores in human skin or in tight rock structures (de Boer, 2003).

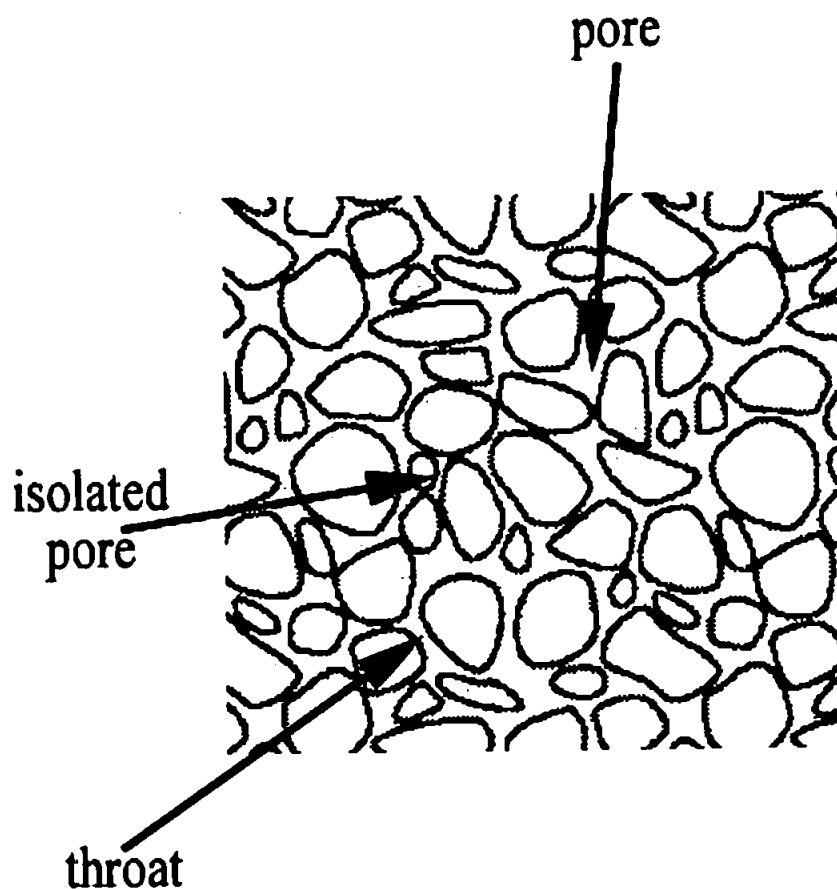


**Figure 1.1 Representation of a porous medium showing isolated pores, pores and interconnecting throats (Laudone, 2005)**

Although porosity is a useful characterisation parameter, it is not possible to describe the full structural parameters of a porous media by this term alone. Pore/throat size distribution, connectivity, surface area, tortuosity and permeability are of fundamental importance in giving a valid description of the sample in question. Schoelkopf (2002) gives a good schematic representation of differing categories of porous media as reproduced in figure 1.2.

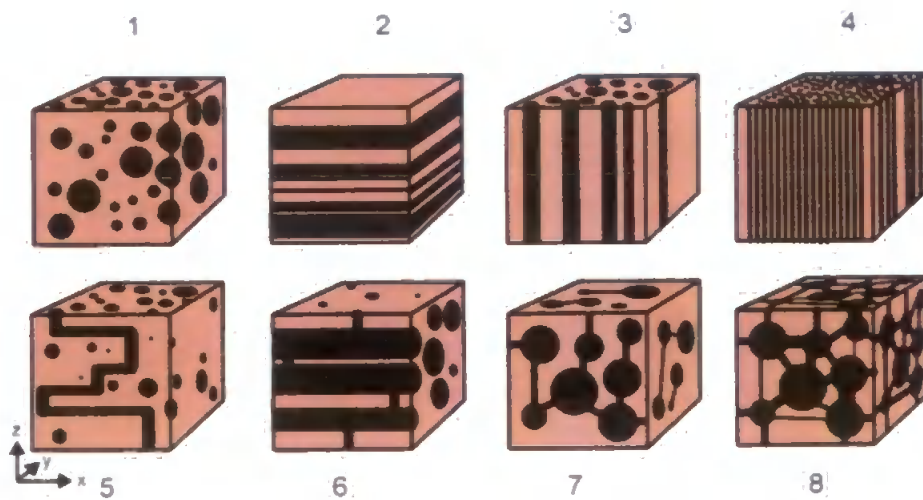


Figure 1.2 Schematic of various porous media types (Schoelkopf, 2002)

In the schematic (1) shows a porous media solely containing isolated pores, while (2) shows a strongly anisotropic structure. Representations (3) and (4) show two bundle-of-capillary structures which contain similar porosity but differing average pore diameters. (5) depicts a structure which contains no connectivity between pores but has a high tortuosity through the structure, while (6) shows a structure containing a small connectivity parameter and high tortuosity and isotropism. Structures (7) and (8) show pore and throat network structures both containing similar levels of tortuosity but, differing in their respective permeability.

### **1.3.2. Filtration**

Filtration is a unit operation designed to separate suspended particles from a fluid stream by passing the solution through a porous medium, the porous medium thus being termed the filter. The process of liquid filtration may be classified into two main types (Cheremisinoff, 1983), these being cake filtration and filter-medium filtration. In filter-medium filtration, the media provides a filter with a significant depth profile so that the porous path is both tortuous and random in design. Retention efficiency of fluid stream particulate then occurs by means of a series of low efficiency capture mechanisms within the pore structure of the media (Dickenson, 1997). Filter-media filtration is generally used with fluid streams containing dilute suspension of particles ranging in size from 0.1 to 60  $\mu\text{m}$  (Osmak et al, 1997) although in specific cases particle sizes may be outside this range. The dilute nature of the suspension leads to a higher probability of particles entering the porous structure rather than undergoing particle-particle interactions which may lead to the blocking of the filter surface by formed aggregates.

Cake filtration relies on solid particles found in the fluid stream being collected on the upstream surface of the filter medium, thus forming a cake of contaminant particles over time. This cake itself forms a filter which is found to offer an increasing filtration efficiency over time as the filter-cake evolves to trap finer particulate (Dickenson, 1997).

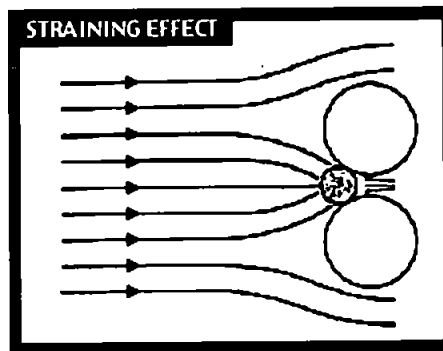
#### **1.3.2.1. Filtration in the context of this thesis**

The work found in later chapters of this thesis is solely directed at the study of the 'filter-medium' classification of filtration and associated media characteristics. One of the most important considerations, in terms of producing an effective model, is how to simulate

particulate deposition in the filter media. There are six main categories of interactions that cause particle deposition within filtration media. As such it is necessary to decide on a balance between inclusion of these mechanisms into a final model and the complexity and computational time increase that is incurred to deliver a sufficiently accurate model for the given media. The mechanisms of particle capture can be summarised as follows:

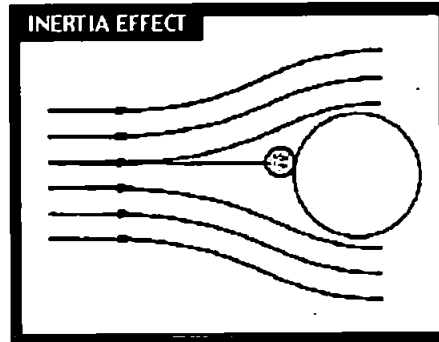
### 1) Straining

Straining is also referred to as Sieving, and occurs when particles are found to be larger than the opening of a given pore or throat feature. The particles can not pass through the opening and are thus collected at its entrance, blocking the feature from further active flow.



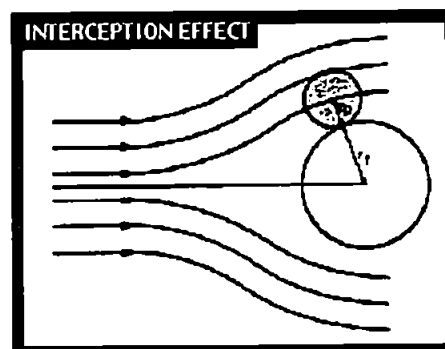
## 2) Direct Impact

Direct Impact, also referred to as Inertial Impingement, relies on flow velocity and particle mass to cause particles to leave the fluid stream and impinge (or impact) the pore/fibre surface directly.



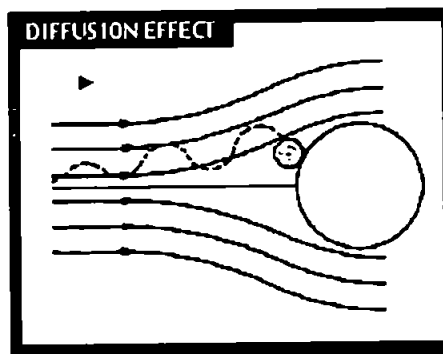
## 3) Interception

Interception occurs when particles are small enough to follow the fluid stream through pore space and around the solid phase features (particles/spheres) of the media. They are intercepted by the feature surface due to the dimension of the particle radii being larger than the distance between the feature and fluid stream path the particle is following. Upon interception the particle becomes held to the fibre by Van der Waals forces and other electrostatic effects if present.



#### 4) Diffusion

Diffusion, also referred to as Super Interception, occurs on particles of  $<1\mu\text{m}$  diameter which have sufficiently low mass as to exhibit Brownian motion. Brownian motion causes the particle to diffuse through fluid streams and thus increases the probability of the particle coming in contact with the surface of the solid phase features. The smaller the particle, the more pronounced its diffusion becomes and the stronger the effect.



#### 5) Critical velocity deposition

Another mechanism of particle deposition found in filter media is similar in principle to that of direct interception, and is termed Critical Velocity Deposition. Due to the complex and often inhomogeneous character of filtration media, it is found that the velocities of fluid streams through a given unit are changeable according to the surrounding pore geometry. If the fluid stream velocity drops below the level required to keep a particle of a given mass suspended in solution, the particle will drop out of solution and adhere to the pore surface with the aid of Van der Waals' forces.

## 6) Other factors

In addition to the previously stated mechanisms, there are a number of other complicating factors that affect a particle's deposition. These include particle-particle interactions in the fluid stream, and also the surrounding chemistry of particles, filtration media and carrier fluid. Also to be considered is the effect each deposition of a particle has on the given pore or throat fluid velocity. The nature of such dynamic velocity changes within a filter can also lead to re-entrainment of particles into the fluid stream. This combined with particle-particle interactions can lead to the requirement of the filter to undergo a second collection of the same or larger size particles in the auxiliary pore network.

In this work the model only takes account of straining processes and basic critical velocity deposition. Diffusion phenomena are not significant for the particles in the size range we are considering ( $>1\mu\text{m}$ ). As shown in the following figure (Figure 1.3), a relationship can be seen between capture efficiency ( $\eta$ ) and particle size ( $d_p$ ). Particles decreasing in size from  $1\mu\text{m}$  show an increased capture efficiency due to the increased effect of Brownian motion (as particle mass is reduced) creating higher rates of diffusion and thus rendering them more susceptible to particle deposition through the diffusion mechanism. In contrast to this, as particle sizes increase above the  $1\mu\text{m}$  point, the particles are found to experience greater capture efficiency. This is explained in terms of the higher particle size (and consequently mass) offering a greater level of inertia in fluid streams, thus leading to them becoming more susceptible to undergo straining, direct impact and interception.



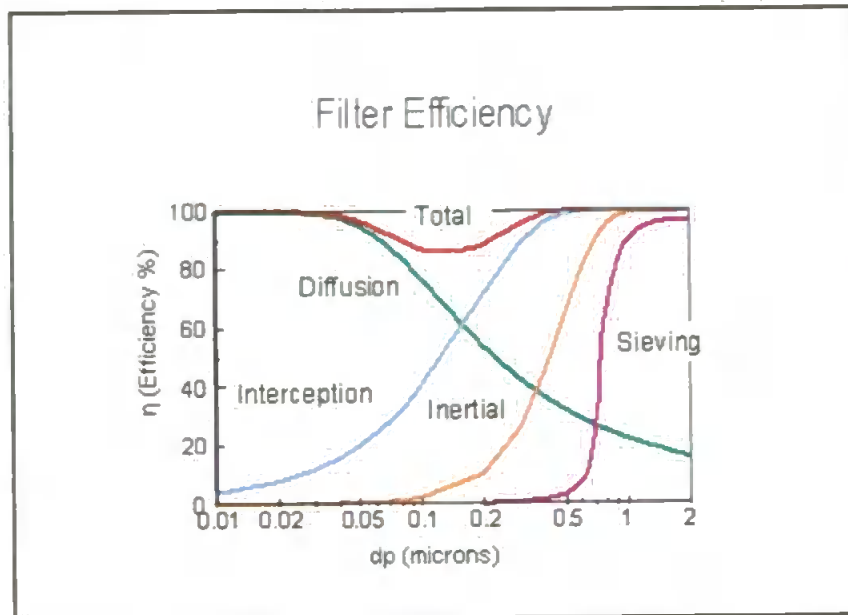


Figure 1.3 Graph showing relationship between particle size ( $d_p$ ) and capture efficiency ( $\eta$ ) for the four main particle capture mechanisms.

### 1.3.3. Fluid flow in porous media

The physical basis of both saturated and un-saturated flow in porous media has been understood for over a century (Mathews, 1999). The result of this understanding has led to the derivation of a number of mathematical expressions to describe situations of varying complexity from microscopic scale studies through to field and reservoir scale scenarios. Microscopic level studies are generally aimed at describing the pore level interactions of fluid flow and media interaction while the larger field and reservoir studies have aimed to characterise how these pore level mechanisms manifest over length and depth scales from less than one meter to large scale field studies of pollutant transport through such porous media as soils and oil reservoir sandstones (Butters, 1989; Yao, 1997).

### 1.3.3.1. Hydrodynamics of fluid flows

#### 1.3.3.1.1. Saturated flow

Historically the theory of saturated flow within porous media is based on the experiments of Henry Darcy in 1856. Darcy presented a phenomenological law based upon his study of the flow of water through granular media used as filters for the supply of water to the French city of Dijon. The law states:

$$q = \frac{K \Delta p}{L} \quad \text{Equation 1. 1}$$

where  $q$  represents the flow rate ( $\text{m s}^{-1}$ ) through the porous bed,  $\Delta p$  is the hydrostatic pressure difference across the porous bed,  $L$  is the length of the porous bed in the direction of flow and  $K$  is a constant dependant on the properties of the fluid and the porous medium.

The permeability ( $k$ ) of the bed may be defined as:

$$k = K \eta \quad \text{Equation 1. 2}$$

where  $\eta$  is the fluid viscosity. Permeability is measured either in area or Darcy units:

$$1 \text{ Darcy} = 9.87 \times 10^{-13} \text{m}^2.$$

The Darcy law is a phenomenological rule that ascribes a permeability to any system where experimental values of pressure drop and flow rate can be measured. However in the modelling of hydrodynamics it is necessary to consider the fluid mechanics of the fluid

within the porous media itself. There are two possible aspects of the mechanics of fluids: macroscopic and microscopic (Bodurtha, 2003). The macroscopic aspect is manifested in the 'continuous matter theory', meaning the fluid is treated as a continuous medium and the microscopic aspect is obtained if the molecular structure of the fluid is taken into account.

The motion of a continuous fluid can be described geometrically if the position of every material point of the fluid is known at every time-instant. This is achievable using the Navier-Stokes equations, applicable to incompressible viscous fluids (Borhan et al, 1993; Moshinskii, 1997) which may be stated as:

$$\mathbf{v} \text{ grad } \mathbf{v} + \delta \mathbf{v} / \delta t = \mathbf{F} - (1/\rho) \text{ grad } P - (\mu/\rho) \text{curl curl } \mathbf{v} \quad \text{Equation 1.3}$$

Here  $\mathbf{v}$  is the local velocity-vector of a point of the fluid,  $t$  the time,  $\mathbf{F}$  the volume force per unit mass, and  $P$ ,  $\mu$  and  $\rho$  are the pressure, viscosity and density of the fluid respectively (Scheidegger, 1974). The boundary conditions prescribe that the fluid velocity at the walls of the container equal zero hence,  $V = 0$  at the container wall. This assumption may be considered valid when considering the parabolic velocity profile of laminar viscous flow of an incompressible fluid in a capillary tube and the velocity distributed about the axis of the tube. The maximum velocity is found down the centre of the tube and represented by  $V_{\max}$  as shown in Figure 1.4

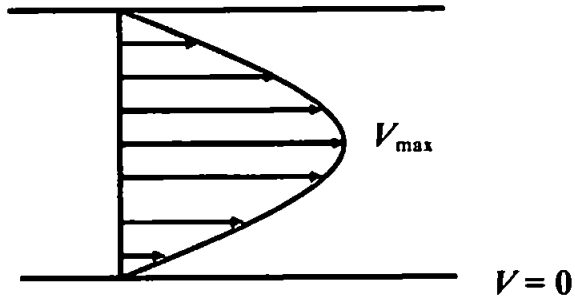


**Figure 1.4** Parabolic velocity profile for laminar flow in a cylindrical tube.  $V_{\max}$  shows the point of maximum fluid velocity and at the container walls  $V = 0$ .

The Navier-Stokes equation can be implicitly solved for a straight cylindrical tube by use of the Hagen-Poiseuille equation:

$$Q = -\frac{\pi \Delta P r^4}{8 h \eta} \quad \text{Equation 1.4}$$

where  $Q$  is the volume flow rate passing through the cylindrical tube of radius  $r$  and length  $h$ , with a pressure difference from end to end of  $\Delta P$ . If a simplistic approach is taken to the structure of a porous medium and it is represented as a bundle of straight capillary tubes as shown in Figure 1.5, the Hagen-Poiseuille equation may be used to give an overall permeability of the medium.

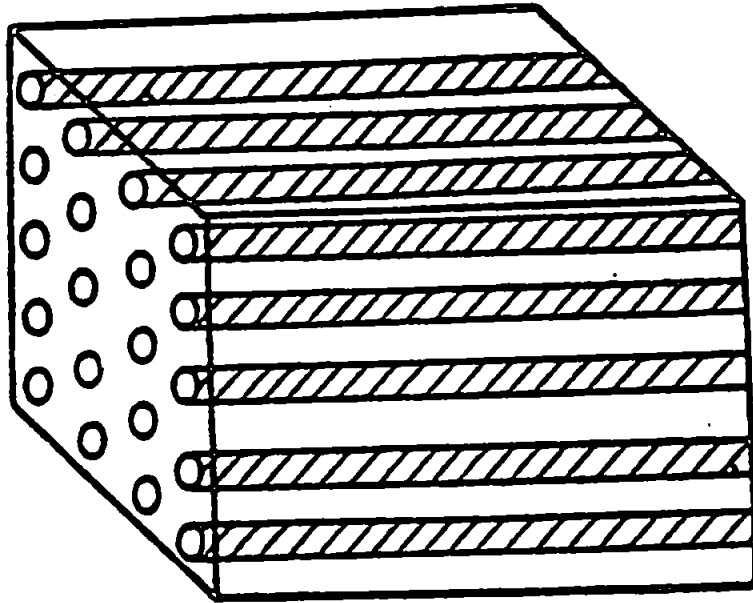


**Figure 1.5** A classical representation of a porous medium using a bundle of straight cylindrical tubes as the porosity fraction of a solid.

If the medium has  $n$  capillaries per unit of cross sectional area the flow, per unit area, of the medium can be stated in terms of the Hagen-Poiseuille equation as:

$$q = \frac{n \pi d^4}{128 \eta} \frac{dp}{dx} \quad \text{Equation 1.5}$$

where  $\frac{dp}{dx}$  is the pressure gradient across the capillaries. According to Darcy's law the

same volume of flow per unit area can be expressed as  $q = -\frac{k}{\eta} \frac{dp}{dx}$  so it follows that:

$$k = -\frac{n \pi d^4}{128} \quad \text{Equation 1.6}$$

If  $d$  is considered to be an averaged representative pore diameter of the given medium it is also possible to express the permeability ( $k$ ) of the medium in terms of its porosity ( $\phi$ ) as:

$$k = \frac{\phi d^2}{32} \quad \text{Equation 1.7}$$

However this is a very simplified model of flow through porous media as it does not consider the complexities of a real sample, such as tortuosity and connectivity. This theory is therefore only valid for the simplest of capillaric models namely, the parallel straight cylindrical tube representation (Figure 1.5). This has led to a number of efforts to improve this simplistic approach.

One of the most widely accepted improvements to the early capillaric models of permeability is the 'Kozeny theory', although there have been some severe objections against its validity to all porous media (Coulson, 1949; Childs et al., 1950). The Kozeny theory relates the flow rate to a nominal thickness/length of the sample. It achieves this by representing the medium as a collection of flow channels of various cross sectional area but of a fixed length. The sum of these cross sectional areas represents the specific surface,  $S$ , of the medium which is active in transferring flow. The difference between specific area and the total surface area of the medium is attributable to solid. In relation to the previous discussion,  $S$  may be visualised as a surface porosity. The Navier-Stokes equations are then simultaneously solved for all channels passing through a cross-section normal to the flow in the porous medium. The permeability may then be expressed in terms of the specific area by:

$$q = -\frac{c\phi^3}{\eta S^2} \text{grad } p \quad \text{Equation 1.8}$$

Comparing this with Darcy's law we obtain for the permeability:

$$k = c\phi^3/S^2 \quad \text{Equation 1.9}$$

where  $c$  is the 'Kozeny constant' and all other factors are as previously attributed. The theoretical Kozeny constant is found to fluctuate very little depending on the geometric shape of the capillary channels. For comparison, for a circle  $c = 0.50$ , for a square  $c = 0.5619$  and for an equilateral triangle  $c = 0.5974$ . The relationship shows that the flow velocity of the porous medium,  $q$ , is inversely proportional to the square of the specific surface area per unit volume,  $S$ .

The Kozeny equation may also be adapted to include a tortuosity term  $T$ , which although arbitrary allows the variance in length of the capillary channels away from the apparent media length to be considered. It indicates that the flow path of fluid is  $T$  times longer than the direct or straight path length across the medium. This leads to an expression for the permeability:

$$k = c\phi^3/(TS^2) \quad \text{Equation 1.10}$$

The Kozeny theory is intended to have general applicability to all porous media as the constants  $c$  and  $T$ , theoretically, involve only the detailed structure of the medium. However it should be noted that the concept of tortuosity does not appear in the actual deduction of the equation and is only justifiable as an extended fitting parameter.

A much used modification to the Kozeny theory is that postulated by Carmen (Carmen, 1939). The Kozeny-Carmen equation is:

$$k = \phi^3 / [5S_o^2(1 - \phi)^2] \quad \text{Equation 1. 11}$$

where  $S_o$  is Carmen's 'specific' surface exposed to the fluid, i.e. the surface exposed to the fluid per unit volume of solid (not porous) material. Equation 1.11 is often used with the Kozeny constant,  $c$ , equal to 0.2, as according to Carmen this gives the best agreement with empirical findings. This is in contradiction to the earlier Kozeny theory which suggests that values of  $c$  are approximately around 0.5. This contradiction provides one of the doubts to the validity of the Kozeny theory mentioned previously.

#### 1.3.3.1.2. Unsaturated flow

When a source of wetting liquid comes into contact with a porous structure, capillary forces at the interface between the fluid, pore walls and displaced fluid (usually air or vacuum) cause the fluid to enter the pore network. The fluid must accelerate from rest, against its inertia (Matthews et al., 2008). Individual wetting events may be described approximately



by the Bosanquet equation (Bosanquet, 1923), which, in a force balance equation, equates the inertial and viscous forces to the force due to applied pressure and the capillary force, respectively:

$$\frac{d}{dt} \left( \pi r^2 \rho x \frac{dx}{dt} \right) + 8\pi \eta x \frac{dx}{dt} = P_e \pi r^2 + 2\pi r \gamma \cos \theta \quad \text{Equation 1. 12}$$

Here  $x$  is the distance travelled by the liquid front in time  $t$  into a cylinder of radius  $r$ ,  $\rho$  is the liquid density,  $\eta$  its dynamic viscosity,  $\gamma$  is the interfacial tension and  $\theta$  is the contact angle of the fluid meniscus with the wall of the tube.  $P_e$  is the external pressure applied at the entrance of the capillary tube.

Wetting according to the Bosanquet equation causes advance wetting tracks, often in features of low volume, which occur at very short time intervals (Schoelkopf et al, 2000). At longer times, the wetting process integrates (Bodurtha et al, 2005) to a behaviour described by Washburn (1921) and Lucas (1918). They obtained a time-dependency for the uptake of a wetting fluid into a cylinder, by assuming that the flow was laminar and could therefore be described by both the Poiseuille and Laplace equations. The Lucas-Washburn equation is:

$$x^2 = \frac{r_h \gamma \cos \theta}{2\eta} \quad \text{Equation 1. 13}$$

where  $x$  is the distance travelled by the liquid front in time  $t$ ,  $r_h$  is the effective hydraulic radius and  $\eta$  is the dynamic viscosity. The equation assumes there is no applied pressure,

and there is no effect due to a hydrostatic head. Many permeation experiments show at least superficial agreement with Equation 1.13, with an uptake distance approximately proportional to  $\sqrt{t}$ . The equation therefore continues to be used, despite the fact that in porous networks  $r_h$ ,  $\theta$  and  $\gamma$  have no precise physical basis.

This approach to modelling the unsaturated flow of liquid into porous media is generally accepted although it fails to consider the detail of wetting fluid imbibition shown in Figure 1.6, to which the following numbers in parentheses refer.

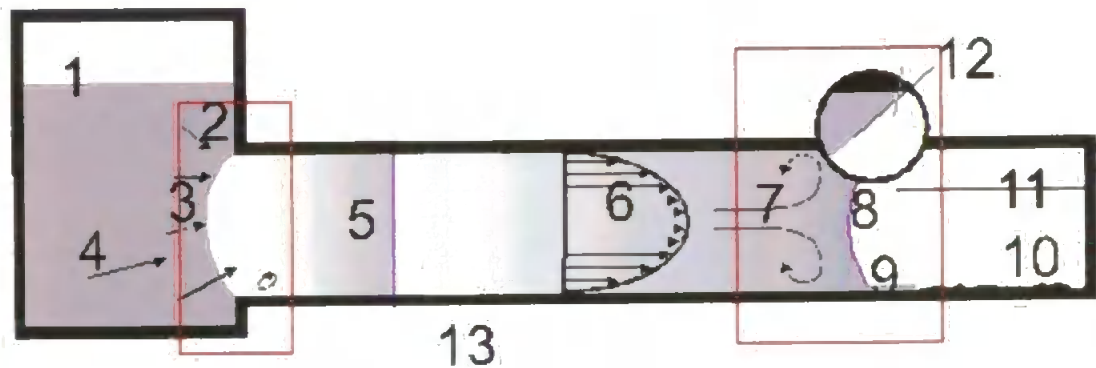


Figure 1.6 Schematic overview of the of the influences dictating unsaturated flow in porous media from a reservoir (left) into an evacuated capillary tube (Scoelkopf et al., 2000).

The first is the uncertainty in the contact angle between the fluid and respective media (12), and the exact meniscus shape that is ensuing (8). Although easily observable these characteristics are related to more subtle factors such as the condition of the capillary's inner surface, such as cleanliness and the existence of micro roughness (10, 11). Wetting events under this level of inspection are also found to be greatly affected by the

development of pre-cursive wetting films (9) which can be anything from a monolayer to a bulk mass of fluid. There are also meniscus distortions due to 'fountain flow' close to the wetting front (7) and the presence of dynamic effects at the reservoir entrance region (1-5) that are complex in nature. There is also inconsistency between the implicitly assumed flow profiles as the Poiseuille flow velocity profile is incompatible with the concave nature of the meniscus caused by the force along the contact line (6).

Although these complexities do exist, they are rarely addressed in literature. In this work, the generated network structures are constructed from highly simplified pore geometries, so it is reasonable also to use simplified descriptions of imbibition and flow.

#### **1.3.4. Modelling of Porous media and filtration processes**

The understanding of porous media and hydrodynamics associated with them, described previously, is directly applicable to the discussion of filtration and its related principles. As this knowledge has increased there has been a correlated rise in studies which aim to model these phenomena, and as such a diverse range of filtration models has already been reported in the literature. The scale of the models varies from pore level to characterisation of total pore structure of a filter, and the approaches range from the purely mathematical (Osmak et al, 1997; Free et al, 1998; Polyakov et al, 2003) to semi-empirical (Lin, 2004; Le Coq, 1999). Due to the diversity of these models it is necessary to classify them.

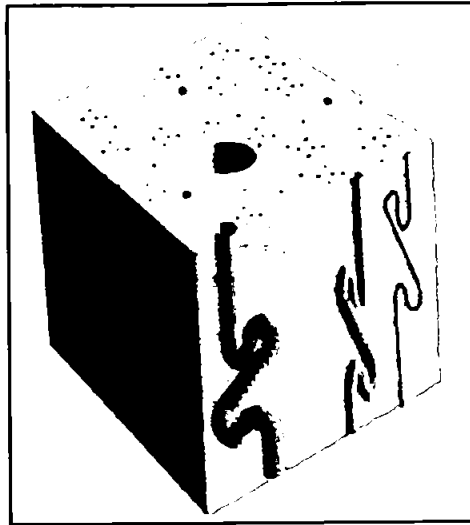


**Figure 1.7** A conventional capillary bundle type model of porous media using capillary worm holes as a simplification of the true connectivity and tortuosity of a real sample.

The simplest classification applied is whether the structure used to represent the filtration medium is realistic in nature. Models based on highly idealised structures, such as capillary bundle approximations (Figure 1.7), are referred to as “*conventional*” models, whereas those utilising a realistic structural approach (e.g. pore and throat void space between packed sphere structures) are classified as “*advanced*” models (Figure 1.8). Conventional structures lack the realistic pore representation found in the advanced model simulations, but lower the complexity of calculations used to model fluid dynamics, interactions between contaminant particles and filter media (Guo et al, 2002). It should also be noted that these conventional models fail to predict (with any reasonable accuracy) the reduction in media permeability and macroscopic pressure drop as these phenomena are very sensitive to the connectivity of the pore structure, which is not considered in these conventional approaches (Sahimi et al., 1990). In contrast the advanced model approaches require much more sophisticated calculations of fluid dynamics and particle deposition, due to the variable nature of these factors and the inclusion of connectivity and tortuosity.

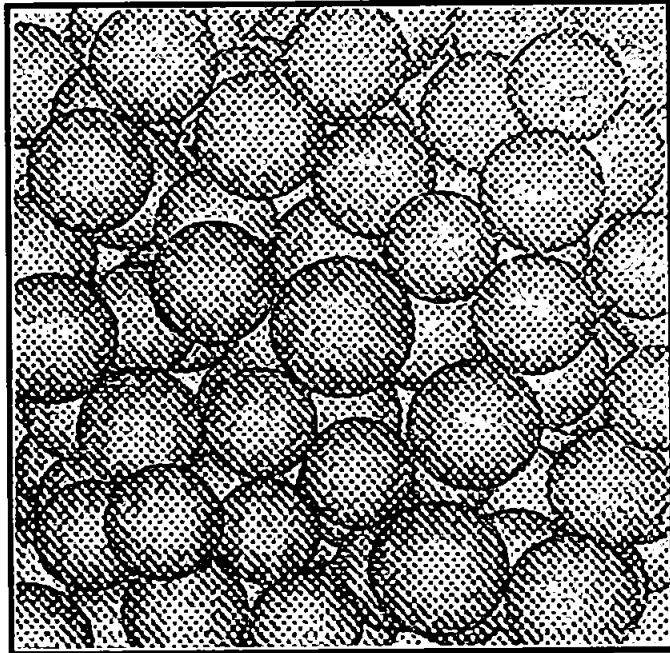


**Figure 1.8** A Monte-Carlo type generation of an advanced packed sphere pore network utilised in determining pore structures of some advanced models.

Another method of classification for distinguishing between filtration models is that of “*external*” or “*internal*” flow (Rajagopalan and Tien, 1979). External flow models consider the fluid flow to be passing over a series of collectors (elements within a flow stream onto which particles may collide and adhere) instead of pores. In this case the media is modelled as orderly packed spheres (Figure 1.8) or solid cylinders to build the collector network. In internal models the emphasis is placed upon the pores, with the media generally represented as a capillary bundle (Figure 1.7) or constricted tube type arrangement (Elimelech, 1995). This simplification of pore structure, again containing a lack of multiple connectivity between pores, reduces the complexity of calculations required to model particle deposition but leads to problems when particles are similar in size to capillary openings (Lee & Koplik, 2001; Sahimi et al., 1990).

A further classification of porous media/filtration models is that of the '*continuum*' or '*discrete*' approach. The continuum approach to modelling represents the classical engineering approach to describing materials of complex and irregular geometry characterised by several length scales. The approach uses the averaging of properties such as permeability, effective transport coefficients and reaction rates over a given volume of the media. This volume must however be large enough for these properties to manifest a sufficiently accurate value but small compared to the overall volume of the system so that heterogeneities in observed samples may be accounted for. The continuum approach cannot describe microscopic phenomena such as pore plugging or changes in connectivity of the system. The application of such an approach offers a greatly simplified picture of the complexities involved and, where it is suitable (Whitaker, 1967; Slattery, 1967), gives a sound macroscopic description of the media in question.

The discrete approach to modelling frees itself from the limitations described above by taking a more advanced description of the system and its microscopic complexities. These models are found to give a much more realistic view of the media in question and aim to describe the overall system phenomena such as permeability and particle capture through the amalgamation of the microscopic terms (although generally simplified) within the media. This enables the modelling of permeability and pressure difference of the system at the pore level and also the dynamic changes in pore plugging and resultant decline in connectivity. The main shortcoming of such approaches is the large computational power that is required for a fully realistic discrete treatment of a system (Sahimi et al., 1990). The ever increasing power of modern computers has allowed large steps forward in such approaches, although a desktop level model with true predictive capability remains elusive.

#### **1.3.4.1. Model types associated with filter-medium filtration**

Filter medium filtration (in the form of deep bed filtration (DBF)) has been used to remove polluting particles from drinking waters since the early 1800's. Although the technology is widely applied today in many fields, the underlying mechanisms responsible for particle removal are not well understood and are still the subject of much research.

Particle capture in filter-medium filtration (FMF) includes the following mechanisms: straining, interception, diffusion and impaction and other media-fluid-particle interactions (as given in section 1.3.2.1). In liquid FMF, inertial forces are not important (Tien, 1989) and the impaction mechanism is only applicable to gas filtration. As has already been stated (1.3.2.1) brownian size particle ( $<1 \mu\text{m}$ ) transport is dominated by convection and diffusion (Elimelech and O'Melia, 1990; Tien, 1989) which is not generally considered in liquid FMF. In the case of particles in the range  $1 \mu\text{m}$  to  $10 \mu\text{m}$ , the transport process is dominated by physical forces (gravity and fluid drag) and by interception due to the finite size of the particles while particles greater than  $10 \mu\text{m}$  tend to undergo straining (sieving) processes (Yao et al., 1971; Tien, 1989).

Elimelech and O'Melia (1990) divided the process of the deposition of fines into two sequential steps: transport and attachment. In the first step, particles are transported from the bulk of the fluid to the vicinity of the modelled pore system and then in the second step they undergo some form of capture mechanism. The development of a filtration model should consider a three step process (Elimelech, 1995). The first of these is to produce a representative network. The second is to then develop a system for representing fluid flow through the given network and the final step is to apply the particle contamination and relevant capture mechanisms.

FMF analysis and modeling was mainly empirical until Herzig et al. (1970) developed the conservation equations that govern the process. A key parameter used in the FMF or DBF equation is the particle capture efficiency of suspended fines that must be acquired or estimated by a particle capture model.

There are many models reported in literature which aim to provide an acquisition or estimation of valid results for particle capture efficiency, permeability and pressure drop functions within simulations of filtration processes. Models can be divided according to the following classification (Rege and Fogler, 1988):

- Empirical models
- Stochastic models
- Trajectory Analysis
- Network models

Excellent reviews on the subject can be found describing the limitations and capability of each model type; e.g., Tien and Payatakes (1979), Herzig et al. (1970), Rege and Fogler (1988) and Burganos et al. (2001). In the following text only brief summaries of these modelling approaches are provided with the exception of the network model approach, the most relevant to this work, which is discussed in greater depth.

#### **1.3.4.1.1. Empirical models**

Empirical models, originally developed by Ives (1960) and Heertjes et al. (1967), solve a simplified filtration equation that includes simple laws involving empirical parameters developed from observational facts for the rate of deposition. They manifest as models



adhering to the continuum approach of porous media and as such have been criticised for their lack of consideration of pore morphologies, and in ability to predict permeability decline and effluent concentrations. Depending on the events observed during the filtration process, the rate of deposition is related to the initial or clean filter coefficient, a function of the velocity and concentration of fines. Most of the parameters used must be obtained by retro-fitting experimental data. Examples of empirical models can be found elsewhere (Tien, 1989; Herzig et al. 1970; Tien and Payatakes, 1979); while simple in nature, these models do not provide insights into the mechanisms of filtration and are naturally, by design, restricted to the studies for which they were developed. More sophisticated empirical models have been devised such as that by Gruesbeck and Collins (1982) where the productivity of producing wells was predicted using a model which considered two pore types. The first were those smaller in size than the suspended particles and hence susceptible to straining (pore plugging) and the second, larger pores where a non-plugging deposition could occur. Deposited particles found in the larger pores could also be re-entrained into the system leading to secondary events blocking the smaller pore representations. The model allowed the estimation of permeability decline for the media although this was undertaken using unquantified phenomenological constants.

#### **1.3.4.1.2. Stochastic models**

Stochastic models use a probabilistic approach in considering FMF (Rege et al. 1988). An example of this type of model was developed by Hsu and Fan (1984). The state of a pore (clean or plugged) is considered an event whose probability is determined by solving a certain probability law related to the velocity of the fluid and the local permeability (Hsu and Fan, 1984). This model has parameters that must be obtained by retrofitting

experimental data. The model does not however consider the effects of pore size and particle size distributions as it is developed for pores of uniform size. It also fails to consider effluent concentration profiles, so its usefulness is rather limited.

#### **1.3.4.1.3. Trajectory analysis models**

Initially developed by Payatakes (1973), trajectory analysis models represents the filter media as a number of unit bed collectors, as in the external classification mentioned previously. Particle deposition is then calculated using streamline Lagrangian trajectory calculations of the fluid stream particles and their interaction with the collectors from several forces such as gravitational, hydrodynamic, van der Waals and electric double layer. The deposition is calculated by constructing appropriate equations of motion that include the short and long range forces acting on a spherical particle. Depending on the distance separating the particle and the surface of the collector, long and short range forces are developed and are considered within the force balance affecting the particle. If the particle is far from the surface of the collector, the force balance will include gravity and the drag forces exerted by the liquid. When the particle is close to the collector (within a few particle diameters) short range forces, such as the surface forces (van der Waals and Double Layer if present) will be included along with the gravity and liquid drag force. Deposition will then occur if the forces acting upon the particle are sufficient to adhere it to the collector surface.

While this approach to modelling filtration has been fairly successful in predictions of filter coefficient and filtration coefficients it has been found to have a number of limitations (Rege et al., 1988). Early models (such as those proposed by Payatakes, 1973) are found not to accurately predict the permeability decline due to particle deposition in filtration.

This is attributable to the use of the Kozeny-Carman equation, which is not applicable in this case due to the representation of the interconnected pore space in the modelled media (Tien et al., 1979). Many attempts at using this approach also fail to consider the change in the characteristics of the collector after deposition has occurred and as such limited the early models to representing a clean filter medium approximation. Since the development of these early models, there has been much improvement in the trajectory analysis approach which has led to a greater understanding of the pore level processes in filtration (Sahimi, 1990). One such example is that undertaken by the Fraunhofer Institute (Kaiserslautern, Germany) who, with the aid of a large dedicated team, produce highly realistic structures and particle capture processes occurring in simulated filtration runs. However, there is a huge computational requirement to run such simulations, with one simulation possibly taking a whole day to generate. At present this approach is still far beyond the capabilities of a standard desktop computer, and has little merit in the reduction of time compared to standard wet bench testing.

#### **1.3.4.1.4. Network models**

Since their inception by Fatt (1956), network models have been applied to the modelling of FMF with varying degrees of success. Network models represent the structure of porous media by construction of a network (generally 2-dimensional) of interconnected bonds or 'arcs' meeting together at nodes. The network is generally arranged under a set or random geometry that represents a level of connectivity of the structure (Figure 1. 9).

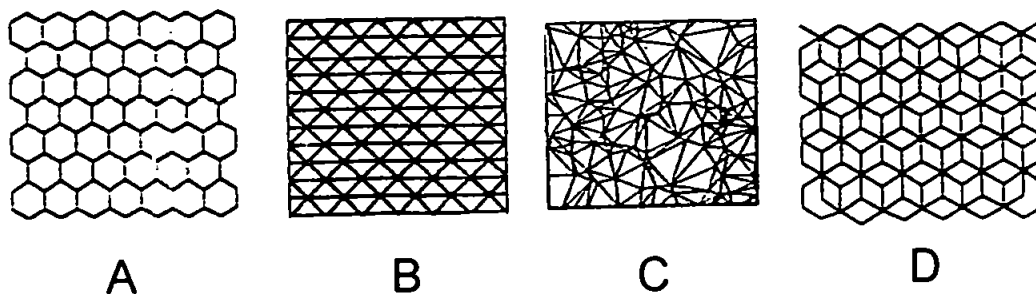


**Figure 1.9** Visualisation of some constructed 2-dimensional networks used in filtration modeling. A = Hexagonal network, B = Triangular network, C = Voroni network and D = Double Hexagonal network.

After the network geometry has been constructed each bond is then represented as a given pore or throat diameter representative of a pore/throat size distribution of the media that is being studied. This application can be randomly applied to the network by using pore size distributions obtained from experimental techniques such as mercury porosimetry or photomicrographic techniques (Dullien et al., 1970). Subsequent random applications can be undertaken a number of times so that statistical variations, 'realisations', of the structure may be achieved and later results given as averages of the media (Rege and Fogler, 1988). The bond length must also be considered and either assigned as random or related in some manner (such as directly or inversely proportional to the bond diameter) so that the structural characteristic of the network gives a valid representation of the studied media.

As stated many early uses of network models to simulate filtration have relied on 2-dimensional networks although it has been suggested (Constantinides et al., 1989) that a 3-dimensional approach is much more favourable to allow for areas of a media which contain low flow, possibly after plugging events of pores, and hence the realistic bypassing of these low permeability areas. Similarly many of these early models have relied on the use of only one void type representation (typically cylindrical throats) which are joined at nodes

representing a zero volume (Rege et al., 1988; Imdakm et al., 1991). The other problem which was apparent in early network models such as that devised by Todd et al. (1984) was the delivery of particles, 'fines', to the network and the capture mechanisms applied. Todd et al. devised a model whereby the delivery of fines around the network was undertaken by an unbiased random walk method which fails to consider the hydrodynamics and flow-field routing which is found in the dynamic flow of a real filtration media. The authors found that the model was not in quantitative agreement with the experimental data and attributed this to the inadequacies of the particle capture mechanisms that were applied. However it is suggested that the absence of a realistic flow field representation is more likely a plausible explanation to the failings of the model (Sahimi et al., 1991). These shortfalls in the simulation of particle movement around the networks have since been overcome with the application of flow-biased routings of fines through the network. This process was first developed by Sahimi et al. (1983, 1986 a,b). It allows particles to follow a realistic route through the network by first calculating the flow field in each bond by way of the Hagen-Poiseuille equation so that it is the product of its pressure difference between the two nodes and its hydraulic conductance (Imdakm and Sahimi, 1987, 1990). Once this is achieved particles may then be applied to the network via the start bonds of the network. If a particle passes through this bond without capture it arrives at the terminating node of that bond. At this point the particle selects one of several connecting bonds by a probability proportional to the flow rate of these bonds. Thus the particle undergoes transport through the network in accord with the realistic flow dynamic of the media.

Particle capture mechanisms that have been applied to such models have varied significantly in both application and success. The straining of particles from the fluid stream can be undertaken using a size exclusion process involving the relationship between

the particle diameter and the effective radius of a given pore or throat feature that is encountered as the particle passes through the network. If the particle is the same size or larger than the given feature it encounters, it can be classified as captured and as such stop flow through the following blocked bonds of the network. It must be noted however that if successful network representations are achieved, the blockage of flow to subsequent bonds may not be affected as good connectivity and consequent flow routing around the blocked feature may be present.

One problem associated with the development of network models is the application of deposition mechanisms other than straining such as those against pore/throat walls due to physio-chemical interactions. As the models are representative of the internal type classification mentioned in 1.3.4, the fluid flow is generally modelled by way of the processes analogous to the Hagen-Poiseuille flow described previously and as such does not consider the pore/throat walls as features or collectors within the flow but boundaries containing the flow. To model additional mechanisms of deposition, i.e. non-straining, it is therefore necessary to devise a secondary system characteristic whereby the contaminant particles, fluid, walls of the network or all three are assigned some given values that may be used to calculate the interaction of a particle with its environment.

Attempts to improve such models in this way have been undertaken, and have offered reasonable levels of improvement to modelling filtration where straining is not the only deposition mechanism. Imdakm and Sahimi (1987, 1991) developed a model in which the movement of particles through the network was calculated using the flow biased routing model developed by Sahimi (1983, 1986 a,b). However if a contaminant particle was directed into a network bond without its effective radius causing a straining event, its fate

became controlled by the trajectory analysis model of Payatakes and Tien (1973, 1979) until the next node was reached. Although this produced good correlation to experimental results, the model was computationally complex in nature.

Rege and Fogler (1987) developed a 2-dimensional model where, in addition to the straining principle, a probabilistic calculation was used to determine whether a particle would deposit in a throat feature of the network. The calculations effectively evaluated effective size of the given particle in terms of its physio-chemical relationship with the fluid stream and surrounding flow velocity characteristics. This effective size was then used to determine deposition by considering a simplified relationship between itself and the radius of the given throat feature. If the result of the calculation tended toward unity the deposition probability was high, and as it reduced in magnitude the particle was more likely to pass. This model proved reasonably successful in modelling various experimental results and as consequence it has been adapted elsewhere (Wenrong et al., 1996).

### **1.3.5. Pore-Cor**

#### **1.3.5.1. Structural characteristics and construction of the model unit cell**

The Pore-Cor software which was continually developed throughout the course of this study contains features of all the model classifications described above (Section 1.3.4). It represents a compromise between the highly advanced models and those of simplified nature derived from empirical data. Pore-Cor stands for Pore level properties Correlator. It is a software package which allows the study of any mesoporous or macroporous solid, i.e. a solid with pore sizes  $> 2$  nm (Rouquerol et al, 1994). Pore-Cor has been previously used

to model a range of materials such as soil (Pete et al., 2000; Johnson et al., 2003), sandstone (Matthews et al, 1996) and paper coating (Gane et al, 1996; Laudone, 2005). The model approximates the geometry of each void network as a unit cell with periodic boundary conditions containing 1000 cubic pores connected by up to 3000 cylindrical throats, arranged in a regular Cartesian array (Figure 1. 10).

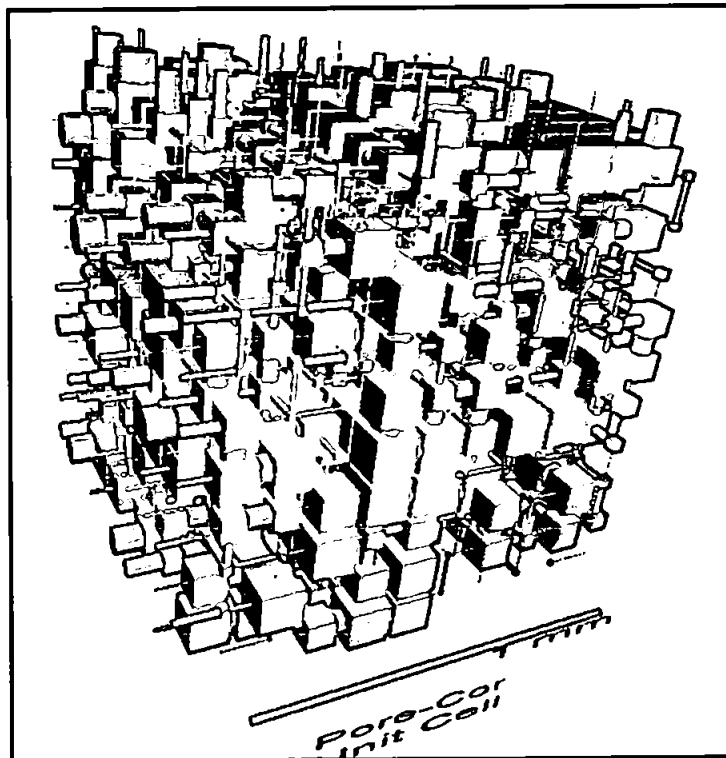


**Figure 1. 10** Simulated Pore-Cor network representation showing cylindrical throat and cubic pore representation arranged in a 3-dimensional cartesian array.

Although this unit cell may not be wholly representative of the analysed sample, its size is constrained by the computational capability of modern CPU's and the effectiveness of the Dinic flow field calculation inherent in the software. Ahuja et al (1997) have shown that that the Dinic algorithm increases CPU time requirement in the order  $n^2m$ , where  $n =$



number of pores and  $m$  = number of throats, therefore even small increases in the number of pore features used for the calculation create huge increases in the computation time of flow through the network structures. It is for this reason that the current model utilises the  $10 \times 10 \times 10$  cubic format. Future advancements may aim to increase this size to make it more representative of the reality although at present it is deemed sufficient in most cases and were not, sets of unit cells are used so that an averaging function may be used to give a more “useable” result.

The generated network structures created by the software are constructed under the criterion that they hold the same percolation characteristics as those derived from an experimental mercury intrusion experiment. A stochastic generation of the experimental mercury intrusion curve is undertaken by the iterative fitting of pore and throat sizes until a “closest fit” structure is found. This fitting process is undertaken using an annealed simplex algorithm which is analogous in working to finding the global minima of a 5-dimensional surface. Here we present an overview of the relevant aspects of the software to this work while a detailed discussion of the advanced computational aspects of the algorithms used in Pore-Cor may be found in literature (Matthews, Bodurtha, Price *et al*, 2004).

To simulate mercury intrusion a computational representation of mercury is applied to the maximum  $z$  (top) face of the unit cell only, and percolates in the  $-z$  direction, (Figure 1. 10) The throat skew, pore skew, connectivity (average number of throats per pore), and short-range size auto-correlation are adjusted by the 5-dimensional Boltzmann-annealed amoeboid simplex (Johnson et al., 2003; Teukolsky, 1991) to give a close fit to the entire experimental mercury intrusion curve. There are three additional Boolean constraints on

the simplex: it rejects structures in which the network is fragmented, in which voids overlap, or which cannot be adjusted to give the experimental porosity without contradicting the experimental percolation characteristics.

The throat size distribution is of a flexible log/Euler-Beta form, which encompasses Gaussian like, Poisson like and bimodal distributions. The probability density function, representing the probability that the distribution lies in a small interval  $[x, x+dx]$  is

$$f(x; \zeta, \eta) = \frac{1}{\Psi(\zeta, \eta)} x^{\zeta-1} (1-x)^{\eta-1} \quad \text{Equation 1. 14}$$

where:

$$\Psi(\zeta, \eta) = \int_0^1 x^{\zeta-1} (1-x)^{\eta-1} dx \quad \text{Equation 1. 15}$$

is the ‘Beta function’.

The Log/Beta distribution uses two parameters, known as ‘Throat Deviation’ and ‘Throat Skew’. Throat Deviation is a measure of the ‘fatness’ of the distribution. Throat Skew is a measure of the ‘asymmetry’ of the distribution, with positive corresponding to favouring bigger sizes, negative favouring smaller sizes and 0 being symmetrical.

The parameters  $\zeta$  and  $\eta$  are related to the mean,  $\mu$ , and standard deviation,  $\sigma$ , of the distribution as follows:

$$\mu = \frac{\zeta}{\zeta + \eta} \quad \text{Equation 1. 16}$$

$$\sigma^2 = \frac{\zeta \eta}{(\zeta + \eta)^2 (\zeta + \eta + 1)} \quad \text{Equation 1. 17}$$

These expressions may be recovered by using the result that:

$$\Psi(\zeta, \eta) = \frac{\Gamma(\zeta) \Gamma(\eta)}{\Gamma(\zeta + \eta)} \quad \text{Equation 1. 18}$$

Where the 'Gamma function' is defined as:

$$\Gamma(x) = \int_0^{\infty} t^{x-1} e^{-t} dt \quad \text{Equation 1. 19}$$

and noting that:

$$\Gamma(x) = (x-1) \Gamma(x-1) \quad \text{Equation 1. 20}$$

The expressions for the mean and standard deviation may be inverted:

$$\zeta = \frac{\mu^2 - \mu^3 - \mu\sigma^2}{\sigma^2} \quad \text{Equation 1. 21}$$

$$\eta = \frac{\mu - 2\mu^2 + \mu^3 - \sigma^2 + \mu\sigma^2}{\sigma^2} \quad \text{Equation 1. 22}$$

The distribution is therefore completely specified if  $\mu$  and  $\sigma$ , and therefore the quantities on the right hand side, are known.

The ‘Throat Spread’ is defined as twice the standard deviation  $\sigma$ . The ‘Throat Skew’ has a more complex definition in order to allow a balanced sampling of the simplex parameter space. It requires four quantities. The first two are the minimum  $\mu_{\min}$  and maximum  $\mu_{\max}$  possible means for a given standard deviation.

$$\mu_{\min} = \frac{1}{2} \left( 1 - \sqrt{1 - 4\sigma^2} \right) \quad \text{Equation 1. 23}$$

$$\mu_{\max} = \frac{1}{2} \left( 1 + \sqrt{1 - 4\sigma^2} \right) \quad \text{Equation 1. 24}$$

These can be found by substituting the following conditions into Equation 1.21 and Equation 1.22:

$$\zeta = \eta = 0 \quad \text{Equation 1. 25}$$

If there exists a region where the distribution is unimodal for a given standard deviation then we define the minimum and maximum unimodal means as  $\mu_1$  and  $\mu_2$  respectively. The boundary case is a uniform distribution with:  $\alpha = \beta = 1$ ,  $\mu_1$  and  $\mu_2$  are obtained by solving a

cubic equation, and then choosing the correct root (i.e the one nearest the median, which is always 0.5) (Flannery et al., 1986):

$$\mu^3 - \mu^2 + \mu\sigma^2 + \sigma^2 = 0 \quad \text{Equation 1. 26}$$

### 1.3.5.2. Percolation simulation in Pore-Cor

Percolation is simulated in the model by successive piston-flow intrusion of throats as governed by the Washburn equation (Washburn, 1921):

$$d = \frac{-4\gamma \cos\theta}{P} \quad \text{Equation 1. 27}$$

which gives the diameter  $d$  of the smallest cylindrical throat in an incompressible solid exposed to mercury, which is intruded when a pressure  $P$ , is applied to the mercury.  $\gamma$  is the interfacial tension between mercury and air (assumed  $0.485 \text{ N m}^{-1}$ ), and  $\theta$  is the contact angle between the edge of the advancing convex mercury meniscus and the solid surface, assumed to be  $140^\circ$  (Figure 1.11).

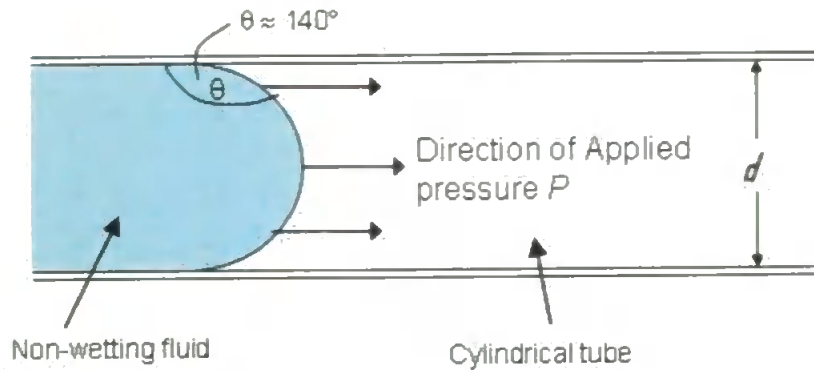


Figure 1.11 Schematic of a non-wetting fluid entering a cylindrical tube and showing some of the variables found in the laplace equation.

These values are typical of those used for mercury intrusion experiments where the true contact angle is ambiguous or unknown. Uncertainties in their values, and the shortcomings of the equation, are well known and have been discussed by Van Brakel (Van Brakel et al, 1981).

### 1.3.5.3. Compressibility Correction

Due to the high pressures involved (up to 60000 psi) and the differing compressibilities of mercury, penetrometer-glass and sample, mercury porosimetry experiments are subject to various compressibility errors. The raw mercury intrusion curves from the instrument can be corrected for these errors using the Pore-Comp module of the Pore-Core software. Pore-Comp allows correction of these phenomena by utilizing the following equation (Equation 1.28):

$$V_{int} = V_{obs} - \delta V_{blank} + \left[ 0.175(V_{bulk}^1) \log_{10} \left( 1 + \frac{P}{1820} \right) \right] - V_{bulk}^1 (1 - \phi^1) \left( 1 - \exp \left[ \frac{(P^1 - P)}{M_{ss}} \right] \right)$$

Equation 1. 28

Here,  $V_{\text{int}}$  is the true sample intruded volume,  $V_{\text{obs}}$  the observed intrusion volume,  $\delta V_{\text{blank}}$  is the total volume change of mercury in a blank run;  $V_{\text{bulk}}^1$  is the bulk volume of the sample at 1 atmosphere,  $\phi^1$  is porosity of the sample at one atmosphere,  $P$  is applied pressure and  $M_{\text{ss}}$  is the bulk modulus of the samples solid phase. Further reading into the derivation of this equation may be found in literature (Gane *et al*, 1996) and gives a comprehensive insight into how the correction procedure is used to provide true volumes of intrusion for a sample and also its calculated bulk modulus. Bulk modulus refers to a ratio of applied pressure to the decrease in sample volume when a uniform pressure is applied to the surface of a material. This is the inverse of compressibility and is given in units of pressure. Samples with large values of bulk modulus are relatively incompressible and those with small values are highly compressible. For comparison diamond has a bulk modulus in the region of 440 G Pa whereas polystyrene has a bulk modulus of around 3.5 G Pa.

#### **1.3.5.4. Model Permeability and Flow Characteristics**

The absolute permeability and flow regime of the simulated structure is found by first calculating the flow capacity  $F_{\text{arc}}$  of each pore-throat-pore arc (Figure 1.12) within the unit cell network, using parameterised Navier-Stokes equations for both cylindrical and square tubes combined together in a similar principle to an electronic ‘series resistor’ type calculation as shown in Equation 1.29 (Scheidegger, 1974):

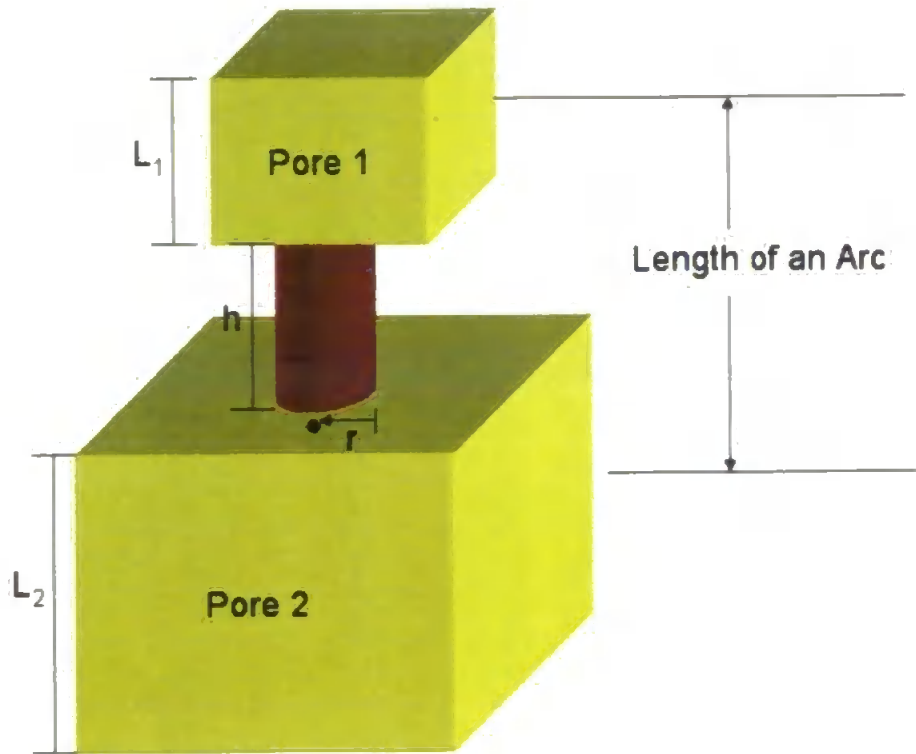


Figure 1.12 Schematic representation of an 'arc' as defined by the Pore-Cor software. Annotation refers to values found in Equation 1.29.

$$F_{\text{arc}} = -\frac{8}{\pi} \cdot \left[ \frac{1}{\frac{57}{4L_1^3 \left(1 + \frac{8.8\lambda}{L_1}\right)} + \frac{8h}{\pi r^4 \left(1 + \frac{4.4\lambda}{r}\right)} + \frac{57}{4L_2^3 \left(1 + \frac{8.8\lambda}{L_2}\right)}} \right]$$

Equation 1.29



Here  $h$  is the length of the throat of radius  $r$  connecting two cubic pores with sides  $L_1$  and  $L_2$  respectively.  $\lambda$  is the mean free path between collisions in the fluid. In this case the fluid is water, and  $\lambda$  is taken to be zero. The model may also be used to calculate gas permeabilities by inclusion of the relevant value of  $\lambda$  for the respective gas (i.e.  $\lambda = 6.98 \times 10^{-8}$  m for nitrogen). Although  $\lambda$  is pressure and temperature dependant, the slip flow which it predicts changes the flow in a 1  $\mu\text{m}$  tube by only about 1%, so this order-of-magnitude value suffices and does not need to be corrected for temperature or pressure when used to simulate laboratory measurements of absolute permeability. A form of Equation 1.29 may also be derived for anisotropic structures in which throats with ellipsoidal or slit-shaped cross-sections join orthorhombic pores (Bodurtha et al., 2005).

It is assumed that the flow of liquid through the network is laminar, and so obeys Poiseuille's equation. Combining Poiseuille's equation with the Darcy equation results in an expression for the network permeability independent of the pressure gradient imposed on the sample (Bodurtha et al., 2005):

$$k = \frac{\pi}{8} \Omega_{cell} (F_{arcs}) \frac{l_{cell}}{A_{cell}} \quad \text{Equation 1.30}$$

Here  $l_{cell}$  is the length of the unit cell of the network model, and  $A_{cell}$  is the unit cell's cross-sectional area. A network analysis approach to this problem supplies the term  $\Omega_{cell}(F_{arcs})$  as the maximal flow capacity through the network of pores and throats. It is calculated by means of the 'Dinic' network analysis algorithm (Ahuja et al., 1997). There is an overall conservation of flow, so that the entire volume of fluid entering the top of the unit cell

emerges at the bottom, with no build-up through the network. The value obtained, as the maximal flow, is based on the capacities of only the channels found to carry flow.

The solution derived is analogous to the 'trickle flow' of an incompressible fluid, which finds various tracks through the unit cell in the  $\pm x$ ,  $\pm y$  and  $-z$ , directions. Flow along each trickle-flow route is limited by the arc along the route with least flow capacity, so the overall flow solution is closely related to  $I_{cell}$ . The solution would converge on the full solution to multiple simultaneous Navier-Stokes equations for unit cells with straightforward flow paths, which are more likely to occur through networks of void features which have simple connectivity and cover a small size range. In practice, however, full solutions to the Navier-Stokes equations always require pruning of the matrices involved in their solution, and the current method can be regarded as analogous to an automatically pruned Navier-Stokes solution. The current method is a more precise approximation than the other main method of solving the flow in void networks, namely the effective medium approximation (Berg, 1995).

## **2. Sample sets and methodology**

Before incorporation into a filter unit, it is necessary that the filter medium is classified so that its efficiency and working capacity is understood. The aim of this chapter is to:

- (i) Describe the current techniques used in the characterisation of sintered filtration media in industry,
- (ii) Provide the rationale for the sample sets chosen for investigation.

### **2.1. Filter media testing in industry**

Initial selection of filtration media, in industry, for development of new filtration units is still largely undertaken by means of an 'educated guess' (Sexton, *Pers. Comm.* 1). When considering a sintered filter media for inclusion in a filtration device, the industrial engineer is initially concerned with two main characteristics of the material, namely its pore size distribution and filtration efficiency. These characteristics are directly related to the evolution of secondary phenomena of the media such as permeability, pressure drop and dirt holding capacity. To gain this information from a given media, the industrial sector uses standard wet bench techniques that are highly demanding in both financial terms and time allocation.

#### **2.1.1. Existing techniques applied in industry**

There are many analytical methods available to measure structural and flow-pressure relationships of filter media. Some of these techniques must be regarded solely as research tools while others are found to provide valuable property information and are good measuring tools without an excessively difficult methodology (Wakeman, 2007). Techniques currently used in the study of sintered filtration media in industry include scanning electron microscopy (SEM), mercury intrusion porosimetry (MIP), porometry

and pass tests. Each of these techniques provides information which may be used to determine the working capability of a media.

#### 2.1.1.1. Scanning electron microscopy (SEM)

In a typical SEM configuration electrons are emitted from a cathode filament towards an anode. Upon placing a thin section sample of filtration media between the cathode and anode components the electron beam is focused on the surface, by successive magnetic lenses, into a very fine spot (ca. 5 nm diameter). As the electrons strike the sample surface, they are inelastically scattered by its component atoms. Through these scattering events, the beam spreads and fills a teardrop shaped volume penetrating about 1  $\mu\text{m}$  into the sample surface. Interactions in this region lead to the subsequent emission of electrons and X-rays, which are then detected. The electrons are emitted from the surface of the material and are used to produce an image of the representative sample (Figure 2.1). Such backscatter cross sectional images may be used to view the skeletal particle, pore-size arrangement and connectivity of the filtration media.

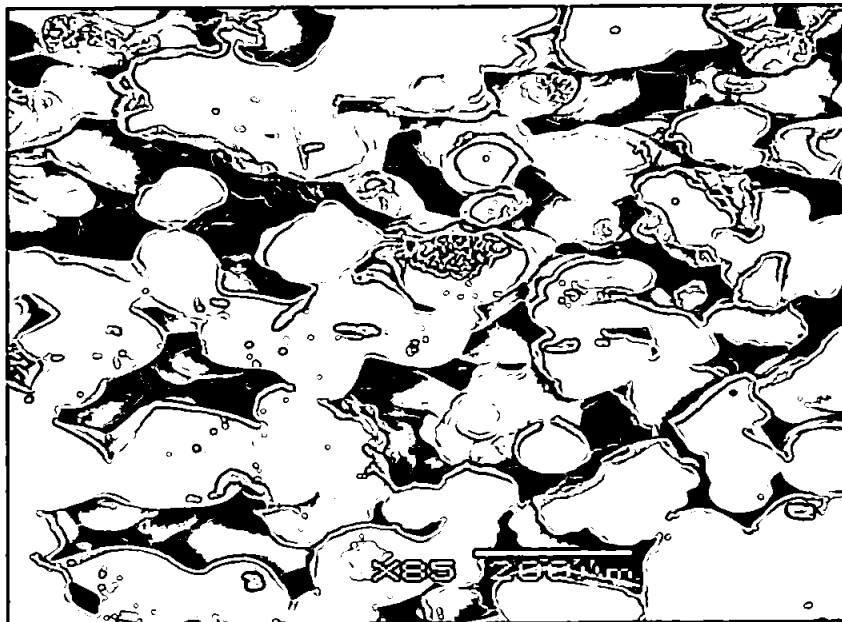


Figure 2.1 A scanning electron micrograph of a resin impregnated sample of Vyon T filtration media showing magnification factor and scale bar.

The SEM technique is extremely useful in order to obtain visual and qualitative information of the filter's pore level structure. By applying image analysis procedures (Toivakka and Nyfors, 2000) to the scanning electron micrographs, quantitative information on skeletal particle size distribution and/or void structure can also be obtained by using successive thin layer analysis of the media. However such procedures are very time consuming, and limited due to the preparation and resolution level achievable through production of ultra thin sections of the media.

#### **2.1.1.2. Mercury intrusion porosimetry (MIP)**

The behaviour of a nonwetting liquid about an inundated porous object was first described by E. W. Washburn (Webb & Orr, 1997) and the governing basic equation bears his name. Due to the highly nonwetting properties of mercury to most substances, it is found that the equation is directly applicable to it. Therefore mercury remains the only known liquid suitable for porosimetry measurements. By nature mercury will not enter pores by capillary action (Figure 2.2) and consequently penetration requires an applied pressure in inverse proportion to pore diameter as depicted by the Washburn equation previously described in chapter 1 and shown again here for reference:

$$d = \frac{-4\gamma \cos \theta}{P} \quad \text{Equation 2. 1}$$

where  $d$  is the pore diameter,  $\gamma$  the interfacial tension of mercury,  $\theta$  the contact angle between mercury and the sample surface and  $P$  the acting pressure upon the bulk volume of mercury. The most commonly used values of  $\gamma$  and  $\theta$  for mercury intruding an evacuated sample are  $0.485 \text{ N m}^{-1}$  and  $140^\circ$  respectively. It is this principle of intrusion under applied pressure which leads to the MIP methodology being a viable

technique for the study of many porous samples including the investigation of porous sintered filtration media.

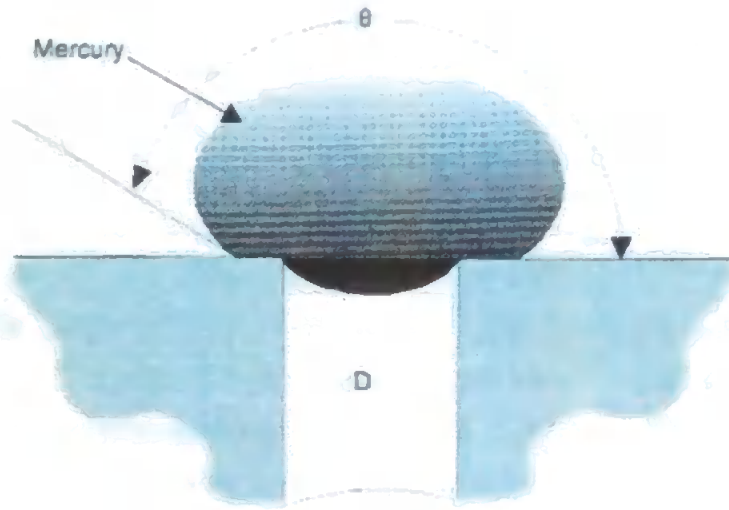


Figure 2.2 Mercury in contact with a porous solid at the opening of a pore and under insufficient applied pressure to undergo intrusion.

In MIP a porous sample is placed within a volume calibrated penetrometer (Figure 2.3) and evacuated of trapped gasses and moisture by vacuum pump. The penetrometer is then filled with mercury and due to sample displacement the bulk volume of the sample,  $V_{bulk}$ , may be calculated by difference between the mercury volume of the penetrometer with and without (blank run) sample.

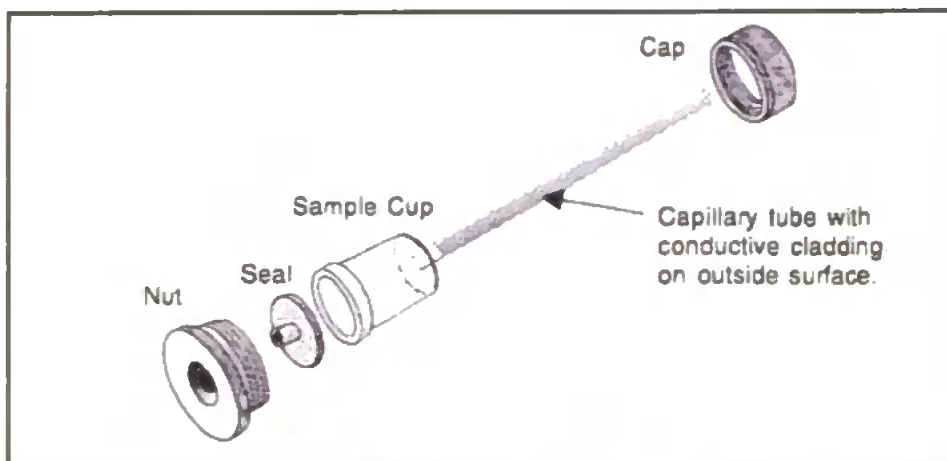


Figure 2.3 Exploded diagram of a MIP penetrometer showing the volume calibrated sample cup, capillary stem and closure components used to seal the sample within the assembly (Webb & Orr, 1997).

A series of directed pressures are then applied to the penetrometer assembly according to a predetermined pressure table covering a range of “Washburn diameters” that are appropriate to the given sample. As this pressure is increased, the mercury within the stem volume of the penetrometer is forced into the pore volume of the media (Figure 2.4). As this occurs, and due to the presence of a conductive coating along the penetrometers capillary stem, the intruded volume of mercury may be calculated by the change in capacitance along the stem. Following this intrusion of the sample a similar procedure, but with pressure reduction, allows the drainage, or extrusion curve to be obtained as the mercury emerges from the sample.

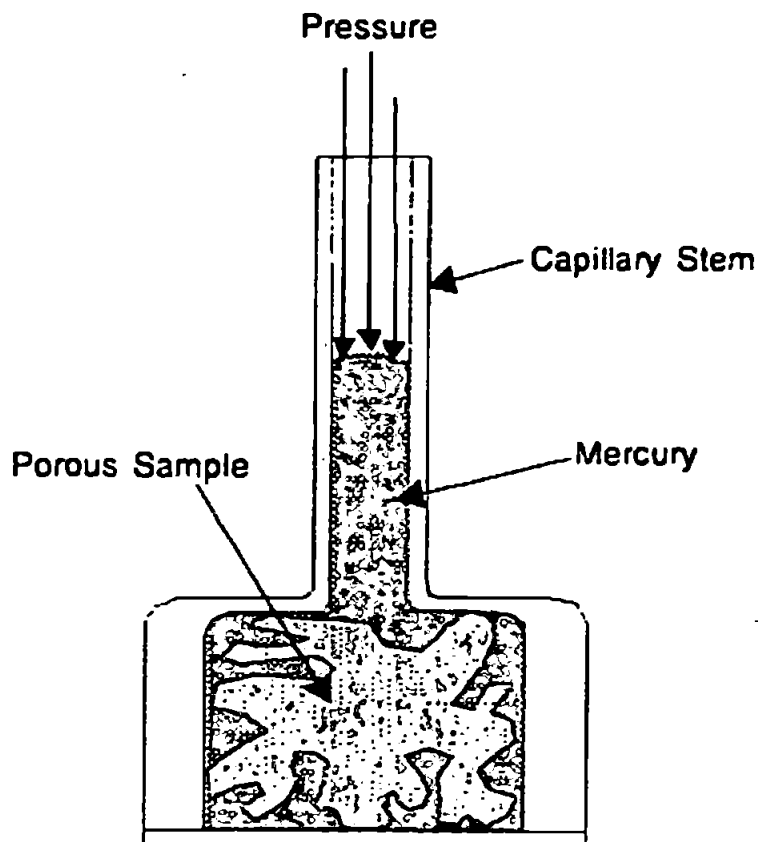


Figure 2.4 Penetrometer containing a sample of porous media after mercury has been forced into pores. The diameter of the capillary is exaggerated for clarity. (Webb & Orr, 1997)

The resulting data from such experiments allows the plotting of a mercury volume intrusion curve per unit weight of sample as a function of applied pressure. This curve may also be expressed as a function of pore size by utilizing the Washburn equation to convert the results to representative cylindrical pore diameters (Figure 2.5).

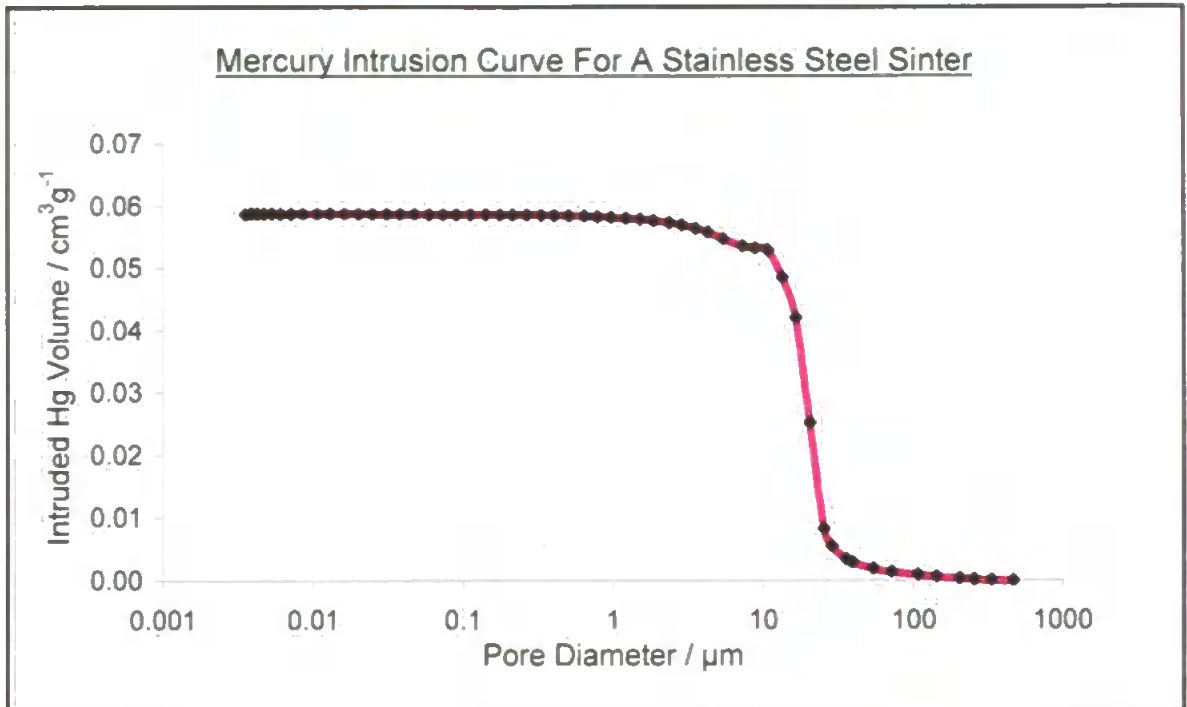


Figure 2.5 A mercury intrusion curve derived from collected porosimetry data. Curve is plotted as an intrusion volume per unit weight of sample as a function of respective pore diameter as found by way of the Washburn equation.

The pore size distribution obtained by taking the first derivative of the intrusion curve and applying the Washburn equation is representative of a “capillary bundle” model of the porous media in question. However this model cannot explain some of the results of MIP (Laudone, 2005). For example the intrusion and extrusion curves differ. This hysteresis effect is caused by “shielding” of large void spaces, or pores, by those of a lower Washburn diameter and as consequence requires a higher than expected pressure for these larger areas to fill. Further descriptions of the associated problems inherent within MIP have been reviewed in literature (Web & Orr, 1997), some of which may



now be overcome by using a void space network model, such as Pore-Cor described in chapter 1.

### 2.1.1.3. Porometry

Porometry is a non-destructive technique which may be utilised for determination of a media pore-size distribution. The method utilises a liquid expulsion technique whereby a sample, fully wetted with a low surface tension wetting liquid, is placed in a sample holder and subjected to a continually increasing gas pressure across one face. As the gas pressure exceeds the capillary pressure of a given pore the wetting fluid is expelled and is replaced by the gas phase (Figure 2.6). Capillary pressure is the pressure required to overcome the surface tension that retains the wetting phase within the pore structures.

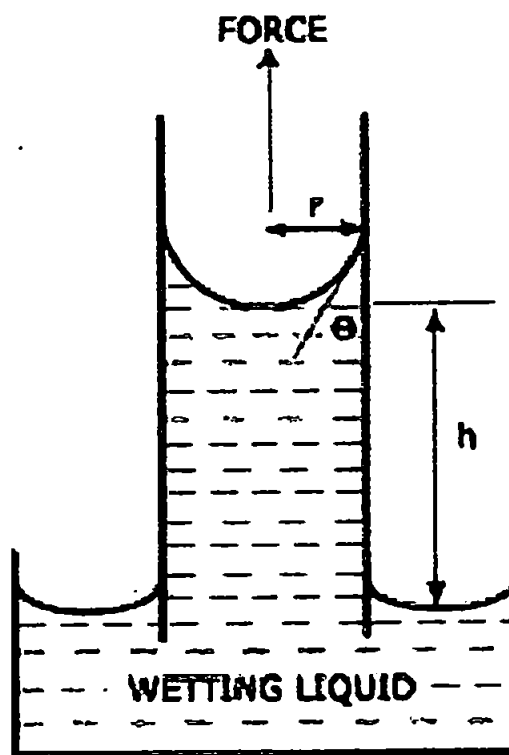


Figure 2.6 Porometry sample intrusion showing the acting capillary pressure against the intruding gas phase (Xonics data sheet).

To obtain the pore size distribution the sample is first saturated and run under a pre-determined incremental pressure table thus emptying the wetting phase from pores in accordance with the Washburn equation. The collected data in this run is characteristic of the media pore size distribution (Equation 2.1). Results achieved by use of this equation provide an 'equivalent cylindrical pore size' at each pressure rather than a true geometric analysis. The sample is then run dry under the same incremental pressure table to provide a 'dry' reference curve.

The pore size distribution of the media is calculated by conversion of difference between the wet and dry flow data to a cumulative flow distribution and differentiated to produce the 'differential flow distribution' which is plotted against the respective pore size increments obtained from the recorded pressure and the Washburn equation (Figure 2.7). Pore number distributions are also considered assuming a cylindrical pore structure, and that open area is related to the number of pores with a square relationship (Xonics data sheet). The computational side of the porometry instrument allows values of maximum, minimum and mean pore size to be reported as well as the total pore size distribution for a given sample of media.

Little work has yet been carried out to determine the validity limits of porometry. Porometry is used within the filtration industry both to characterise filters, and as a quality control tool to ensure filter media do not differ between batches.

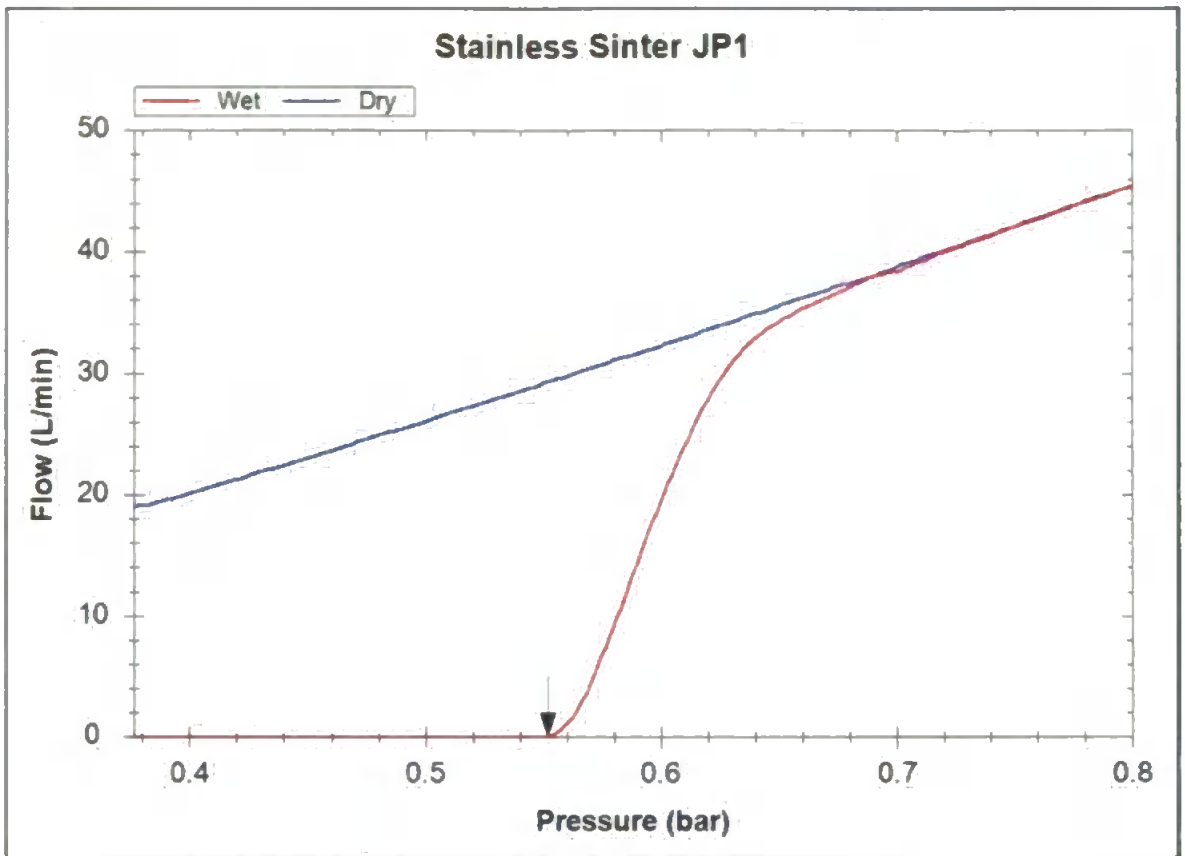


Figure 2.7 Graphical representation of porometry data showing gas flow rate as a function of pressure for a standard test sinter. The plot shows both the wet and dry runs of the analysis which are used to calculate pore size distributions of the media.

#### 2.1.1.4. Pass tests

There are two classifications of pass tests: the first is multi-pass and the second is single-pass. The methodologies involved may be used to either test filtration units before release to market or as an initial media screening test to ensure the media type is suitable for inclusion in a filtration device.

The multi pass test is used to establish the  $\beta$  ratio of hydraulic and lubrication filters such as stainless steel sintered media. The  $\beta$  ratio is a form of particle collection efficiency expression, derived from upstream and downstream counts of contaminant particles across a filter media.

The  $\beta$  ratio may be calculated for each or any contaminant particle size. It may be expressed by the equation:

$$\beta_x = \frac{\text{Number of particles } > \text{ size } x \text{ } \mu\text{m upstream}}{\text{Number of particles } > \text{ size } x \text{ } \mu\text{m downstream}} \quad \text{Equation 2. 2}$$

where  $\beta_x$  is the ratio at a determined size  $x$ .

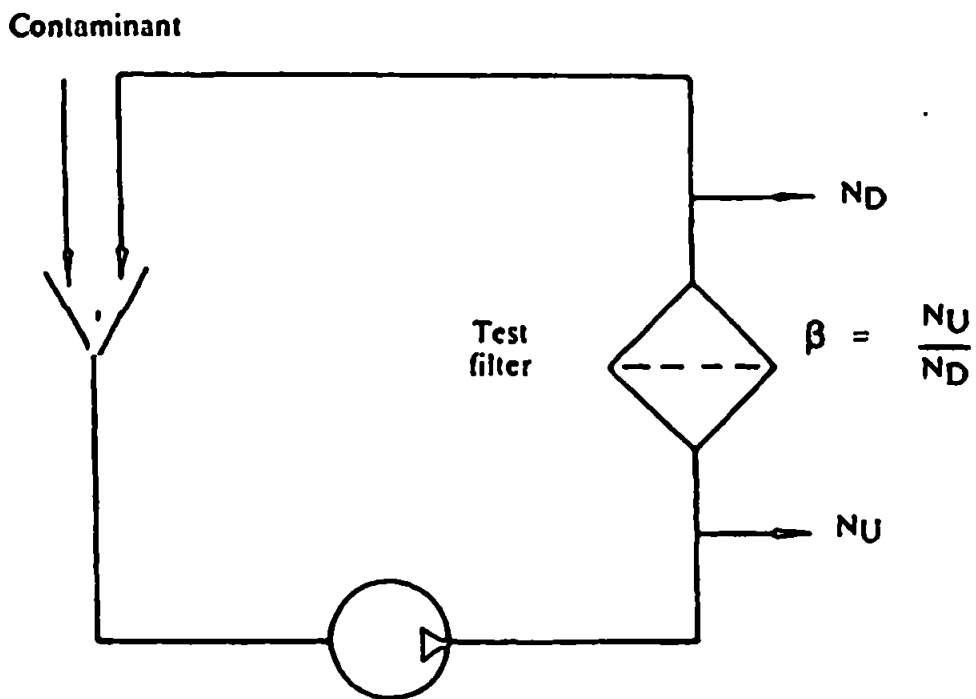


Figure 2.8 Schematic of a multipass test system showing the cycled nature of contaminant fluid and particle counters  $N_U$  and  $N_D$  as upstream and downstream respectively.

The test utilizes a wet bench system as depicted in Figure 2.8. The fluid is circulated at a fixed flow rate with contaminant in the form of a 'test dust' fed continuously into the system so that the same contaminant level is maintained in the fluid. Make-up

contaminant is added throughout the test to replace that collected by the filter under testing (Dickenson, 1997). To calculate the  $\beta$  ratio, samples of the test fluid are drawn simultaneously up-stream and down-stream of the tested filtration media and contaminant particles are counted by automated laser light scattering particle counters. In conjunction with this data collection, the pressure difference across the media is recorded to ascertain a terminal working condition of the media in terms of its percent blockage or maximum permitted system pressure to maintain a fixed flow rate.

Various characteristics may be calculated from the measured data. A filter efficiency rating, corresponding to the  $\beta$  ratio, may be calculated for each particle size investigated by the formulas:

$$E_x = \frac{\beta_x - 1}{\beta_x} \times 100(\%) \quad \text{Equation 2. 3}$$

or

$$E_x = 100 - \frac{100}{\beta_x} (\%) \quad \text{Equation 2. 4}$$

where  $E_x$  is the filtration efficiency of the measured particle size. Also the percent blockage of the filter may be monitored so that the filter may be studied in a situation representative of a predetermined working criterion. The percentage blockage is determined by the equation:

$$\% \text{Blocked} = 100 \times \frac{(1 - (\text{clean pressure drop} - \text{housing loss}))}{\text{current pressure drop} - \text{housing loss}} \quad \text{Equation 2. 5}$$

Here the housing loss is the pressure difference across the systems sample holder without a sample of the media *in situ*, and the clean and current pressure drops are those recorded at the start of the test and while the test is in progress respectively.

In the single pass test (Figure 2.9) contaminated fluid is also continually passed through the test filter media. However under single pass criteria the downstream effluent is either cleaned of contaminant by means of ‘clean-up’ filters or collected in a separate reservoir (Dickenson 1997). The contaminated fluid therefore only makes a ‘single-pass’ through the test filter. Monitoring of the filter efficiency,  $\beta$  ratio and the associated pressure drops or percentage blockage calculations due to particle retention is undertaken as in the multi-pass method.

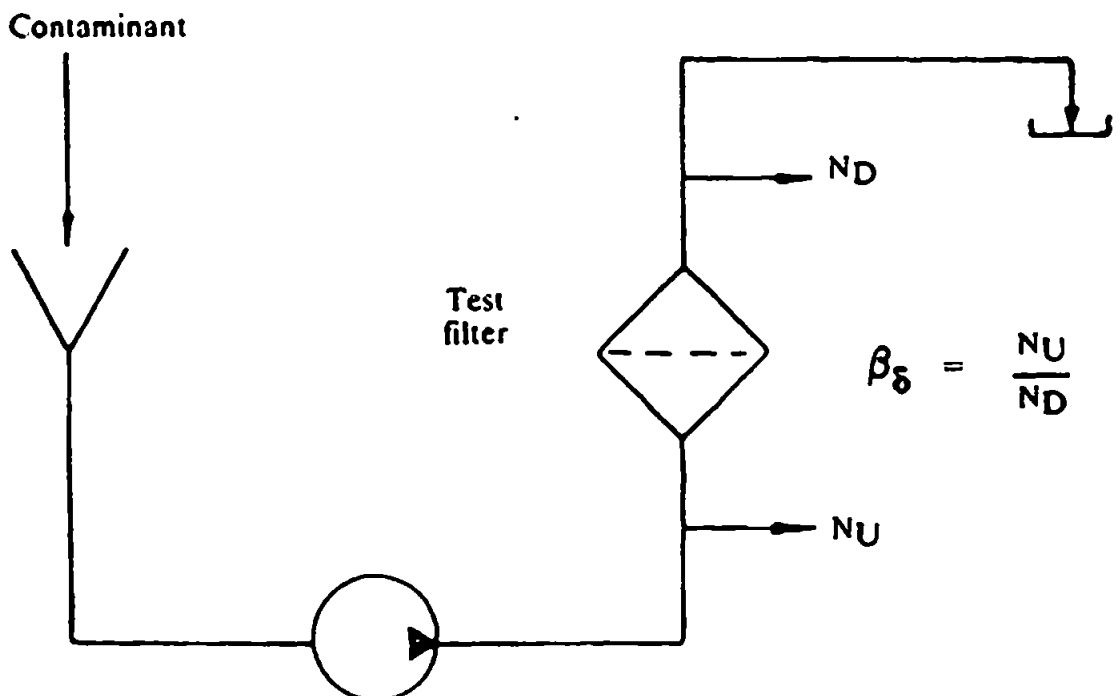


Figure 2.9 Schematic of a single pass test system showing the cycled nature of contaminant fluid and particle counters  $N_U$  and  $N_D$  as upstream and downstream respectively.

The two test methods offer different approaches to the problem of investigating the performance of filter media. Although the multi-pass methodology better represents the working conditions of a filter in a hydraulic system, due to the recycling of uncollected contaminant, the single-pass test is deemed more appropriate for the investigation of the factors which may influence a filter media performance. In the single pass test and its associated use of a constant concentration of contaminant particulate, changes in media performance are directly reflected by the changes in downstream conditions.

## **2.2. Sample selection and rationale**

Sample sets selected for the research were carefully considered through a number of meetings with Porvair Filtration's research and development department. The samples finally chosen for investigation were in accord with the principle aims of the thesis, and needed to be highly reproducible. Two sample types were chosen. The first was a porous stainless steel sintered media, namely Sinterflo®, and the second a sintered porous polymer media known as Vyon®. It was judged that these media types would allow the development of a working filtration model (Sinterflo®), and the study of wicking properties (Vyon®) as would be utilised in the emanation of fragrance chemicals to a home or sanitary environment.

### **2.2.1. Sinterflo® media**

Porous metals are ideal for filter applications that involve aggressive environments, including high temperatures and pressures. These applications can range from hydraulic fluid filtration through to polymer processing and catalyst recovery (Porvair data sheet 1).

Sinterflo® porous sintered stainless steel media is available in seven off-the-shelf grades exhibiting standard mean pore sizes between 6 and 60 microns with absolute filtration ratings from 0.5 micron in gas and 4.5 microns in liquid. They can be used up to temperatures of 400°C (540°C in reducing or neutral atmospheres) and are resistant to most chemicals. The media can be formed in a wide variety of flat sheet shapes and cylindrical formats (Figure 2.10). The cylinders are produced without any seam welding by first undertaking production of a “green form” compression of graded stainless steel powder which is then sintered to form the finished media. This results in a superior media uniformity and higher corrosion resistance to the working environment. The inherent strength and resistance to high temperature and pressures also means that the filters can be cleaned and reused many times, to achieve cost efficient operation. Technical information available for the different grades of Sinterflo® media can be viewed in

Table 2.1.



**Figure 2.10** Examples of flat sheet and cylinder forms of Sinterflo® media produced by green form sintering.



Table 2.1 Physical properties of Sinterflo® stainless steel media PTL Ltd.

PORVAIR TECHNOLOGY LIMITED										
Grade	Air Flow 1/hr/cm <sup>2</sup> at ΔP = 10 cm WG 2mm thick		Water Flow 1/hr/cm <sup>2</sup> at ΔP = 10 cm WG 2mm thick		Minimum Bubble Pressure  Cm WG	Maximum Pore Size  microns	Gas Filtration Removal Efficiency In microns		Liquid Filtration Removal Efficiency In microns	
	Min	Max	Min	Max			98%	99.9%	98%	99.9%
S16	1.2	2.8	0.02	0.05	74	13	0.2	0.5	3.2	4.5
S21	3.8	7.7	0.1	0.2	42	23	0.4	1.2	5.9	9
S26	7.7	13	0.2	0.4	28	34	0.7	2.3	12	16
S31	13	24	0.4	0.53	20	47	1.2	3.6	16	24
S36	24	35	0.53	1.25	14	67	2	6	26	37
S41	35	60	1.25	2	10	94	3.2	8.6	40	58

Sinterflo® media was chosen as the main sample set for use in the development of a working filtration model within the Pore-Cor software. It was deemed suitable as the manufacturing expertise of the Porvair Filtration Group allowed the production of consistent sample batches in a series of forms that were suitable for the experimental techniques that would be undertaken in the study. These samples included the production of small discs (Figure 2.11) that were suitable for porosimetry experiments and also larger flat sheet discs for single pass tests.

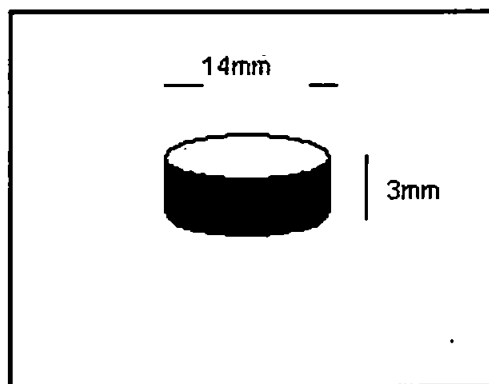


Figure 2.11 Sample plug dimensions for stainless steel Sinterflo® media as used in mercury porosimetry experiments (MIP).

The modelling expertise found in the Environmental and Fluid Modelling group at the University of Plymouth also suggested that the sintered construction of the Sinterflo® media was suitable for reliable mercury porosimetry and for producing data suitable for modelling in the Pore-Cor software. Certain materials such as fibrous mats are found to be difficult to model consistently within the software as they provide a high porosity which is difficult to interpret in terms of the model's cylindrical throat and cuboid pore geometry.

### **2.2.2. Vyon® media**

Porous plastic media is by no means as robust as porous metal media. However it does have many applications for which it is preferred over other filtration media. These applications range from process chemical filters to biomedical applications where the media may be sterilised and, due to its low cost starting material, used as a cheap 'use once' filter.

Vyon® is a porous sintered plastic media produced in either high density polyethylene (HDPE), ultra high molecular weight polyethylene (UHMWPE) or polypropylene (PP). It is available in a number of standard pore sizes from 10 to 100 microns (Table 2. 2) controlled primarily by the starting powder size. The media may be produced in sheet or moulded format depending on application requirement (Figure 2.12). The sheet format can be produced in widths of 6 mm to 1 meter and a thickness of 0.75mm to 10mm (Table 2. 2). Due to the production process these sheet forms of Vyon® can be produced to any reasonable length and supplied in sheet or roll format. Mouldings may be produced in almost any three dimensional shape to suit a customer specification (Porvair data sheet 2).

In working conditions Vyon® media is resistant to most acids, bases and many organic chemicals and may be used in working temperatures of up to 110°C. Complex composites can be made to alter the properties to provide optimum performance for specific applications. By nature the media is hydrophobic although Porvair Filtration Group offer a number of surface modifications to the material to make it suitable for an even broader range of applications. These modified forms of Vyon® are named i-Vyon®. Modifications include making the media permanently hydrophilic or highly hydrophobic, and inclusion in composites to offer a range of materials that are particularly suitable to bioscience industries. The internal pore surfaces of the material may be functionalised with a variety of chemical groups; for example: -CO, -COOH and NH<sub>2</sub>. The functionalised material may also be modified further with linker molecules of carbon chains from C<sub>2</sub> to C<sub>20</sub> in length. Chemically active or biologically active species may then be attached to the linker chains making the media an extremely useful support for organic synthesis and biomedical applications (Porvair Data Sheet 3). As such i-Vyon® porous polymeric materials are used in applications involving fluid transfer, filtration and chemical separation, including sample preparation for chemical analysis, chemical wicking, reagent support and diagnostic devices.



**Figure 2.12** Examples of Vyon® media in both sheet, roll and moulded formats. (change for PV ref show sheet and moulds)

Table 2.2 Physical properties of Vyong<sup>®</sup> polymeric media as measured by porometry (PTL)

TRADE NAME	MATERIAL TYPE			TYPICAL THICKNESS (mm)	TYPICAL PORE SIZE (μm)			TYPICAL REMOVAL EFFICIENCIES (μm)	
	HDPE	PP	UHMWPE		MAX	MEAN FLOW	MIN	Air Normal	Water Normal
<b>VYON D</b>	*			3.2	30	16	8	6	10
	*			4.75	27	16	8	6	10
	*			6.0	-	35#	-	6	10
	*			8.0	-	30#	-	6	10
	*			10.0	-	27#	-	6	10
<b>VYON PPD</b>		*		3.2	30	10	2	1	5
		*		4.75	30	8	2	1	5
		*		6.0	-	35#	-	1	5
<b>VYON F</b>	*			0.75	127	40	12	25	40
	*			1.00	120	38	10	20	35
	*			1.50	105	36	10	20	30
	*			1.68	95	35	9	-	-
	*			2.0	78	30	9	20	30
	*			2.50	65	25	8	15	25
	*			3.20	55	23	8	15	25
	*			4.75	50	20	7	10	20
	*			6.00	56	22	10	10	20
<b>VYON PPF</b>		*		1.50	145	40#	8	10	20
		*		2.00	140	35	8	10	20
		*		2.50	105	30	5	5	15
		*		3.20	75	23	5	5	15
		*		4.75	75	23	4	5	15
		*		6.00	-	88#	-	5	15
<b>VYON PORVENT</b>	*			2.00	55	20	5	5	15
	*			2.50	55	20	6	5	15
	*			3.20	55	20	6	7	17
<b>VYON HP</b>	*			2.00	>300	91	27	50	70
	*			2.50	>300	98	21	80	100
	*			3.20	>200	100	30	50	70
	*			4.75				50	70
	*			5.30	-	125#	-	50	70
	*			6.00	-	180#	-	50	70
<b>VYON PPHP</b>		*		2.00	>300	90	15	50	70
		*		2.50	>300	87	14	50	70
		*		3.20	>300	80	22	40	60
		*		4.75	170	60	10	40	60
		*		6.00	-	135#	-	40	60
<b>VYON T</b>			*	1.00	40	18	10	2	10
			*	1.50	30	12	8	2	8
			*	2.00	15	10	6	1	5
			*	2.50	15	9	6	1	5
			*	3.20	15	9	6	1	5
			*	4.75				1	5
			*	5.00	20	9	4	1	5

Vyon® and i-Vyon® was chosen for inclusion within the research for a number of reasons. The first is that, like Sinterflo®, the manufacturing process expertise offered by Porvair Filtration Group allowed the production of consistently reproducible sample sets in forms that were suitable for experimental techniques involved in the study. The second reason is that due to the low production and material cost of the media it offered an ideal starting material to optimise the experimental porosimetry and to assure that the proposed investigations were valid. Thirdly and probably most importantly the i-Vyon media is an important product in the advancement of Porvair Filtration Group into the biomedical and chemical emanation market. It was decided that an investigation into the wicking process of the material would allow it to be optimised during manufacture and give rise to further market applications. In this research Vyon® samples were provided in sheet forms of 3mm thickness an approximately 80 mm x 20 mm for wicking studies and discs of the same batch sheet of 3mm thickness and 14 mm diameter for porosimetry studies.

### **3. Porosimetry, modelling and validation of modelled structures**

The starting point of any porous media network model is the generation of a suitable representative void network simulation of the studied sample media. Although the network may be simplified in terms of void geometries, some correlation between the modelled parameters and the real world situation must exist. The objectives of this chapter are to:

- (i) Discuss the mercury intrusion methodology, results and data manipulation,
- (ii) Show the modelling of representative networks in the Pore-Cor environment and their validation by highlighting their trends relative to existing industry data.

These objectives will support the overall aim of validating Pore-Cor void network structures as a representative networks for developing a successful filtration model.

#### **3.1. Mercury Porosimetry – measurement and data manipulation**

Mercury intrusion porosimetry (MIP) was carried out using an Autopore III porosimeter (Micromeritics Inc., Atlanta) (Figure 3.1). The instrument is designed to cover two pressure ranges: 0.5 to 30 psia, and 30.25 to 60000 psia. The maximum pressure corresponds to a minimum pore/throat size of 4 nm via the Washburn equation (Equation 2.1). The mercury porosimetry is achieved by way of an initial gas-aided intrusion (up to 30 psia), followed by a high pressure oil-aided intrusion up to 60000 psia. The instrument has four low pressure sample ports and two high pressure ports so that different samples may be run concurrently.



**Figure 3.1** Picture of the Auto-Pore III Micromeritics porosimeter showing the four low pressure ports at the top of the instrument (grey cylindrical covers) and the two high pressure oil filled ports (black vertical closure units on the horizontal base).

Mercury porosimetry was initially undertaken on samples of Vyon® HP and Vyon® T, which were selected to cover the extremes of pore sizes that would be investigated. This enabled the development of good working practices in MIP and also a standard pressure table to be constructed for further samples. The pressure table is used by the porosimeter as a program file, and sets the pressure points at which intrusion data is to be collected. This pressure table development is important in that it must cover the sampled range of pore sizes according to their pressure-related Washburn diameter, and also minimise any excess data collected before and after the sample intrusion. In the Pore-Cor simplex fitting of an intrusion curve, each data point is treated the same with no difference as to whether it is pre- or post-intrusion, or close to the inflection point of the intrusion curve. Thus thinning of tailing points pre- and post- intrusion, i.e. points

close to 0% or 100% intrusion, would make the Pore-Cor simplex more sensitive to the inflection curve rather than unimportant tailing data. In practice this proved difficult due to the large variation in the pore size characteristics across the sample range. Depending on the given pore size distribution of a selected sample, the inflection point of intrusion shifted. It was decided that this problem would be countered by undertaking manual correction of data files, post MIP, to remove the excess data points pre- and post inflection. The typical plot shown in Figure 3.2 shows a large number of points near maximum intrusion, which were manually trimmed. After the working pressure table was constructed, it was used as the principle working file to study all the samples of Sinterflo® and Vyon® media.

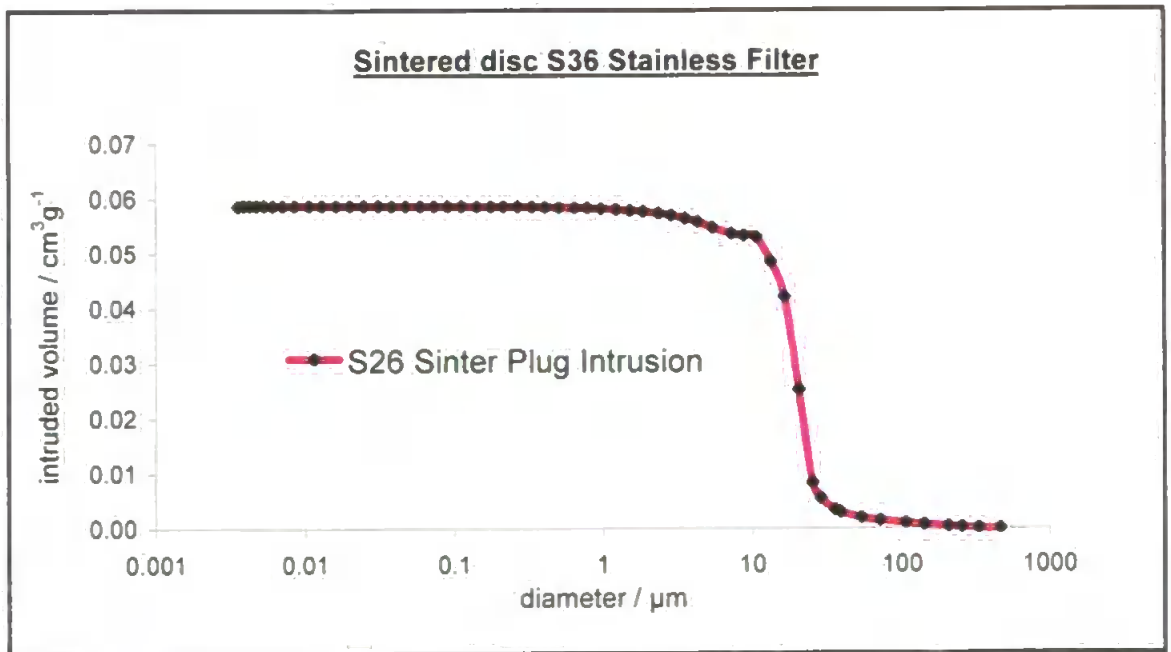


Figure 3.2 Microsoft Excel plot of MIP data for a S26 Sinterflo® plug as delivered by execution of the principle pressure table constructed for all sample sets (sample is corrected for compression effects).

As the aim of the research is to develop a working filtration model which will be desktop applicable, there is a requirement that any data manipulation must follow a



designed method. Following such a method of data manipulation ensures that the porosimetry data is treated equally in all cases and that future investigations would be directly comparable to each other in their initial network representations. The initial step in the manipulation of all porosimetry data collected was the correction for compression effects during the high pressure porosimetry.

MIP data is very susceptible to compression effects as discussed in section 1.3.5.3. It is therefore necessary to utilise the Pore-Comp module of the software so that the raw data can be viewed as a set of true intrusion curves corrected for all sample, mercury and penetrometer compression artefacts. This results in an intrusion curve which is representative of the sample's void structure independent of compression of its solid phase (Figure 3.2)

Once compression corrections of the intrusion data were made, a sensible approach to trimming the data had to be considered. An artefact of the Pore-Cor model is that it uses the maximum pore size /minimum pressure on the experimental curve as the maximum feature size on the model, and the maximum pressure/minimum pore size as the smallest feature within the model. Therefore an experimental intrusion curve that had many readings at zero % intrusion, before the mercury reached sufficient pressure to intrude, would generate a different structure from one where all the initial 0% readings had been discarded. Similarly, it matters whether the curve at maximum pressure / minimum size has a long 'tail' of 100% readings.

The first method investigated was the trimming of intrusion data with trim limits set by the maximum and minimum experimentally intruded pore sizes, as derived by the Washburn equation (Equation 2.1). To ensure all intrusion data was covered it was

decided that the maximum pore size included in the data should be set at twice that of the actual intruded maximum pore size and the minimum value for investigation to be set at half the minimum intruded pore size. However this did not result in a large reduction of the overall data set.

An alternative method is to scale the minimum and maximum simulated sizes relative to the Washburn sizes at which intrusion curves attain 90 % and 10 % of the total experimental intrusion volume. Due to its success in previous investigations (Matthews et al. 2006; Bodurtha, 2003) it was deemed a valid technique for all the intrusion data presented in this study. The fully corrected and scaled intrusion curves for Sinterflo® and Vyon® medias are shown in Figure 3.3 and Figure 3.4 respectively. Each curve has been trimmed so that its maximum and minimum pore sizes, which we refer to as  $r_{100}$  and  $r_0$ , obey the ratios  $r_{100} = r_{90}/11.5$ , and  $r_0 = r_{10}/0.132$ . The ratios 11.5 and 0.132 were somewhat arbitrarily chosen such that the trimming was fairly tight (i.e. did not leave a long 0% or 100% tail), but so that the trimming always occurred within the 0% or 100% tail regions. The arbitrariness of the choice is not entirely satisfactory, as the ratios will vary from sample type to sample type, so a more systematic approach to this needs to be considered for future version of the software.

Due to the above trim function being sufficiently held within the 0% and 100% intrusion tails the data points lost are of no significance to the overall intruded volume of the sample. It is this intruded volume which sets the experimental and modelled porosity values and therefore the sensitivity of the porosity results are found not to differ by more than the experimentally found 3 % porosity between replicates (Section 3.1.2). Sensitivity of the modelled permeability may however be effected due to the removal of the tailing points. As previously described (Section 1.3.5.4) the model

constructs the unit cell representations from a number of arc features derived from all the available pore and throat sizes present on the experimental input curve. Even though there is no intrusion in the 0% and 100% tails the fact the points are measured allows the software to presume their existence and it will consequently include a small fraction of smaller, and larger, pore features than is actually present in the sample. As such it is feasible that they may cause some influence in the fluid flow paths and permeability function of the model. However due to the fact that each unit cell is stochastically generated and that each experimental replicate may be subject to small heterogeneities the variance caused by the inclusion of such features is complex to evaluate and was not undertaken within the scope of this project.

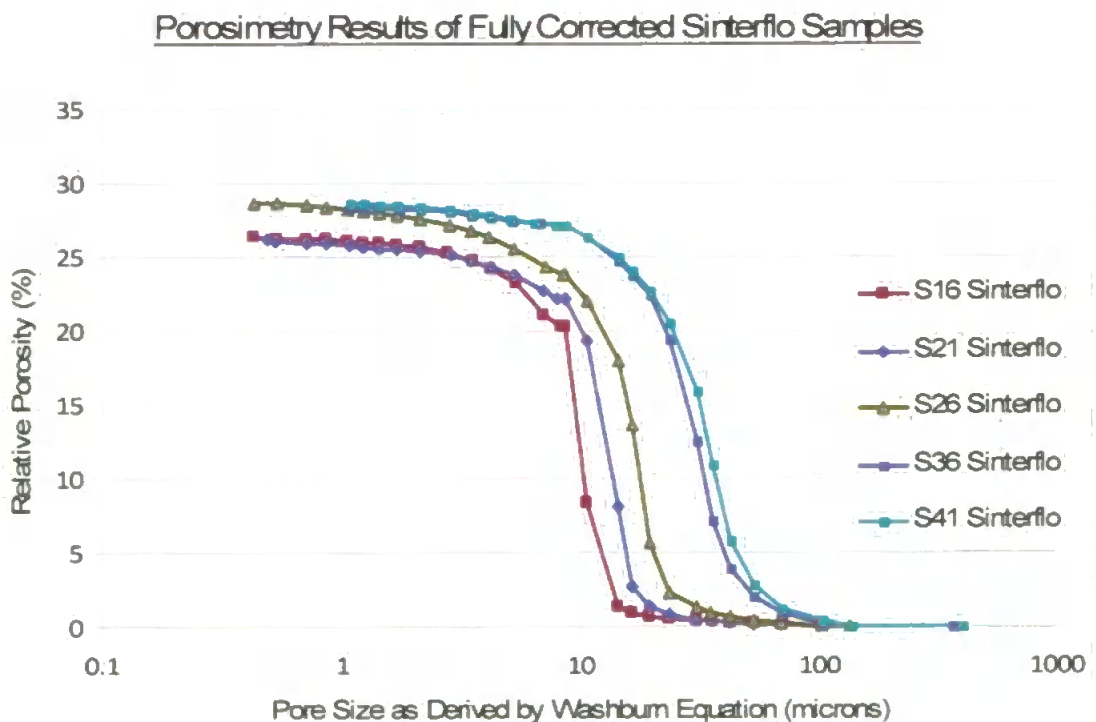


Figure 3.3 Mercury intrusion porosimetry curves for Sinterflo® samples S16, S21, S26, S36 and S41. Results shown are scaled by the 90% 10% trim method as stated above.

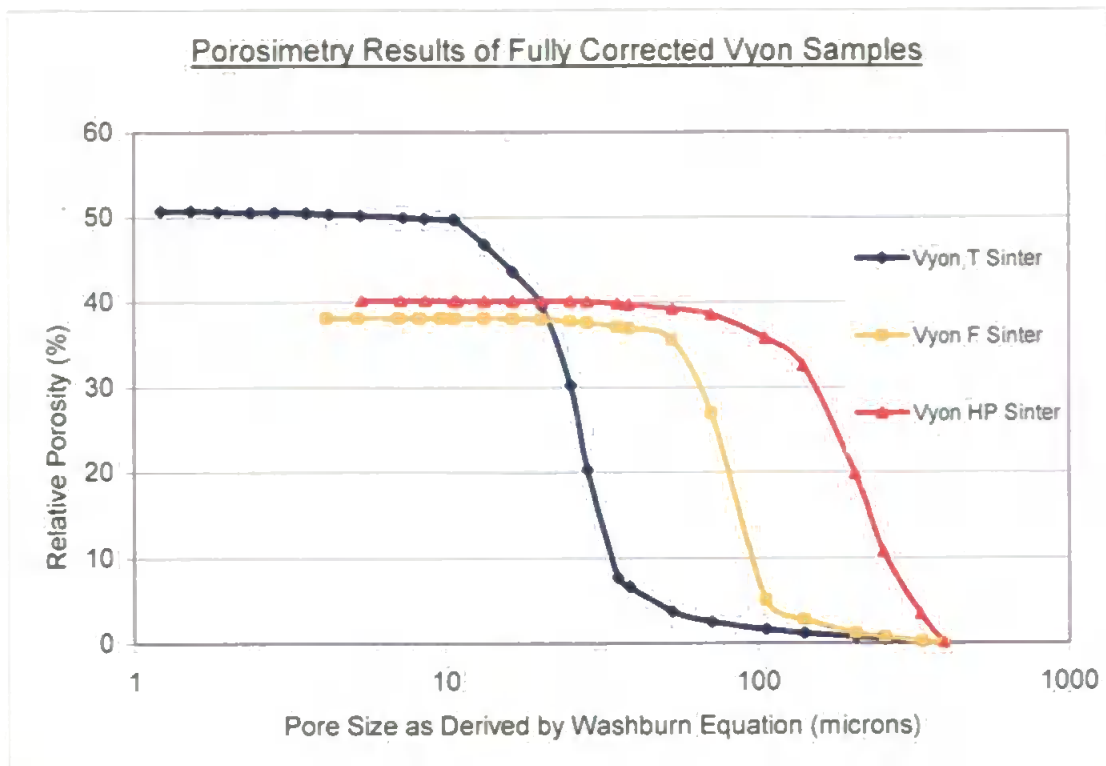


Figure 3.4 Mercury intrusion porosimetry curves for Vyon® samples F, T and HP. Results shown are scaled by the 90% 10% trim method as stated above.

### 3.1.1. Sinterflo® results discussion

As may be seen from Figure 3.3 the experimental intrusion curves displayed for the series of Sinterflo® media show a correlation between the representative pore size, taken as the points of inflection of the intrusion curves, with an increase in the sample grade number. From the graphical representation (Figure 3.3) it is shown that the range of pore sizes intruded range from a maximum ca. 100  $\mu\text{m}$  in the S41 grade media to a minimum ca. 10  $\mu\text{m}$  in the S16 media. This is directly comparable to available manufacturing data (Table 2.1) which shows the same trend. Further experimental results for duplicate samples show that this porosimetry process is reproducible and repeated runs only have minimal differences in total porosity values (ca.  $\pm 0.5\text{-}1\%$ ) with identical pore size profiles.

The porosimetry runs do show some intrusion at pore sizes above those that are stated as maximums in Table 2.1 and on first consultation of the data it would suggest that this is incorrect. However the maximum pore sizes shown in the manufacturing data presented in chapter 2 are recorded by 'bubble point' methodology. This relies on the same principle of the porometry experiments where wetting liquid is expelled from the sample by a gas phase. The 'bubble point' occurs when the gas first penetrates through the sample and is observed on the downstream side. This does not necessarily show the largest pore in the given sample, but the largest pore size which is overcome to allow the gas an uninterrupted flow stream through the entire sample, a small part of which is shown in Figure 3.5. These inconsistencies in results between experimental techniques need to be considered in all cases where data from two different measurement methods is compared.

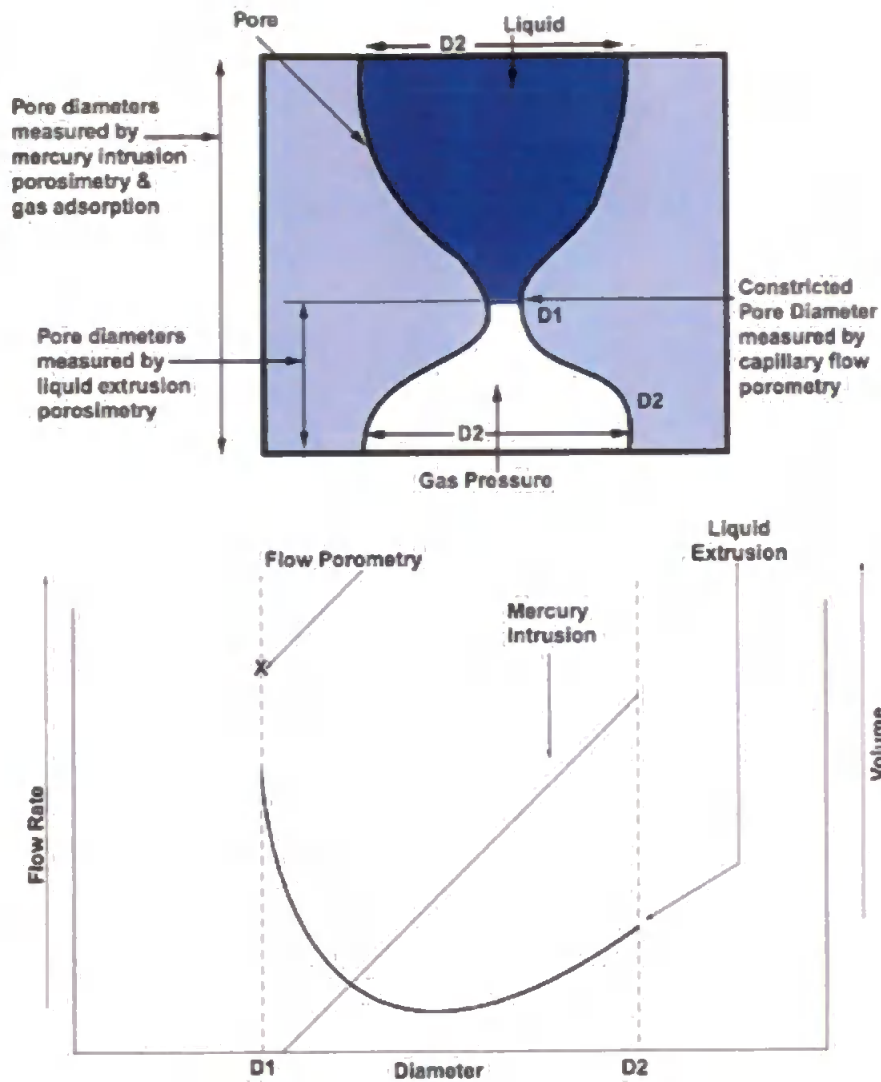


Figure 3.5 Diagram and graph showing the comparison between pore size measurements as found by various techniques. The largest pore size determined in bubble point methodology is equivalent to D1, where the pore is most constricted. (Gupta and Jena, 1999)

### 3.1.2. Vyon® results discussion

Vyon® and i-Vyon® samples used in this study were all of 3 mm in thickness. This is important to note as the pore size characteristics of Vyon® and i-Vyon® stated in Table 2.2 are seen to change with sheet thickness. Again it is apparent, observing the points of inflection of the intrusion curves, that the displayed data in Figure 3.4 shows some deviance from the stated pore size characteristics stated in the manufacturing data for 3mm sheet thickness (Table 2.2). These discrepancies are possibly attributable to the

fact that the Vyon® media used in the study is a custom-built batch and is not directly comparable with the manufacturing data found in Table 2.2. Also as in the Sinterflo® media the measurement technique of MIP may offer differing results to those previously derived by bubble point methods.

Further samples of the Vyon® were run under a quick screening method on the porosimeter to check for reproducibility and as displayed in Figure 3.6, the results are very reproducible between duplicate sample sets. In this situation porosities are calculated using the total intruded volume at 1  $\mu\text{m}$ . Due to the quick screening method applied, full Pore-Comp corrections could not be used due to the fact that the data was not always collected up to the maximum 60000 psia. The data is also un-trimmed by the 90 % and 10% trimming method used on the full experimental curves. However on observation of the data it seems clear that all samples have reached total saturation at or before 220 psia (1  $\mu\text{m}$ ), and this quick screening method was therefore deemed valid for quick reproducibility comparison.

As may be seen (Figure 3.6) the Vyon® F sample has a very reproducible pore size, pore volume and porosity profile as shown by the overlapping of the two replicate runs. However the Vyon® HP samples do show some difference in total intruded volume/porosity, but the actual pore size distribution (represented by the similar intrusion curve shape) remains constant between all replicates. The Vyon® T samples showed a step in the intrusion curves at the instruments change over pressure of 30 psia. For this reason the sample was run again only using the low pressure port but up to a pressure of 50 psia. It can be seen in this case that the intrusion curve for this sample does not have such a sharp step at this point and the step was attributed to the inconsistencies in the change over between low and high pressure measurements. It was

also noted that the Vyon® T sinters have a much higher porosity value than the Vyon® F and Vyon® HP sinters.

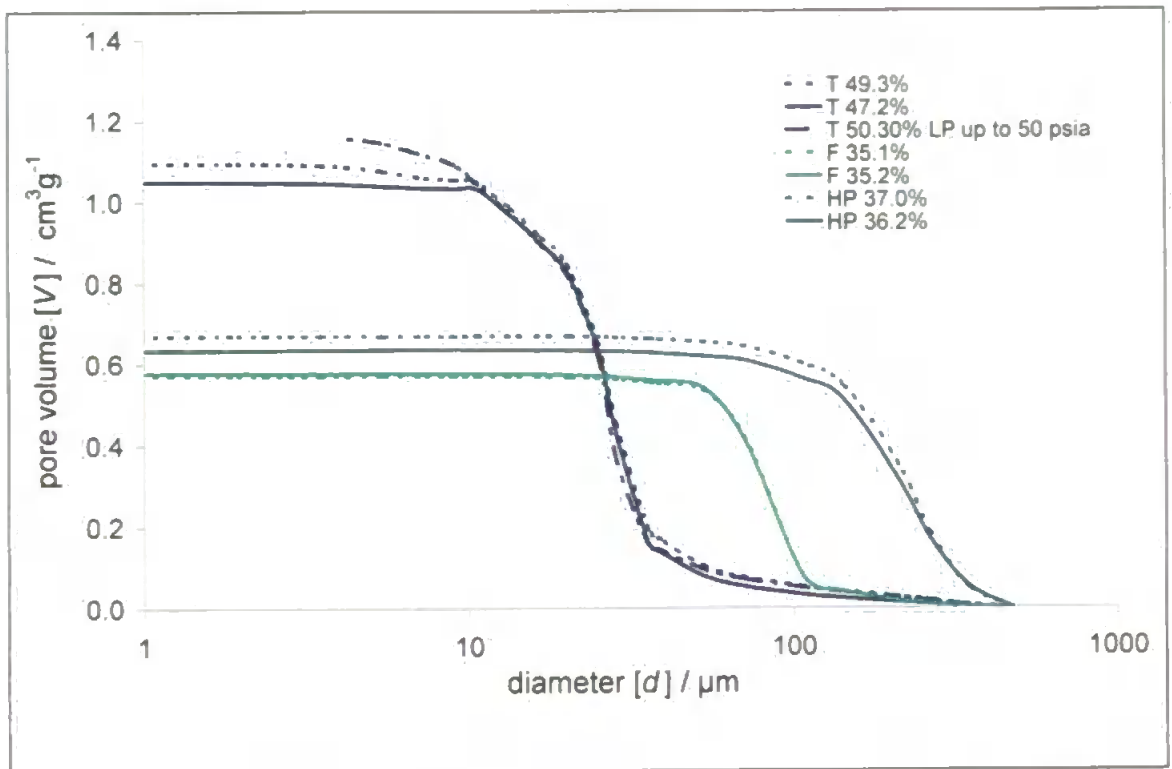


Figure 3.6 Results from the quick screening MIP of Vyon® samples for reproducibility, showing repeat intrusion curves of duplicate samples and relative porosity values.

It is noted that in the case of Vyon® media the reproducibility of all samples shows a higher variation in the porosity values between samples than in the Sinterflow® media (up to 3 % in the case of Vyon® T ) although the pore size distributions are equally consistent as represented by the overlapping replicates in Figure 3.6.. The differences observed in the porosity values of the replicate samples are possibly attributable to the quick screening method used or possible small heterogeneities between samples.



### **3.2. Modelling of representative network representations**

From the trimmed and corrected porosimetry data for both Vyon® and Sinterflo® media, the Pore-Cor software (Version 6.11) has been used to generate representative 3-dimensional ‘unit-cell’ pore network models (Figure 3.7 - Figure 3.14 for Sinterflo® then Vyon® respectively). These representative networks show good agreement when compared to the manufacturing data for pore maxima, minima etc.

The measure of success in the model producing unit cell networks of the same percolation characteristics as an experimental sample, is given by a “goodness of fit” value. This “goodness of fit” or “distance” is a percentage distance value between the experimental and simulated, as generated by the software’s simplex (Section 1.3.5.1), intrusion curves. The percentage values are calculated by plotting the curves on a graph with logarithmic horizontal, pore size, axis and linear vertical, intrusion, axis with the spread of the experimental points being 100% in each direction. The distances between each experimental point and all the simulated points are then calculated. The closest distances between experiment and simulation are then averaged over the number of experimental points to give the “goodness of fit” distance percentage.

The fitting parameters (Section 1.3.5.1) and goodness of fit value after optimisation by the simplex are shown in Table 3.1. The corresponding 3-dimensional images of the structures are shown in Figure 3.7 - Figure 3.14. The optimised values of the fitting parameters were saved in a modelling archive file so that future investigations may be based on the same structures.

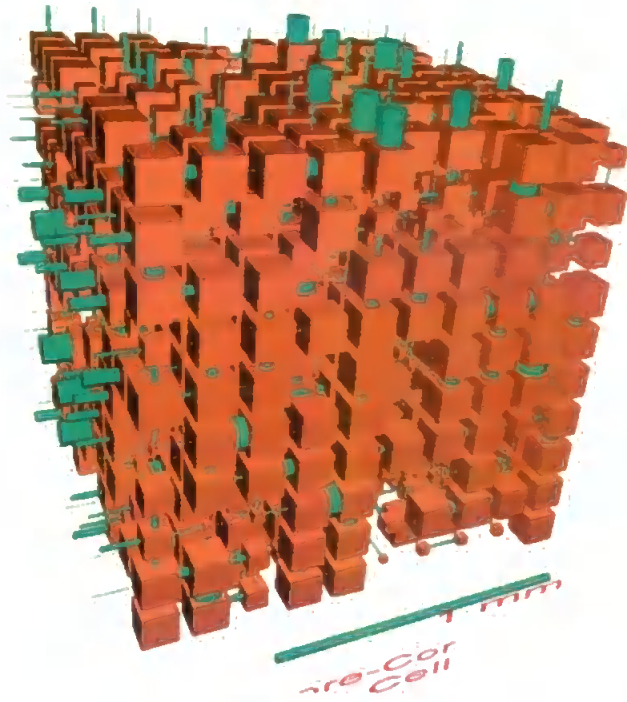


Figure 3.7 Stochastic realization of an S16 Sinterflo® sample showing the representative cubic pores and cylindrical throat features that are fitted to the experimental intrusion curve by way of the Pore-Cor simplex. Note the 1 mm scale bar at the underside of the unit cell.

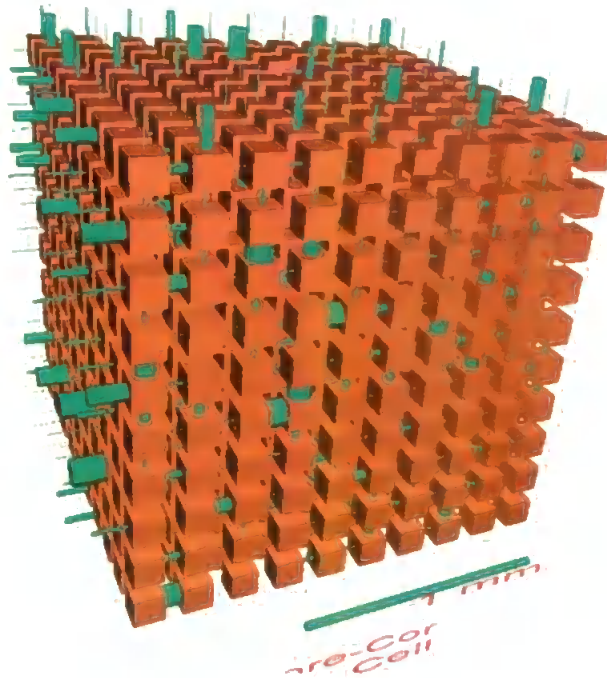


Figure 3.8 Stochastic realization of an S21 Sinterflo® sample.

Figure 3.10 Stochastic realisation of an S36 SinterNo® sample. It may be seen in this structure that a lower value of pore skew has given a greater range of pore sizes.

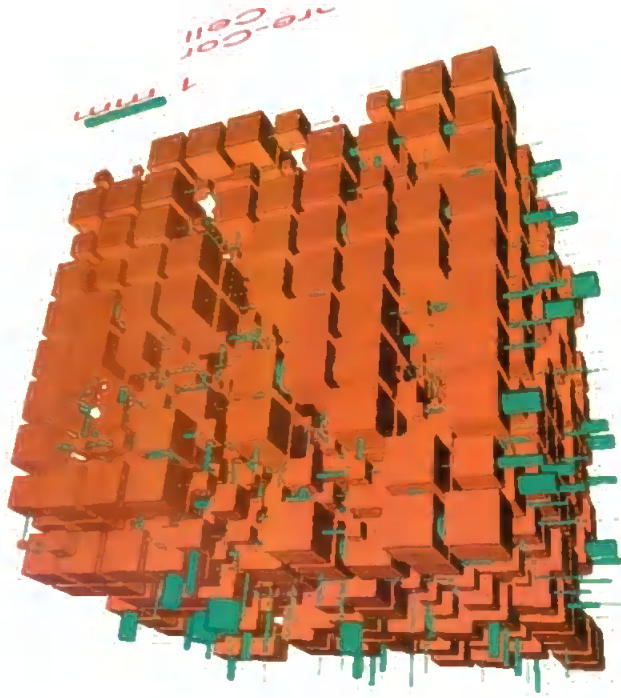
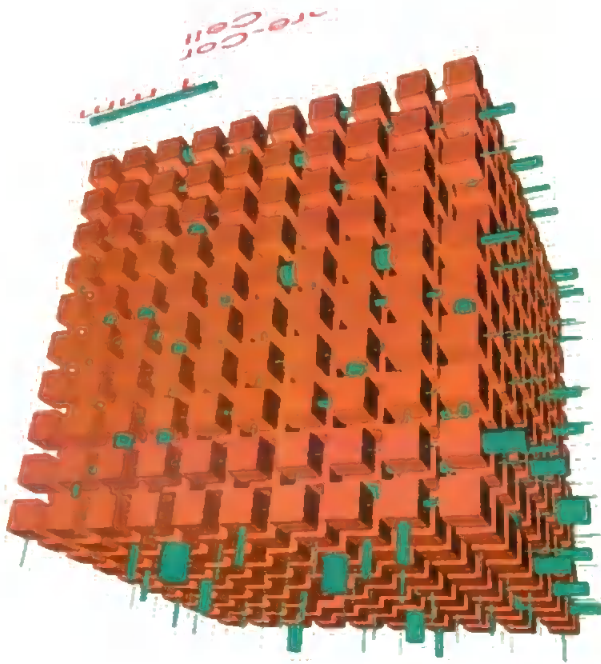


Figure 3.9 Stochastic realisation of an S26 SinterNo® sample.



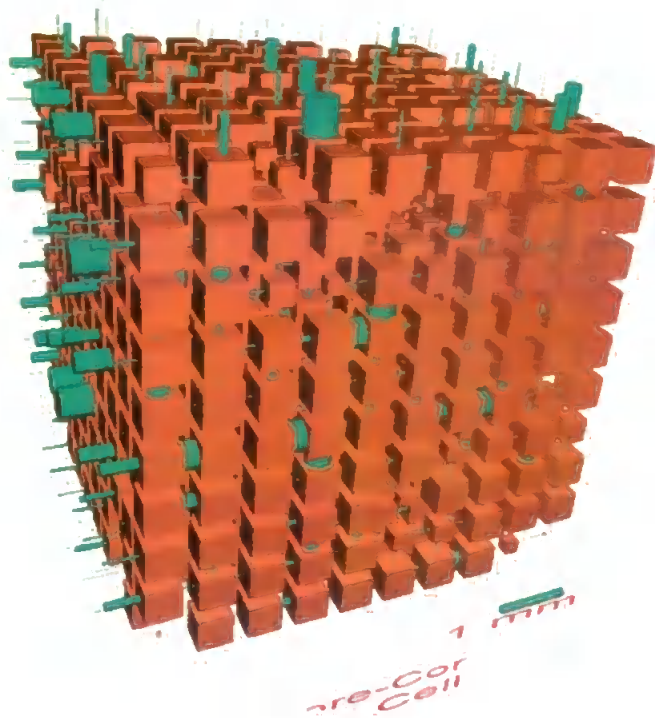


Figure 3.11 Stochastic realisation of an S41 Sinterflo® sample. Note that in the S36 and S41 samples the scale bar is proportionally smaller, indicating the higher pore sizes in these media. This is also evident directly from the intrusion curves (Figure 3.3).

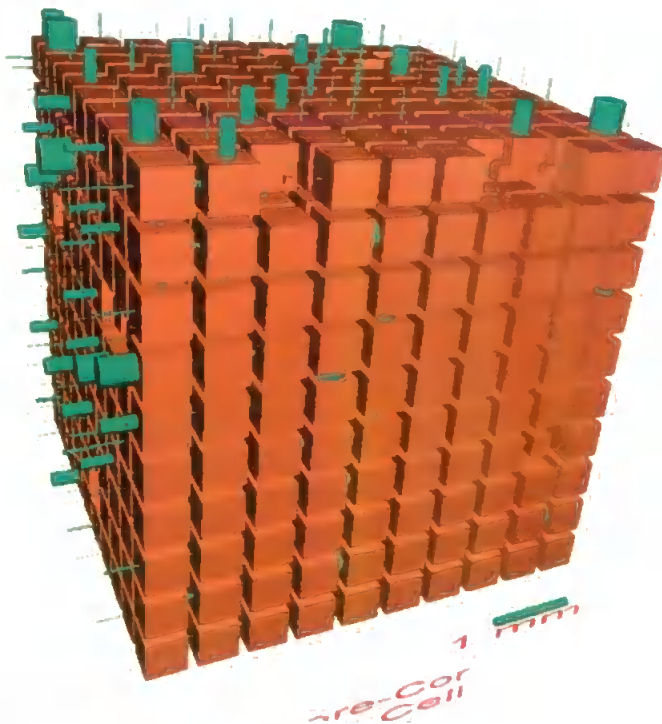


Figure 3.12 Stochastic realisation of a Vyon® T sample.

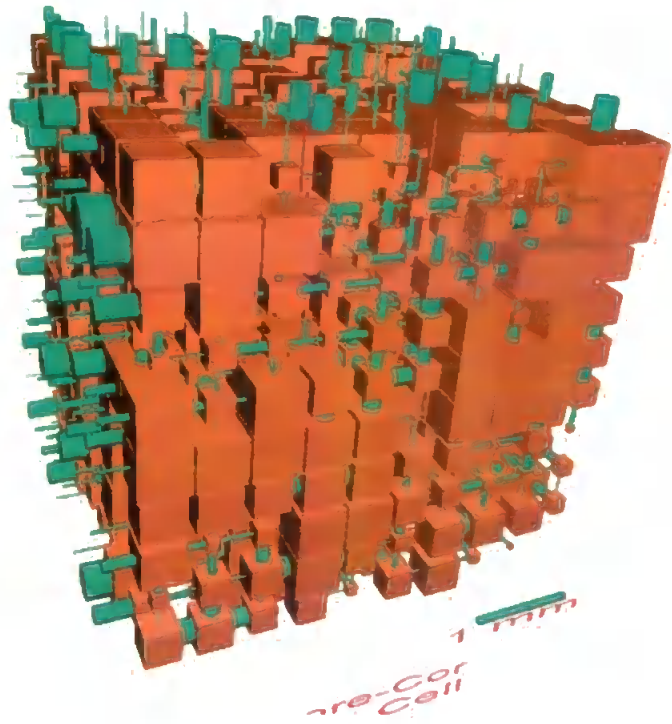


Figure 3.13 Stochastic realisation of a Vyon® F sample. Note the apparent loss of the pore structures but apparent increase in throat sizes compared to the higher porosity Vyon® T (Figure 3.4 and Figure 3.6).

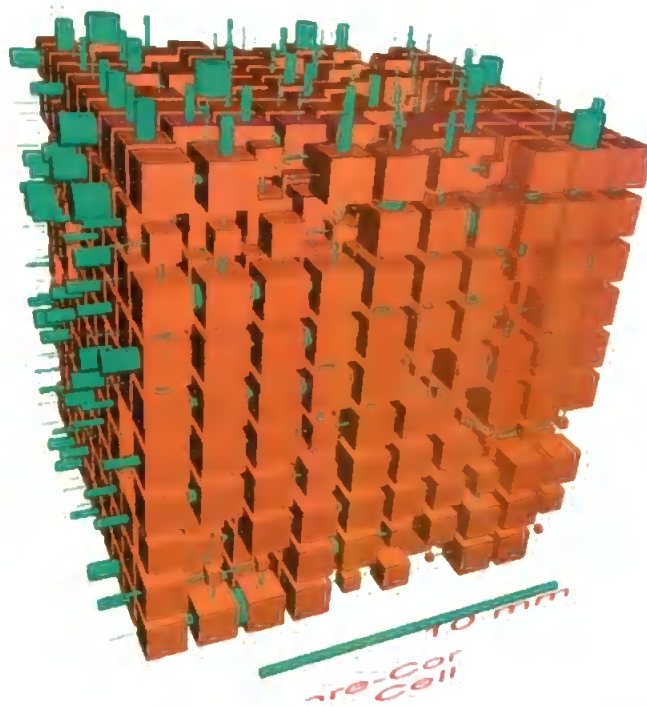


Figure 3.14 Stochastic realisation of a Vyon® HP sample. Note the increased size in scale bar due to Vyon® HP media having a much larger experimental pore size.

**Table 3.1** Table highlighting the fitting parameters used in the Pore-Cor stochastic realisations (Figure 3.7 - Figure 3.14). Feature diameters are governed by the experimental data file and all other values are derived by the software in obtaining a closest fit approximation of the experimental values.

<b>Sample</b>	<b>Stochastic realisation</b>	<b>Minimum feature diameter / <math>\mu\text{m}</math></b>	<b>Maximum feature diameter / <math>\mu\text{m}</math></b>	<b>Porosity</b>	<b>Throat skew</b>	<b>Pore skew</b>	<b>Connectivity</b>	<b>Correlation level</b>	<b>Goodness of fit</b>
Sinterflo® S16	3	0.428	103.592	26.28	-1.003	3.322	3.63	0.181	1.06
Sinterflo® S21	3	0.491	103.652	26.12	0.702	56.673	3.72	$6 \text{ E}^{-2}$	0.97
Sinterflo® S26	3	0.428	174.993	28.64	0.202	183.500	3.75	0.076	0.75
Sinterflo® S36	3	1.080	366.526	28.39	-0.529	3.174	3.43	0.172	1.06
Sinterflo® S41	2	1.075	403.701	28.58	-7.308	10.079	3.74	0.177	0.98
Vyon® T	2	1.219	397.652	50.67	-7.400	26.882	3.99	0.039	0.68
Vyon® F	2	13.365	397.652	39.74	-11.920	1.477	3.78	$8 \text{ E}^{-2}$	0.86
Vyon® HP	1	7.189	1047.639	40.27	3.0539	4.438	4.13	0.247	0.74

### **3.3. Assessing Validity of Modelled Data**

#### **3.3.1. Validation using modelled parameters and experimental data**

As stated at the beginning of this chapter, there is a requirement for the void network simulations to be ‘representative of sample’ in their structural characteristics. This then allows them to be used as the base networks upon which a filtration model may be developed. Therefore it has been necessary to identify whether the networks delivered by the Pore-Cor software show sensible trends in terms of their structural characteristics, when compared with the trends observed in the manufacturing data provided by Porvair Technology Ltd.

At first it was noted that modelled cubic pore sizes seemed unfeasibly large when compared to the manufacturer’s data that had been provided for the media. However, careful visual inspection of the Pore-Cor unit cells, in the Pore-Eye environment, revealed that the simulated cylindrical throat diameters showed good agreement with pore sizes on the manufacturer’s data sheets (Table 2.1 & 2.2) measured by the bubble point and porometry methods (where pore size relates to the restrictive diameter or “throat” of a pore feature). These throats are the controlling factor in fluid flow through a unit cell and control the percolation characteristic. The experimental pore sizes therefore do correspond to the modelled throat diameters, while the modelled pore sizes appear larger than expected to control the porosity of the sample. This may be partly visualised with respect to the Vyon® T and Vyon® F. Figure 3.4 shows that experimentally Vyon® T has a larger porosity than Vyon® F (relative porosity asymptote as pore size decreases), but smaller pore sizes (indicated by the point of inflection of the intrusion curves). These characteristics are represented in the simulated structures (Figure 3.12 and Figure 3.13) by smaller cylindrical throat features in Vyon® T than Vyon® F but a greater proportion of cubic pore space to simulate the

higher experimental porosity. This and other semi-quantitative checks show that the generated model structures do trend in the right direction in terms of their structural characteristics, when compared with the given sample data.

### **3.3.2. Breakthrough pore/throat size**

A further check is the variation of “breakthrough pore/throat size” and the experimental porosity against modelled porosity. Breakthrough pore size relates to the diameter of the pore, or throat, with which an applied non wetting fluid breaks through to the bottom layer ( $z = 0$ ) of the unit cell. Mercury is applied to the top (max  $z$ ) surface of the unit cell and gradually percolates downwards ( $-z$  direction) and laterally ( $\pm x$  and  $\pm y$  directions). As applied pressure is increased, the Washburn diameters of pores are increasingly overcome and mercury eventually percolates to the bottom ( $z = 0$ ) layer. The breakthrough pore/throat size is the first Washburn pore diameter represented by the applied pressure at which mercury leaves the bottom layer of the modelled structure as it has an unrestricted path through the network. This effect can be measured experimentally using an electrode at the bottom of the porous media and utilising the mercury as another electrode. Upon breakthrough the two electrodes connect and the electrical conductivity of the circuit abruptly increases.

The breakthrough pore size is close to the point of inflection in a mercury intrusion curve, as this is the point at which mercury overcomes the most restrictive, or representative, throats and percolates throughout the cell. As such the modelled breakthrough pore sizes may be tabulated to see if they a), increase with respect to the expected increase in media pore size and b), whether the values of the modelled breakthrough pore size correspond to the experimental points of inflection for the samples.



In combination with this the experimental porosities may be compared with the modelled values to assess whether the modelled structures also hold the correct porosity terms with relation to the experimental samples. This allows us to validate whether pore size and porosity characteristics of the simulated networks relate sensibly to the available manufacturing data.

**Table 3.2** Showing modelled breakthrough pore size, in relation to experimentally derived maximum pore size and comparison of experimental and modelled porosity.

<b>Sample</b>	<b>Experimental porosity</b>	<b>Modelled porosity</b>	<b>Modelled breakthrough pore size (<math>\mu\text{m}</math>)</b>	<b>Experimentally derived maximum pore size (<math>\mu\text{m}</math>)</b>
Sinterflo® S16	26.31	26.28	12.6	13
Sinterflo® S21	26.14	26.12	14.8	23
Sinterflo® S26	28.66	28.64	16.3	34
Sinterflo® S36	28.41	28.39	32.8	67
Sinterflo® S41	28.60	28.57	44.0	94
Vyon® T	50.71	50.67	32.2	n/a
Vyon® F	39.78	39.74	88.0	n/a
Vyon® HP	40.31	40.27	220.1	n/a

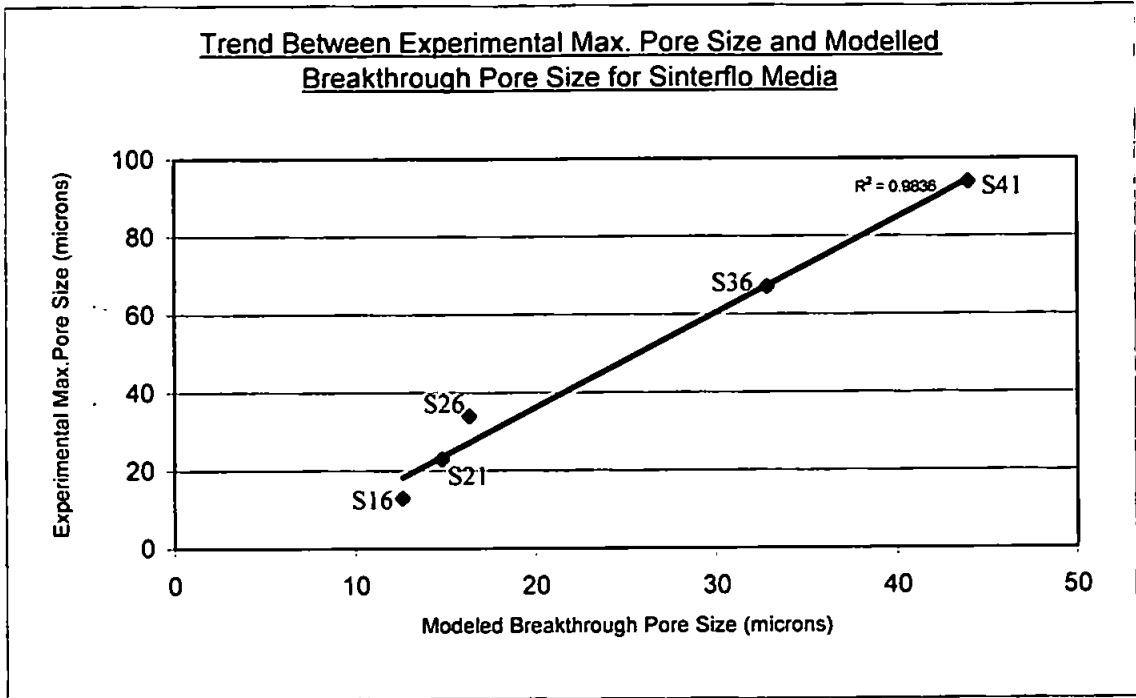


**Figure 3.15** Graph showing the trend in Sinterflo® media between maximum experimental pore size and modelled breakthrough pore size. Data points are labelled to corresponding media grade.

From the tabulated and graphical data it is apparent that the modelled media show a closely linear correlation with the experimental data (Table 3.2 and Figure 3.15). Another interesting point to note, although not currently investigated, is that the modelled breakthrough pore size, with the exception of Sinterflo® S16, is approximately half the diameter of the experimental maximum pore size in Table 2.1. This correlation is represented graphically in Figure 3.16 by doubling the modelled values of breakthrough pore size for comparison with the experimental maximum pore sizes.

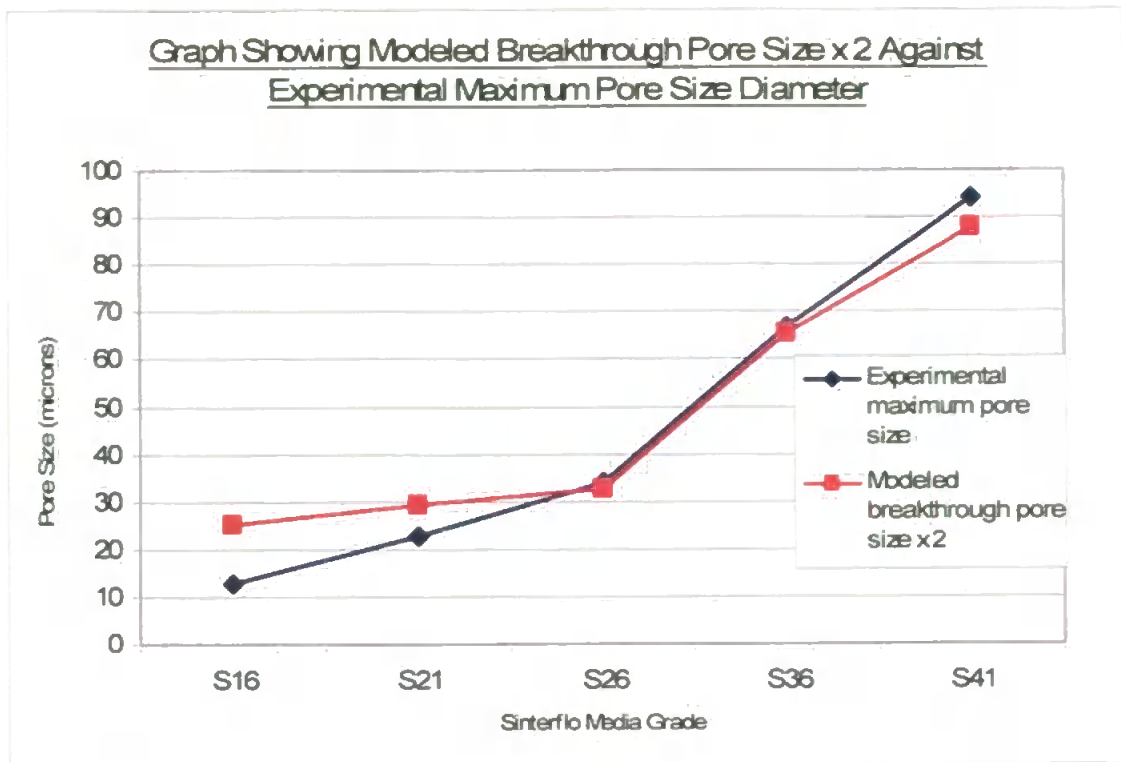


Figure 3.16 Graph showing how the experimentally derived maximum pore size correlates with the doubled modelled breakthrough pore size of the simulated Sinterflo® structures.

The largest deviation is for the Sinterflo® S16 media. This may be due to its very small range of pore sizes arising from a fine and uniform starting material. This narrow band of pore sizes may also be seen in the range between the 98% and 99.9% liquid removal efficiency columns in Table 2.1. Although the trend of modelled breakthrough pore size against maximum pore size of media has been derived from only a few samples, it is possibly worth investigating in future as a means of validating the modelled data. The experimentally derived maximum pore sizes are not stated for the Vyon® media as the samples provided for this research were manufactured as a bespoke sample set specific to the study. Therefore the manufacturing data (Table 2.2) is not directly applicable to the studied samples and can only be used as a general guide to Vyon® sample trends exhibited.

### 3.3.3. Validation of void networks using formation damage simulations

From initial work undertaken on Vyon® samples it was also found that the non-dynamic filtration or ‘formation damage’ calculation within the software may also be used to indicate whether the modelled structures trend in a logical manner. Formation damage simulations entail flooding the unit cell with simulated colloidal particles of a given size which in turn block any throat feature smaller than the designated particle size. This is repeated at up to 100 different particle sizes until the simulated permeability tends to zero. The flooding of particles and blocking of pores in this way is not controlled by a flow through the network and is more akin to an instant elimination of all void features of a given size from the structure. The simulation also makes an allowance for the shielding of large pores by small throats, which is not undertaken in more simplistic capillary approximations (*Application Note 1*). This results in pore voids being cut off when an upstream throat (of smaller diameter) becomes blocked, unless there is another ‘by-pass’ route in the 3-dimensional network by which the space can be accessed.

If the modelled structural representations of these media are correct, then a permeability decline against contaminant particle size addition should see the permeabilities of the structures tending to zero at increasingly larger particle sizes through the series S16 to S41. Results are presented graphically for both the Sinterflo® and Vyon® media samples (Figure 3.17 and Figure 3.18). Permeability values for the media have been normalised and are presented as relative permeability declines against applied particle size addition.

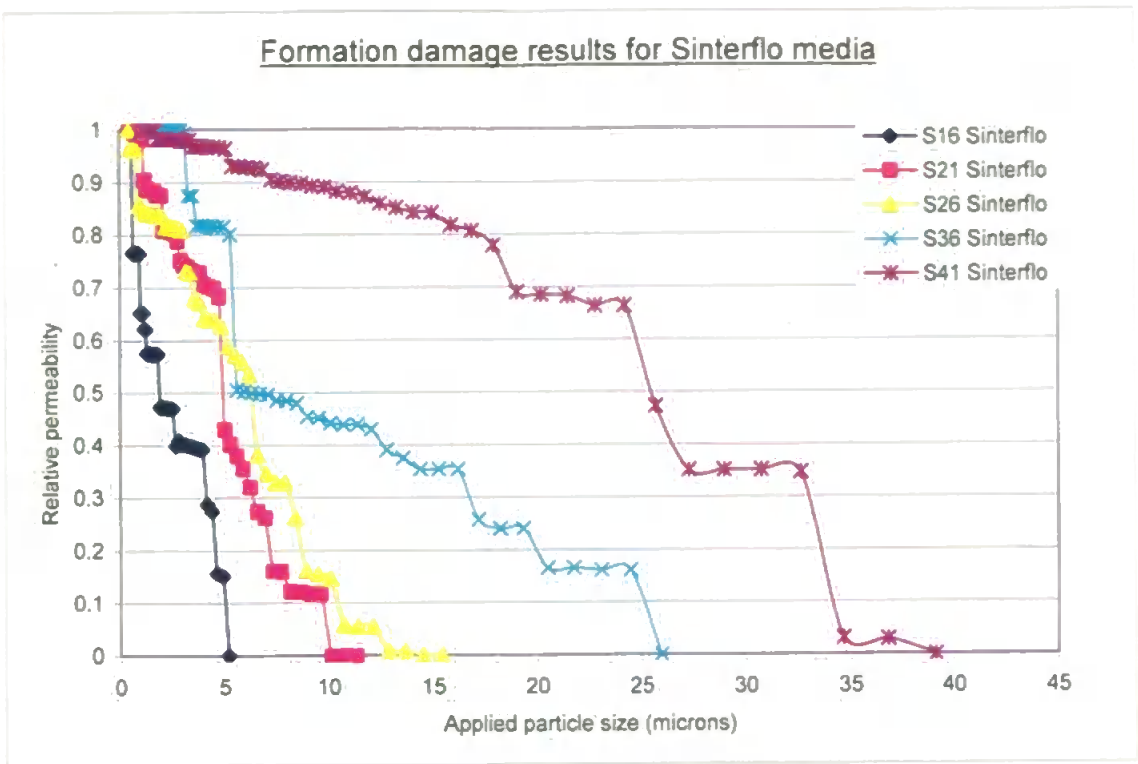


Figure 3.17 Results of formation damage simulations on Sinterflo samples. Permeability values have been normalised and represented as relative permeability's for ease of sample comparison.

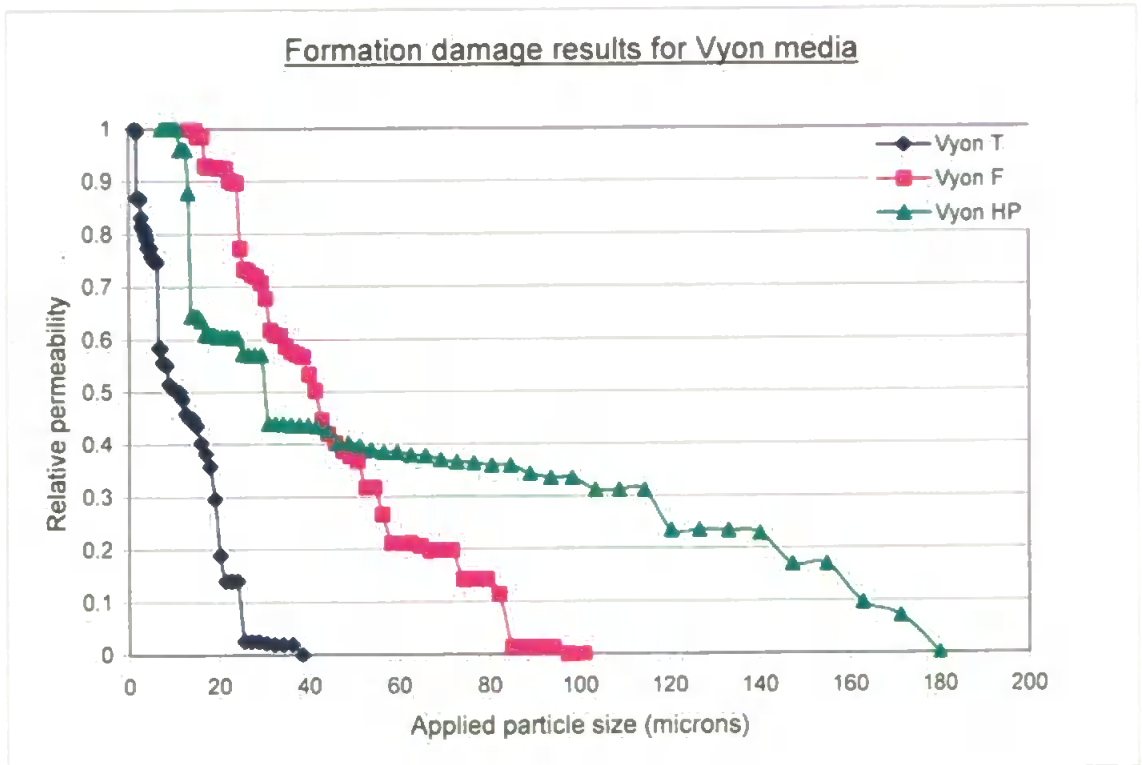
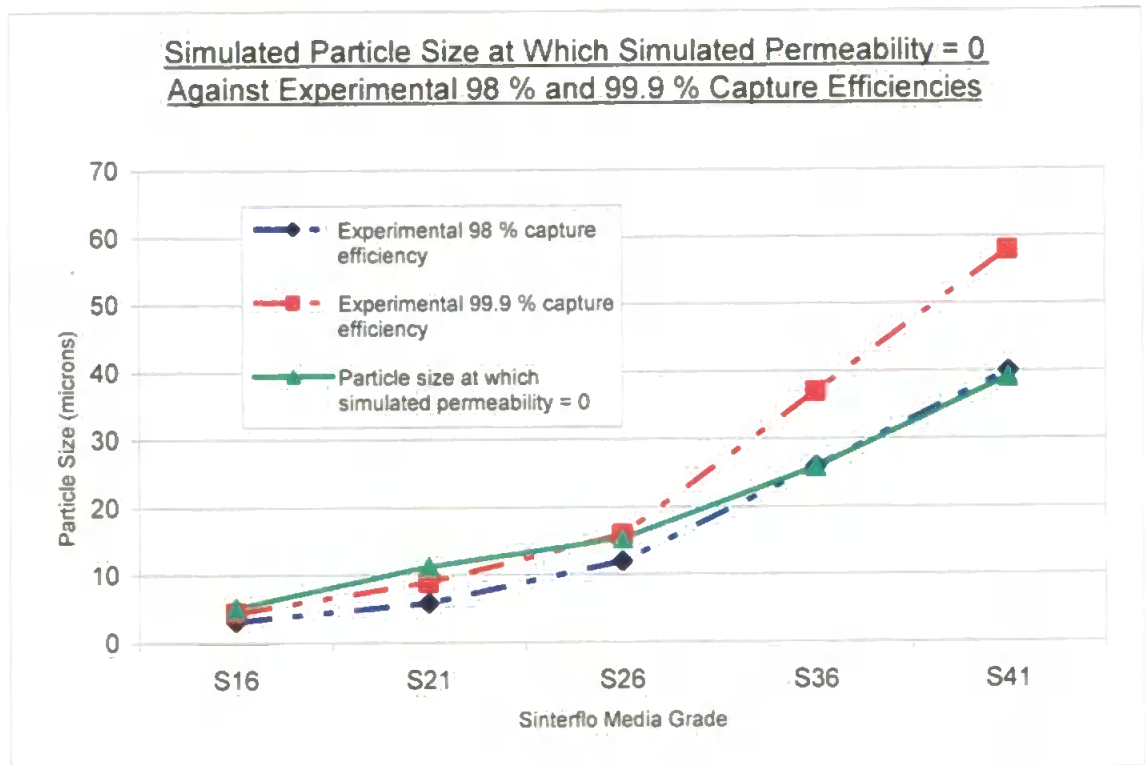


Figure 3.18 Results of formation damage simulations on Vyon samples. Permeability values have been normalised and represented as relative permeability's for ease of sample comparison.

**Table 3.3 Results for Sinterflo® formation damage simulations shown against 98 % and 99.9 % experimental capture efficiencies. Note the closeness of simulated results to experimental values.**

Sample	Simulated particle size at which permeability = 0 (µm)	Experimental 98 % capture efficiency (µm)	Experimental 99.9 % capture efficiency (µm)
Sinterflo® S16	5.2	3.2	4.5
Sinterflo® S21	11.3	5.9	9
Sinterflo® S26	15.4	12	16
Sinterflo® S36	25.9	26	37
Sinterflo® S41	39.1	40	58



**Figure 3.19 Comparison of the simulated formation damage results with the experimentally stated 98 and 99.9 % capture efficiencies. Formation damage results are presented as the particle size at which permeability = 0.**

It is seen by tabulating and plotting the data from Figure 3.17 against the data from Table 2.1 that the results for Sinterflo® media trend not only in the expected manner but also hold very good agreement with the 98% and 99.9% capture efficiencies stated for the media (Table 3.3, Figure 3.19 ). This closeness of the simulated applied particle size to the known capture efficiencies of the media is a highly successful validation. In reality it shows that if we completely flooded the simulated filter with particles that the pore volume is deemed to be 98 - 99.9 % successful at capturing, we would completely block its void structure and hence make its permeability plummet to zero. This situation would also arise in an industrial fluid stream. If we took an infinite amount of contaminant that a filter is 99.9 % efficient at collecting and then challenged it against the filter, it would be expected to block very quickly. The additional variable in an industrial fluid stream would be the flux rate of particle matter that controls the speed at which the filter became un-usable.

It is seen in the Vyon® data that is presented (Figure 3.18) that the applied particle size at which permeability tends to zero is 38 µm, 100 µm and 181 µm through Vyon® grades T, F and HP respectively. This trend is agreement with an increasing capture efficiency rating and maximum expected pore size for these media. However remembering that these Vyon® samples have been created specifically for this research, it is not possible to correlate the trends directly to sizes quoted in Table 2.2.

It must be remembered that the structures generated by Pore-Cor are non-unique solutions to the percolation characteristic of the experimental sample. The levels of uncertainty can be seen visually (Figure 3.20) where the averaging of ten stochastic generations that have been subjected to the formation damage calculation is represented by the pink series on the graph.

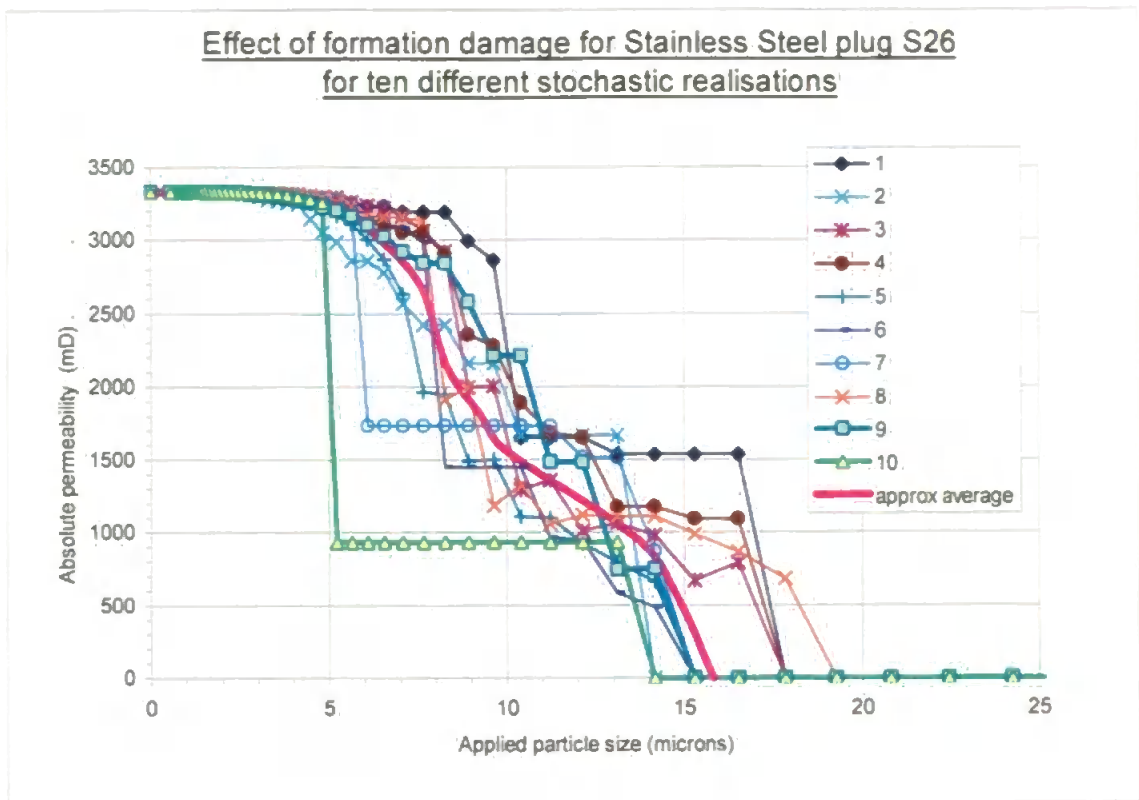


Figure 3.20 Effect of formation damage graph for 10 stochastic realisations of the Sinterflo® S26 media. The uncertainty of the particle size at which the permeability tends to zero is averaged for the 10 generations and represented by the average value.

Many different approaches may be undertaken in the study of formation damage in terms of the effective particle size. In the present study, single particles have been used for blockage, although in other studies (*Application Note 1*) it has been suggested that due to particle-particle interactions particles can block throats three times the diameter of their own diameter. This is termed the Three Particle Bridging approximation and is used in cases such as the analysis of oil well damage (Gruesbeck and Collins, 1982). This process is dependant on the particle and fluid chemistry and occurs due to attractive interactions between particles which collide to form an aggregated particle. This aggregate then travels through the fluid stream until it blocks a pore/throat feature smaller or equal to its size. To represent this or any other particle aggregation size, the data file can be modified to plot the renewed formation damage approximation by



simple division of the single particle size by assumed number of particles in a given aggregate.

### **3.4. Conclusions**

It has been shown that the simulated void network structures delivered by Pore-Cor show a satisfactory correlation with the manufacturer's data for the Vyon® and Sinterflo® media samples. This leads to the conclusion that the network simulations are a valid starting point for development of a dynamic filtration model. The porosimetry of the samples has been shown to be reproducible, and therefore is considered a reliable basis for modelling the pore size distributions for use in this work.

The data manipulation process (Section 3.1), has been shown to offer a sensible approach to standardising porosimetry data sets for use in the modelling of network structures. Results have shown that the use of the trimming function under the controlled parameters has no effect on the sensitivity of the porosity analysis and results are found to mirror the experimental variance of < 4% between replicates which may be attributed to small sample heterogeneities. This may be explained in that the porosity is calculated from the intruded mercury volume of the analysis and the trimming of tailing points at 100% and 0% intrusion volumes has no effect on this value. There does however exist a possibility (Section 3.1) that the trimming process may have some effect upon the permeability and flow path calculation in the software. Due to the stochastic nature of the unit cell, the associated changes in representative permeability values and the reality that replicate samples may have their own structural variance a sensitivity analysis of permeability has not been investigated. This investigation may be

required for future validation of the model although at present focus has been directed at development of the models functionality.

Modelled breakthrough pore sizes have shown a correlation with the experimentally derived maximum pore size as measured by bubble point analysis. This correlation has been used to show a trend of agreement between the analysed samples and modelled network representations of filtration media. Although this process has been useful for the analysed Sinterflo® and Vyon® media it would need to be tested further on other media types to prove a useful tool in validation of unit cell networks before and automatic inclusion to the model can be considered..

It has also been shown that the use of the formation damage simulation offers a good validation technique for the porosimetry data and the modelled structures. This is confirmed by the closeness of match to the experimentally derived 98 – 99.9 % capture efficiencies of the Sinterflo® samples.

## **4. Development of a filtration model in Pore-Cor**

The development of the Pore-Cor software to include a dynamic filtration module is one of the main aspects of this study. Previous programming of the software had already been undertaken to allow an initial non-dynamic filtration model, in the form of a formation damage simulation (Section 3.3). From this the unit cell may be viewed in Virtual Reality using Pore-Eye, and an image generated to show how much of the unit cell porosity and permeability has been lost at a given applied particle size. This however is not dynamic in nature as the contaminant particles are flooded into the cell rather than gradually challenged against it, as would occur in real industrial fluid streams (Lee and Koplik, 1996). This therefore leads to the requirement of a dynamic, sequential model. This chapter aims to:

- (i) Show the systematic approach taken in developing the Pore-Cor software into a dynamic filtration model,
- (ii) Highlight the reasoning behind the selected processes that have been included to deliver the final filtration model.

### **4.1. Approaching the problem**

The requirement for an effective desk top applicable filtration model has been the main aim of this research. The initial step in adding such a model to the existing void network simulator is to decide upon a suitable systematic approach that may be executed sequentially in the final product. Much investigation was undertaken into comparable previous filtration models; their varying degrees of success were considered in deciding upon a scientifically sound method that could be applied to the Pore-Cor software to provide a working predictive filtration model.

As stated in chapter one, Elimelech (1995) suggests that to produce a sound filtration model three steps must be undertaken. The first of these is to produce a representative network; this was already achieved and validated within the previous chapter. The second is to then develop a system for representing fluid flow through the given network, and the final step is to apply the particle contamination and relevant capture mechanisms. The validity of considering the development of filtration models in this way is supported by the same systematic approach taken to a 2-dimensional network filtration model by Ochi and Vernoux (1999).

Inline with this reasoning it was apparent that the development of the standard Pore-Cor 3-dimensional networks into a dynamic filtration model would require the programming of an active flow-field. This would subsequently act as the carrier of contaminant particulate through the representative void networks. Many models, such as that provided by Houi and Lenormand (1986) have initially been based upon the work of Todd et al. (1984) whereby no active flow field was actually used in the movement of particles through a filter. Instead a random walk approach of particle migration through the network was used. Not using a realistic flow field in such models means that the simulated contaminant particle migration is effectively being undertaken without any consideration for the pore size distribution of the modelled network. Pore size distributions are known to strongly affect macroscopic properties of the system (Sahimi et al., 1990) and as such it is deemed necessary that a good model needs to incorporate a valid flow field simulation as a means for contaminant particle migration through the network, and to allow successful modelling of permeability decline and associated pressure drop across the media. This is further highlighted with the success of later models based on the 'flow-biased' movement of particles through networks as first proposed by Sahimi et al. (1983, 1986) and Sahimi and Imdakm (1988).

The flow of fluids through a porous system is controlled by a number of factors. These include the structural geometry, fluid properties and the driving force applied to them (Dodson and Sampson, 2000). In stochastic models such as Pore-Cor, properties such as geometry are much simplified and require a different consideration when developing a simulated fluid flow through the stochastic media (Section 1.3.5.4). Also to be considered in terms of providing a successful filtration model, and one that provides improvement on past attempts, is the pore level flow characteristic of the structure. This needs to be elucidated explicitly rather than relying on a continuum approach or fitting against empirical data (Ives,1960; Heertjes et al.,1967; Tien, 1989). A pore level elucidation of such a flow field allows us to consider its effects in simulating particle movement and capture processes within the model. Subsequently it allows consideration of how such capture processes change both the void structure and the flow regime of the filter on both a pore and representative unit cell level, under filtration conditions.

Also to be considered is the actual contaminant particle addition and capture mechanisms that will be applied to the model. Both the individual particle size and the overall distribution of particles, within a suspension to be filtered, need to be considered. It is known that both these parameters are of high importance and influence the overall filtration efficiency of a given filter (Osmak et al., 1997). During the filtration process it is understood that the filter porosity decreases and the interfacial fluid velocity increases with the capture of such contaminant particles (Herzig et al., 1970; Ojha and Graham, 1991). This occurs not only on the macroscopic unit length scale but also at the pore level. Therefore consideration needs to be given to not only the size and distribution of particles added to the proposed model but also as to how

their capture and entrapment in the network effects the porosity and permeability of the 7 modelled filter on both a pore and unit cell scale.

Capture mechanisms need realistically to reflect the filtration processes that are to be investigated. For example it has already been stated (Section 1.3.2.1) that the proposed model should only consider those capture mechanisms that are relevant to liquid filter medium filtration (FMF) of particles  $> 1 \mu\text{m}$  in size. This automatically eliminates the inclusion of capture mechanisms such as diffusion, due to its applicability only to particles  $< 1 \mu\text{m}$  in size, and also impaction mechanisms due to the fact that in liquid filtration inertial forces are not important (Tien, 1989).

Using this knowledge of previous filtration models and their associated successes and downfalls it was necessary to develop a model plan that could be incorporated into the existing Pore-Cor software to deliver the proposed filtration model, shown overleaf (Figure 4.1). The Pore-Cor software is based on a Fortran language with a Visual Basic user interface. Over the many years development of the software the working program has become extremely complex and it now involves many sub routines that need consideration when adding new modules to the core program. Due to this complexity a new Fortran compiler was procured to allow a user friendly programming environment, and allow for easy mapping of programming modules. Programming is now carried out in a Compaq Visual Fortran Compiler (Version 6.6A) and is coded in Fortran 90 language. This is combined with a user interface which is coded in Microsoft Visual Basic (Version 6.0). The complete Pore-Cor software, as an end product, can be run in a Microsoft Windows 98 or Windows Vista environment on any stand-alone or networked 32-bit or 64-bit PC.

**Flow Chart Showing Modelling of Experimental Intrusion Data  
and Simulation of Filtration**

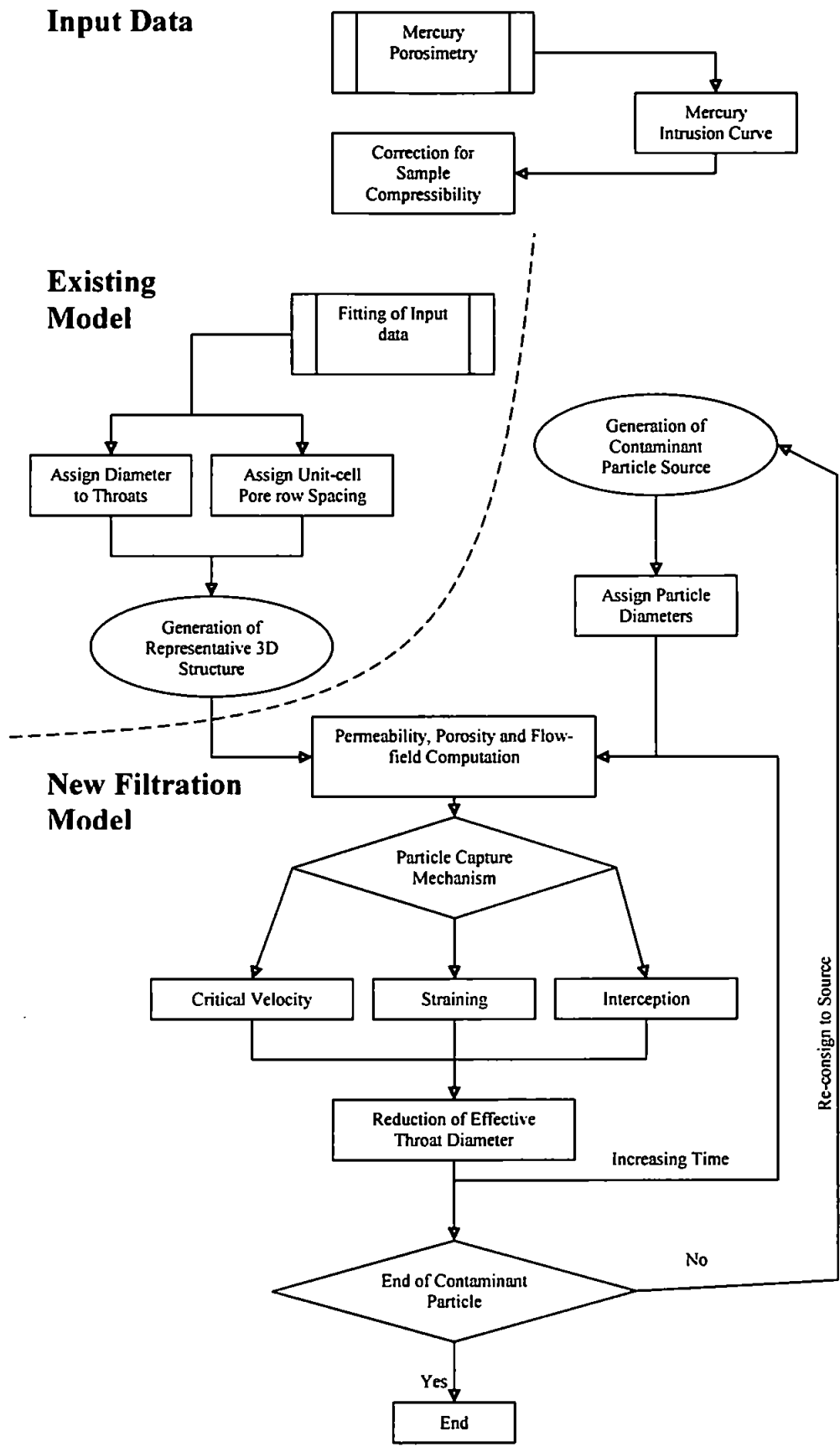


**Figure 4.1** Systematic flow diagram of the filtration model developed in the Pore-Cor software package.

## **4.2. Programming of the active flow field in the Pore-Cor model**

Although not originally accessible from the output data for permeability calculations, it was known that the flow calculation for each arc feature of the unit cell was inherent in the Dinic algorithm calculation for network permeability (Section 1.3.5.4). Current programming from this research focused on disentangling the current Fortran coding to allow this information to be accessible for use in a calculation of the flow capacities and flow rates of the individual arcs found throughout the representative networks.

The programming associated with this untangling of the Dinic algorithm has been extremely complex and time consuming. It was found that the Dinic algorithm undergoes five different rearrangement stages and two renumbering stages in its calculation of individual arc capacities. Thus the same arc is given a different identity on several occasions as the algorithm progresses. Due to this it was necessary to develop a “tracking” method whereby each arc was ‘tagged’ and followed through the algorithm. Only then was it possible to know which throat the final flow and capacity data referred to. From elucidation of this information it has been possible to assign the Dinic flow rate and capacity values to each active arc (one which has an active flow volume) in the unit cell.

Although the individual arc flow-rates were identified within the program, it was also deemed necessary to visualise the results so that a clearer understanding of the network flow was available. To achieve this, a new algorithm was developed to allow the Pore-Eye module of the software to show flow regimes within the simulated networks by use of colour contouring. The representation of flows in this manner also led to a number of difficulties which have had to be overcome. The first of these was the elucidation of flow directions and the combined effect of opposing flows. In each arc, flow is able to



travel in both directions, with the exception of the vertical return on the + z Cartesian coordinate as mentioned in section 1.3.5.4. Overcoming this problem required programming to show flow in each of the individual directions (+ve and -ve directions) on each representative axis. Based on these flows a net flow representation of the network was also constructed using colour contouring. The contouring is controlled by the programmed user interface for viewing permeability results (Figure 4.2). Net flows are shown as a red to blue colour gradient in the +ve Cartesian directions and in a red to yellow colour gradient in the -ve Cartesian direction.

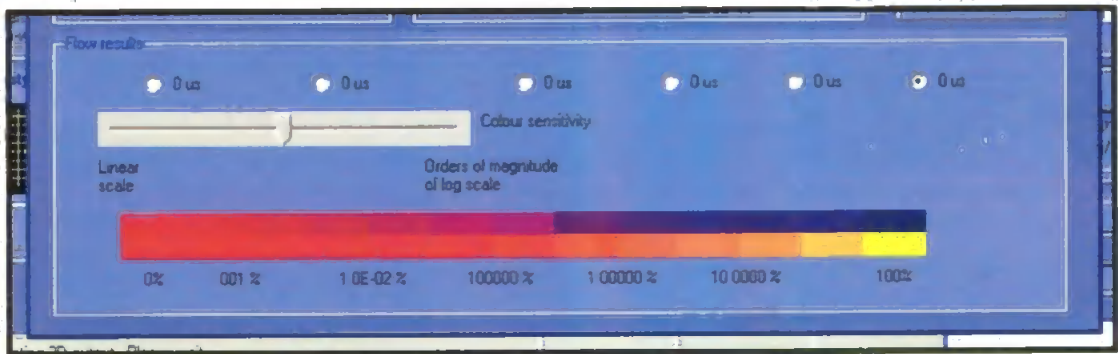


Figure 4.2 Screen shot of the colour gradients as seen on the user interface. Red to blue representing flow in the positive direction and red to yellow for flow in the negative direction. Also indicated is the sensitivity control bar so that results may be expressed in a log or linear scale.

The new programming module has been called "Colour Flow" and forms the basis of the filtration model. In Figure 4.2 areas of highest flow rate are represented in the most blue and most yellow for +ve and -ve directions respectively. The progressive colour gradient between red and these high flow colours represents differing flow rates within features as a function of the maximum flow value of the cell.

#### 4.2.1. Testing and demonstration of the Colour Flow algorithm

Pore-Cor has a range of geometric structure types which can be used for the modelling of different types of materials, as shown below (Figure 4.3). After the user chooses the structure type, the simplex can test correlation levels from 1 (fully correlated) to 0 (random), as shown by the dashed lines in Figure 4.3, while also varying the other fitting parameters. To test and demonstrate the new Colour Flow algorithm, seven structures were chosen, at correlation levels of 0.95 or 0.5, as shown numbered 1 to 7 (Figure 4.3). The unit cell generation algorithm is unable to generate some structures with correlation level 1 because of difficulties in positioning the throats, so a correlation level of 0.95 rather than 1.0 was used throughout for all fully-correlated structures. All structures contained throats and pores over the size range 1 to 100  $\mu\text{m}$ , with a flat log/linear throat size distribution as shown in Figure 4.4 (Pore-Cor version 6.12, throat skew = 0.0, throat spread = 0.575, connectivity = 3.5, porosity = 10%). The pores were set as being equal to the size of the biggest throat entering them (pore skew = 1.0), so the sizes of the pores varied from structure to structure. In Figure 4.4 for example, the pore sizes oscillate as the throats are grouped within each layer.

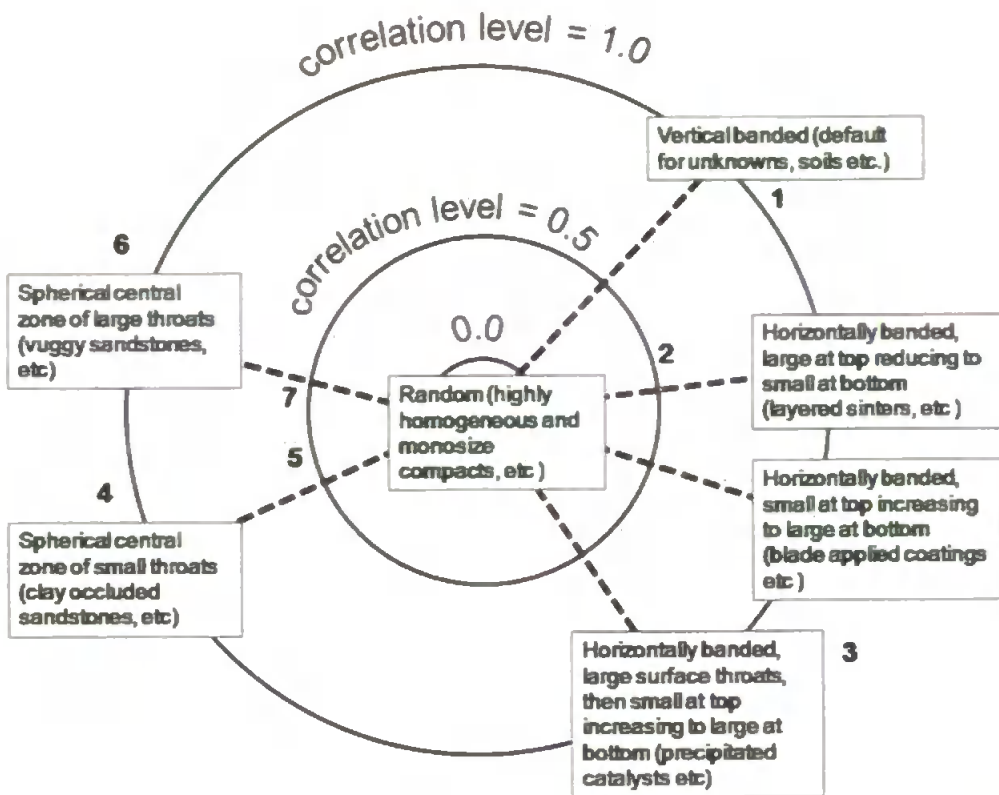


Figure 4.3 Diagram showing structure types available in Pore-Cor simulations. Bold numbers 1 – 7 refer to the structures used for testing the Colour Flow algorithm within this section.

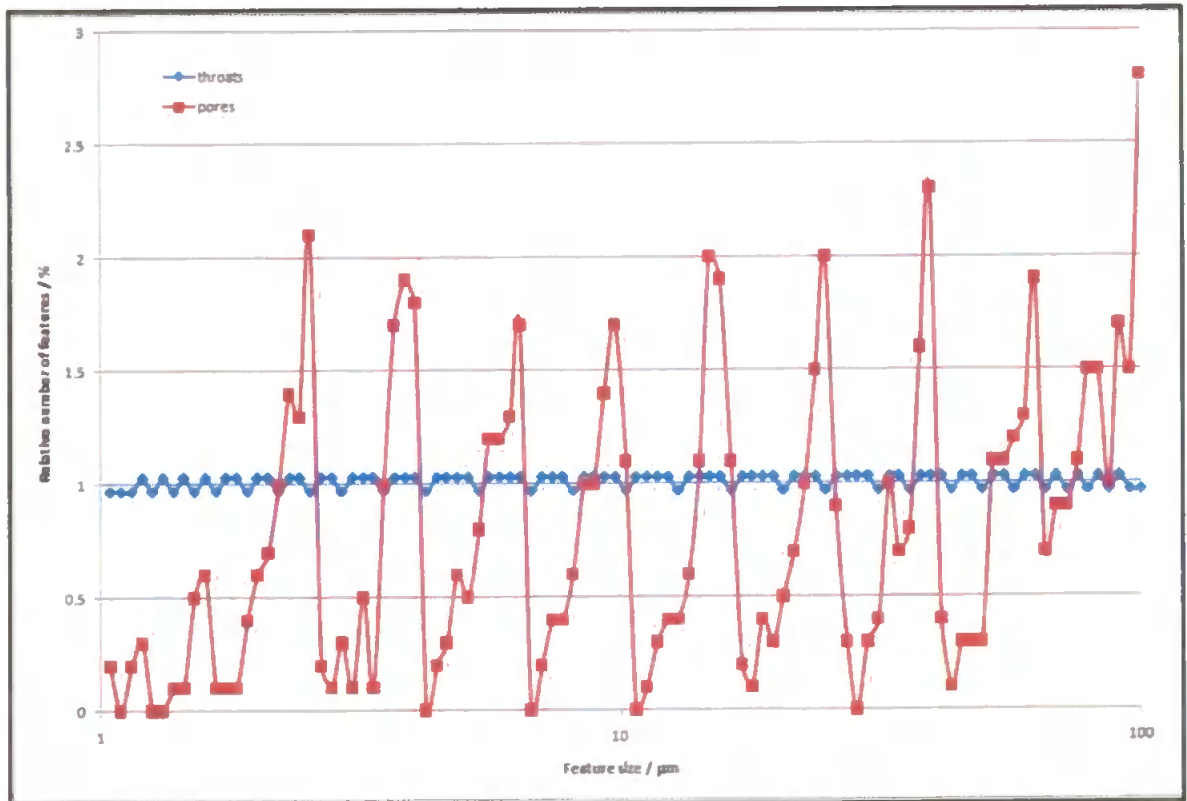


Figure 4.4 Pore and throat size distribution for vertically banded structure.

Flow is induced from the  $xy$  plane at maximum  $z$  (i.e. the top face shown in the diagrams below) in the  $-z$  (downwards) direction. Figure 4.5 shows this flow colour-contoured as shown in the scale bar with blue as maximum flow, and colours changing with the logarithm of the flow relative to the maximum arc flow in the network, as shown. Figure 4.5 shows only the flow in the  $-z$ ,  $-y$  and  $-x$  directions. As expected, the flow is concentrated through the wider pores and throats. The flow is not exactly in layers, because the layers themselves have a slight curvature into a spherical locus. This curvature ensures that changes in correlation level produce the smoothly changing structural properties necessary for successful movement of the simplex around parameter space. Structures shown in this section are shown as a group of four repeating unit cells so that the flow may be visualised crossing the boundary condition of the network representations.

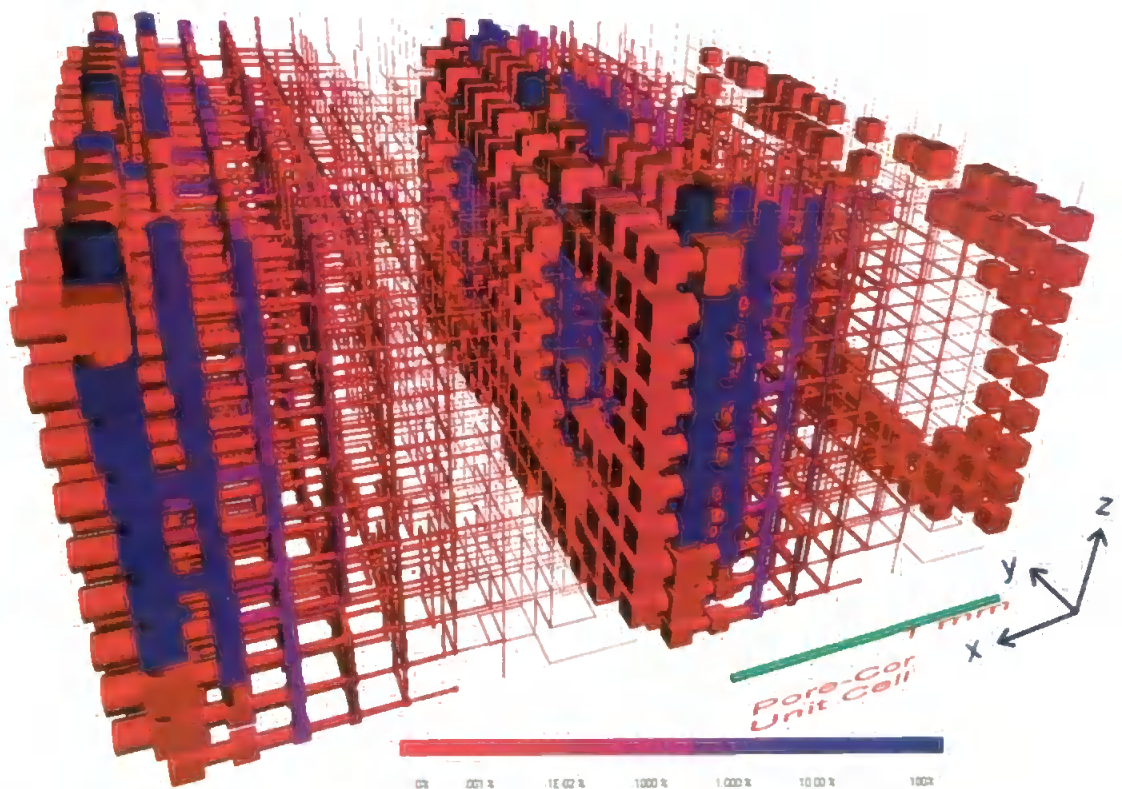


Figure 4.5 Negative-direction flow ( $-x$ ,  $-y$ ,  $-z$ ) through vertically banded structure (1 in Figure 4.3), correlation level = 1

Figure 4.6 shows flow through the same structure in the positive  $x$  and  $y$  directions ( $+z$  flow is disallowed). As may be observed from the diagram there is very little flow in these directions and this positive flow direction, in this case, serves to connect up the flow paths for the major  $-z$  direction flow shown in the previous figure (Figure 4.5). It is also useful to view net flow – i.e. the sum of the two flows in each direction, expressed with the same colour contours (Figure 4.7).

Net flow is also shown in the pores, but is difficult to represent, since it includes flow in three orthogonal directions. The simple arithmetic sum of the resultant flow from all positive and all the negative directions is shown, but often produces a counterintuitive colour contour for the pores. Nevertheless, it provides a useful overall summary, and so all the subsequent structures are shown with net flow only.

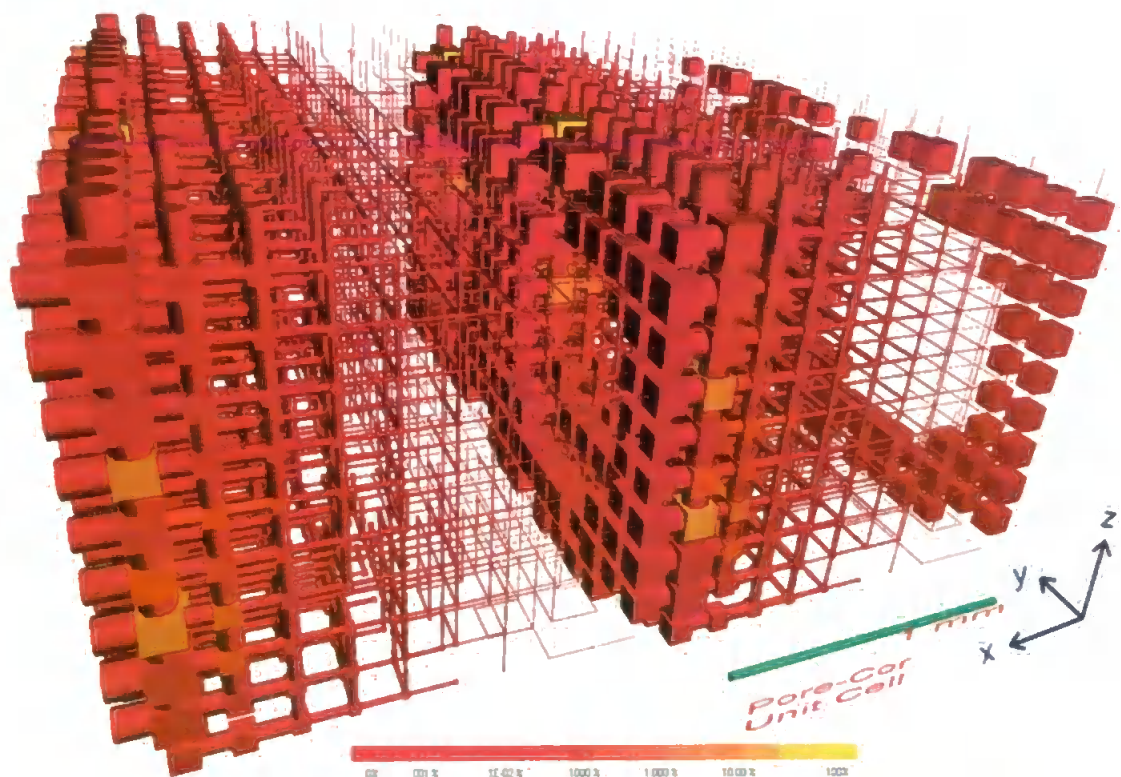


Figure 4.6 Positive-direction flow ( $+x +y +z$ ) through vertically banded structure (1 in Figure 4.3), correlation level = 1

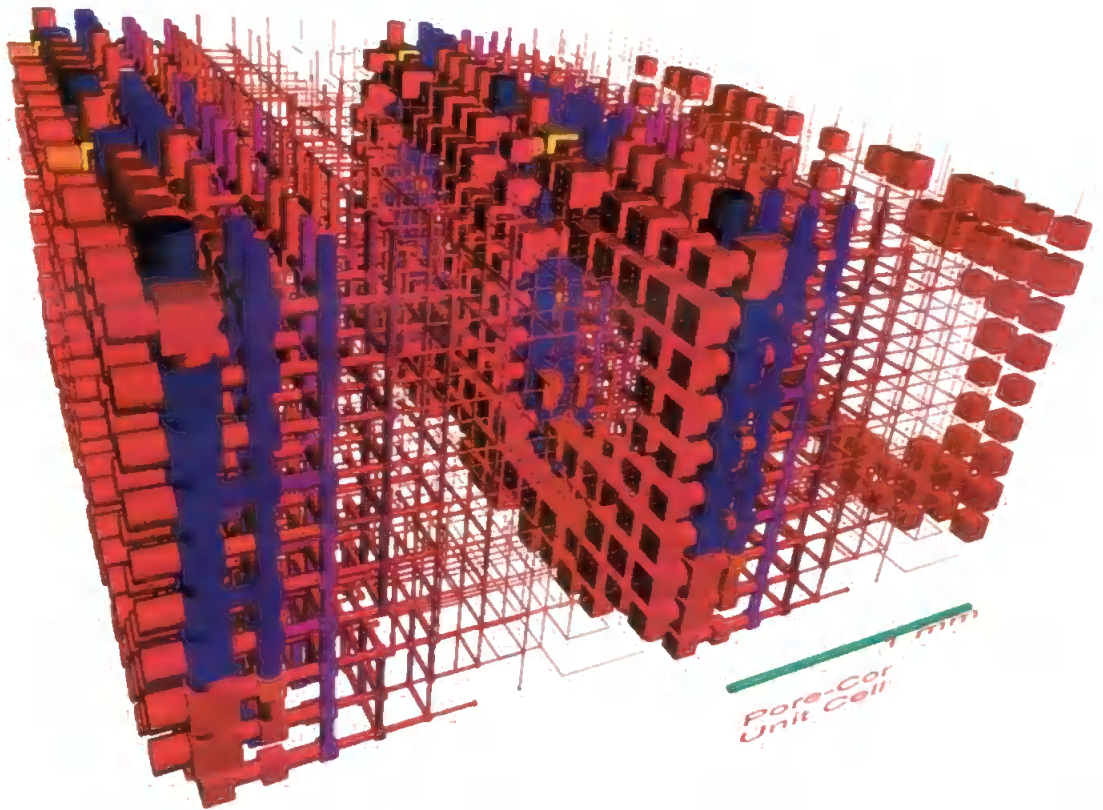


Figure 4.7 Net flow through vertically banded structure (1 in Figure 4.3), correlation level = 0.95

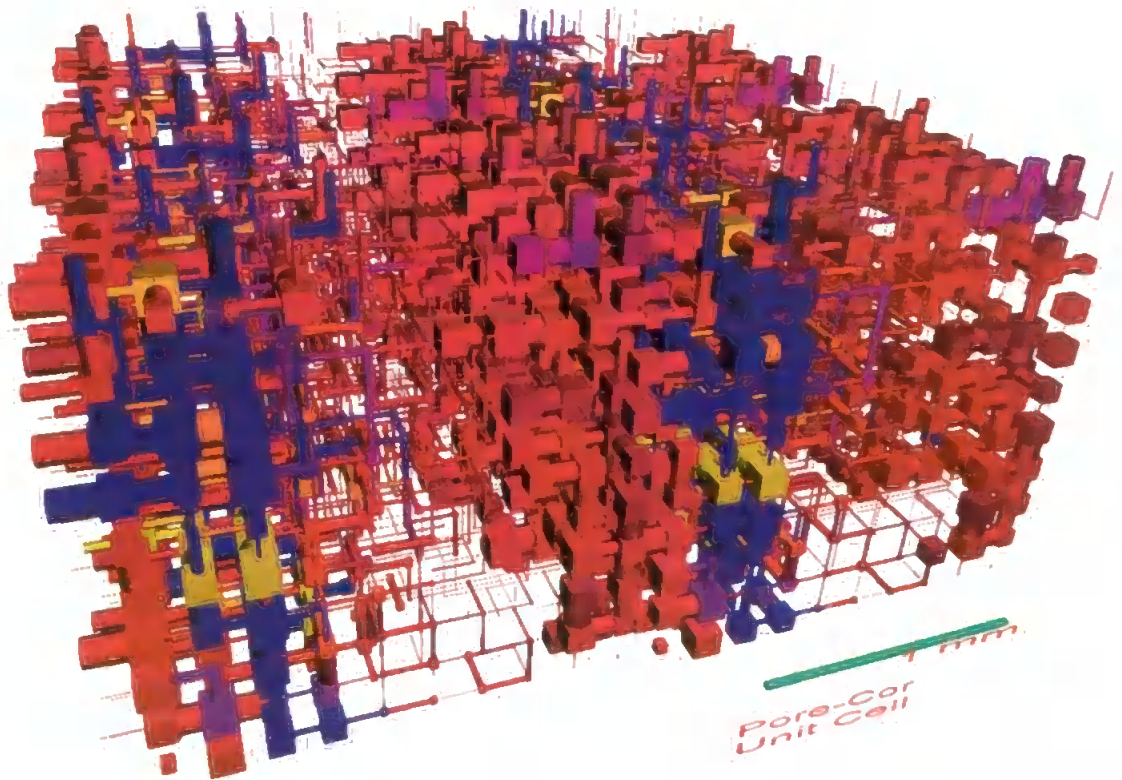


Figure 4.8 Net flow through vertically banded structure (2 in Figure 4.3) with correlation level 0.5. The increased randomness of structure has caused an increased randomness of flow relative to Figure 4.6.

In Figure 4.8, it can be seen that as expected, if the correlation level is reduced to 0.5, i.e. half way towards random, there is a greater positional spread of flow routes.

Figure 4.9 shows net flow through a fully correlated structure with large surface (max  $z$ ) throats, then very small throats at smaller  $z$ , increasing again to large throats at minimum  $z$  (bottom of the structure). The repeat of large throats and pores at the bottom of the structure is again due to the repeating boundary condition set by the repeating unit cell approximation. Again, the slight circular loci of the maximum flow paths arise from the slightly spherical loci of the layers.

Figure 4.10 shows that with spherical loci of small throats at the centre of each unit cell and a totally correlated structure (correlation level = 1), the maximum flow tracks down through the edges of the unit cells, as expected. If the correlation level is reduced to 0.5, (structure 5 in Figure 4.3), the flow paths become more randomly positioned (Figure 4.11) and the flow is seen to again spread with less constraint around the unit cell network.

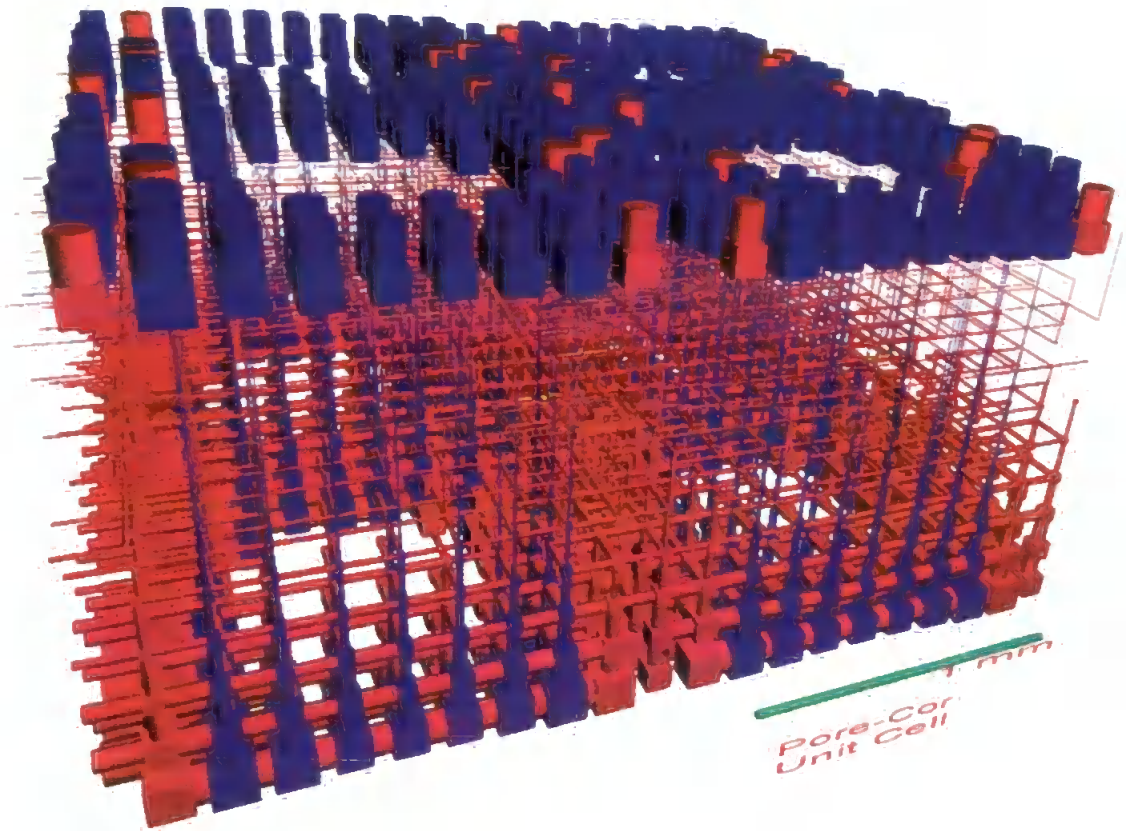


Figure 4.9 Net flow through structure with large surface throats (3 in Figure 4.3), correlation level = 1

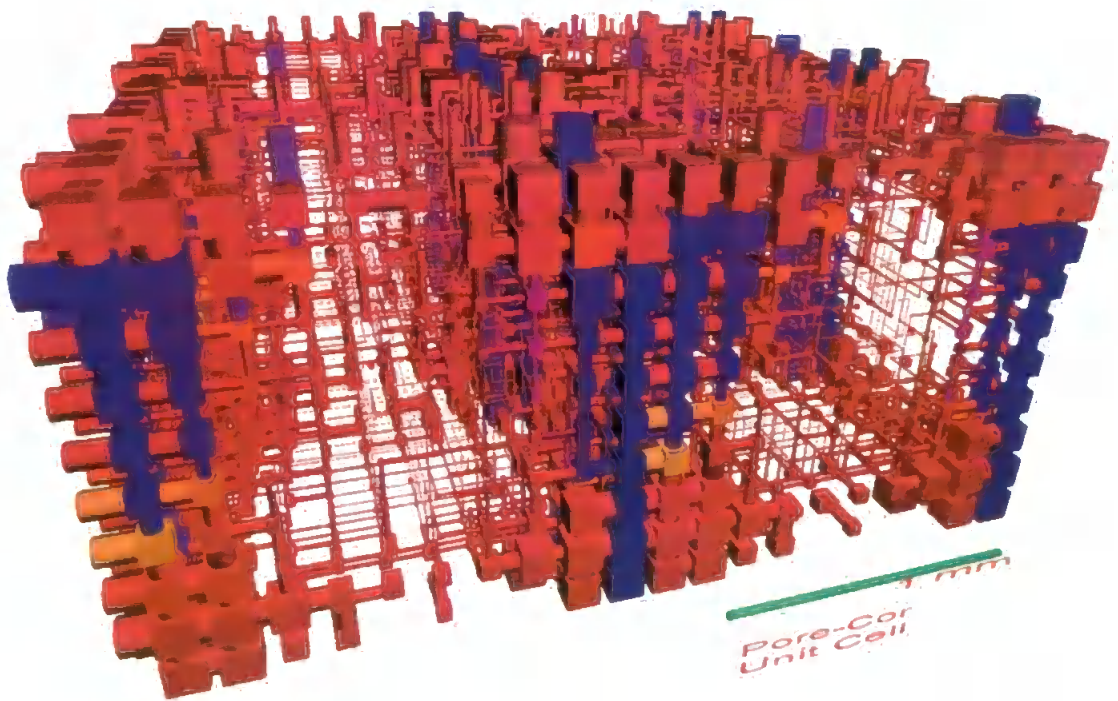


Figure 4.10 Net flow through small central pore type structure (4 in Figure 4.3), correlation level = 0.95



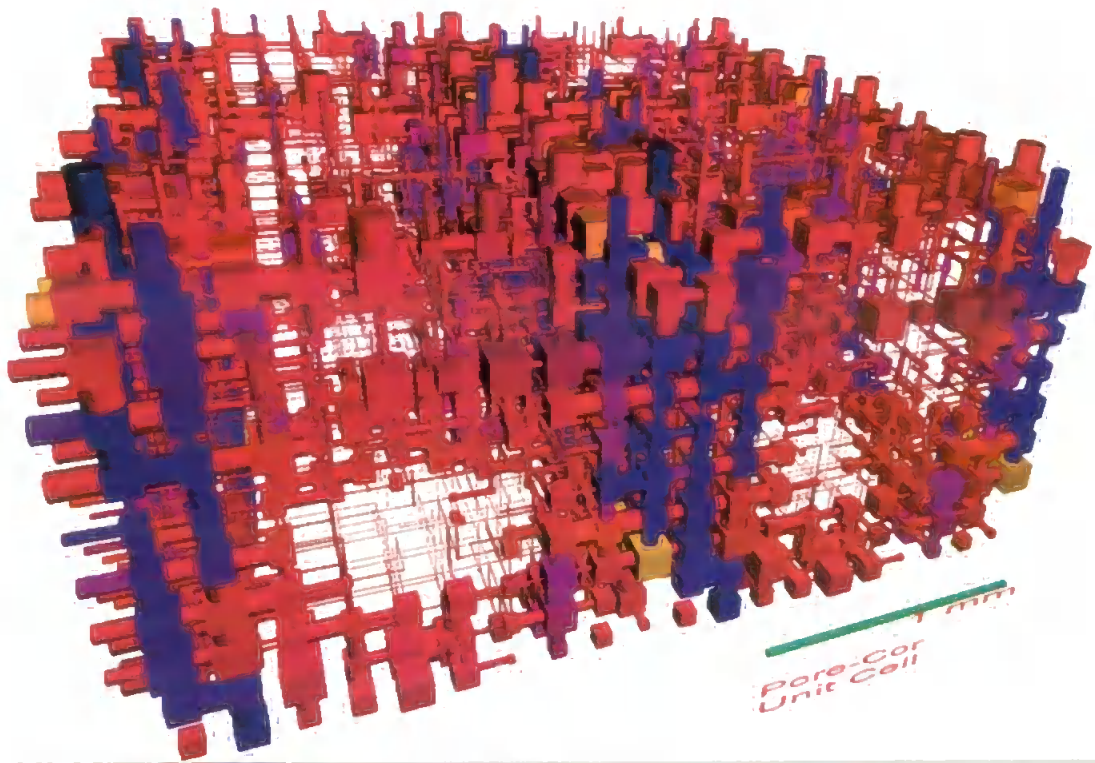


Figure 4.11 Net flow through small central pore type structure (5 in Figure 4.3), correlation level = 0.5. The increased randomness of structure has caused an increased randomness of flow relative to Figure 4.9.

For structures with spherical loci of large pores and throats at their centres (structures 6 & 7 in Figure 4.3), the flow is expected to track down through the centre of the unit cell. As expected this is more greatly defined for the highly correlated structure (correlation level = 1) and less defined at the lower structural correlation (correlation level = 0.5). Indeed this is again seen to be true when observing Figure 4.12 and Figure 4.13 respectively.

When consulting the displayed images (Figure 4.7 - Figure 4.13 ) it is apparent that there is very marked preferential flow through these structures. This may seem an unrealistic approach to modelling of flow within a filter, as we would assume the filter to be fully saturated and the flow to travel through all the network arcs. However, the preferential flow routes provide a way of modelling the passage of particles through a filter as described below.

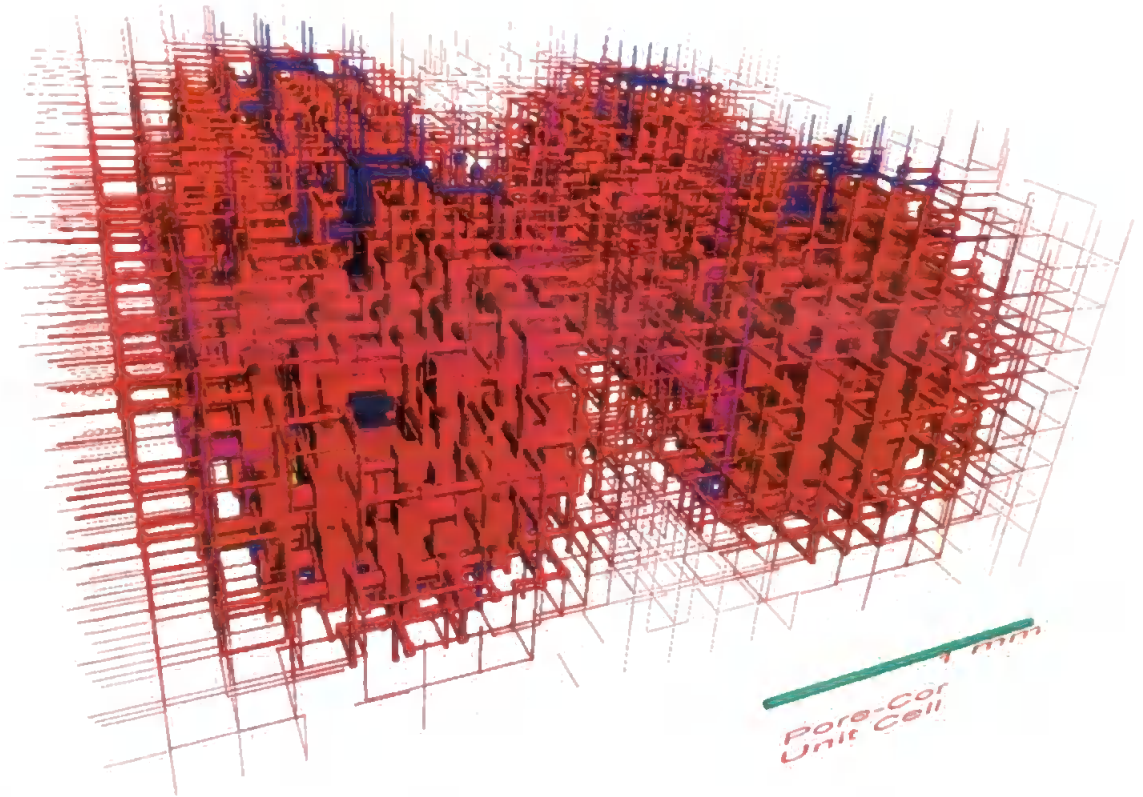


Figure 4.12 Net flow through large centred structure (6 in Figure 4.3), correlation level = 1

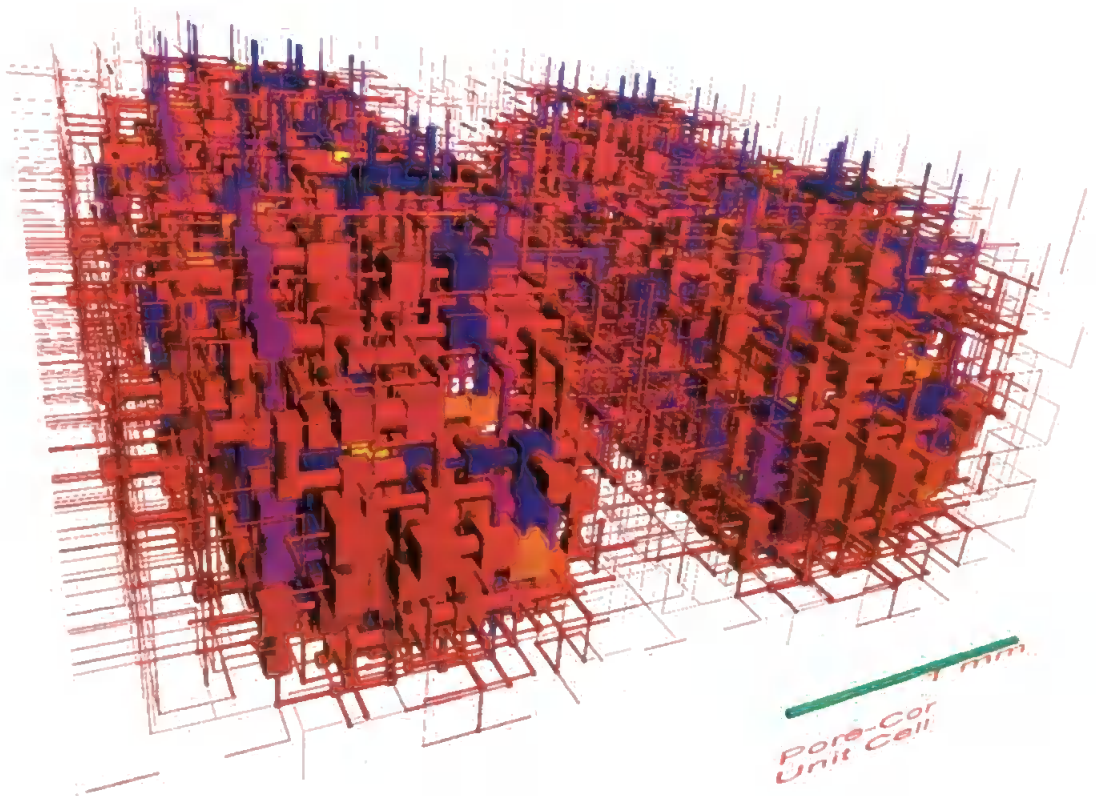


Figure 4.13 Net flow through large centred structure (7 in Figure 4.3), correlation level = 0.5. The increased randomness of structure has caused an increased randomness of flow relative to Figure 4.11.

### **4.3. Addition of contaminant particles to the Pore-Cor model**

The next step in the model development was to apply a contaminant particle input, and capture mechanisms so that simulations of particle deposition could be undertaken in the modelled networks. As previously mentioned, there exist two approaches to particle deposition in filtration: Lagrangian and Eulerian (Polyakov et al., 2003; Tien, 1989; Elimelech, 1995). Lagrangian methods are used to describe the trajectory of particles approaching a collector and the Eulerian method deals with the variation in concentration of particles in time and space. It is also found (Polyakov et al, 2003) that as a rule the Lagrangian methods are used to describe deposition of particles  $>1\mu\text{m}$  in size, which possess trajectories governed by Newton's second law. As the particle depositions we are initially modelling are believed to be in this range, the direction of study into particle deposition will now focus on these Lagrangian based simulations.

Deposition requires a collector (Tsiang, 1982; Herzig, 1970; Temu, 2000;). Collectors are usually represented by spheres or networks of uniform fibres (Tsiang, 1982) in the flow path of the particulate carrying suspension. However this process of using such collector features was found to be analogous with the particle trajectory based models as described in Section 1.3.4.1.3. As the Pore-Cor model is represented as cylindrical and cubic void space networks there are no such collectors present within the void structure. However as the model is based on a network of pores between skeletal particles (Laudone, 2005) it was considered possible to overcome this problem by treating the simulated throat walls as collection surfaces as well as the boundary constraint for the fluid flow through the pore/throat features. This assumption is found to be comparable with 'parallel-plate' channel deposition processes that have been used previously in several theoretical and experimental studies (Bowen et al., 1976; Adamczyk and Van de Ven, 1981; Sjollema and Busscher, 1989 & 1990). Using this principle it was felt that a

valid starting point was to use the principle of 'critical velocity', elucidated by way of the Colour Flow algorithm, to govern basic particle capture and transport mechanisms within the model.

It is known that the rate of particle capture and re-entrainment is related to the difference between a microscopic velocity of the carrier fluid and a critical velocity (Ochi, Vernoux, 1999). It is also known that permeability decrease within porous media is directly related to throat diameter reduction by mechanisms such as straining or direct interception (Rege & Fogler, 1988). However, fouling of a given throat may not initially lead to a permeability decline as it has been observed that the fluid flow may re-arrange to find another available path through the media (Frey *et al.*, 1999). Considering these factors initial programming was undertaken to allow the manual addition of contaminate particulate to the modelled networks. Manual addition of particulate in this way allowed the observation of the individual pore blocking events and their effect on modelled networks by way of the exhibited changes in flow regimes. The addition of trapped particles to the network models allowed the calculation of straining and FMF effects. Particle deposition was modelled by calculating the progressive aggregation effects within individual void features.

Simulations of straining and critical velocity FMF deposition (along throat walls) have been undertaken on the network simulations according to set criteria. First the network is calculated in terms of its flow character (Section 4.2) and the path of highest active flow velocity is chosen for particle transport through the network, analogous to flow biased routing previously described (Section 4.1). Particles then become strained when they encounter a throat narrower than their own diameter. It is also possible, depending on fluid, particle and media chemistry, to account for particle aggregation effects by

controlling the effective particle diameter to a corresponding final aggregate diameter. Critical velocity deposition phenomena upon throat walls are based upon the velocity of liquid through the network arcs. Depending on particle diameter and density, a critical velocity at which a particle will no longer be moved by the surrounding fluid stream can be implemented and subsequent deposition upon the throat wall is assumed. Although the process of critical velocity deposition was possible and could be controlled as a manual input into the model it is not at present fully included into the final working model. The reason for its lack of inclusion is the difficulty in obtaining relevant experimental measurements of particle, media, and fluid interactions. Without these measurements for each media, fluid, and contaminant particle combination, the modelling of critical velocity deposition is non-realistic and merely a retro-fitting of data by altering numerical control parameters in the model. The lack of this data has meant that the only attempts to model critical velocity deposition have involved laborious manual data inputs and calculations on the representative void networks. It is however felt that even with its lack of inclusion into the final model the computational process should be highlighted here and an example of the effect demonstrated in view to its possible inclusion into future model developments.

In the manual process the initial critical velocity capture probabilities of particles within the representative network were calculated using an adaptation of Stein's relationship (Equation 4.1 and Figure 4.14) as described in literature (Rege & Fogler, 1988). Adhesion between the particle and throat wall is assumed, and re-entrainment was not considered.

$$\text{Probability} = 4 * \left[ (\theta a / R_0)^2 - (\theta a / R_0)^3 \right] + (\theta a / R_0)^4$$

Equation 4.1

where  $a$  is the radius of the simulated particle,  $R_0$  is the radius of the associated network throat feature and  $\theta$  is a lumped parameter. The lumped parameter  $\theta$  accounts for the controlling 'critical' fluid velocity term and can be adjusted to account for increased or decreased capture probability due to fluid, particle and media chemistry such as ionic conditions, pH and particle characteristics. This also allows simulations to be undertaken according to different "real life" situations of carrier fluid and material property and the relationship between the particle density and size correlation.

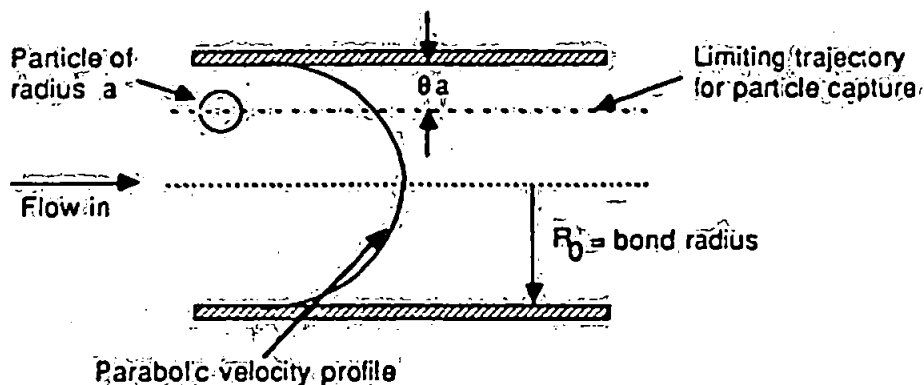


**Figure 4.14** Diagram showing where parameter values for the Stein relationship equation (Eqn 3.1) arise from in a standard throat feature. Note that any changes in fluid chemistry or velocity will either decrease or increase the effective value of  $\theta a$  thus decreasing or increasing the probability of deposition respectively.

Once a particle is deposited the simulated throat dimensions are re-calculated to take account for its presence in the throat feature. Recalculation of new effective throat radii may be undertaken by the application of Equation 4.2 and Equation 4.3 to all throats where deposition has occurred.

$$\frac{1}{R_{new}^4} = \frac{1}{R_0^4} + 0.1875 \sum_{i=1}^N \frac{a_i}{L} * \left[ 1 - (1 - a/R_0)^2 \right]^2 * K_1$$

Equation 4.2

Where  $N$  is the number of particles deposited and  $K_1$  is given by the application of Equation 4.3.

$$K_1 = \frac{1 - (2/3) * (a/R_0)^2 - 0.202(a/R_0)^5}{1 - 2.1(a/R_0) + 2.09(a/R_0)^3 - 1.71(a/R_0)^5 + 0.73(a/R_0)^6}$$

Equation 4.3

This re-calculation of throat feature radius is necessary due to the fact that as particle capture occurs there is a parallel increase to the overall fluid flow resistance (pressure drop) of the network and the individual throat feature. On the unit cell level this may result in a redistribution of flow through other less resistive pathways of the network. Once such reductions in throat diameters have been considered and accounted for the corresponding pore/throat level and network permeability, porosity and flow field computation of the modelled structure may be re-evaluated by way of the ‘‘Colour Flow’’ algorithm. In the manual application of this process the  $\theta$  term in Equation 4.1 was only concerned with a velocity parameter. In this study the value of  $\theta$  was controlled by implying a particle would deposit only when the velocity within a throat feature was found to equal a pre-determined fraction of its potential maxima depicted by the initial Colour Flow analysis of the representative void network.

### 4.3.1. Testing of the particle capture mechanisms

Manual control of the networks was utilised and the deposition phenomena modelled in stepwise processes. These manual applications of deposition were undertaken in two parts, firstly straining occurrences and secondly critical velocity throat deposition. This was followed by the recalculation of new flow regimes (as described in Section 4.3). Results can be visualised as the “Colour Flow” unit cells described in section 4.2, and compared with visualisations of clean unit cell networks of the media to show the differences in the mapped flow regimes.

It is found that the manual application of deposition phenomena to the network models showed results which show that straining events cause rapid re-direction and elimination of flow routes with a large associated permeability decline. This is exhibited in the representative network representation of a clean network and one undergoing straining of large particles (Figure 4.15 and Figure 4.17). It can be seen by observing the Colour Flow unit cell that upon the application of straining events (Figure 4.17) a high number of flow paths were eliminated, when compared with the clean network (Figure 4.15), and the remaining active flow features appear to be more localised and intense in their colouring. This represents the total blocking of throat features by way of straining and an associated shift of the network flow to the least resistive paths remaining in the unit cell.

Critical velocity depositions were manually undertaken using only particles of 10  $\mu\text{m}$  in size and setting the condition that the contaminant particulate would deposit at a critical velocity  $v^*$ , less than or equal to quarter of the maximal flow velocity  $v_{\text{max}}$ , so that deposition  $v^* = 0.25 v_{\text{max}}$ . Throats were then resized using the actual 10  $\mu\text{m}$  particle size and the respective throat diameter. Compared to straining the manual critical



velocity depositions within throats caused more subtle changes to the flow regime of the given unit cell (Figure 4.15 and Figure 4.16) while gradually improving removal efficiency of such particles over time. The gradual increase in removal efficiency exhibited in the critical velocity depositions is attributed to the gradual fouling and associated reduction in diameter of throat features over time by previous deposition events. This is also in agreement with previous studies of 2-dimensional networks in literature (Gruesbeck & Collins, 1982; Rege & Fogler, 1988)

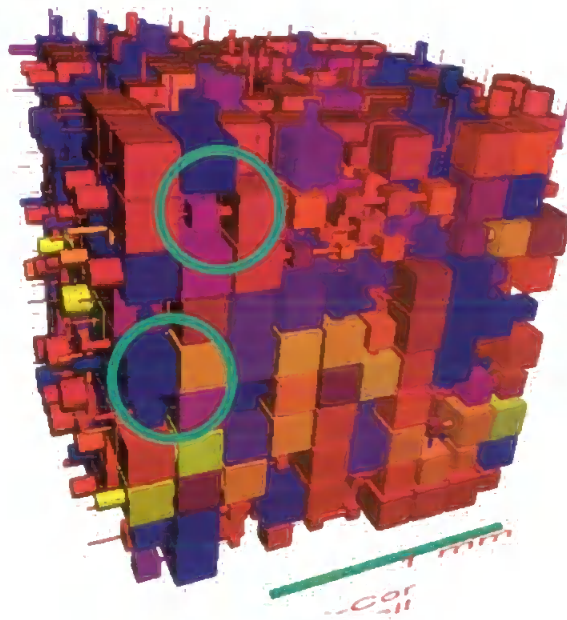


Figure 4.15 Pore-Cor Network simulation of S41 stainless steel filtration media prior to any filtration events, and showing calculated flow regimes by way of the “colourflow” algorithm. Areas within green circles are for comparison with Figure 4.16 to show flow affected by critical velocity deposition.

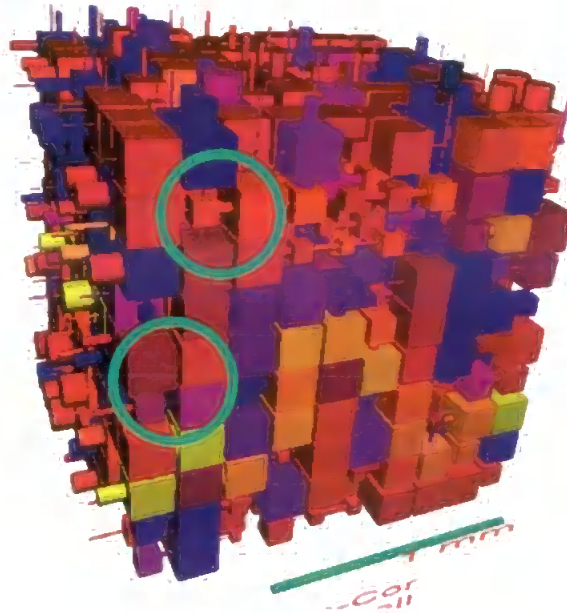


Figure 4.16 Pore-Cor Network simulation of S41 stainless steel filtration media as above, but after a series of critical velocity deposition events by manually controlled 10 micron contaminant particles set to deposit where  $v^* = 0.25 \times v_{max}$ . Note areas in green circles have decreased flow intensity when compared with Figure 4.15. Changes in flow regime for such deposition events are found to be subtle over time due to small particle size and the associated gradual fouling of throat features.

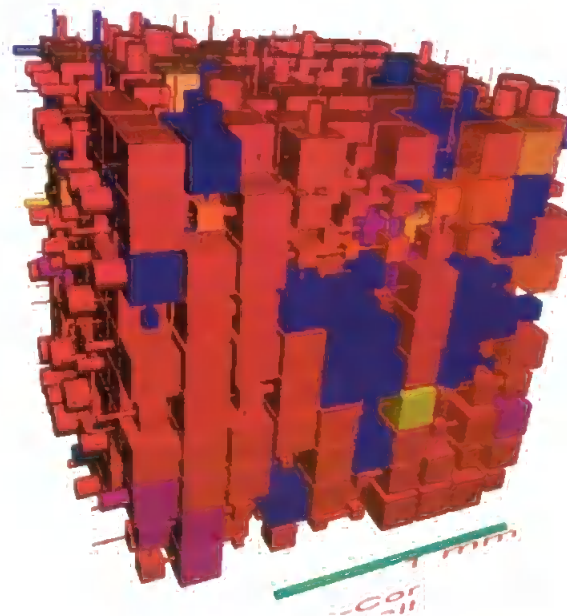


Figure 4.17 Pore-Cor Network simulation of S41 stainless steel filtration media as above, but after the application of straining simulations using a 20 micron particle size. Note the large changes in the flow regime when compared with figure 3.4. It is found that the instant plugging of such straining events has an instant effect on the structure of flow through the unit cell.

#### **4.4. Automation of the model and introduction of the user interface**

To develop the model into a useable tool for predictive filtration simulations it was necessary to introduce an automated aspect to the software. This allowed simulated filtration runs to be undertaken quickly and efficiently upon the simulated network representations. To do this a number of points had to be considered against the end users requirement. Filtration testing requires a number of outputs; these include the respective changes in filter performance against a number of different contaminant particle size distributions, the capture efficiency at a given particle size in terms of its individual and cumulative effect to the filter, and the associated decline of a filter's working capability in terms of permeability decline and associated loss of network porosity.

In consideration of these factors a control algorithm was created to undertake the filtration process in a stepwise manner. First the overall network flow is calculated by way of the Colour Flow algorithm followed by the addition of a contaminant particle from a pre-determined particle size distribution. Once added to the network the particle path follows the route of highest flow velocity (not volume) through the network. At reaching each throat feature a calculation is undertaken to determine whether the particle is strained, or continues to the next feature. This occurs systematically until it either passes through the unit cell network or becomes trapped. On conclusion of either of these events the algorithm loops and the process is undertaken again until a pre-determined number of contaminant particles is challenged against the void network. The programming of such an algorithm within the software is highly complex as it necessitates the consideration of many previously programmed sub-routines to gain information included in the filtration process such as void feature position, permeability and the ever changing porosity.

One time-consuming area of the algorithm development was the inclusion and control of the simulated contaminant particle distribution. It is illogical to assume that a distribution of particles would challenge the filter in a non-random manner but more acceptable that each particle within the given distribution has an equal probability of being involved in the next challenge event. For this reason consideration was given to how a random particle selection could be delivered to the program whilst also being representative of a pre-determined distribution profile. In other words the algorithm had to randomly select a particle from the distribution but with some bias to the overall number of particles in each size fraction.

First attempts to create the oxymoronic 'biased random selection sequence' evolved from consideration of Gaussian type distributions. Programming was undertaken to return a Gaussian selection of particle size from a given range of particle sizes ( $n_1 - n_{max}$ ) determined by a distribution. However it was quickly found that this process of selection did not return favourable results when consideration was given to the number of particles in each size fraction of the returned distribution compared to an observed sample of glass bead test contaminant as shown in Figure 4.18.

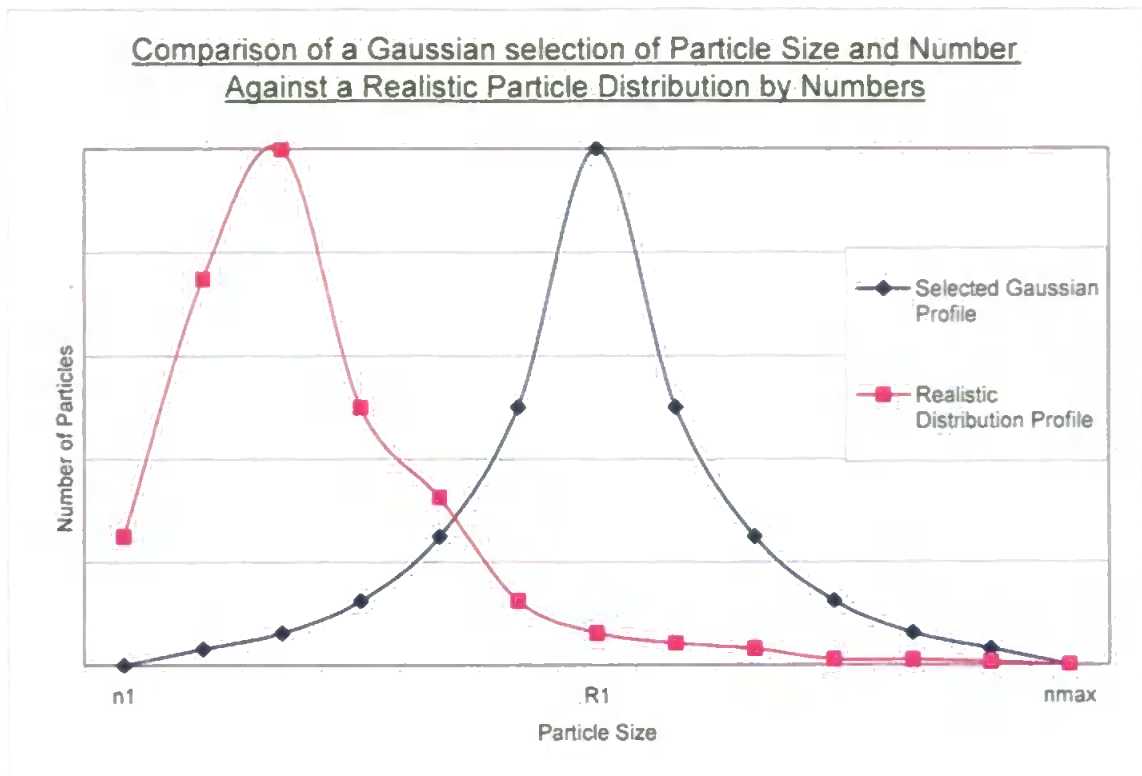


**Figure 4.18** Comparison between a challenge particle profile returned by way of the Gaussian consideration of a distribution size range and a realistic distribution profile of particles.

As can be seen (Figure 4.18) the Gaussian selection of distribution profile considers the particle size range based around the median size,  $R_1$ . This is established by the size constraints  $n_1$  and  $n_{max}$ . However if Figure 4.18 is observed it is seen that although the  $R_1$  particle size is present in numbers within the realistic distribution, the main 'bulk' volume of contaminant particulate is found at a considerably lower particle sizes. Although the Gaussian approach to modelling the particle challenge was random in relation to the next chosen particle applied it can clearly be seen that its consideration of the distribution profile is controlled in an unsatisfactory way by the size constraints of  $n_1$  and  $n_{max}$ .

This failure of the random Gaussian selection to achieve a realistic representation of the skewed realistic profile, by not considering numbers of particles at each size fraction, led to the current biased random selection process that is included in the model. The

initial step in programming the successful code was to consider the distribution profile of particulate not just as a size range but also as numbers of particles within each size fraction of the distribution. This allowed the simulation of any required distribution profile as a set of particle size fractions containing a representative number of particles in each.

From this applied distribution the 'biased random selection' of the next challenge particle was undertaken. Each particle of the distribution, rather than particle size, was numbered  $n_1$  to  $n_{\max}$ . A random number generator was then used to return a value set between the limits 0 – 1 at a level of significance correlated to  $n_{\max}$ . This returned random number was then multiplied by  $n_{\max}$  and rounded the nearest integer value. This generated an integer within the particle number constraints  $n_1$  to  $n_{\max}$ . This returned integer value is thus representative of an individual particle within the distribution and that particle is consequently chosen as the next challenge particle. The total number of remaining particles now holds the value of  $n_{\max} - 1$ , and the next selection is considered using the new distribution. This feedback system continues until no particles remain within the applied distribution.

Consideration of the distribution in this way means that the selection of an individual particle is still random in nature but biased to size fractions of the profile that have larger numbers of particles. For example consider a distribution of 100 particles in 3 size fractions of 10, 20 and 30 microns where numbers of particles in each are shown in Figure 4.19.

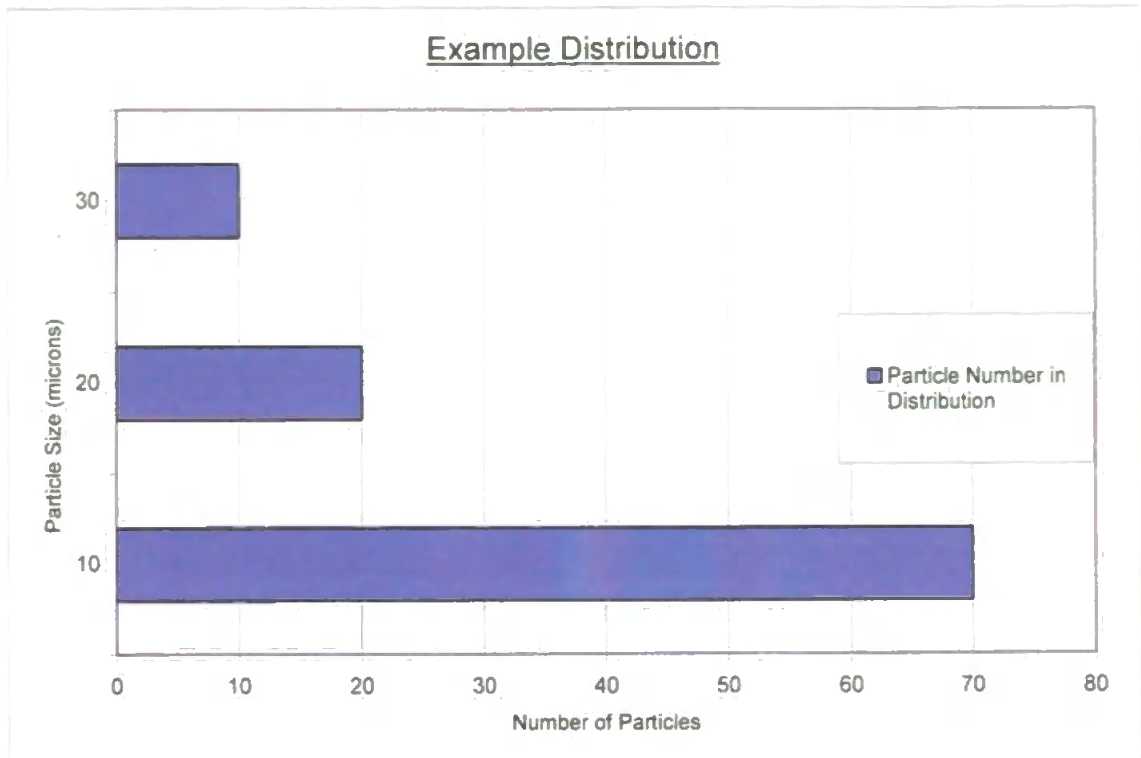


**Figure 4.19** Simplistic example distribution to explain weighted selection of integers in the random biased number selection of challenge particle. Size fractions are, 30 microns = 10 particles, 20 microns = 20 particle and 10 microns = 70 particles.

The 70 particles in the 10 micron fraction are labelled 1 – 70, the 20 in the 20 micron fraction 71 – 90 and the 10 in the 30 micron fraction 91 – 100. Thus, using the random number generator between 0 -1, any value returned between 0.001 and 0.704 would equate to a particle in the 10 micron fraction, whereas only a returned value of 0.905 to 1.000 would equate to a particle in the 30 micron fraction. As can be imagined this provides a realistic approximation to the selection of challenge particles weighted by their frequency within a distribution profile.

#### **4.4.1. The Final Product**

After the development and consideration of the previously discussed requirements for an end product the automated algorithms had to be compiled into a complete filtration module of the software. A user interface based on the previously discussed requirements of the end user (Section 4.4) also had to be included. Programmed in Visual Basic 6.0 the final user interface is shown in Figure 4.20.

The user interface allows control of the filtration module and also the acquisition of related data files to allow presentation of the resulting filtration simulations. The user can determine up to ten particle sizes of interest (1), and within each of these sizes control the number of particles present within the total distribution (2). From this the distribution may be saved as a data file so it is instantly accessible in later simulations (3). The filtration simulation upon the selected network may then be run (4) and the real time progress observed (5) & (6). While the simulation is running the individual particle fate may be observed in terms of whether it has become captured or passed by way of the Filter Status output (7). This is shown as a network feature number and its associated characteristics of flow, radius, diameter and node position if the particle is captured otherwise a no strain verdict is returned. Also shown within the Filter Status output (7) is the % blockage of the filter as a function of the network permeability. Results of the simulations may be outputted either as a function of the filters % blockage calculation or as a function of a number of challenges of a given particle size (8). These results are stored in a datafile at each acquisition point and can further be saved as a full set of process results or as a summary file to later be used in presenting the acquired data (9). Once the simulations have been undertaken on a given void network the clogged unit cell may again be viewed as a Colour Flow representation and also be subjected to further secondary processes available in the software.



**Filtration characteristics of clashac**

**Particle challenge characteristics**

Characteristics of suspension		Number of particles remaining in suspension		Number of particles challenging filter	Number of particles filtered	% capture efficiency	
diameter / um	number of particles	discrete	cumulative			% capture	% cumulatv efficiency
7.5	78	78	78	0	0		
12.5	11	11	89	0	0		
17.5	15	15	104	0	0		
22.5	22	22	126	0	0		
30	23	23	149	0	0		
40	2	2	151	0	0		
55	0	0	151	0	0		
70	0	0	151	0	0		
90	0	0	151	0	0		
120	0	0	151	0	0		

(1) & (2) → Characteristics of suspension  
 (3) → Particle size distr. Load Save  
 (4) → Auto filter: 151 different particles from suspension  
 (5) → Filtration simulation: Calculate flow routes through unit cell, Write flow routes, Read flow routes, Find high flow throats and check for straining, Write process and interim result files, Allow next strain event to modify unit cell, Write geometry of clogged filter  
 (6) → Calculation progress  
 (7) → Filter status: Permeability of clean filter 4.884245 mD, Permeability of clogged filter, Blockage %, strained at feature  
 (8) → Now filtering particle number: diam  
 (9) → Output interim results every time blockage increases or permeability decreases by this % 1 or there are this number of challenges at one size 10

Figure 4.20 Screen shot of the programmed user interface for the final filtration module. Numbers in parentheses relate to descriptions in text.

#### **4.5. Other Programming Aspects**

Throughout the initial stages of the study it has been necessary to renew certain sections of the software coding to allow the new features to be integrated. This has included such areas as adapting existing user interfaces, so aspects such as the Colour Flow unit can be accessed, and also altering the many output arrays of the previous software versions so that necessary data may be accessed for use in the new algorithms.

The earlier software was also reprogrammed so that the Pore-Cor and Pore-Eye units would accept datafiles containing only low pressure mercury intrusion data. This was undertaken due to initial problems with the porosimeter only allowing the acquisition of low pressure data. This initially allowed some initial results and modelling practice to be attained without the requirement for high pressure data, but also enabled time reductions in the acquisition of suitable data for samples that did not require high pressure mercury intrusion porosimetry.

#### **4.6. Conclusions**

It has been shown that the development of the final filtration model has been achieved by following a stepwise process. The Dinic algorithm has been interrogated successfully and this has led to the development of a successful mapping algorithm for flow regimes. The success of this algorithm has also aided the production of further algorithms that allow simulated addition of particle transport through the modelled networks in a realistic manner.

Validation of the model has been undertaken on highly correlated structures to determine the effective working mode of the developed algorithms. Results show that the developed model is behaving correctly in its calculation of flow regimes and also its

capture of contaminant particulate. At present only straining processes are considered and fully automated into the present model.

## **5. Modelling the real filtration environment**

The development of a filtration model, as described in the previous chapter, is no more than an academic exercise unless it can be usefully compared to experimental testing. A model exhibiting the same trends as experimental results would allow the industrial sector to reduce wet bench testing while still offering characterisation of the tested media by sound scientific principles. As such this chapter aims to:

- (i) Describe the methodology used for the “wet bench” single pass testing,
- (ii) Explain the parameters used in the calculation of filter efficiency,
- (iii) Discuss these parameters and consequently propose a new parameter, the alpha efficiency,
- (iv) Present the results from experimental single pass tests carried out on the Sinterflo® media,
- (v) Show simulated single pass test results for the Sinterflo® media achieved by use of the model described in Chapter 4.

### **5.1. Single pass test methodology used in this study**

Direct measurements of filter efficiency were carried out using a pass test rig constructed by Porvair Filtration Group (PFG), using a single pass protocol (Dickenson, 1997; Porvair data sheet 4), (Figure 5.1). The test fluid was DTD585 aviation grade hydraulic oil, equivalent to Castrol Aero HF 585B. The rig was first run empty, i.e. with no test filter and no seeded contaminant. The oil was then pumped through it at 5 or 7 litres per minute, the flow rates having been chosen on the basis of preliminary tests described below (Section 5.2.1).

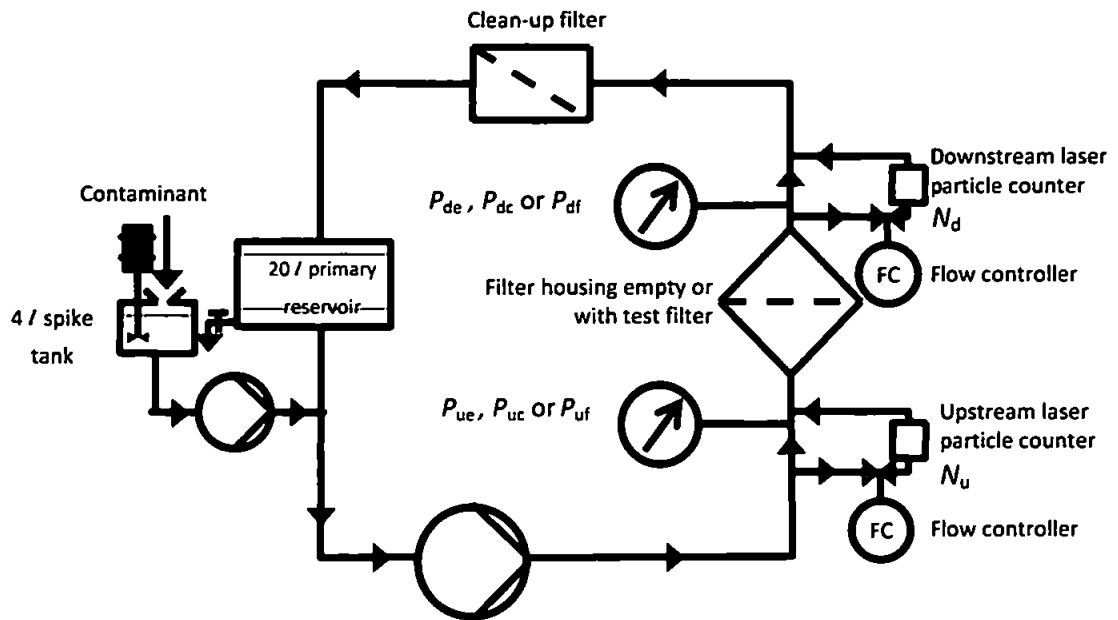


Figure 5.1 Schematic of the experimental single pass test apparatus.

For purposes of description and discussion, we will define four spherical-equivalent particle sizes only,  $s_1, s_2, s_3, s_4$  ( $s_1 < s_2 < s_3 < s_4$ ), although in practice, between 6 and 10 sizes were used,  $s_1, s_2, \dots, s_{\max}$ . For the experimental tests,  $s$  represented the maximum of the corresponding size interval, so for the four sizes used in the later discussion, the intervals which we will refer to as  $s_1, s_2, s_3$  and  $s_4$  were in fact 0 to  $s_1$ ,  $s_1$  to  $s_2$ ,  $s_2$  to  $s_3$ , and  $s_3$  to  $s_4$  respectively. The numbers of particles upstream,  $N_{u1}(\text{background}), N_{u2}(\text{background}), N_{u3}(\text{background}), N_{u4}(\text{background})$  at these sizes, and the equivalent measurements downstream,  $N_{d1}(\text{background}), N_{d2}(\text{background}), N_{d3}(\text{background}), N_{d4}(\text{background})$ , were measured with a Hiac Royco particle counter incorporating a Beta Ratiometer. This device comprised two laser particle size counters, and manually operated flow rate controllers to balance the flow rate through each counter loop, as shown in Figure 5.1. Pumping continued until all the background particle counts reached a low and constant value, indicating that the clean-up filter could

not clean the oil further from contamination from previous runs. The upstream and downstream pressures  $P_{ue}$  and  $P_{de}$  were then measured to give the 'housing loss'  $\Delta P_h$ , defined as  $(P_{ue} - P_{de})$ .

A test filter was then inserted into the housing. Oil was pumped at  $7 \text{ L min}^{-1}$  or  $5 \text{ L min}^{-1}$  around the main circuit. The 'clean' pressure losses were measured upstream,  $P_{uc}$ , and downstream  $P_{dc}$ . 4 litres of oil was then tapped from the primary reservoir. 1 g of Accublast glass beads as contaminant was added to this oil, and the suspension was poured into the spike tank where it was stirred. For a main circuit pumping rate of 7 litres per minute, the suspension was then pumped into the main flow at a rate of 50 ml per minute, corresponding to a contaminant dosage rate of 12.5 mg per minute. For a main circuit pumping rate of 5 litres per minute, the suspension was pumped in at a proportionally reduced ingress rate of 36 ml per minute. The upstream and downstream pressures  $P_{uf}$  and  $P_{df}$  were then measured, together with the upstream and downstream particle sizes and numbers,  $N_{u1}$ ,  $N_{u2}$  ... and  $N_{d1}$ ,  $N_{d2}$  .... This was undertaken once every 3 minutes for the duration of the experimental run allowing result profiles to be achieved for capture efficiency against pressure drop changes.

### 5.1.1. Standard characterisation of filters

The most direct measure of filter efficiency is to compare the capture efficiency  $C$ , at any particular particle size  $s$ , for example at size  $S_2$ :

$$C_{s2} = 1 - \frac{\text{Number of particles of size } S_2 \text{ downstream}}{\text{Number of particles of size } S_2 \text{ upstream}} = \frac{N_{u2} - N_{d2}}{N_{u2}} \quad \text{Equation 5.1}$$

The cumulative capture efficiency  $C_{cum}$  is defined as the sum of all efficiencies of capture up to and including that size, for example at size  $S_2$ :

$$C_{cum2} = 1 - \frac{N_{d1} + N_{d2}}{N_{u1} + N_{u2}} \quad \text{Equation 5.2}$$

We also define a normalised cumulative efficiency  $\mathcal{C}_{cum}$ . If  $C_{cum}$  tends to  $C_{cum,max}$  as  $s$  tends to  $s_{max}$ , then the normalised cumulative efficiency is:

$$\mathcal{C}_{cum} = \frac{C_{cum}}{C_{cum,max}} \quad \text{Equation 5.3}$$

Filters can be characterised in terms of a beta ratio  $\beta$ , which ranges from 1 (no filtration) to infinity (total filtration). This is defined as number of particles greater than the specified size upstream of the filter, divided by the equivalent number downstream.

The defining equation, for size  $S_1$ , is:

$$\beta_{s_1} = \frac{\text{Number of particles} > \text{size } s_1 \text{ upstream}}{\text{Number of particles} > \text{size } s_1 \text{ downstream}} = \frac{N_{u2} + N_{u3} + N_{u4}}{N_{d2} + N_{d3} + N_{d4}} \quad \text{Equation 5.4}$$

For modelling purposes and also frequently in experimental measurements, individual particle sizes  $s_1, s_2 \dots$  are used which are considerably different from each other, so it is most representative to define the beta ratio  $\beta'$  as referring to size range above and including the specified size, i.e. for size  $S_1$ :

$$\beta'_{s1} = \frac{\text{Number of particles } \geq \text{ size } s_1 \text{ upstream}}{\text{Number of particles } \geq \text{ size } s_1 \text{ downstream}} = \frac{N_{u1} + N_{u2} + N_{u3} + N_{u4}}{N_{d1} + N_{d2} + N_{d3} + N_{d4}}$$

Equation 5.5

The filter efficiency rating  $E$  is then calculated from the  $\beta$  ratio for each value of  $s$ , using the following relationship which is incorrect in a standard text (Dickenson, 1997) and often misquoted :

$$E_s = \frac{\beta_s - 1}{\beta_s}$$

Equation 5.6

The corresponding parameter  $E'$ , which includes the stated size, obeys an analogous relationship to  $\beta'$  rather than  $\beta$ .

The normalised relative pressure drop  $\Delta \bar{P}_{rel}$  is defined as:

$$\begin{aligned} \Delta P_{rel} &= \frac{\text{current pressure drop} - \text{housing loss}}{\text{clean pressure drop} - \text{housing loss}} \\ &= \frac{\Delta P_f - \Delta P_h}{\Delta P_c - \Delta P_h} = \frac{P_{uf} - P_{df} - P_{ue} + P_{dc}}{P_{uc} - P_{dc} - P_{ue} + P_{dc}} \end{aligned}$$

Equation 5.7

The blockage  $B$  of the filter may also be calculated, defined as:

$$B = 1/\Delta P_{rel}$$

Equation 5.8



When modelling, there is no housing loss, and therefore  $B$  is defined simply as:

$$B_{\text{model}} = \frac{\text{clean pressure drop}}{\text{working pressure drop}}$$

$$= \frac{\text{absolute permeability of working filter}}{\text{absolute permeability of clean filter}} = \frac{k_f}{k_c}$$

Equation 5.9

The method of calculating the absolute permeabilities  $k$  is described previously (Section 1.3.3.1.1). For practical purposes,  $C$ ,  $\mathcal{C}$ ,  $B$  and  $E$  above are usually multiplied by 100 and expressed as percentages.

### 5.1.2. Problems with the characterisation of filters in the context of this study

The characterisation of filters is fraught with both theoretical and experimental difficulties, which will be briefly discussed in the context of the present work. For purposes of discussion, it is assumed that  $s_1$  represents “fines”, i.e. particles that remain in the body of the test liquid, even after the use of so-called “clean-up filters”, because they are too fine to be removed; they thus represent a “background” particle size.  $s_2$  and  $s_3$  represent particles capable of being filtered within the body of the filter. In practice, these higher size ranges also contain particles which effectively act as fines, but we will ignore those, so that  $N_{u2}(\text{background})$ ,  $N_{u3}(\text{background})$ , ... are zero, and  $N_{d2}(\text{background})$ ,  $N_{d3}(\text{background})$ , ... are also zero.  $s_4$  is a size of particle which forms a filter cake at the filter surface.

Suppose we study a filter using a single pass test for which the oil contains a large number fraction of fines from previous tests. Then,

$$N_{u1}(\text{background}) = N_{d1}(\text{background}) = N_{u1} = N_{d1} \gg N_{u2}, N_{d2}, N_{u3} \dots$$

Equation 5.10

Under these conditions, Equation 5.4 shows that  $\beta_{s1}$  gives a falsely high impression of the filter performance at size  $s_1$ , because the large values of  $N_{u1}$  and  $N_{d1}$  are missing from the definition. Conversely, it follows from Equation 5.5 that if  $N_{u1}$  and  $N_{d1}$  are large,  $\beta_{s1 \text{ model}} \rightarrow 1$ . However, at higher sizes, the absence of  $N_{u1}$  and  $N_{d1}$  from the definition allows  $\beta$  to converge to high performance quickly and realistically.  $\mathcal{E}_{\text{cum}}$  suffers from a converse problem. At  $s_1$  it correctly indicates a zero performance of the filter, but as  $s \rightarrow s_{\text{max}}$ , it converges too slowly onto high efficiency values because it is dragged downwards by the large values of  $N_{u1}$  and  $N_{d1}$ . As such a new measure called 'alpha efficiency' (so called because it is more fundamental than the beta efficiency) is proposed, which combines these two parameters in a simple algebraic relationship with the correct asymptotic behaviour:

$$\alpha = E^{1/4} C_{\text{cum}}^{1/4} \left[ 1 - \left\{ (1-E)(1-C_{\text{cum}}) \right\}^{1/2} \right]^{1/2} \quad \text{Equation 5.11}$$

The alpha efficiency  $\alpha'$  is based on the specified particle size as well as those above it, and hence is defined by a similar relationship involving  $E'$  rather than  $E$ .

The final problem is that  $\beta$  is actually a dynamically changing characteristic of the filter. It is a function of the pass test time  $t$ , relative pressure drop  $\Delta \mathcal{R}_{\text{rel}}$  and blockage  $B$ .  $t$  is

dependent on flow rate and particle concentration, whereas both  $\Delta \mathcal{R}_{rel}$  and  $B$  depend only the flux of particles challenging the filter, so have one fewer degrees of variability.  $\Delta \mathcal{R}_{rel}$  is a standard parameter in filter testing, so the various measures of efficiency can be usefully compared by expressing them as three-dimensional functions of both  $s$  and  $\Delta \mathcal{R}_{rel}$ .

For a particular particle size distribution, the performance of the filter also varies according to the order in which the particles hit it. If large particles, particularly in the cake-forming  $s_4$  range, hit first, the filter will block more quickly and some become more efficient for particles of all sizes. Furthermore,  $C$ ,  $\mathcal{C}$ ,  $B$ ,  $E$  and  $\alpha$  all vary with particle size distribution, for both experimental and simulated filters. Such variability proved a major problem in this study. To control it, a distribution of 151 particles numerically proportional to the experimental distribution, measured by the Beta Ratiometer, was chosen. This is shown as Default in Figure 5.2. Further distributions comprised the default distribution with sizes multiplied by 2 (Mult2) or divided by 2, 4 or 8 (Div2, Div4 and Div8 respectively), Figure 5.2. The sizes of the fines in these distributions were multiplied identically to all the other particles, which could be considered unrealistic, but removed the need for defining the degree of overlap of fines with the other sizes, a problem mentioned earlier. Also the behaviour of the S41 filter was simulated with 3020 particles (rather than the sizes) of the default distribution multiplied by 20 (Mult#20), and also simulated with this Mult#20 distribution was a single extra particle of size 55  $\mu\text{m}$ . This provided a series of correlated size distributions that could be input to the modelled networks of Sinterflo® media that were not directly measurable by the controlled experimental technique (Section 5.1).

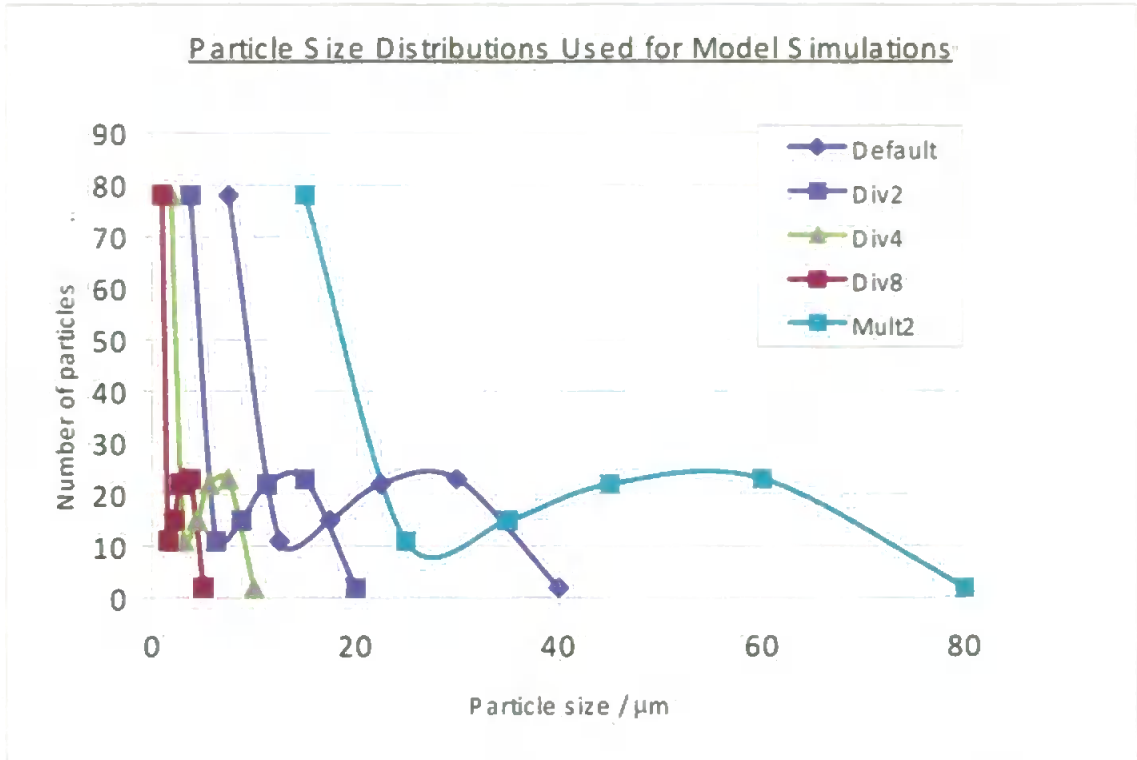


**Figure 5.2** Graphical representation of the simulated particle size distributions used in simulations of pass tests on the Sinterflo® media. Note that all distributions are proportional to the experimental distribution exhibited by the betaratiometer.

## 5.2. Results and discussion

### 5.2.1. Experimental pass tests

Experimental pass tests were undertaken using the methodology described in section 5.1. Initial trials were run to determine correct experimental flow rates to be used in the final experimental runs. Two criteria had to be met: firstly that the rate was sufficient to deliver contaminant particulate around the test rig without any deposition in the delivery system itself, and secondly to determine whether the combination of flow rate and contaminant loading offered the required depth filtration rather than cake filtration as discussed in chapter 1.

Particle capture efficiencies were measured at various flow rates to find a rate at which there were no rate-dependant effects. A flow rate of  $3.5 \text{ L min}^{-1}$  proved insufficient to transport all of the contaminant around the test rig, leading to fluctuations in the concentration of contaminant challenging the filter. Tests at flow rates of  $5 \text{ L min}^{-1}$  and  $7 \text{ L min}^{-1}$  showed a stable upstream contaminant concentration, no filter caking and capture efficiencies that were independent of rate, so these rates were used for the tests.

Due to the financial costs associated with the required calibrated contaminant for such tests, it was only possible to utilise the experimental technique upon the Sinterflo® media grades, S36 and S41. Tests were run on both grades at the predetermined 5 and 7  $\text{L min}^{-1}$  flow rates to check for any flow-rate dependant deposition mechanisms. This was achieved by normalising the time axis of the data at both flow rates to  $5 \text{ L min}^{-1}$ , an example of which can be viewed in Figure 5.3.

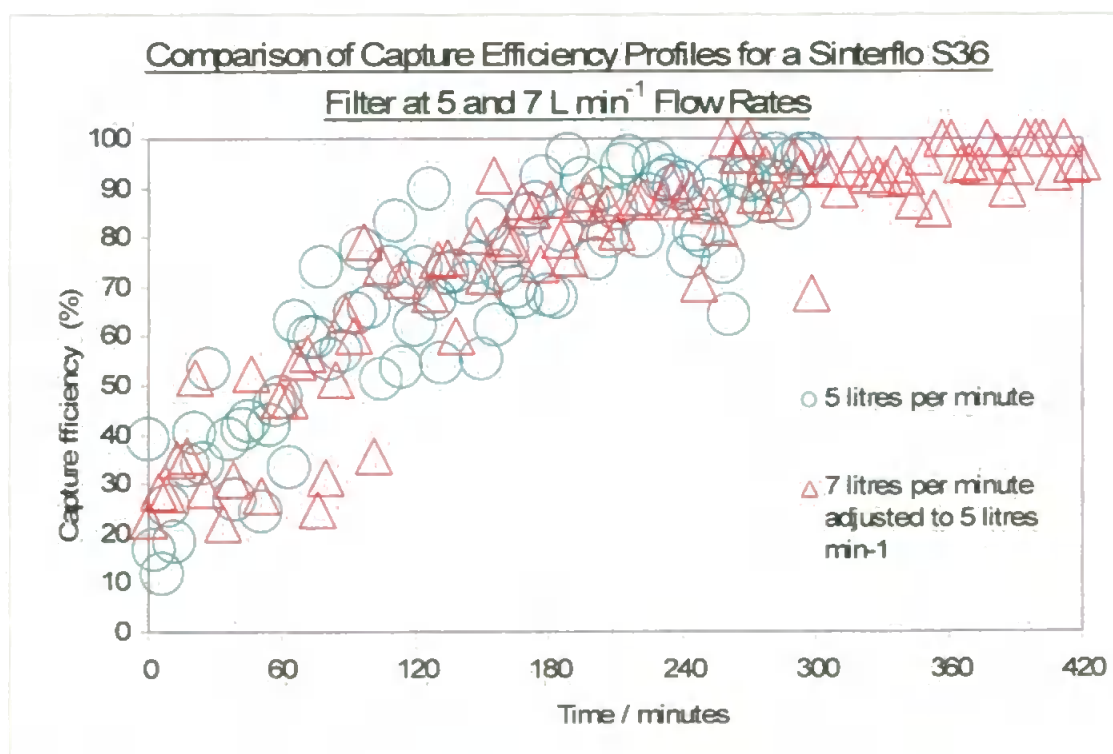
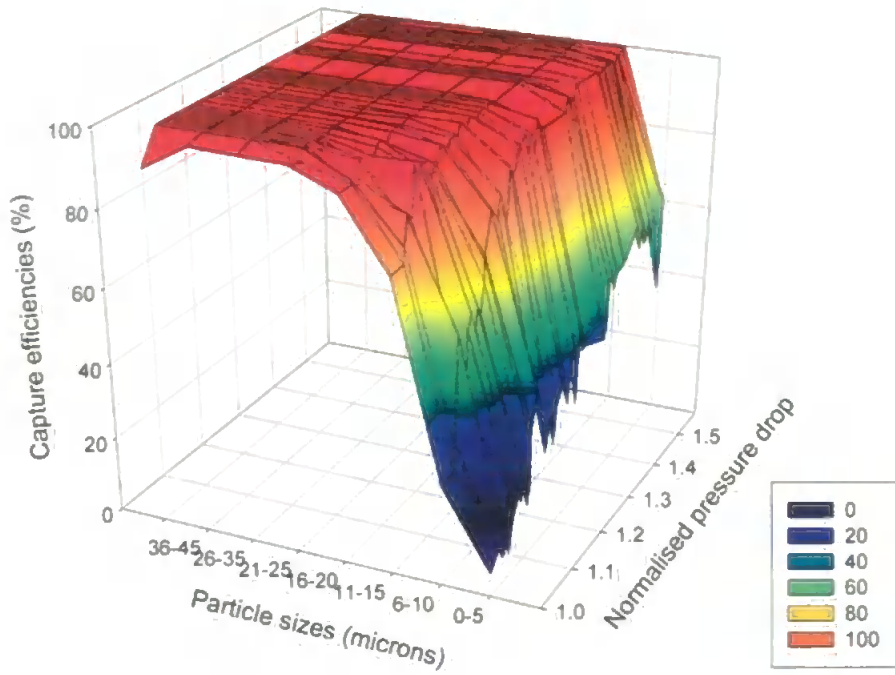


Figure 5.3 Sinterflo® S36 capture efficiency profiles for the  $6\text{-}10 \mu\text{m}$  contaminant particulate, as measured by betaratiometer. Results are normalized on the time axis to the  $5 \text{ L min}^{-1}$  flow rate.

As can be seen, the capture efficiency profiles show a close overlap. This suggests that the deposition mechanisms at each flow rate were equivalent and independent of flow-induced concerted particle effects. Observation of the filters post-test confirmed a lack of cake filtration.

Results of the experimental pass tests are shown in Figure 5.4 and Figure 5.5 as the efficiencies  $C(\Delta \mathcal{R}_{rel}, s)$  of S36 and S41 respectively. They are shown 3-dimensionally rather than a 2-dimensional depiction of the data at one particular pressure drop or blockage value, as is normally shown in filtration literature.

### Sinterflo S36 Capture Efficiencies at 7 L min<sup>-1</sup>



### Sinterflo S36 Capture Efficiency at 5 L min<sup>-1</sup>

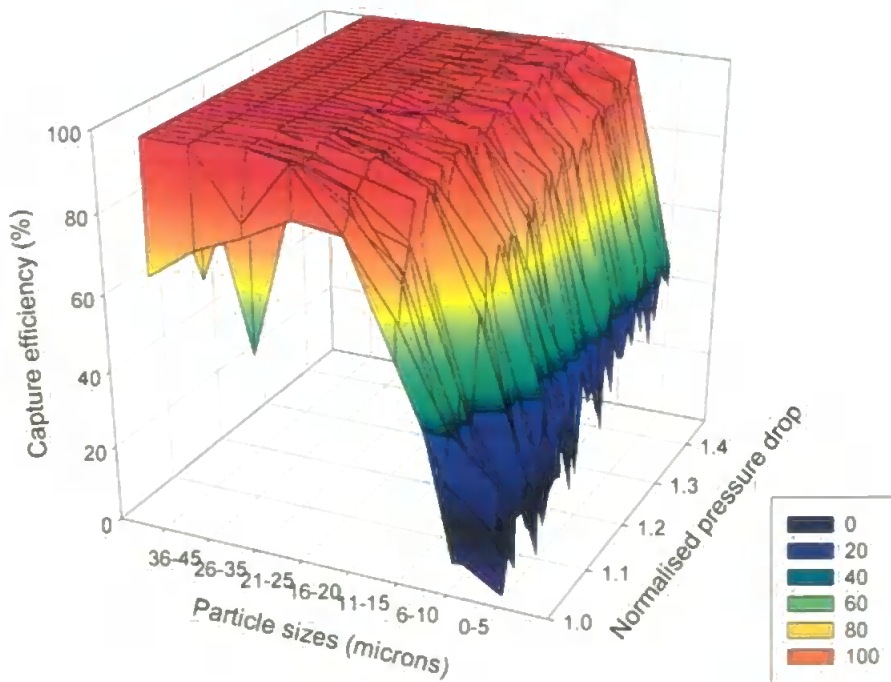
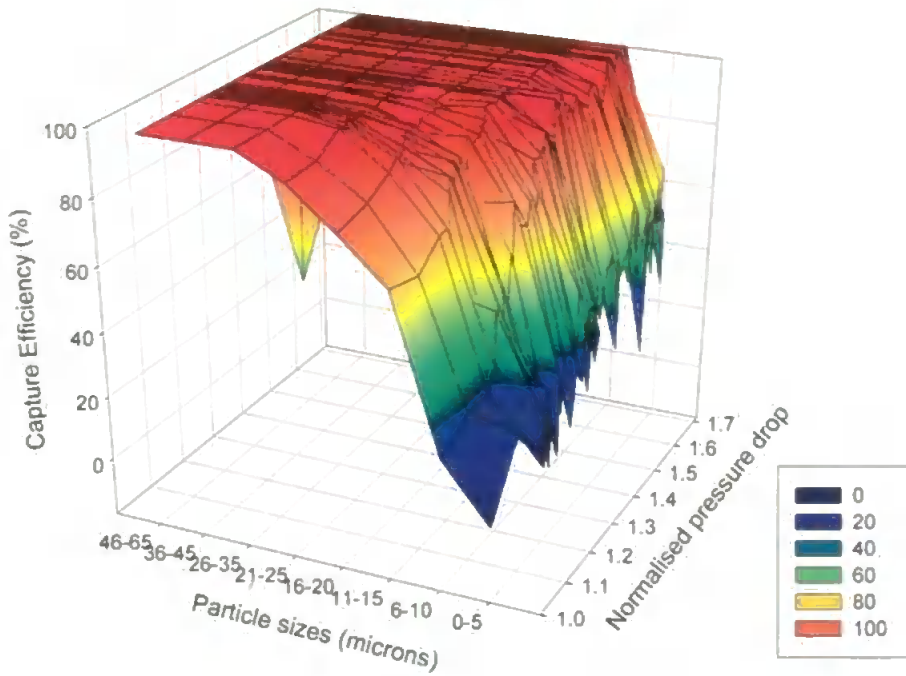
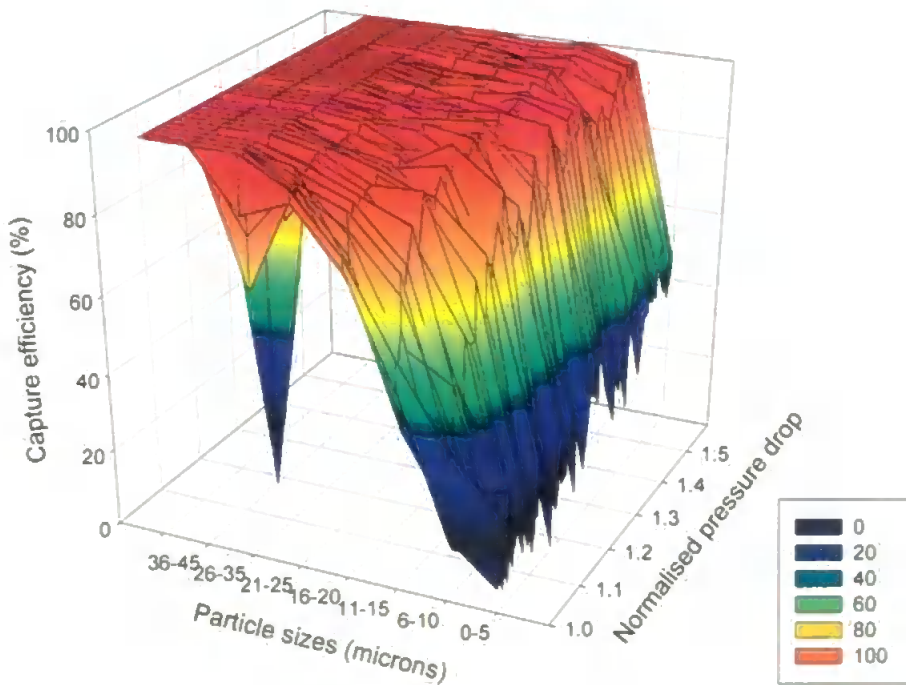


Figure 5.4 Capture efficiency graphs for S36 Sinterflo® media at 5 & 7 L min<sup>-1</sup> flow rates against the normalized pressure drop data.

**Sinterflo S41 Capture Efficiency at 7 L min<sup>-1</sup>**



**Sinterflo S41 Capture Efficiencies at 5 L min<sup>-1</sup>**



**Figure 5.5** Capture efficiency graphs for S41 Sinterflo® media at 5 & 7 L min<sup>-1</sup> flow rates against the normalized pressure drop data.



To avoid having to correct for the different flux rates between experiment and simulation, the experimental pass test efficiencies are plotted against normalised pressure drop.

The experimental permeabilities of all Sinterflo® media were measured by determining the flow of water through each filter at a fixed pressure head of 10 cm Water Gauge or 970 Pa. The results are expressed as milli Darcies (mD) so that they were directly comparable to permeabilities generated for the modelled structures, (Table 5.1).

**Table 5.1 Results of experimental permeability tests for each Sinterflo® grade tested.**

<b>Sinterflo® sample grade</b>	<b>Size for 98% liquid removal efficiency / <math>\mu\text{m}</math></b>	<b>Maximum effective pore size in media / <math>\mu\text{m}</math></b>	<b>Experimental absolute liquid permeability / mD</b>
S16	3.2	13	18.2
S21	5.9	23	81.2
S26	12	34	162.4
S36	26	67	467.2
S41	40	94	907.6

### **5.2.2. Model simulations of single pass tests and filter characteristics**

Simulations of the single pass filtration process were undertaken using the model, described in Chapter 4, and using the simulated structures for the Sinterflo® media detailed in Chapter 3. Each structure was subjected to the range of particle size distributions shown in Figure 5.2, with probability of individual particle selection within each distribution being determined by the biased random selection mechanism described in Section 4.4. As previously described each particle was fed through the maximal flow route to provide a realistic representation of particle transport through the void network

and if straining occurred, all flow routes were recalculated. Filter characteristics were calculated according to Equations 5.1 to 5.3, and pressure drop and blockage values determined using Equation 5.9, Equations 1.29 to 1.30 and an equation obtained from rearrangement of the Darcy equation so that the pressure drop term,  $\delta P_{\text{filter}}$ , may be extracted:

$$\delta P_{\text{filter}} = - \frac{\mu l_{\text{filter}} \left( \frac{dv}{dt} \right)_{\text{filter}}}{k A_{\text{filter}}} \quad \text{Equation 5. 12}$$

#### 5.2.2.1. Assessing blockage rates of simulated structures

Simulated void network representations of the filters were initially tested against each of the particle size distributions (Figure 5.2). Results are shown here graphically as the blockage rate of each simulated filter against the number of challenged particles from each of the corresponding contaminant distributions. Using this graphical representation allows assessment of the progressive blockage of a filter's void structure. For example if the particles in a suspension were of the  $S_4$  range, compared to the specific filter tested as described in Section 5.1.2, it would be expected that the filter would block rapidly as the particles would block the near surface void structure. In contrast with this, particles small with respect to the voids in the filter, i.e. in the  $S_1$  range, would undergo zero or minimal straining. In an industrial context this approach enables the selection of a filter against a pre-determined particle size distribution profile. Ideally the correct filter for FMF filtration purposes should show a progressive blockage profile as the suspension passes through the filter medium. This progressive blockage arises from the particles gradually being collected in the void structure of the

media while it maintains sufficient redirections of flow on the pore level to maximise dirt holding capacity and life time of the filter material under FMF conditions.

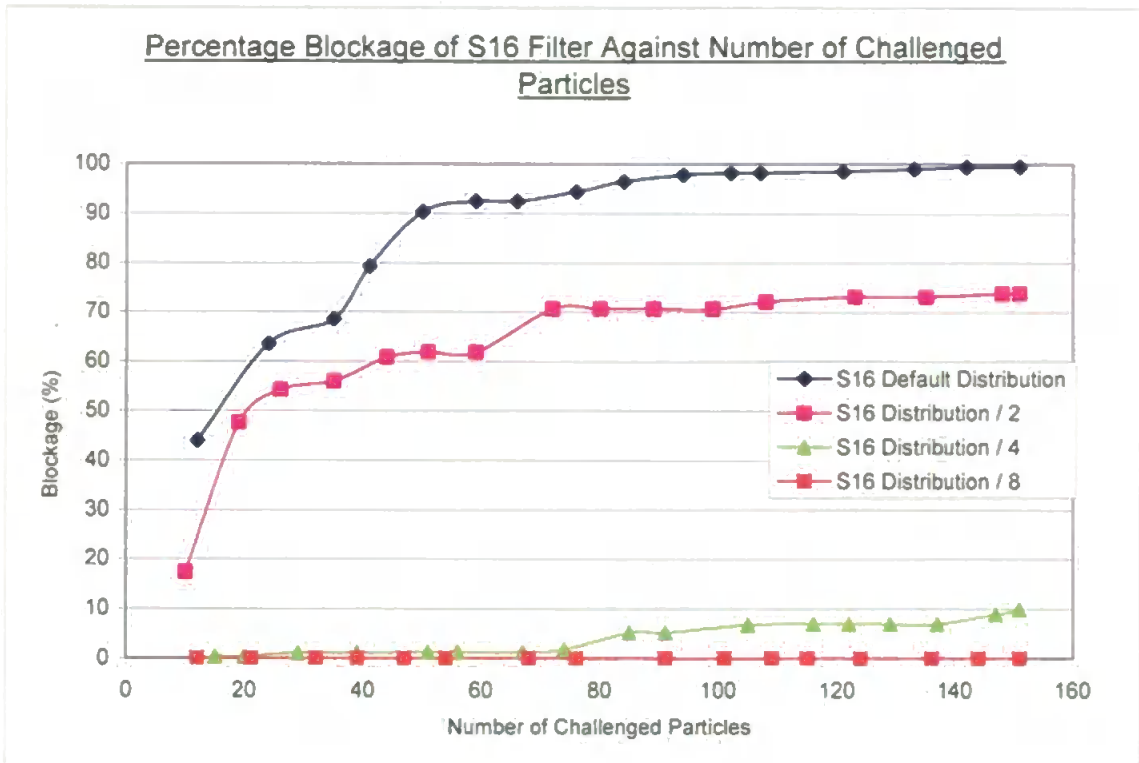


Figure 5.6 Graph showing blockage rate of simulated S16 Sinterflo® media against selected particle size distributions outlined in Figure 5.2.

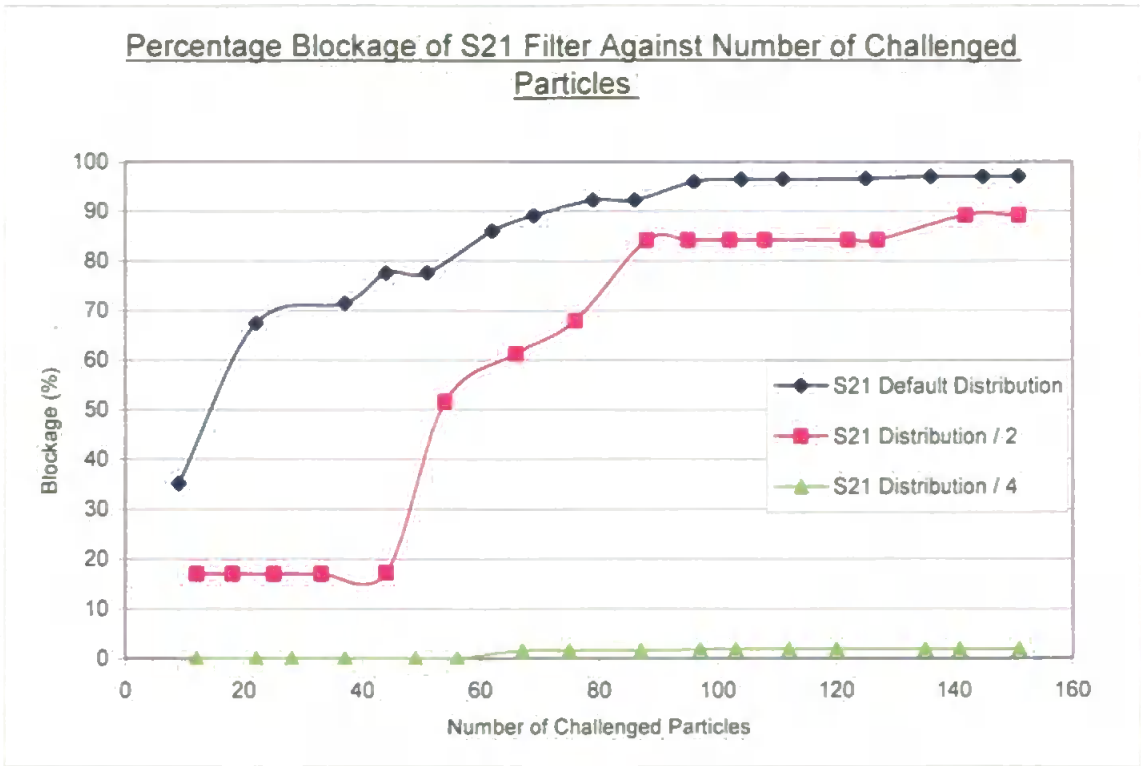


Figure 5.7 Graph showing blockage rate of simulated S21 Sinterflo® media against selected particle size distributions outlined in Figure 5.2.

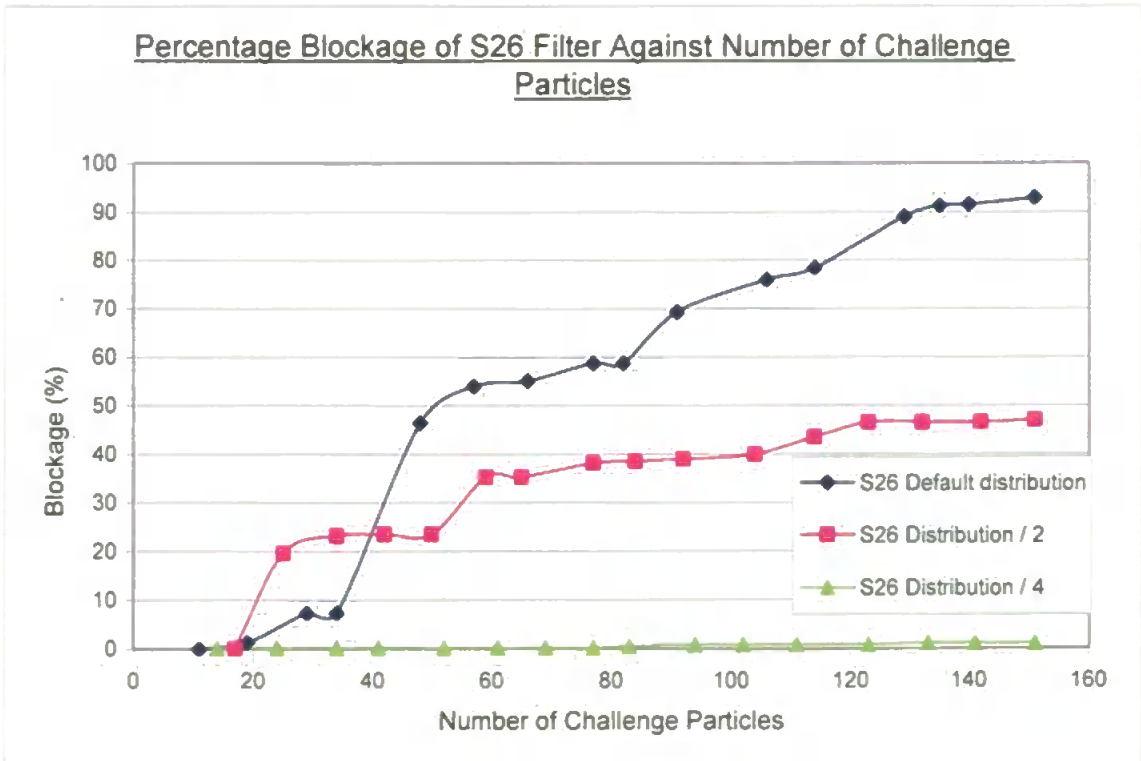


Figure 5.8 Graph showing blockage rate of simulated S26 Sinterflo® media against selected particle size distributions outlined in Figure 5.2.

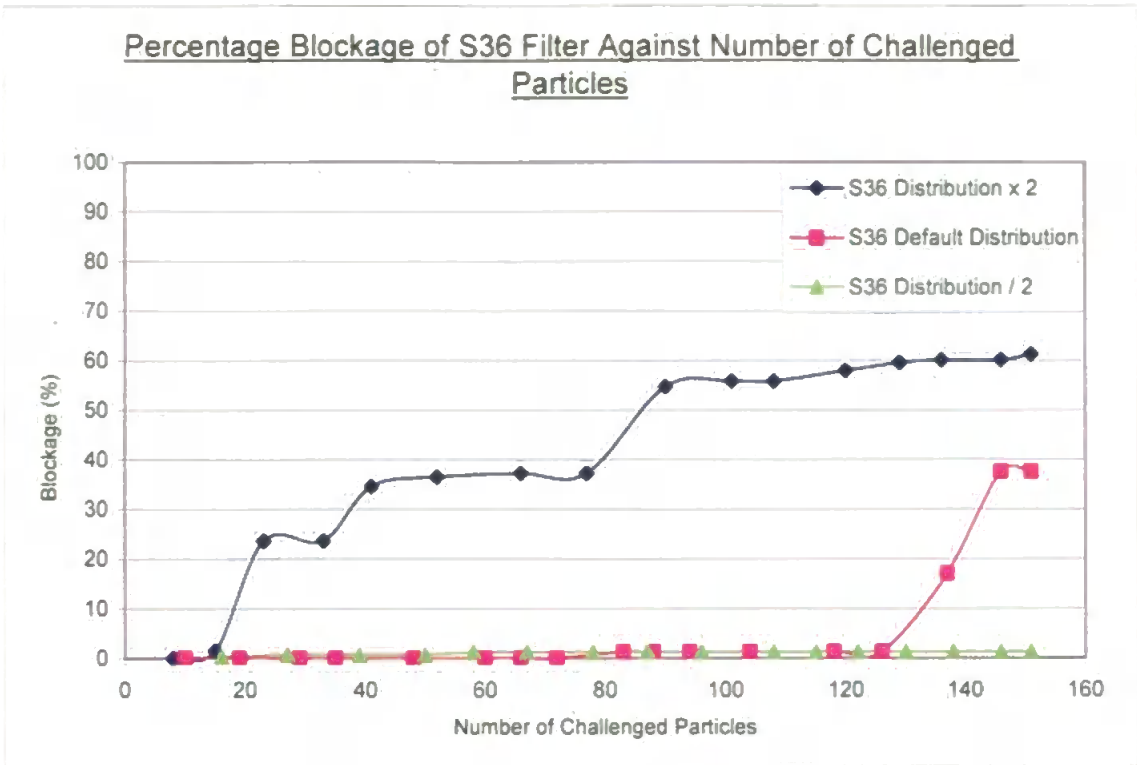


Figure 5.9 Graph showing blockage rate of simulated S36 Sinterflo® media against selected particle size distributions outlined in Figure 5.2.

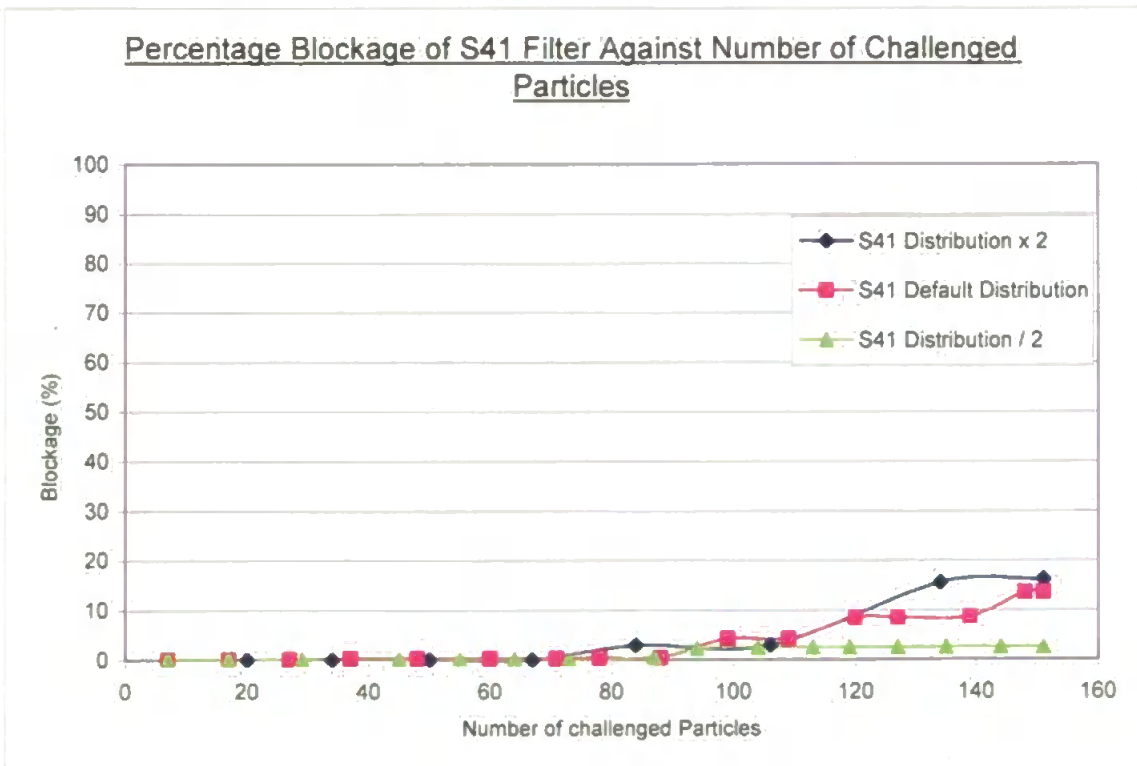


Figure 5.10 Graph showing blockage rate of simulated S41 Sinterflo® media against selected particle size distributions outlined in Figure 5.2.

Results range from the rapid blockage of the simulated S16 media by the default distribution (Figure 5.6), to the absence or near absence of blockage of the S41 media by the Div2 distribution (Figure 5.10). Results shown do not include simulations where selected distributions offered either no filtration (i.e. the Div4 or Div8 distribution on S41 media) or instant blocking or cake type filtration (i.e. the Mult2 distribution on S16 media).

Results show, as expected, there is a trend in the relationship between the increasing pore sizes of the filter void structures determined by porosimetry, and the increasing contaminant particle sizes strained from the distributions (Figure 5.2). The results show that the default distribution, proportional to the real experimental distribution, is quickly blocked by all the media except the S36 and S41 simulations. This shows further justification for not being able to undertake experimental pass tests on the finer media grades due to the occurrence of filter cake formations whilst using the available experimental contaminant (Accublast glass bead).

The influence of the blocking events on the flow characteristics of the simulated filter structures was visualised with the Colour Flow programming module (Section 4.2). Figures 5.11 and 5.12 show the complete flow mapping of an S41 simulation for the clean and half blocked filter respectively. The features blocked due to straining are shown green in the lower figure, but are too small to see at the given magnification. However, they can be viewed further in virtual reality, and by close-up inspection of a wire-frame version of the structure in the Pore-Eye software module. Reduction in flow volumes of the individual pores and throat features of the structure are represented by the changes in colour gradient as described in Section 4.2.

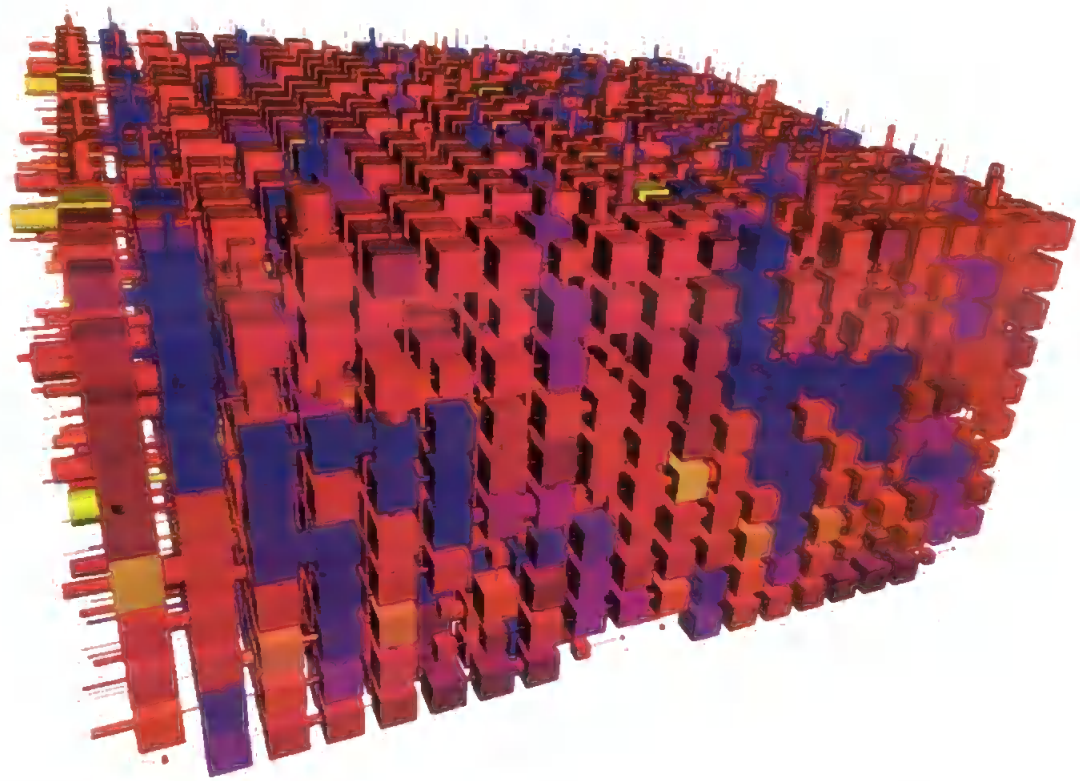


Figure 5.11 Colour Flow representation of a clean S41 filter sample prior to any filtration events.

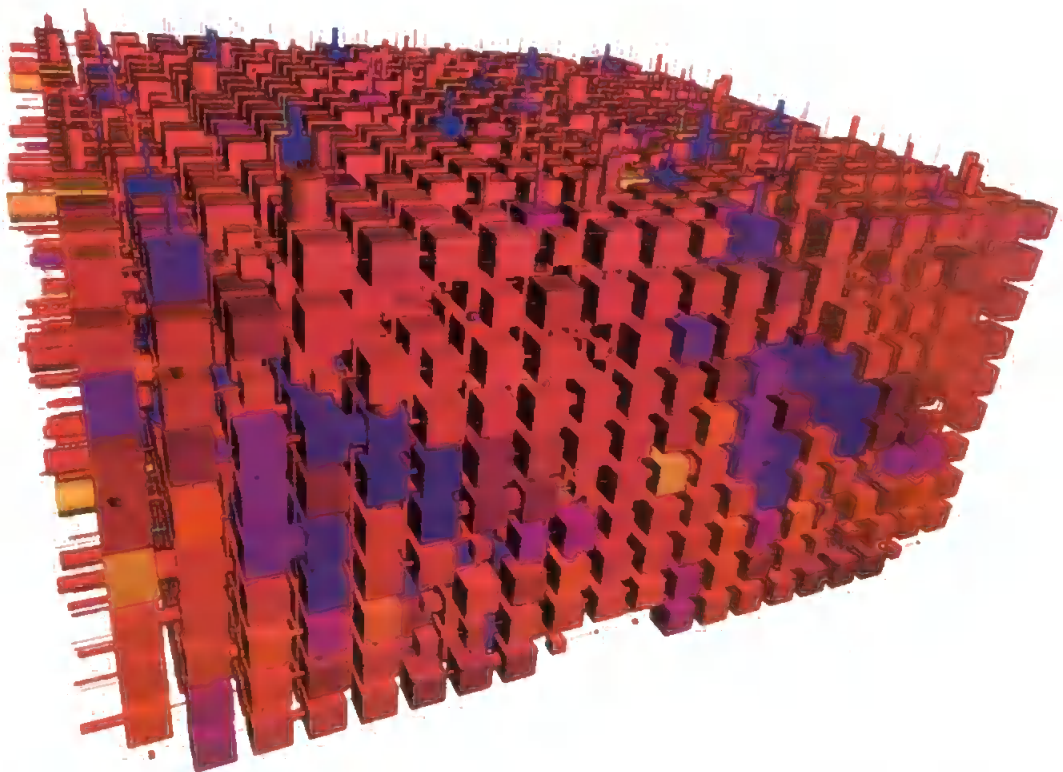


Figure 5.12: Colour Flow representation of 50 % blocked S41 filter. Comparison with Figure 5.11 shows that there are many areas within the structure that have a reduced flow volume due to deposition events in the void structure. Reduction in flow is represented by the changes in the colour gradient as described in Section 4.2.

#### **5.2.2.2. Discussion of the blockage rate assessment in simulated structures**

Examinations of the simulated filtration processes show that most straining occurs near the surface (high  $z$ ) in the upper layers of the void structure, but that several features are also blocked at much lower  $z$ . It is also found upon consulting the output files from the simulations that the collection of larger particles occurs generally at higher  $z$ , while the observed blockages lower in the unit cell structure are generally attributable to particles of smaller diameter. This phenomena is in good agreement with previous research (Ison & Ives, 1961; Tien, 1989), which confirms that the deeper parts (low  $z$ ) of a filter contribute less to the removal of suspended contaminant within fluid stream. However these authors suggest that the deeper parts of a filters structure do contribute temporally later in the filtration cycle. It is suggested that this is due to the re-entrainment of particle clusters from the upper parts of the void structure. Although this current model does not consider such events it is possibly an area for further consideration.

The deposition of smaller contaminant particles at lower values of  $z$  is also in good agreement with previous work by Rege and Fogler (1991), who suggested that the probability of capture, for an independent particle, increases with distance travelled through a void structure. A particle of relatively small size, compared to the relative void structure of the media, will be subjected to an increasing number of alternate flow routes, flow velocities and pore geometries as it progresses through the tortuous path of the filters pore/throat network. Therefore it may easily pass through the upper filter network (high  $z$ ) but due to the increasing probability of favourable deposition situations become collected in the lower (low  $z$ ) network structure.



### **5.2.2.3. Capture efficiency profiles of simulated filters**

Capture efficiency profiles for a given media are generally provided by industry to show the working capability of a filter in terms of particle sizes it will remove from a suspension. These are normally provided as 2-dimensional profiles (Figure 5.13) that show average capture efficiency at a number of predetermined contaminant particle sizes. This however is an ambiguous description as the 2-dimensional profile only indicates average capture efficiency at a particular time or pressure drop within a given pass test, and fails to consider the developing changes in capture efficiencies throughout the duration of the test (Figures 5.4 and 5.5). These continual changes of capture efficiency throughout a given pass test may be critical when considering the filter's real world working conditions. At present it is generally accepted that there is also the requirement to retail filters under "Absolute" ratings which ensure that a particular filter will trap any particle above its designated absolute particle size rating. Again this is far from ideal as it allows no insight into how a filter will perform over a given time period with a given suspension of contaminate. So for the avoidance of such ambiguity, the simulated capture efficiencies are plotted here as 3-dimensional profiles of capture efficiency against normalised pressure drop, with the exception of the initial comparison now described.

#### **5.2.2.3.1. Initial comparison of simulated capture efficiency profiles**

The first step in the comparison of the simulated filtration efficiencies for each of the media tested was to compare them to each other using the default distribution (Figure 5.2). The result is shown here (Figure 5.13) as a plot of simulated capture efficiency, calculated with regard to Equation 5.1, for the default distribution (Figure 5.2). Results given are after the filtration of the 151 default distribution particles.

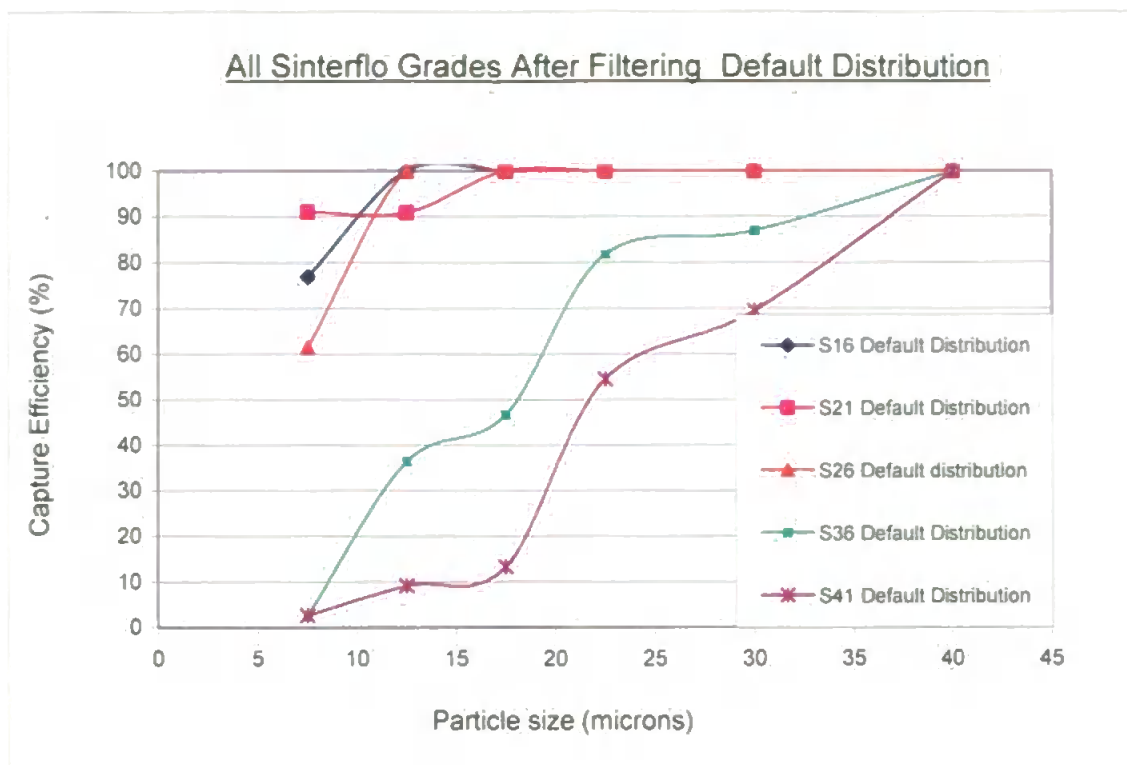


Figure 5.13 Graph comparing capture efficiencies of simulated filters at the applied particle sizes found in the filtration of the default distribution.

The simulated efficiencies in Figure 5.13 may now be compared with the commercial characteristics in Table 2.1. It is observed that the simulated capture efficiencies are generally in close agreement of the 98 – 99.9 % removal efficiencies stated for the Sinterflo® media grades tested. There are however anomalies that require discussion.

#### 5.2.2.3.2. Discussion of the initial simulated capture efficiency profiles

The first anomaly in comparison of the simulated data, with the commercial characteristics is the apparent equivalency in the 100 % capture efficiency ratings for both the S36 and S41 media at a 40 µm particle size. This can be explained in terms of the commercial data (Table 2.1) which suggests that the 40 µm ratings are approximately at the upper (99.9 %) rating of the S36 media and the lower (98 %) rating

of the S41 media. Also, the upper end of the simulated particle size distribution is coarse, jumping from 30  $\mu\text{m}$  to 40  $\mu\text{m}$ . Therefore the true 100 % capture efficiency for both of these filters could lie anywhere between the applied 30  $\mu\text{m}$  and 40  $\mu\text{m}$  particle sizes. Analogous arguments apply to the results for the S16 and S26 media.

The second apparent anomaly is the simulated efficiency profile for the S21 media. In reality the known data for the media prior to simulation is the data presented in Table 2.1. In relation to this and discussion through the course of the study (Quinlan, *Pers. Comm.*), it is known that in the manufacturing of the Sinterflo® media it is not uncommon for variances to occur in the general void characteristic of the filter media depending on the exacting conditions of the manufacturing process. There is also the possibility that the apparent anomaly in the behaviour of the S21 media in this situation is dependant on the stochastic nature of the simulated structure provided by the model. On observing the fitting parameters for the simulated structures (Table 3.1) it is found that the correlation level for the for the S21 media is 0.06 which offers an extremely random structure as described in Section 4.2.1. As the porosimetry data (Chapter 3) is in general agreement with the manufacturing data (Table 2.1) and that the other samples modelled exhibit correlation levels generally an order of magnitude higher than the S21 media, it is concluded that the unexpected efficiency profile exhibited by the S21 media is, in this instance, a result of the models stochastic nature.

#### **5.2.2.3.3. 3-Dimensional simulated capture efficiency profiles**

Simulation data sets are plotted in the same manner as the 3-dimensional experimental data shown in Section 5.2.1. In the case of the S36 and S41 media the filtration simulation has been undertaken using the default distribution, detailed previously. All

other media grades have been simulated using the Div2 distribution to initiate more FMF type filtration as validated by the blockage profile analysis in Section 5.2.2.1. Presenting the results in this way allows insight into both the filters efficiency profile and also the ageing of a filter in relation to the increasing pressure drop caused by particle deposition in the simulated networks.

### S16 Filtration Simulation Using Div2 Distribution

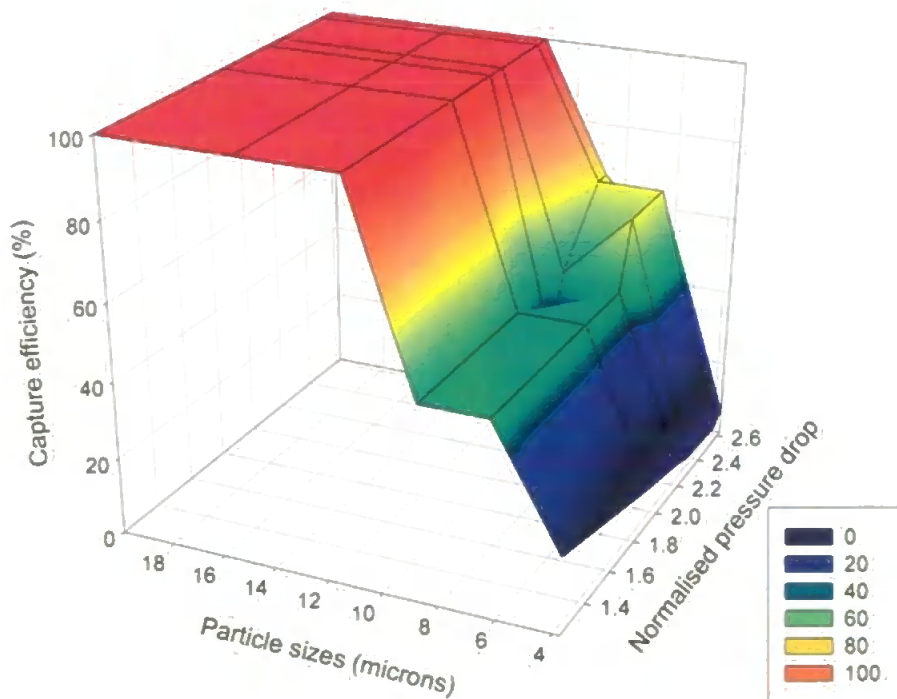


**Figure 5.14** 3-dimensional plot of a simulated single pass test on S16 Sinterflo® media using the Div2 contaminant particle distribution highlighted in Figure 5.2.

### S21 Filtration Simulation Using Div2 Distribution

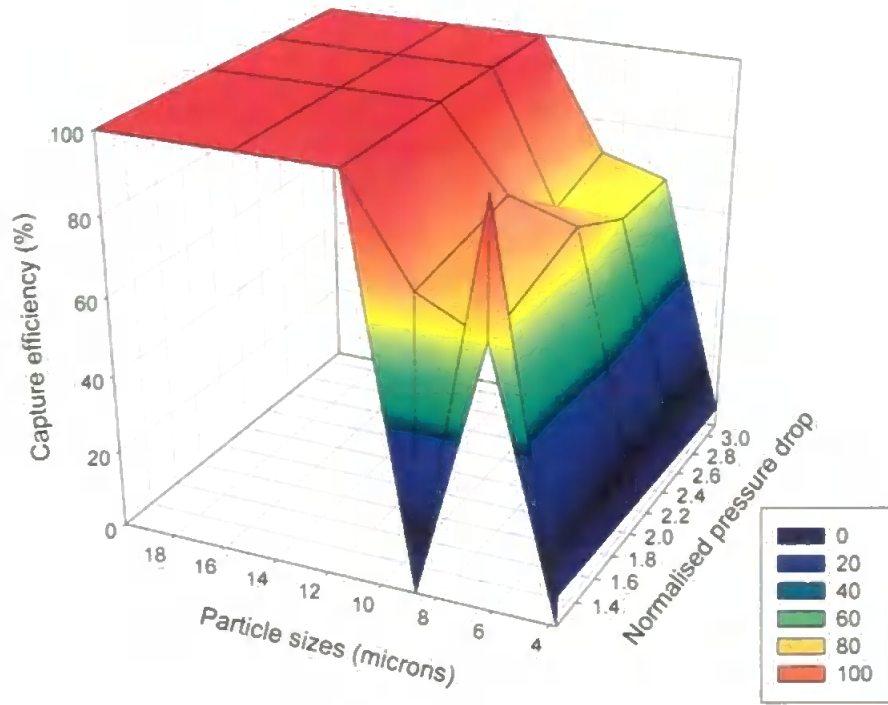


Figure 5.15 3-dimensional plot of a simulated single pass test on S21 Sinterflo® media using the Div2 contaminant particle distribution highlighted in Figure 5.2.

### S26 Filtration Simulation Using Div2 Distribution

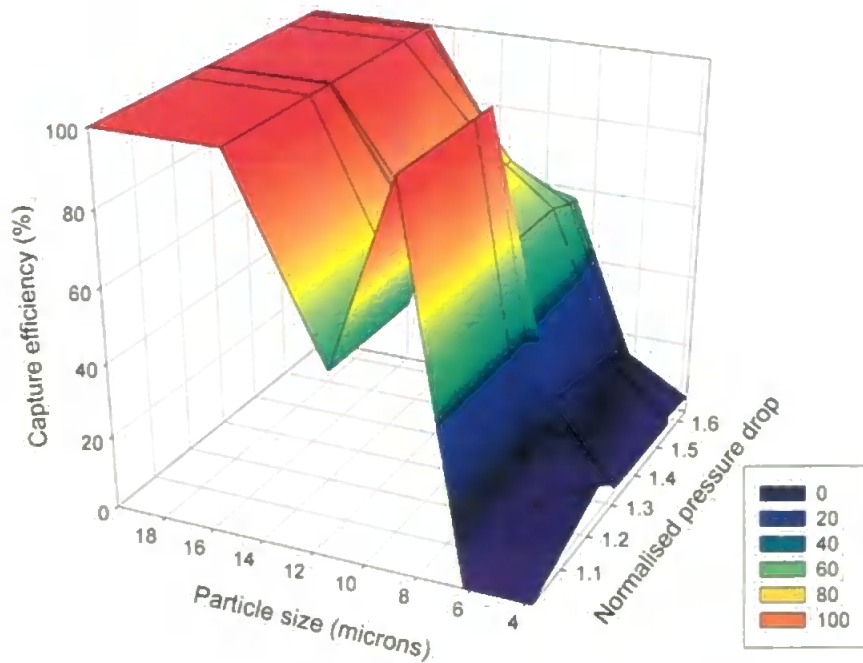


Figure 5.16 3-dimensional plot of a simulated single pass test on S26 Sinterflo® media using the Div2 contaminant particle distribution highlighted in Figure 5.2.

### S36 Filtration Simulation Using Default Distribution

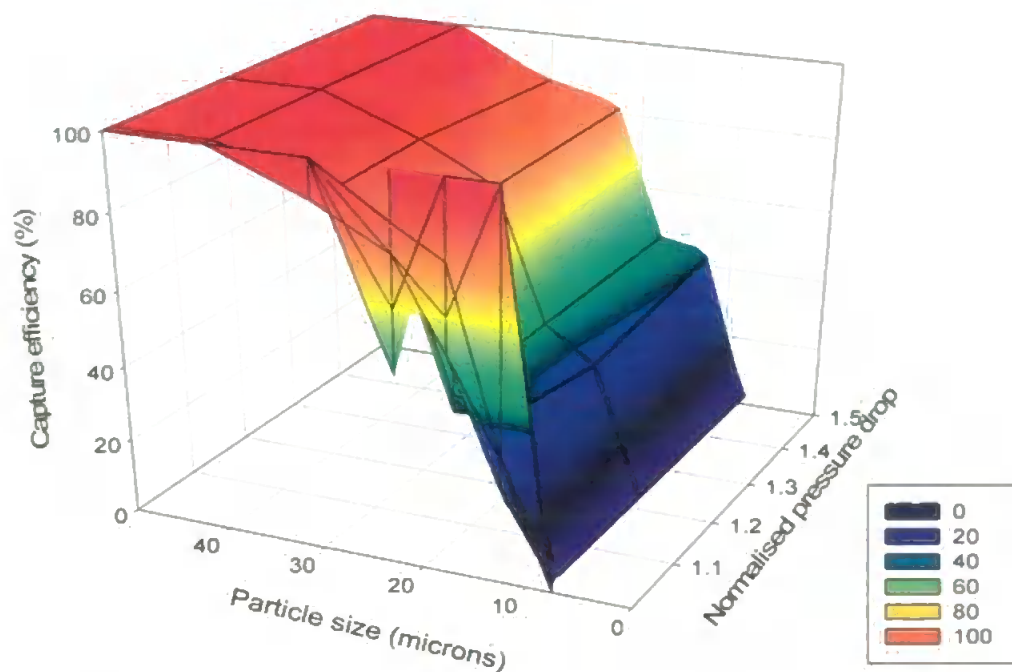


Figure 5.17 3-dimensional plot of a simulated single pass test on S36 Sinterflo® media using the Default contaminant particle distribution highlighted in Figure 5.2.

### S41 Filtration Simulation Using Default Distribution

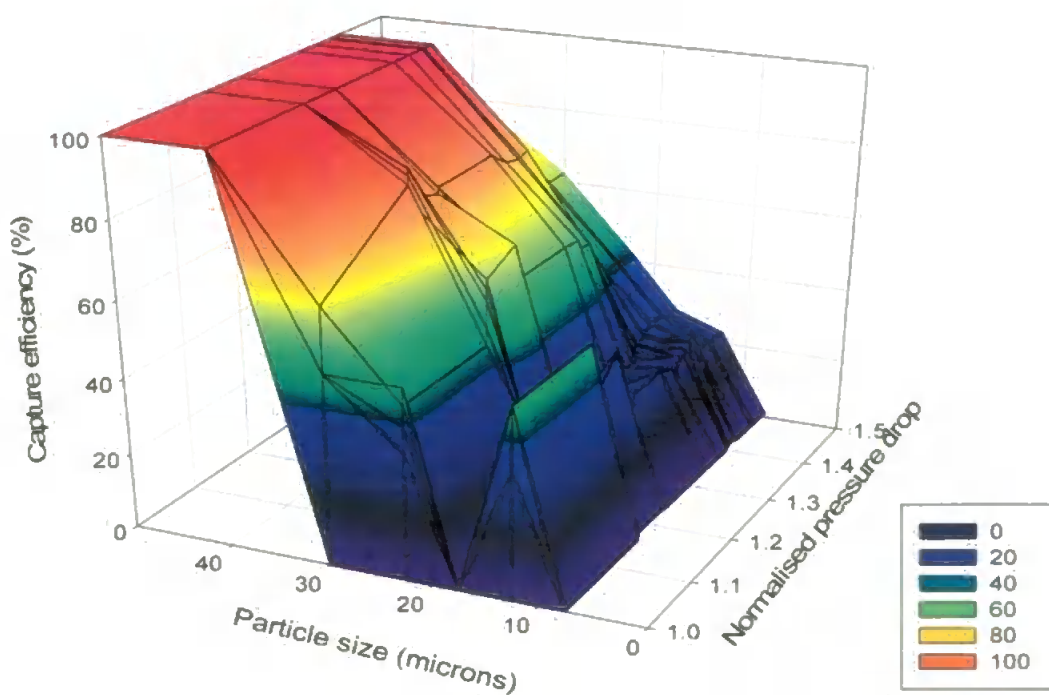


Figure 5.18 3-dimensional plot of a simulated single pass test on S41 Sinterflo® media using the Default contaminant particle distribution highlighted in Figure 5.2.

It can be seen, on observation of Figures 5.14 – 5.18, that the efficiencies of the simulated filtration runs (with exception of the S16 media) oscillate at low particle numbers (low normalised pressure drop). This oscillation is a direct result of the initial particle input into the modelled networks and the output resolution of the filtration simulation. The output resolution may be controlled via the user interface (Section 4.4) either by blockage rate or by a number of challenged particles function. In the current examples it was found that both output methods showed the early oscillation of data due to the low number of particles considered at each output. For example, if an initial output considers a particle size at which only one particle has been challenged and is also filtered its efficiency is 100%, however at the next output a further 2 particles may have further been challenged but neither filtered, automatically lowering the overall efficiency, at that particular particle size, to 33.33 %.

#### **5.2.2.3.4. Discussion of 3-Dimensional simulated capture efficiency profiles**

The oscillation of data seen in the 3-dimensional representations of the simulated filtration tests is generally statistically corrected over time (increasing normalised pressure drop). This is due to the increasing number of challenge particles offering a more rational approximation of filtration efficiency. This does not occur in the experimental curves (Figures 5.4 and 5.5), which are based on independent measurements at each pressure drop (corresponding to the 3 minute sampling rate). For example the dip in efficiency at 26-35  $\mu\text{m}$  at a pressure drop of 1.17, for the S41 media at 5 L  $\text{min}^{-1}$  flow rate (Figure 5.5), are not reflected in adjacent independent measurements.

Also observed in the simulation, the efficiency of the S36 media stays constant (Figure 5.17) whereas in the experimental test (Figure 5.4), it builds up. It is also apparent that the efficiency on the S41 simulation (Figure 5.18) builds up initially, but then drops off. Both these simulations build up substantially at pressure drops higher than those shown, so the discrepancy between these simulations and their corresponding experimental result is because the pressure term in the model builds up substantially faster in the simulation than in the experiment. Therefore, on the scaled graphs, correspondingly less of the simulation is shown than is actually appropriate. However, when compared with the experimental, both the S36 and S41 simulations are in the correct range, which is encouraging for a totally *a priori* simulation.

S36 and S41 Sinterflo® media show a high level of comparability between the experimental and simulated results in terms of both their efficiency measurements, and also the previously validated behaviour of the analysed blockage profiles, under the application of a Default distribution. As such it is reasonable to assume that that the behaviour of the finer media grades (S26, S21 and S16) under filtration of the corresponding Div2 distribution also offers a valid approximation to a real filtration system in the same way. It must be noted however that simulations do not take account of filtration by particle depositions other than straining, and concerted effects of particles forming aggregates. If an experimental filter is exposed to fines only, it will eventually clog because of further, more subtle, effects. At present the simulation will never clog unless all voids are blocked by sufficiently large particles. Also, because of the small number of particles in the simulation, the graphs show the average over the whole history of the simulation. Thus initial low efficiencies can drag down the efficiencies at higher pressure drop.



It is these problems that arise through the use of the standard efficiency equation and also those found in the use of the  $\beta$  ratio calculations (Section 5.1.2) that have led to the initial development of proposed alpha efficiency. Although not fully incorporated into the model at the current time initial comparisons of the differing methods of calculating filter efficiency have been undertaken to justify its future use as a sound description of filtration events.

#### 5.2.2.4. Comparison of efficiency calculations

As mentioned in Section 5.1.2, there are a number of apparent problems associated with the application of the generally accepted efficiency calculations used to describe filter performance. These manifest during filtration testing as the under or over exaggerated performance of a filter at differing sizes of challenged particles ( $S_1$ ,  $S_2$ ,  $S_3$  and  $S_4$  as detailed in Section 5.1). For this reason an initial development and comparison has been undertaken to define the proposed  $\alpha$ -efficiency and to evaluate its use as a more suitable parameter when providing filter classification. Figure 5.19 shows the representation of the same 'capture efficiency' data set using the different analytical calculations of filter efficiency explained in Section 5.1.2 in Equations 5.1 – 5.6 and also the proposed alpha efficiency (Equation 5.11). It may be observed from this analysis that the alpha efficiency  $\alpha'$ , offers a good balance between the efficiency derived by way of beta-ratios,  $E$ , which is known to give a falsely high impression of capture efficiency at smaller sizes, and that found via the cumulative efficiency,  $\mathcal{E}_{cum}$ , analysis which is known to offer an underestimation of performance at higher sizes.

As the alpha efficiency is based on existing measurements obtained during filtration testing it is felt that its acceptance as a new mode of monitoring filtration performance

would require minimal disruption to existing test protocol whilst offering a more realistic representation of a filters true working capacity.

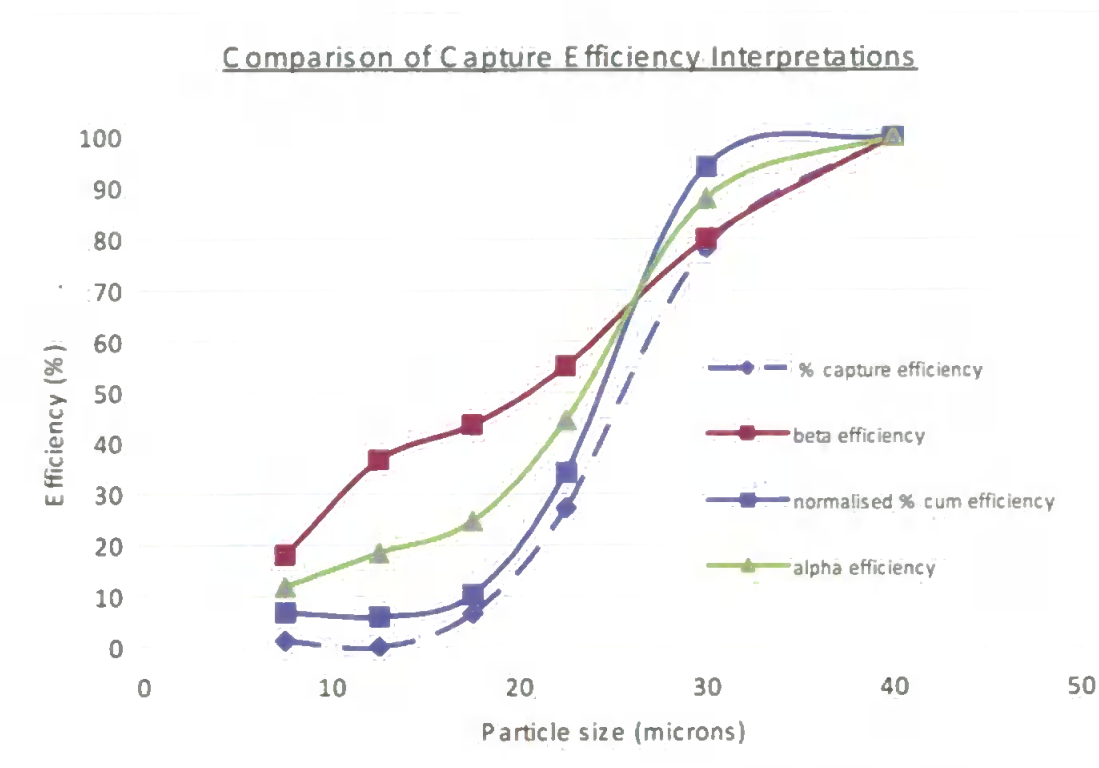


**Figure 5.19** Comparison of filter efficiency interpretations upon the same data set from an S41 Sinterflo® filter under pass test conditions. Different interpretations of data show the associated problems highlighted in Section 5.1.2.

In Figure 5.20, (a), (b) and (c) show the corresponding efficiency  $E$  (Equation 5.6), and alpha efficiencies  $\alpha$  and  $\alpha'$  (Equation 5.11) of an S41 Sinterflo® sinter under single pass test conditions at flow rate of 5 litres per minute. It is seen from this comparison of the empirical data set that the mode of efficiency analysis can lead to a hugely different representation of a filters working capability. Observing the results for the alpha efficiency calculations (b) and (c) indicates a more believable approximation of reality when considering filtration processes. Alpha efficiency is proposed as a useful and realistic characteristic and will be fully incorporated into future versions of the model.

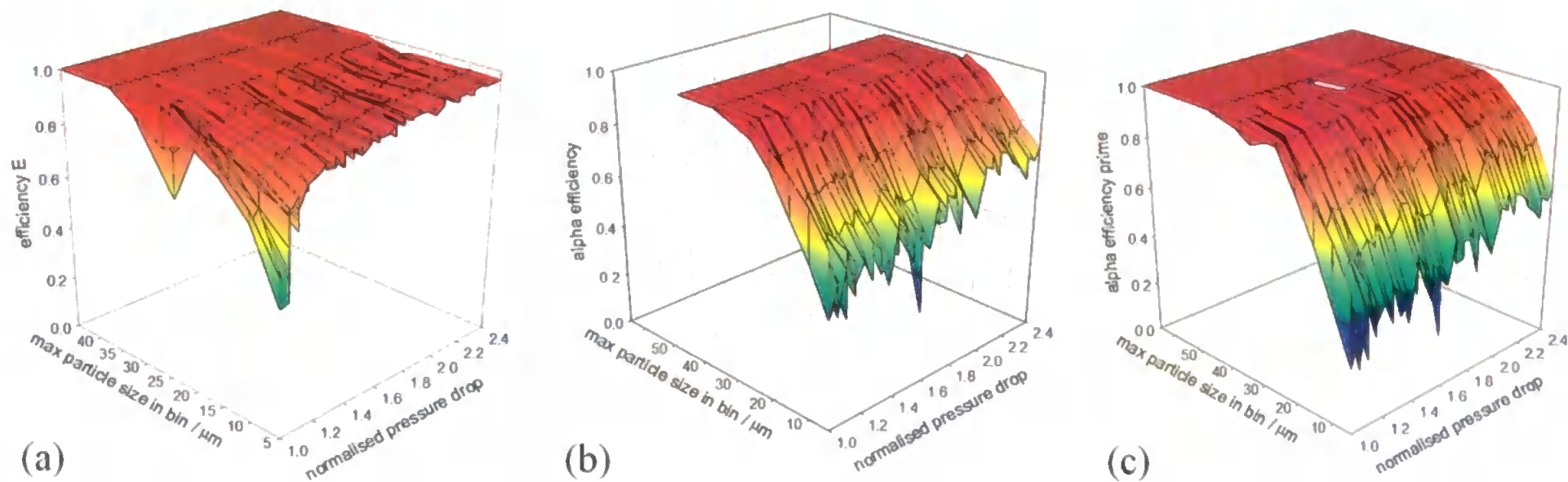


Figure 5.20 Comparison of filter efficiency between that derived from  $\beta$ -ratios,  $E$ , shown in (a) and the two derivations of alpha efficiency,  $\alpha$  and  $\alpha'$ , shown in (b) and (c) respectively. As may be seen although each method of efficiency interpretation holds consistency over the 40  $\mu\text{m}$  particle size their differing effect on the interpretation of capture efficiency at the lower particle sizes of the test are very different.

### 5.2.2.5. Permeability data from “clean” simulated filters

As previously detailed (Section 5.2.1) experimental values of permeability  $k_{\text{expt}}$ , were collected for each of the tested media by way of flow monitoring under a fixed pressure head. Using the permeability algorithm within the Pore-Cor software it has also been possible to determine representative structural permeabilities  $k_{\text{sim}}$ , for the simulated equivalents. Simulated and experimental results are tabulated in Table 5.2 as  $\log_{10}$  experimental values (Section 5.2.1) and the  $\log_{10}$  mean permeability value of the first ten stochastic realisations of each simulated filter. These values are also illustrated graphically in a plot of  $\log_{10}$  experimental against  $\log_{10}$  of the mean simulated values, to determine the correlation between the two data sets (Figure 5.21). Error bars are shown to represent  $\pm 1$  standard deviation of the simulated results so that their statistical independence may be determined. The correlation is determined via linear regression upon the log log plot and the goodness of fit represented by the  $R^2$  determination coefficient.

**Table 5.2 Comparison of experimental and simulated permeabilities. Values of permeability are expressed in milli Darcies (mD). 1 milli Darcy =  $0.987 \times 10^{-15} \text{ m}^2$ .**

<b>Sinterflo® sample grade</b>	<b>Maximum effective pore size in media / <math>\mu\text{m}</math></b>	<b><math>\text{Log}_{10}</math> Mean (<math>\bar{x}</math>) simulated liquid permeability mD</b>	<b><math>\text{Log}_{10}</math> Experimental absolute liquid permeability / mD</b>
S16	13	0.550	1.260
S21	23	0.727	1.909
S26	34	0.524	2.211
S36	67	1.049	2.669
S41	94	1.355	2.958

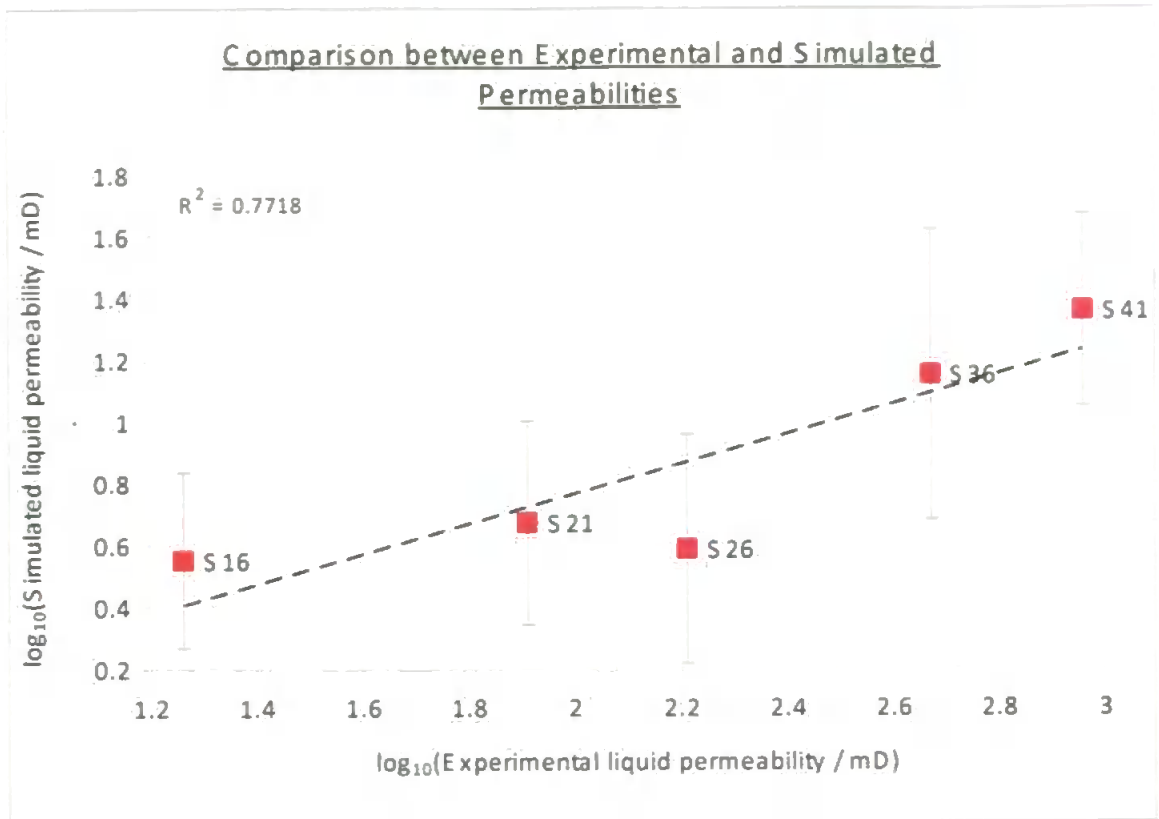


**Figure 5.21** Plot of  $\log_{10}$  experimental permeability against  $\log_{10}$  mean simulated permeability for all grades of Sinterflo® media tested. Error bars represent  $\pm 1$  standard deviation.

It can be seen that the simulated values are between 0.7 – 1.6 orders of magnitude (powers of ten) too low, and that the simulated values trend more slowly with respect to those determined experimentally. The linear regression on the log-log plot corresponds to:

$$\log_{10}(k_{sim}) = 0.485 \log_{10}(k_{expt}) - 0.2055 \quad \text{Equation 5.13}$$

when the units of permeability are in mD, and has an  $r^2$  regression of 0.77. The results also show that both the simulated and experimental results increase in their respective permeability as the maximum effective pore size increases with the notable exception of the S26 simulated result.

#### **5.2.2.6. Discussion of permeability results**

It has been shown (Table 5.2, Figure 5.19) that although the network model simulates the correct qualitative trend, it underestimates the absolute permeabilities of the filter by around 1 order of magnitude, and trends too slowly across the series of samples. The stochastic scatters of the realisations, expressed in terms of standard deviations, are also high. The permeability algorithm has previously exhibited similar characteristics in the prediction of the absolute permeabilities of sandstones (Matthews, et al, 2006). The discrepancies arise because of the approximations inherent in the network and calculation methods described earlier. Underestimation of permeability can largely be explained in terms of the simplified geometry exhibited in the modelled networks. The use of the cubic-pore cylindrical-throat approximations to describe what, in reality, is a very complex structural entity means, that the further applications of the permeability algorithms actually inherit a pre-determined level of simplicity from the networks structural form and also due to the elimination of complex hydrodynamic processes at the cylindrical-throat cubic-pore boundary. The resulting resistor type approximation (Section 1.3.5.4) therefore leads to the observed discrepancy. However, such simplifications are essential to make the filtration simulations computable on fast personal computers rather than super-computers, an essential requirement for a model useful to industry.

### **5.3. Conclusions**

It has been seen from the associated analyses and comparisons with wet bench test methods that the developed filtration model provides a useful tool to characterise many aspects of filtration media. The importance of this work is that it demonstrates simulations of depth filtration by straining which are entirely un-calibrated and *a priori*.

Therefore any filter for which mercury intrusion or void geometric data is available can be simulated.

The simulations do not take account of filtration by particle deposition other than straining, and concertive effects of particles forming aggregates. If an experimental filter is exposed to fines only, it will eventually clog because of these effects, whereas at present the simulation will never clog. The lack of concertive effects also explains the underestimates of filter efficiency in the middle of the particle size ranges. Furthermore, because of the small number of particles in the simulation, the results have to be based on cumulative averages over the whole history of the simulation. Thus initial low efficiencies can drag down the efficiencies at higher pressure drop. This does not occur in the experimental curves, which are based on independent measurements at each pressure drop. For example the dip in efficiency at 26-35  $\mu\text{m}$  at a pressure drop of 1.17 (Figure 5.5) is not reflected in adjacent independent measurements.

An additional strength of the simulations is that because they require no calibration and represent *a priori* simulations of the entire spatially dispersed straining process, other effects can also be observed. For example the ageing of filters can be observed by increasing the numbers of particles challenging the filters. Also, some simulations show that the capture efficiency builds up initially, but then plateaus because of channelling of the flow routes.

## 6. Wicking properties of Vyon® media

### 6.1. Background of the study

Wicking processes in porous media are an area of huge interest to many filtration and bio-medical device manufacturers. An understanding of the processes and optimisation of fluid transport properties through the selection of correct pore size and surface chemistry characteristics can allow huge advancements in production of functional diagnostic devices such as pregnancy or blood sugar tests. However, these improvements and associated manufacturing processes must be measurable and controllable to allow production of consistent wicking media.

An initial modelling study was undertaken in collaboration with the Department of Soil Science at Rothamsted Research Institute (Harpenden, UK) to optimise an experimental protocol for measurement of wicking events. This method may be applied to the study of the porous Vyon® media and a set of hydrophilically treated equivalents (i-Vyon® Section 2.2.2).

In the collaborative soil study, a capillary rise method to measure the wettability of ten agricultural soils taken from Rothamsted long-term experimental sites was described (Matthews et al., 2008). The soils had very similar clay contents, but organic carbon (C) contents from 11.5 to 31.2 g kg<sup>-1</sup>. The wetting rates were interpreted by an improved method of data analysis, consistent with the Washburn equation (Section 1.3.3.1.2), and showed an increase in the effective contact angle between the water meniscus and the soil with increasing C content. This corresponds to a decrease in wettability with increasing C content, and is consistent with other reports in literature. By contrast with water, it was found that capillary rise data for *n*-hexane into soils did not depend on soil bulk density or C content. *A priori* calculations of the expected wetting rates from fluid



properties and an effective hydraulic radius estimated by other methods gave magnitudes and trends that agreed with the experimental data. The results showed that estimates of effective hydraulic radius can provide a useful approximate tool for characterising soil wetting.

Due to the success of this collaborative work it was decided that the improved method of data analysis applied in that project would be ideally suited to the study of wicking performance exhibited by the Vyon® and i-Vyon® samples. As described in Section 2.2.2 the surface modification of Vyon® media by various methods to form the differing i-Vyon® counterparts is of high interest to areas such as organic synthesis and bio-medical applications. A quantification of how a hydrophilic treatment and pore size distribution would influence wettability and wicking properties would allow manufacturing procedures to be optimised, and could widen the range of applications. It should also indicate which material and pore size distribution would offer the best wicking rate of liquid in a required situation.

Therefore the objectives of this chapter are to:

- (i) Explain the experimental technique developed and utilised in this study for the wicking analysis of hydrophilically treated Vyon® media,
- (ii) Report the experimental results,
- (iii) Describe the improved method of data analysis applied to wicking measurements,
- (iv) Discuss the scientific and industrial significance of the results.

### 6.1.1. The improved data analysis of wicking phenomena

In Chapter 1 the basis of capillary rise and its current modelling acceptance were discussed under the title of unsaturated flow in porous media (Section 1.3.3.1.2). The improved data analysis, developed within the collaborative study (Matthews et al., 2008) is now described.

Taking notation from Chapter 1, where  $x$  is the distance of liquid travel in a capillary and  $\rho$  is the density of the associated liquid it can be said that for a sample of porosity  $\varepsilon$  in a sample tube of inner radius  $R$  and cross-sectional area  $\pi R^2$ , the weight of water  $w$  taken up is :

$$w = \varepsilon \rho \pi R^2 x \quad . \quad \text{Equation 6.1}$$

$x$  now becomes the height of the wetting front above the surface of source liquid, rising to a maximum height  $H$  during the experiment. Equation 6.1 is only valid if the experiment is carried out at such short times that the hydrostatic head on the liquid is negligible compared to the capillary forces. Combining Equations 1.13 and 6.1 and eliminating  $x$  gives:

$$w^2 = \left( \frac{\varepsilon^2 \pi^2 R^4 r_h}{2} \right) \left( \frac{\rho^2 \gamma \cos \theta}{\eta} \right) t = c K t \quad \text{Equation 6.2}$$

where  $c$  and  $K$  are the lumped terms in the respective parentheses.  $c$  is a geometric parameter which remains constant between replicate samples provided that the skeletal particles of the replicates are of similar size (Siebold et al, 1997).  $K$  depends on the

characteristics of the fluid, and the way in which it interacts within the porous media.

Taking the logarithms of the square root of Equation 6.2 it follows that:

$$\ln w = \beta \ln(cKt) \quad \text{Equation 6.3}$$

where  $\beta = 0.5$ . In practice, there is a wetting jump at the moment of contact between the sample and the liquid, which causes a rapidly dying weight oscillation  $\delta w$ . This causes an oscillation in the observed weight  $w_{\text{obs}}$  at the observed time  $t_{\text{obs}}$ , and masks the exact start time  $t_0$  of the wetting process. The working equation becomes:

$$\ln \left\{ w_{\text{obs}(t_{\text{obs}}-t_0)} - w_{(t_0)} + \delta w_{(t_{\text{obs}}-t_0)} \right\} = \beta \ln \left\{ c K (t_{\text{obs}} - t_0) \right\} \quad \text{Equation 6.4}$$

Equation 6.4 contains two unknowns,  $t_0$  and  $\delta w$ , and therefore cannot be solved. However, because the two unknowns are linked experimentally, a solution can be found by stepping manually through values of  $t_0$  near the likely observed start of the wetting process, until  $\beta \Rightarrow 0.5$ . (Automated solvers do not work, because of the apparent randomness of the variation of  $\delta w$  when  $t \approx t_0$ ). If, however,  $\delta w_{t_0}$  is large when  $t$  is very close to  $t_0$ , or equal to  $t_0$ , no solution can be found, which was found to be the case in some samples in the collaborative study. Apart from such cases, it is possible to find solutions to Equation 6.4, with  $0.45 < \beta < 0.55$ . Therefore previous suppositions that gradients other than 0.5 could be ascribed to structural or wetting effects in the sample (Siebold et al, 1997) must be viewed with caution. The solution of Equation 6.4 gives a series of weight and time readings for a solved value of  $\beta$ , so the product  $cK$  can be found for any sample  $n$ .

These principles have successfully been applied to the study of soils containing different levels of carbon content (Matthews et al. 2008). Two modifications need to be made for the case of Vyon® and i-Vyon. Firstly, the cross-section dipped into the wetting liquid is now  $LW$  rather than  $\pi R^2$ , where  $L$  and  $W$  are the length and width of the sample respectively. (In the present study,  $L$  was 2 cm and  $W$  was 3 mm.). Also defined in the modified equation is a hydrophilicity factor  $h$ , ranging from 0 (entirely hydrophobic) to 1 (fully hydrophilic). Then equation 6.2 becomes:

$$w^2 = \left( \frac{h^2 \varepsilon^2 L^2 W^2 r_h}{2} \right) \left( \frac{\rho^2 \gamma \cos \theta}{\eta} \right) t = c K t \quad \text{Equation 6.5}$$

Over a particular sample  $S$ , the average hydrophilicity  $\langle h \rangle$  is given by:

$$\frac{\int_S h dL dW dH}{\int_S dL dW dH} = \langle h \rangle_S \quad \text{Equation 6.6}$$

Suppose we take  $N$  replicates, i.e. samples  $S_1 \dots S_n \dots S_N$ . Then

$$\sum_{i=1}^N \text{Var}(h_i) = \text{Var} \sum_{i=1}^N h_i \quad \square \quad \text{Var}(h_i) \quad \text{Equation 6.7}$$

The equality in the equation above follows from the mathematical property of variance, and the approximation from the fact that if the individual samples are of sufficient size to encompass Representative Elementary Volumes of the material, the variance of

hydrophilicity across replicates will be the same as the variance of hydrophilicity within a single replicate. Therefore if a particular surface treatment methodology minimises

$$\sum_{i=1}^N \text{Var}(h_i), \text{ we assume that it also minimises } \text{Var}(h_i).$$

### 6.1.2. Treatment of Vyon® media to enhance hydrophilicity

As previously detailed in Section 2.2.2, the standard hydrophobic Vyon® media may be subjected to a number of different surface modifications that alter its functionality. This study investigates one such modification, namely enhanced hydrophilicity.

The hydrophilicity of standard Vyon® media is enhanced by oxidising the surface layers (including the internal pore surfaces) of the material using a weakly ionised oxygen plasma. Oxidation of the polymers surface layers is responsible for the generation of activated polar sites such as C=O (carbonyl), -COOH (carboxyl) and -OH (hydroxyl) groups which in turn directly enhance the material's hydrophilicity. The effectiveness of oxidation to the polymeric surfaces may be controlled by a combination of modifying oxygen flow levels, plasma energy, time and vacuum levels within the treatment chamber.

Below is shown a schematic of the plasma treatment chamber (Figure 6.1) that is used in preparation of such samples. The polymer based samples are placed upon the mesh support within the chamber which ensures that they are within the discharge region of the plasma. The optimum conditions of the process used in this study are confidential and unpublished. However a similar application of oxidising plasma treatments to enhance hydrophilicity can be found in literature (Grundke et al, 2003).

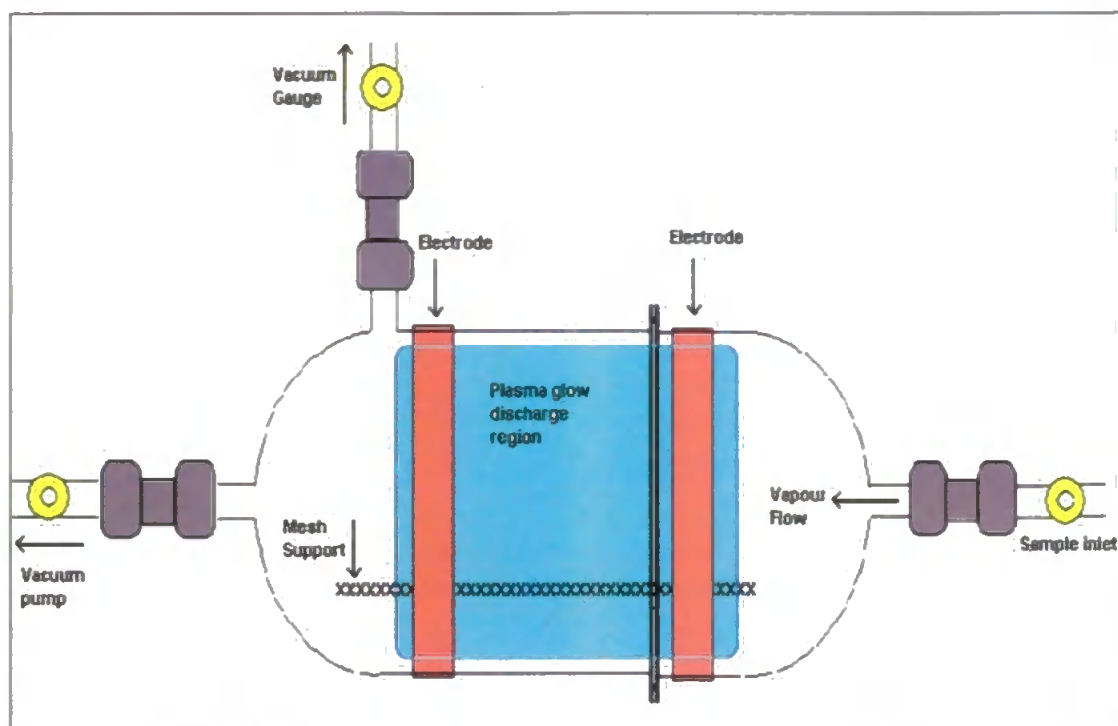


Figure 6.1 Schematic of the plasma chamber used in the oxidization of polymer pore surfaces to enhance media hydrophilicity. Oxygen is fed into the chamber under vacuum through the sample inlet point direct to the electrode set-up.

## 6.2. Experimental apparatus and method for wicking analysis

The rate of liquid uptake into samples after contact with a liquid reservoir was measured using a digital microbalance, namely a PC-linked Mettler Toledo XP504 balance with a precision of 0.1mg. Initial measurements were made by video filming the digital readout next to a stopwatch, and taking the data from sample frames. Subsequent measurements were made using Mettler's BalanceLink software, which captured ca. 25 measurements per second via an USB 2 link. The measurements tended to be constant for groups of 2 or 3 successive readings, so in practice the reading changed every 0.1 seconds. The sensing and equilibration rate of the balance was checked by very gently dropping a 10 mg standard weight onto the balance. The reading changed from zero to 11.3 mg in 0.095 seconds, thus registering the deceleration force on the dropped weight, and then dropped to 10.2 mg, 0.28 seconds after the last zero weight reading. For the

current dynamic wetting experiments, any constant time lag in measurement is corrected by taring the time, so we estimate any time error to be less than 0.1 seconds. Errors in weight were assumed to be less than 0.2 mg, negligible compared to the total weight changes reported below.

Vyon samples were clamped directly into the sample holding point (shown in Figure 6.2 holding a soil containment cell) with a fitting allowing it to be clamped into the slider mechanism on vertical rods, visible in Figure 6.2. The slider was in turn connected to a vertical screw thread which is screwed through the top of the sample chamber. When this screw was manually rotated, the sample descended towards the liquid without itself rotating. The screw thread was pitched so that one full rotation lowered the sample by 1mm.

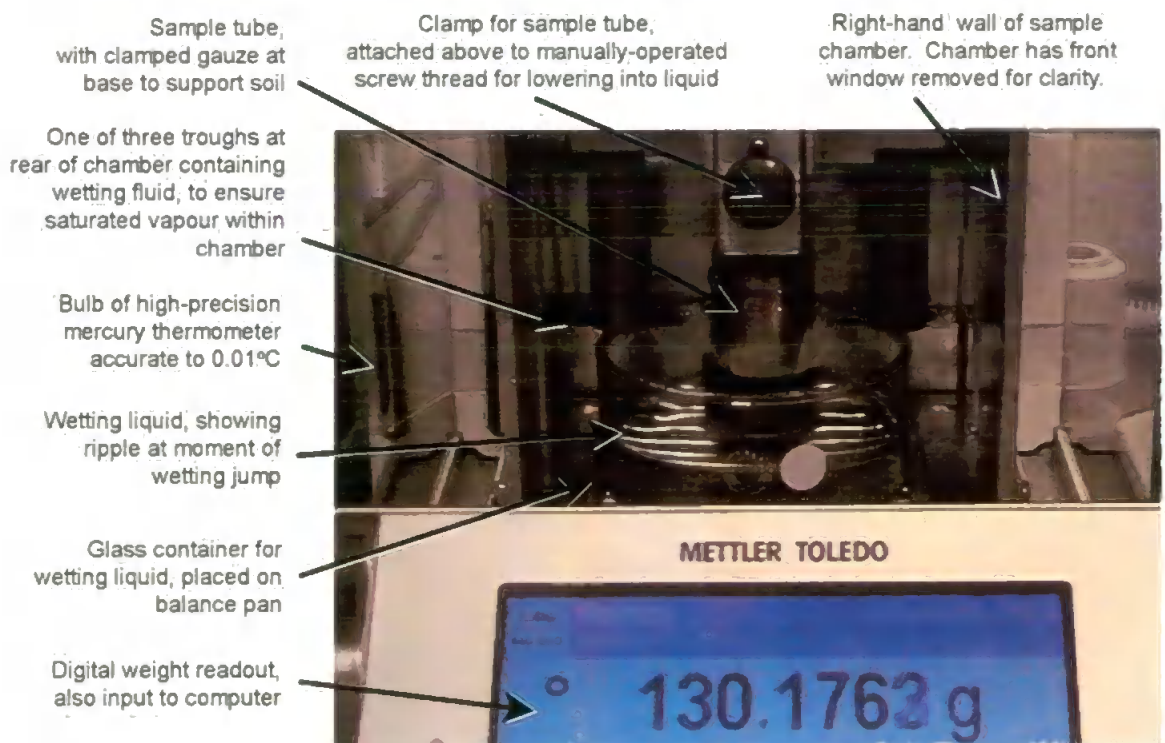


Figure 6.2 Wetting apparatus showing detail of sample holder assembly, balance read out and wetting liquid reservoir. Note that in this diagram a soil sample holder is shown (numbered 3 in centre of diagram) rather than a sample of the Vyon® or i-Vyon® media.

The wetting chamber was a copy of that constructed by Schoelkopf et al. (2000), in whose publication is a schematic diagram, and also contained a slight modification manufactured at the University of Plymouth. The chamber comprised a metal box with glass front and no base, which fitted on the base of the balance without touching the balance pan. It is shown in Figure 6.2 with its front removed for clarity. The wetting liquid is contained in a glass dish, which stands freely on the balance pan. At the rear of the chamber are three troughs, which are filled with the corresponding wetting liquid to ensure a saturated vapour and no evaporation from the reservoir of wetting liquid held in the glass dish. This wetting chamber is in turn mounted in the balance chamber with lifting spacers to assure no contact with the balance pan mechanism. Also inside the balance chamber is the bulb of a high precision mercury thermometer, which is checked to ensure that the temperature of the experiments is at the desired temperature (in the case of the Vyon® and i-Vyon® study this was  $20.00^{\circ}\text{C} \pm 0.10^{\circ}\text{C}$ ). Vyon samples used in this study were manufactured to a pre determined specification and were supplied in standard size strips measuring 20 mm wide and 80 mm long and having a sample thickness of 2mm. This results in the fluid contact area of the 20 mm by 2 mm sample of  $1.6 \times 10^{-5} \text{ m}^2$ .

The experiment was initiated by manually lowering the sample onto the liquid until the balance indicated a wetting jump had occurred, and then quickly giving one extra turn to lower the sample by a further 1mm. Figure 6.2 shows the apparatus at the moment of the wetting jump, which has caused a ripple, visible for about 0.1 s, as the liquid jumps up to the sample. The displacement of the fluid by the descending sample, the wetting jump and ensuing ripple together result in the weight oscillations  $\delta w$  in Equation 6.4. Although shown here with a soil sample containment cell in situ, the same behaviour is



observed with i-Vyon® media samples. Results were run in triplicate for each sample grade in both water and hexane liquids.

### **6.3. Results of wicking analysis**

#### **6.3.1. Initial sample set**

Initial samples of hydrophilic treated i-Vyon® and non-treated standard Vyon® were run on the wicking apparatus as detailed in Section 6.2. On these initial tests it was observed that all standard samples of Vyon® media, independent of grade, exhibited no wicking potential, when water was used as the wetting liquid. This was due to the hydrophobic nature of the standard material. An example of such behaviour is shown graphically in Figure 6.3. When the Vyon is inserted into the liquid, the Archimedes displacement causes an apparent weight rise of 0.4g. The recorded weight then remains constant, indicating an absence of any wetting of the material or wicking through it.

Also apparent was that the hydrophilic treatment of the i-Vyon® samples had a high level of inconsistency with the same wetting liquid. This caused erratic wicking, and resulted in jagged wicking profiles, exemplified in Figure 6.3, rather than the smooth square-root-of-time dependence predicted by the Washburn approximations. The major extent of the inconsistency could be observed visually as non-wetting patches during the wicking experiments with water, exemplified in Figure 6.4. Also shown in Figure 6.3 are the overall characteristics of the wicking results, namely an initial wetting jump followed by a minimal weight gain due to the displacement, and then by a significant wicking event. This wicking is indicated by the progressive loss of weight from the reservoir as observed in the  $y$  axis. The saturation of vapour inside the sample chamber by means of filled troughs at the rear attempted to ensure that none of this apparent

weight loss was due to evaporation. This was confirmed for each measurement in both water and hexane runs by a recorded weight stable to  $\pm 0.1$  mg before the start of each experiment. However, during the wicking itself, as the surface area of wicked fluid increased, evaporation also occurred until finally an equilibrium was set up and no further apparent weight change occurred. Therefore only the initial wicking data in each run were used for analysis.

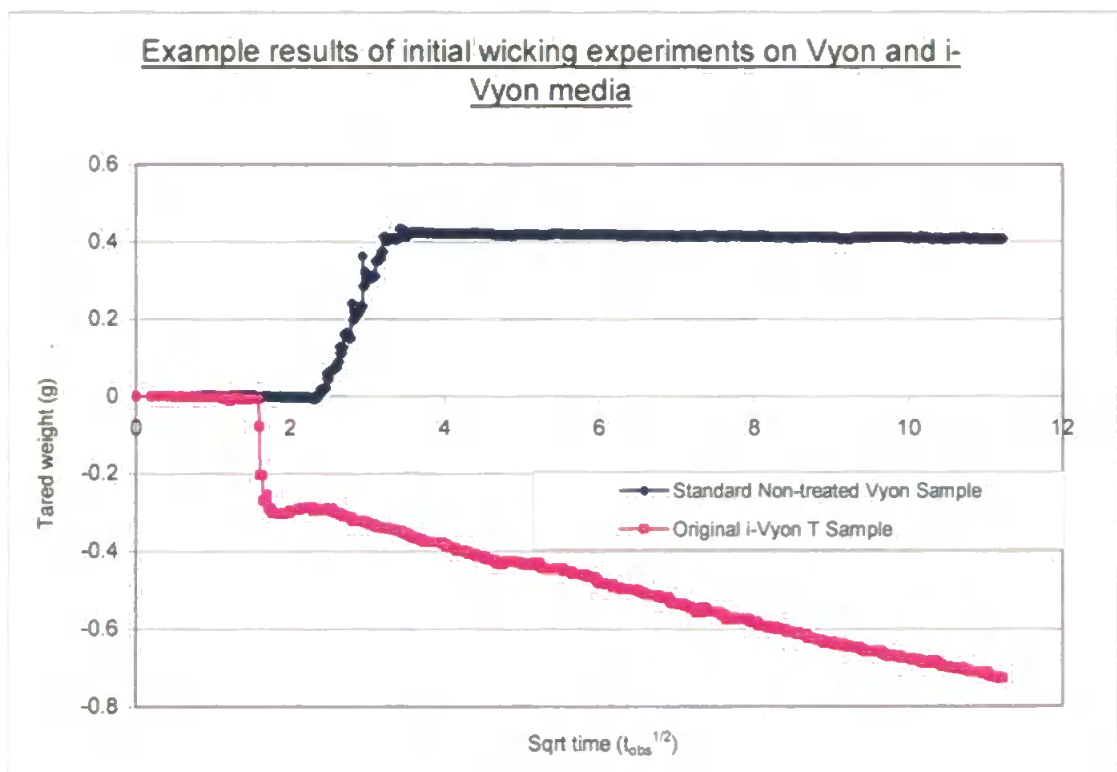


**Figure 6.3** Graphical representation of a non-wicking hydrophobic sample of standard non-treated Vyon® (blue) and a hydrophilicly treated i-Vyon® sample showing inconsistent wicking performance (pink), as shown by the un-smooth wetting curve.

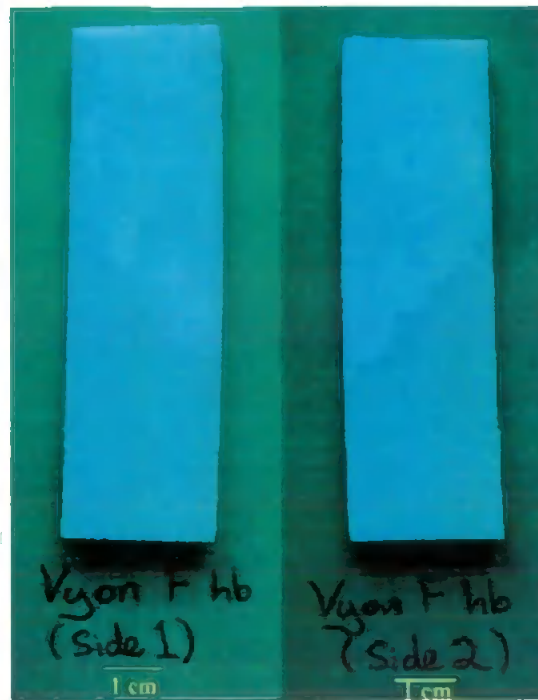


Figure 6.4 Photos of the patchy wicking performance of the hydrophilic treated i-Vyon® samples. All samples in the originally supplied sample set exhibited the same behaviour with large areas remaining hydrophobic in behaviour. The darker areas are those which have wicked wetting fluid effectively and the light patches those which are exhibiting varying degrees of hydrophobicity through the samples depth profile.

After drying of the inconsistently treated Vyon® samples (40 °C oven) it was noted that the initially observed areas of non-wetting were highlighted by brown tide marks (Figure 6.5). These tide mark features led to a concern over the actual feasibility of the plasma treatment and its suitability of the plasma treatment in the production of consistent and permanent wicking samples for biochemical uses. In response to this, Porvair Filtration undertook an investigation into the lack of consistency in the hydrophilic treatment process and the nature of the apparent tide marks upon drying. It was postulated that the apparent tide marks and inconsistencies in hydrophilicity were due to chemical instability of the plasma oxidised surfaces of the sample media. After decay of these surface layers, small amounts of free oxidised polymer are washed through the sample and group around the decay sites. On drying, these molecules turn brown, creating the appearance of tide marks around the patches of now hydrophobic

surface within the sample (*Pers. Comm*, Quinlan). The results of the investigatory process resulted in an optimisation of the plasma treatment process by controlling the plasma conditions described in Section 6.1.2. This led to a more stable and consistent hydrophilic treatment, and a second batch of samples for study under the previously detailed method (Section 6.2).

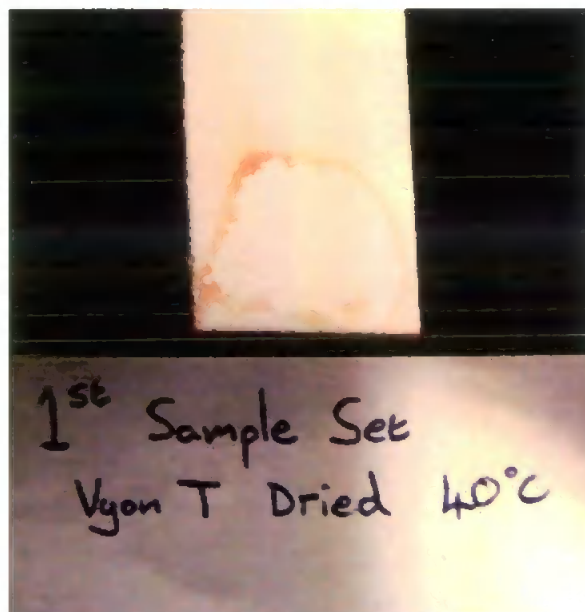


Figure 6.5 Photo showing an example of the brown tide marks that were apparent in the inconsistently treated i-Vygon® samples after oven drying at 40 °C. Marks such as this were apparent around all areas that were observed not to wick water in the initial tests.

### 6.3.2. Optimised second sample set

The testing of the second batch of samples offered a visually more consistent performance, with the exception of some i-Vygon® T samples which still exhibited some hydrophobic areas.

Figure 6.6 shows a set of example results, namely the fastest wetting with water and a typical wetting result with n-hexane for i-Vygon® T. The points ▲ and ■ show typical start and end points respectively of the section for each curve for which the gradient was

measured. The solution of Equation 6.4 corresponds to a taring of time and weight, and a straightening of the wetting curves between the linear-gradient start and end points when plotted against  $\sqrt{t}$  as in Figure 6.6.

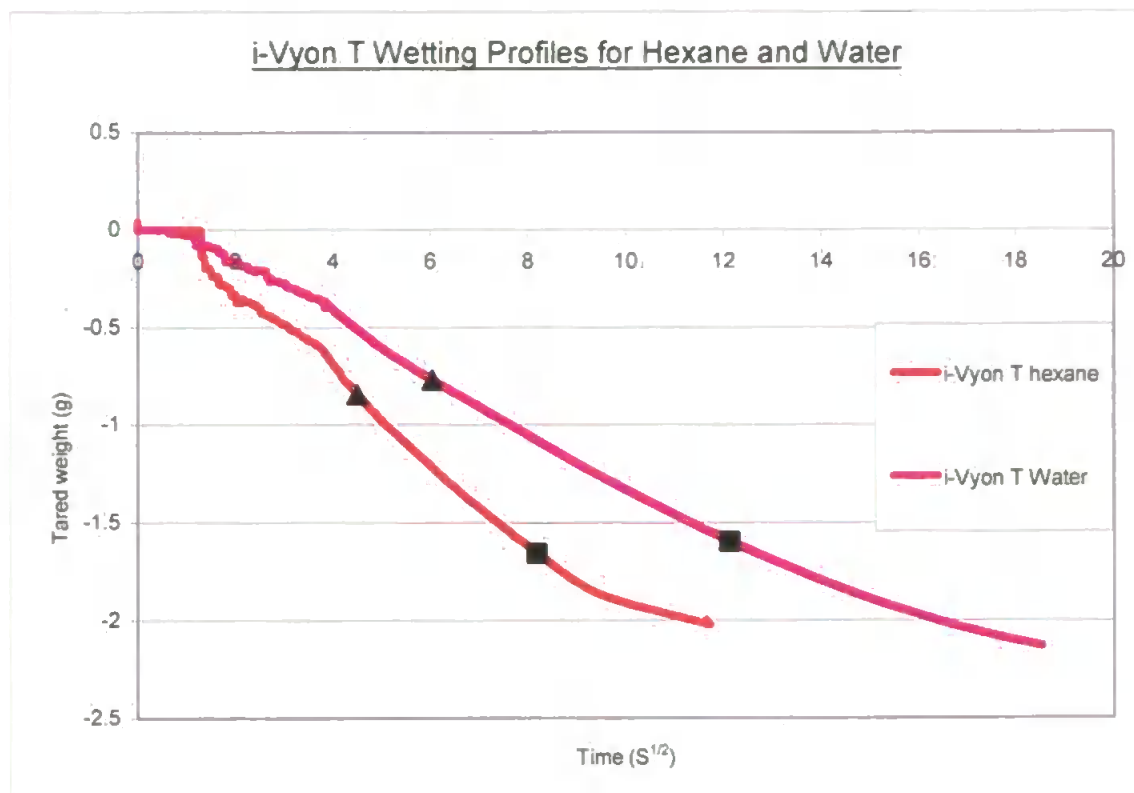


Figure 6.6 Graph depicting a typical wetting profile of the same media (i-Vyon® T) in both water and hexane wetting liquids. Symbols ▲ and ■ represent the start and finish points used in each curve for the calculation of the linear relationship between fluid wicking and the square root of time determined from the solution to Equation 6.4 for  $\beta \Rightarrow 0.5$ .

Apart from the taring, the results are as captured from the balance, and show the initial weight oscillations. Due to the measurement being recorded as the loss of fluid from the reservoir, results appear as an apparent weight loss of the sample liquid as it is wicked up into the sample media. Start and end points for the measured gradient were chosen to select the portion of the representative sample curves between the initial oscillations and the final tail off as the samples approached full saturation or the wetting

front reached a height at which drag due to the increasing hydrostatic head became significant. This selection system was used against all sample curves produced.

Figures 6.7 and 6.8 show comparison results for all grades tested in both water and hexane respectively. The steepness of slope observed in these graphs gives some indication of the speed of the wicking events, with a steeper slope corresponding to faster wicking. It must be noted however that the results shown here are comparisons between individual samples and are not full replicate sets of results for all analyses.

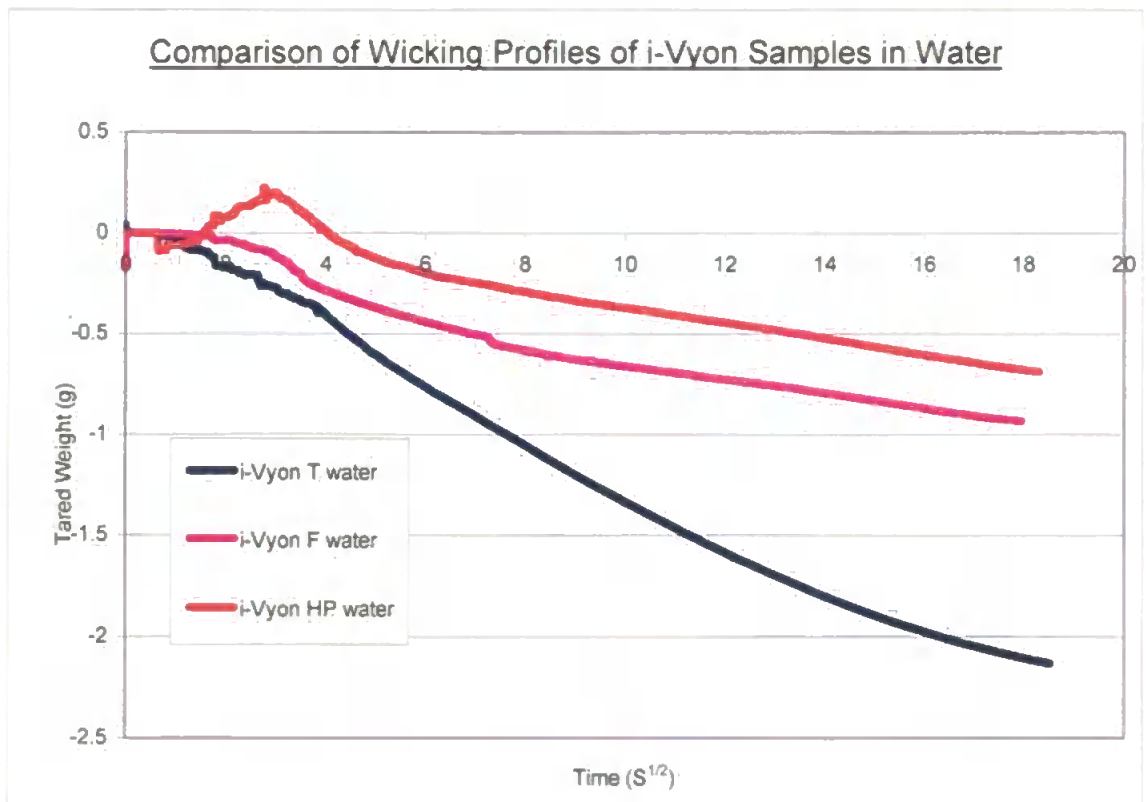


Figure 6.7 Examples of wetting curves for each sample using water as the wetting liquid.

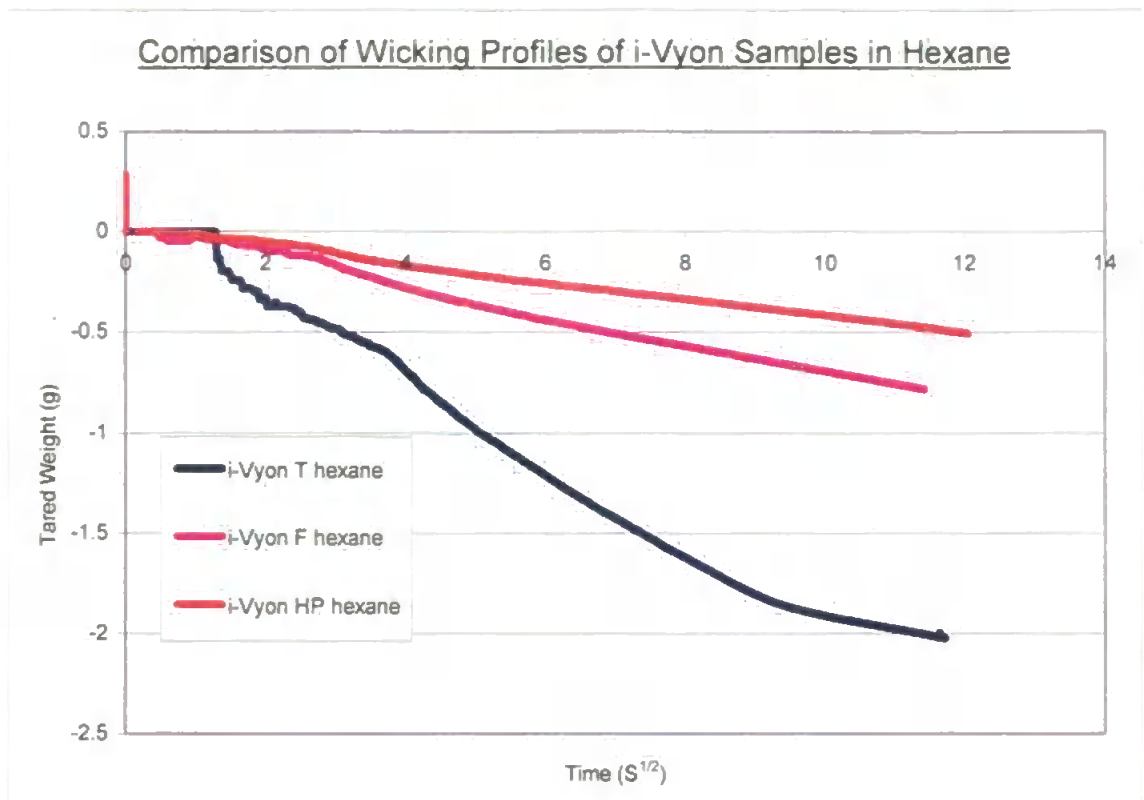


Figure 6.8 Examples of wetting curves for each sample using hexane as the wetting liquid.

The solution of Equation 6.4 gives the product of the lumped constants  $c$  and  $K$  as a value of  $\ln cK$  for both hexane and water. These values are plotted in

Figure 6.9 against the respective grades, which increase in respective pore size in the order of Vyon® T → Vyon® F → Vyon® HP. As expressed by Equation 6.2 the  $cK$  term is composed of the geometric parameter  $c$ , which is representative of the media pore size distribution and  $K$ , which depends on the wetting fluid characteristics. As each sample is run in the same wetting fluids the differences in the returned  $\ln cK$  values are only dependent upon differences in the geometric nature of each sample. Results are shown (Figures 6.9 and 6.10), for hexane and water respectively, as mean  $\ln cK$  values returned from three replicates, with  $\pm 1$  standard deviation to show the degree of variance within media grades tested. In Figures 6.9 and 6.10 trend lines have been applied to indicate the general trend direction of the displayed data, for visualisation purposes only.

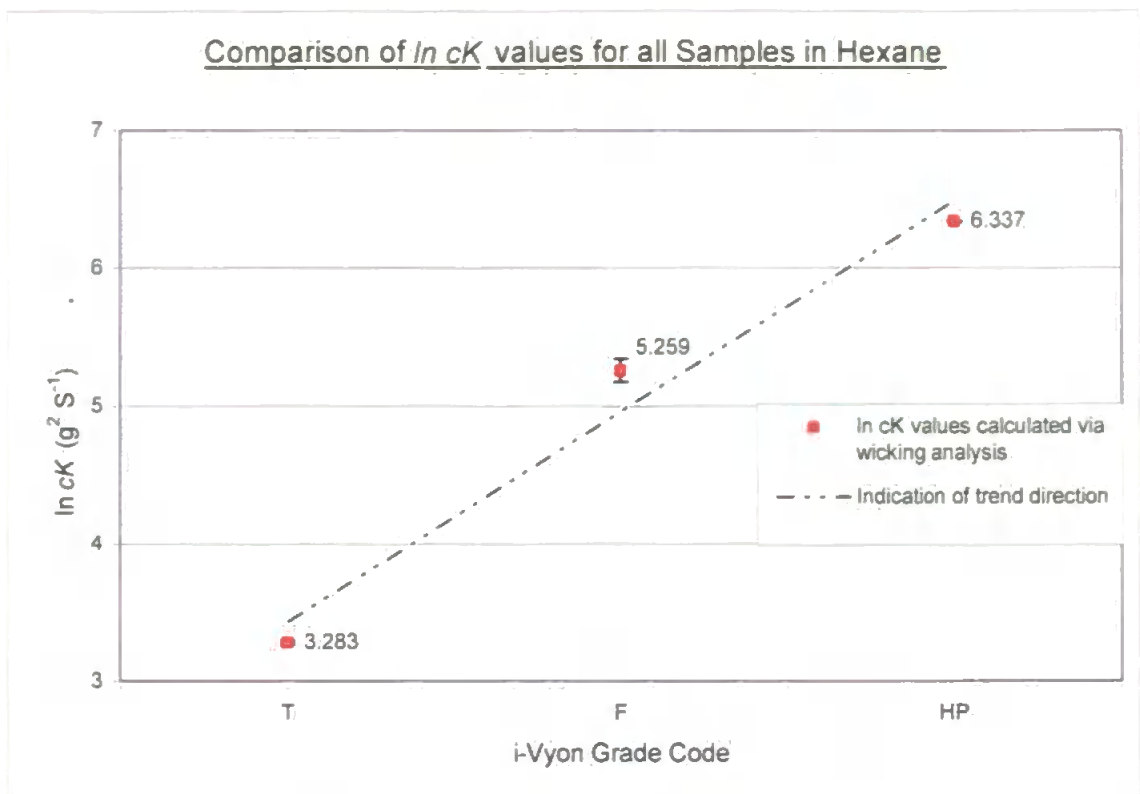


Figure 6.9  $\ln cK$  values for all tested grades in hexane. Results show the mean of three replicates and  $\pm 1$  standard deviation to show the degree of variance.

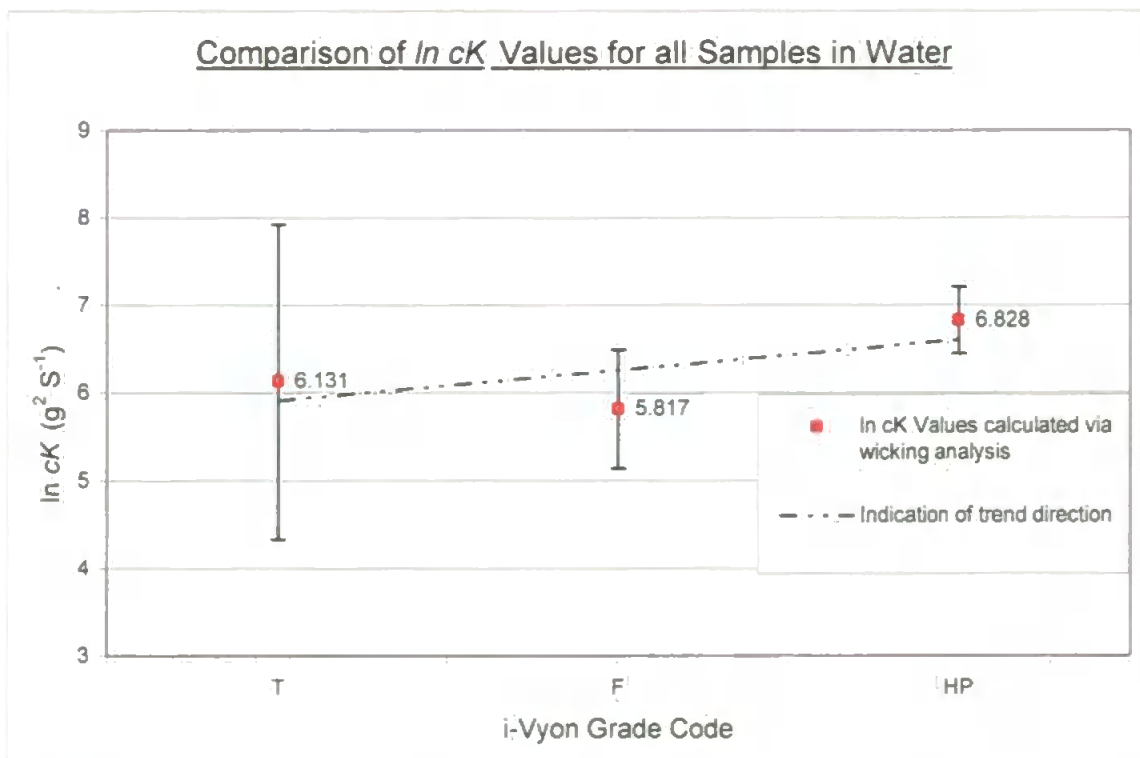


Figure 6.10  $\ln cK$  values for all tested grades in water. Results show the mean of three replicates and  $\pm 1$  standard deviation to show the degree of variance.

It is seen in



Figure 6.9 that wicking events in hexane show a high repeatability, as represented by the low values of standard deviation around the mean value for Vyon® T, Vyon® F and Vyon® HP (Table 6.1). In contrast to this, Figure 6.10 shows that in water the variance between replicates is higher and reduces through the grades Vyon® T, Vyon® F and Vyon® HP respectively (Table 6.1). This indicates that the wicking of water in Vyon® is less repeatable than for hexane, and also is less repeatable in media with smaller pore sizes.

**Table 6.1 Summary of experimental data from wicking experiments undertaken in both water and hexane wetting fluids. Results expressed as a mean  $\ln Ck$  value from three replicates of each experimental set.**

<b>Experimental Set</b>	<b>Wetting Fluid</b>	<b>Vyon® Grade</b>	<b>Mean Value <math>\ln Ck</math> (<math>g^2 S^{-1}</math>)</b>	<b>Standard Deviation (<math>g^2 S^{-1} \times 10^{-2}</math>)</b>
Vyon T <sub>hex</sub>	Hexane	T	3.283	1.4
Vyon F <sub>hex</sub>	Hexane	F	5.259	8.6
Vyon HP <sub>hex</sub>	Hexane	HP	6.337	0.46
Vyon T <sub>w</sub>	Water	T	6.131	179.6
Vyon F <sub>w</sub>	Water	F	5.817	67.55
Vyon HP <sub>w</sub>	Water	HP	6.828	37.97

During the experiments it was noted that the third sample of Vyon® T media to be tested showed a much more consistent wicking performance compared to the previous two “patchy” equivalents, and the lowest value of  $cK$ , namely 4.106. On drying, all samples appeared free of the previously observed brown tide marks found in the original sample sets.

The apparent values of  $\cos \theta$  for water were calculated with Equation 6.5 from the mean  $\ln cK$  values. Results of  $\theta$  could then be expressed, using an inverse  $\text{Cos}$  function, for each of the representative grades. Results are shown in Figure 6.11. It was not possible to obtain a value of  $\theta$  using the mean value of  $\ln cK$ , as the value of  $\cos \theta$  returned by Equation 6.8 was outside its possible mathematical range. The result for Vyon® T is consequently expressed using the value for the 3<sup>rd</sup> replicate of the experimental samples only, as it was felt that this offered a more acceptable value representative of how the media would behave with consistent plasma oxidation.

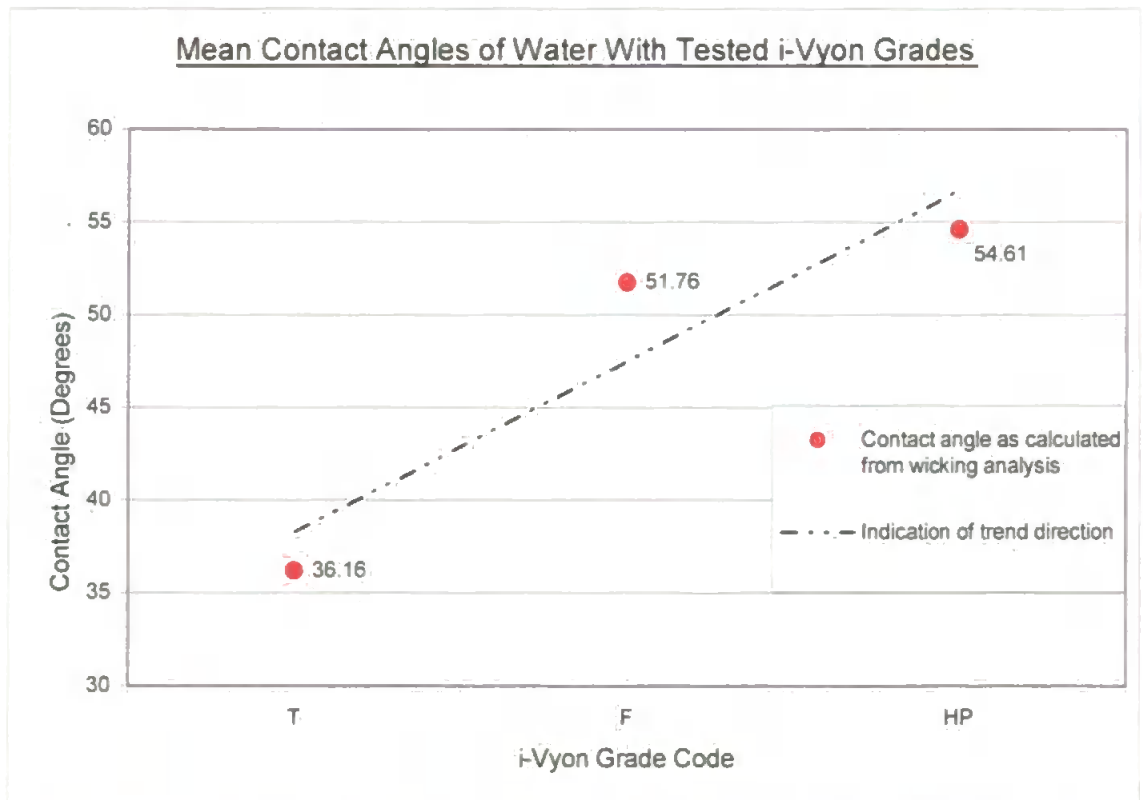


Figure 6.11 Calculated apparent contact angles of water with the tested grades of Vyon® media used in the current wicking analysis.

A general trend line has been applied to the data in Figure 6.11 . As pore size increases through the media grades Vyon® T → Vyon® F → Vyon® HP so too does the apparent contact angle. An increase in apparent contact angle equates to a reduced wicking performance controlled by either changes in wetting liquid or pore geometries within the media. An angle of  $>90^\circ$  would indicate a non-wetting liquid/media relationship and suggest no wicking phenomena. As the results for all tested Vyon® media are calculated using the same wetting liquids, differences in the apparent contact angles must in fact arise from differences in the structural geometries of the pore networks.

In the calculation of contact angles for the respective media (Figure 6.11) the unknown terms in Equation 6.2 are eliminated in Equation 6.5. However, it can sometimes be instructive to investigate how well estimates of various terms in Equation 6.2 may be replicated by using the experimental data to retro-analyse parameter values. Knowing the cross sectional area of the media in contact with the wetting fluid, its porosity, fluid characteristics and the calculated experimental contact angles (Figure 6.11) it is possible to extract information regarding the  $r_h$ , or effective hydraulic radius (EHR) term. The resulting calculated values for the experimental data from these experiments are shown in Figure 6.12. It is suggested (Matthews et al. 2008) that this term has previously been ill defined, although in that study and other work (Petersen et al., 1996) it has shown some accordance to the results. In the present case, the values are several orders of magnitude higher than the known sizes of the pores, and therefore this highly speculative and impressionist parameter is shown to be inappropriate for the wicking of Vyon samples.

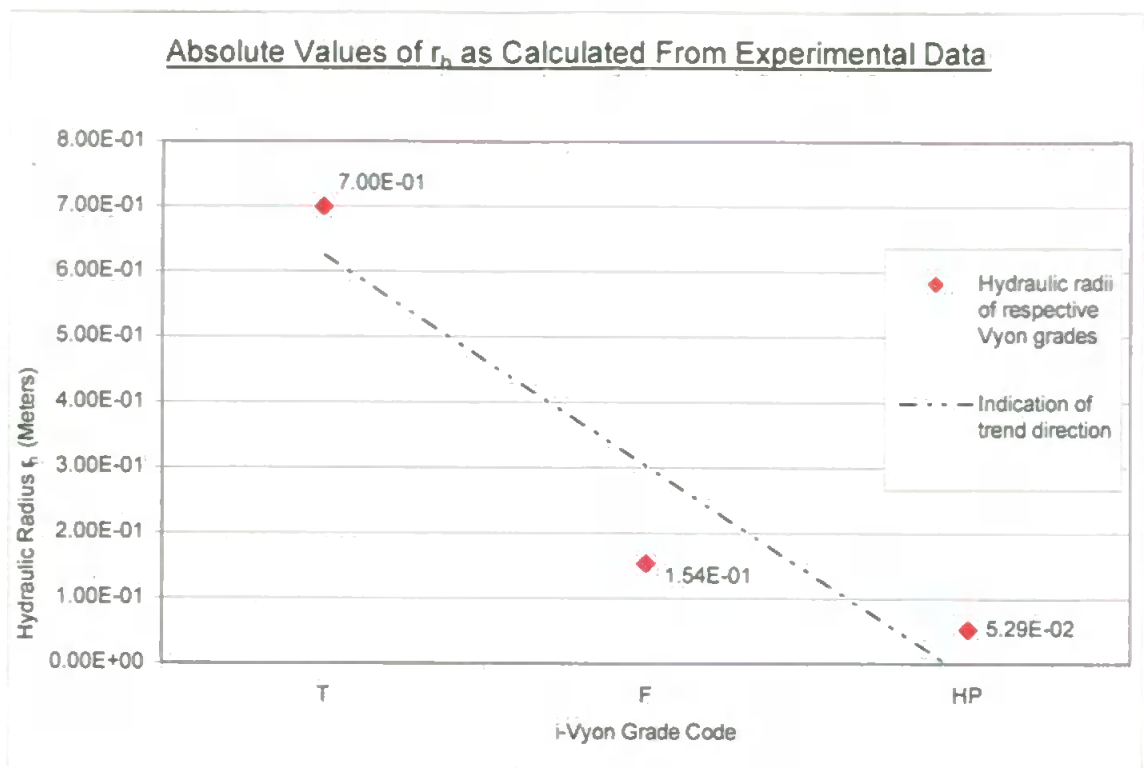


Figure 6.12 Calculated values of  $r_h$  for tested Vyong® sample grades.

#### 6.4. Discussion of wicking properties of Vyong® media

Estimated values of  $\ln cK$  increased with increasing pore size in both hexane and water experiments (Figures 6.9 & 6.10), with the exception of the mean value for Vyong® T in water. This discrepancy in the results is attributed to the known inconsistency in the plasma oxidation of the polymer surface. This trend indicates that as pore-size increases there is a reduction in the wicking rate of the respective media. This is consistent with literature and is also highlighted by the increasing apparent contact angles with the respective increasing pore size (Section 6.3.2).

The study shows the wicking of hexane to follow the same general trend as that with water. However it is apparent from the degree of variance encountered in each set of experiments (Figures 6.9 & 6.10) that the experiments using water as the wetting liquid

show a decreasing level of repeatability with decreasing pore size. This phenomena offers two points of discussion: firstly, that there is a danger in making inferences regarding fluid transport and structural geometry within porous media solely from the wicking of non-polar solvents such as hexane and secondly, that the trend of increasing variance in the experimental repeatability with decreasing pore size must be in some way related to the homogeneity of the oxidation and consequent hydrophilicity of pore surfaces within replicates of the same media grade.

The danger of making inferences from the wicking of non-polar liquids alone is that they give no indication of the liquid/media interaction of polar fluids such as water. This concern was also highlighted in the previous collaborative research (Matthews et al., 2008): similar studies in the wicking of soil structures (Hallet et al., 2001) proposed that ethanol sorptivity can provide a useful estimate of fluid transport properties within porous media although it is felt that this also fails to provide a full picture of the true wicking performance associated with other polar liquids. It is therefore suggested that wicking experiments conducted on porous media are undertaken with fluids that are directly relevant to a particular application. These experiments, when compared to a non polar solvent such as hexane, will then allow reliable inferences to be made with regard to that particular application.

It has been shown that a trend exists in the wicking data, using water as the wetting fluid, whereby the variance in the experimental repeatability increases with respect to a decrease in pore size. As the experimental runs in hexane have shown the method itself to be highly repeatable as indicated by the low variance between replicates in these data (Figure 6.9), then the increased variance exhibited by the wicking of water can be attributed to an inconsistency or inhomogeneity within the plasma oxidation of the

polymeric surface layers. As this variance increases with respect to the reducing pore sizes, it appears that smaller pores cause the penetration of the plasma into the media to be less consistent.

This observation opens up the future possibility of using the experimental method to deduce the optimum plasma conditions to ensure full surface layer oxidation at each specific pore size. In this study, the variance  $\sum_{i=1}^N \text{Var}(h_i)$  (equation 6.7) was reduced from the first to the second batch of samples. Qualitatively, in this study the reduction in variance was from an unuseable to useable amount. For future research studies and in industrial production, the variance could be quantified, and its change from one sample batch to another could be monitored to allow quality control and optimisation of the surface modification procedures.

## 7. Compressibility and porosity loss in Sinterflo® media

### 7.1. Introduction to the investigation

#### 7.1.1. Bulk Modulus and the apparent anomaly within Sinterflo Samples

While undertaking the modelling of the Sinterflo® samples, the initial mercury porosimetry curves were corrected for sample, mercury and penetrometer compression by way of the Pore-Comp software module (Sections 1.3.5.3 and 3.1). From undertaking these compressibility corrections and using the modelled bulk modulus values for the individual samples, an interesting discovery was made with regard to the sintered stainless steel media. Bulk modulus  $M_{ss}$ , is a representation of a samples solid phase compressibility  $\Psi_{ss}$ , which, in experimental terms, may be defined as,

$$M_{ss} = \frac{1}{\Psi_{ss}} = \frac{dP}{\frac{-dV_{ss}}{V_{ss}}} \quad \text{Equation 7.1}$$

here  $P$  is the applied pressure through the mercury porosimeter and  $V_{ss}$  the dynamic volume of the samples solid phase throughout the experiment.

It may therefore be seen with regard to Equation 7.1 that an observed high value of sample compressibility consequently leads to a low value of bulk modulus. A bulk modulus for stainless steel should be in the region of 140 G Pa (Gray, 1972) whereas the modelled values for the tested Sinterflo® sample plugs ranged between 38 – 50 G Pa as shown in Table 7.1. In the case of the stainless steel Sinterflo® samples it was noted that the model calculated bulk modulus was a lot less than expected, this representing a higher than expected compressibility. This discovery led to two possible hypotheses: Firstly, the software is miscalculating bulk modulus due to some

experimental error or secondly the manufacturing parameters of the sinters may have caused some reason for the material to exhibit a bulk modulus less than expected for a skeletal structure derived from stainless steel.

**Table 7.1 Modelled values of bulk modulus as found by Pore-Comp software in initial porosimetry experiments associated with this research.**

<b>GRADE</b>	<b>Porosimeter Run Reference (porosimeter data file)</b>	<b>Modelled Value of Bulk Modulus (GPa)</b>
S21	000-201	50
S36	000-204	38
S41	000-203	49

It was decided to test these hypotheses. Samples of the un-sintered stainless steel base powder would be sourced from Povair Filtration, and analysed under the same porosimetry conditions to compare values of bulk modulus. As base powder is the precursor particles of solid stainless steel used to form the sample sinters; a low value of bulk modulus would indicate a calculation problem in the software whereas an expected bulk modulus of around 140 G Pa indicates that the sintering process used on the sample plugs, which return lower bulk moduli, has led to some material change which manifests as increased compressibility of the final product.

After mercury porosimetry and Pore-Comp analysis of the un-sintered powder data, it was found that a mean bulk modulus of 135 G Pa was returned for two replicates. This result led to the conclusion that the lower than expected bulk modulus observed for the sintered filter plugs was indeed an artefact of manufacturing parameters and not due to experimental error in porosimetry and associated analysis of bulk modulus. From the



basis of this result it was decided that the possible reasons for reduced bulk modulus (increased compressibility) exhibited by the sintered media should be investigated.

### **7.1.2. Manufacturing procedure and its proposed relation with closed pores**

When the sintered filters are produced, the ideal situation is found where individual particles undergo point sintering. Point sintering is achieved where a compacted base powder is heated and achieves a level where sufficient atomic motion leads to the growth of weld bonds between contacting particles. If higher temperatures or longer oven times are used more cumulative atomic motion occurs and weld bonds can be found to increase. Sometimes, in excessive cases, this leads to densification of the sinter to near solid phase density (German, 1998). In the manufacturing of the filter media associated with this research, the ideal situation is found where each contact point of a powder particle becomes physically welded to the adjoining particle under high temperature but short duration conditions, so that minimal densification is found ((A) in Figure 7.1). It is possible, with regard to the sinters associated with this study, that when the sintering of the material is undertaken, the ideal point sintering is lost due either to excess temperature or too long a sinter time. With this in mind the possibility arises that in some instances particles may completely melt together resulting in trapped gas bubbles or void space in the solid phase structure ((B) in Figure 7.1). These closed areas are termed “closed pores”, as in they offer no connectivity and hence are inaccessible to mercury intrusion (Section 1.3.1). This presence of closed pore space in the material could substantially reduce the apparent bulk density of the solid phase due to their non-accessible nature and, the higher compressibility of gas over stainless steel. Also, from a more commercial point of view, closed pore volume gives rise to a loss of active flow volume in the media and subsequent lowering of an individual filter’s dirt

holding capacity. The possibility of these closed pore formations arising is given more substance when initially considering the manufacturing process.

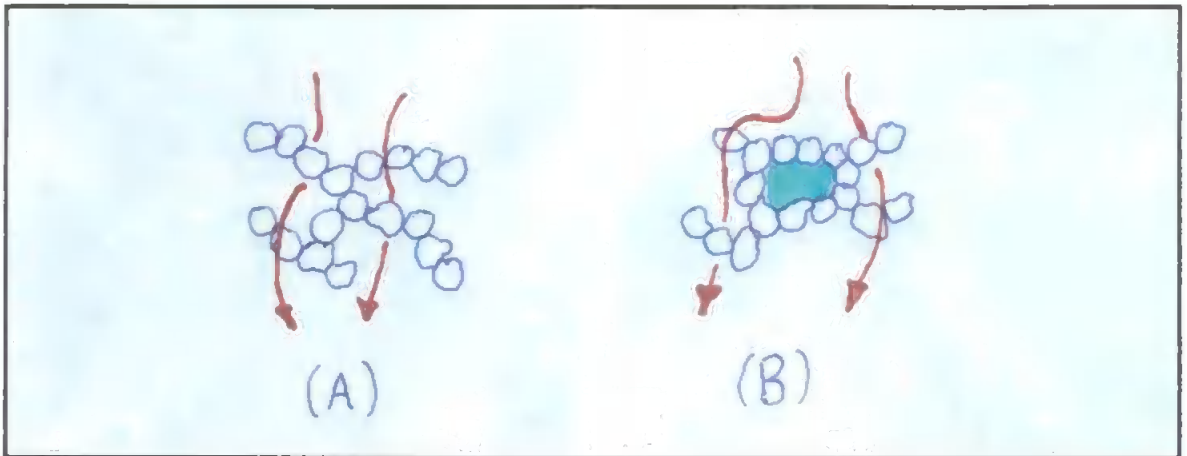


**Figure 7.1** 2-dimensional representation of (A) an ideal sinter where sintering has left flow paths (represented by red arrows) between the sintered particles and (B) where the sintering process has induced particles to melt together to form a closed pore space (represented by green shaded area) inaccessible to intruding mercury and where flow can not enter during filtration.

Initially the stainless steel powder is placed into moulds and then compressed to form what is termed a 'green form' which has a given nominal density, indicating the grammage of raw material per cubic centimetre ( $\text{g cm}^{-3}$ ). This green form compression considerably increases the packing efficiency and also the contact area between the structural particles relative to a loose powder form. It is believed that the application of pressure to create a green form state is also highly relevant to the possibility of closed pores occurring within the final sintered media.

The green form of the filter is then subjected to a high temperature oven for a short time, ideally to point sinter the particles together and give the final sinter its mechanical strength, optimum working void structure and final form (Figure 7.2). Correct temperature and oven duration are critical factors in alleviating densification and minimising the closed pore problem. Considering this and the improved packing efficiency exhibited by the green form stage of the process, it is apparent that the

construction of the sample plugs in this way may be susceptible to the development of non accessible voids within the solid phase of the structure if oven conditions are used that deviate from the optimum.



**Figure 7.2** Examples of sintered stainless steel media in various moulded configurations.

Another possibility of the increased compression can also be found in the manufacturing technique associated with the production of stainless steel particle that is used as the 316L base powder for production of the sinters. The base powder is formed through an atomization of molten stainless steel by water cooling. If this fast cooling process causes gaseous expansion within the atomization process, it is possible for these evolving gas pockets to form particles of stainless steel with incorporated non accessible voids even before they are used to form the filter media. Although not noted previously in the 316L base powders, this phenomenon has been recorded in similar bronze base powders used for producing filter media (*Pers. Comm.* Richard Morgan). In the case of this research however, the initial results from the compressibility analysis of the 316L base powder would dismiss this suggestion.

Based on the considerations highlighted in Sections 7.1.1 – 7.1.2, a study was developed to investigate whether the observed compressibility anomalies are indeed representative of a closed pore formation and associated porosity loss or whether they are due to some other manufacturing or structural phenomena. As such the objectives of this chapter are to:

- (i) Describe the investigation and the systematic processes used to investigate whether changes in observed compressibility are due to closed pore formation in the sintering process of Sinterflo® samples,
- (ii) Deduce whether there is a proportional relationship between green form pressure, a resulting degree of compressibility and proportional loss of active pore volume,
- (iii) Discuss the scientific and industrial significance of the experimental results to the use of Sinterflo as a filtration media.

## **7.2. Method of Investigation**

A series of samples were provided by Porvair Filtration. Each sample was produced from the same 316L stainless steel base powder, density =  $7.95 \text{ g cm}^{-3}$ , to produce a series of S36 grade derivative stainless steel filter plugs based on the diameter previously used in Chapter 2 (Figure 2.11) and only changing in sample thickness due to the differing forming pressure applied. Samples in the series differed only with regard to their initial green form compression density and were provided in nominal densities of 4.2, 4.75, 5.1, 5.4, 5.7 and  $5.9 \text{ g cm}^{-3}$ . Controlling the green form density in

this way provided a series of filter plugs that change in porosity with an inversely proportional solid phase volume fraction. This series allowed an analysis of how green form density affects lost pore volume and the apparent compressibility of the Sinterflo® material post sintering. Highest porosity was expected at a nominal density of  $4.2 \text{ g cm}^{-3}$  and lowest porosity at  $5.9 \text{ g cm}^{-3}$ . All samples were sintered in the same oven under equivalent time and temperature conditions so that the only factor changing was the applied pressure at the green form manufacturing stage and corresponding change in nominal density.

Sample plugs were subsequently analysed using a number of experimental techniques. Firstly, expected sample porosity (active flow volume) was calculated with regard to solid phase material density and the nominal manufactured (green form) density. True sample porosities were then measured firstly by a standard method which entailed measuring the dimensions and the weighing of each sample plug to calculate a weight/volume value which is divisible by an equivalent solid material weight/volume value. Secondly they were measured with an ISO 2738 Determination of density, oil content and open porosity test (BS EN ISO 2738:1999).

Sample plugs were also subjected to mercury porosimetry (Micromeritics Autopore III, Micromeritics, Atlanta) to obtain raw experimental intrusion/extrusion curves for each of the provided sample nominal densities. These raw curves were then corrected for compression with the Pore-Comp software module (Section 1.3.5.3) to measure bulk moduli. These porosimetry measurements also gave a third means of testing the initial “expected sample porosity”, by comparing porosities derived from them with those derived from the other porosity measurements. To remove internal heating effects on mercury porosimetry experiments under high pressure, the experimental pressure table

used by the porosimeter was adjusted to allow a 60 second equilibration and cooling time between each collected sample point.

### 7.3. Results

Using nominal densities and raw material densities, expected porosities may be calculated using the following simple equation:

$$\text{Expected porosity (\%)} = 1 - \frac{\text{Nominal density of green form}}{\text{Raw material density}} \times 100$$

Equation 7.2

The solid phase density of the raw material (316L stainless steel base powder) is known to be 7.95 g cm<sup>-3</sup>. Results are shown in Table 7.2 and also represented graphically to show reducing porosity with increasing green form density (Figure 7.3).

**Table 7.2** Tabulated results for the expected porosity (%) exhibited by differing nominal densities of green form sinters for comparison point of further investigations.

Nominal Green Form Density (g cm <sup>-3</sup> )	Raw Material	Raw Material Density (g cm <sup>-3</sup> )	Expected Porosity of Sinter (%)
4.2	316L Base Powder	7.95	47.2
4.7	316L Base Powder	7.95	40.9
5.1	316L Base Powder	7.95	35.9
5.4	316L Base Powder	7.95	32.1
5.7	316L Base Powder	7.95	28.3
5.9	316L Base Powder	7.95	25.8

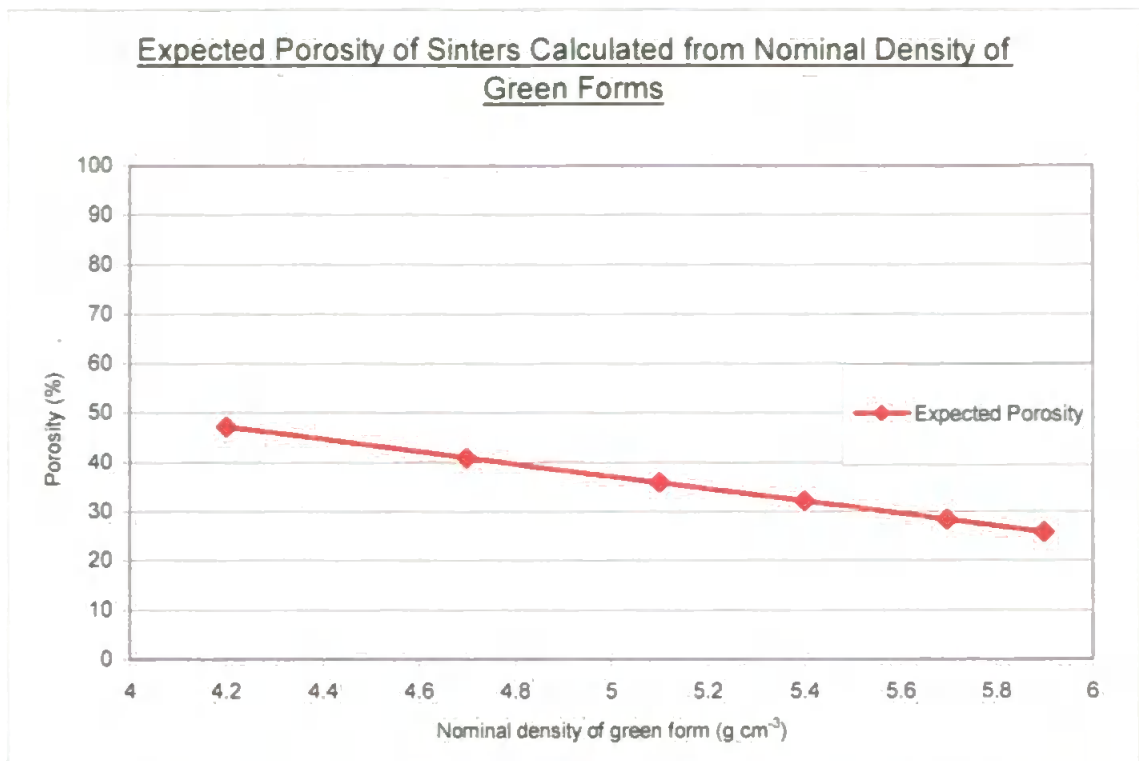


**Figure 7.3** Graphical representation of expected porosity in relation to nominal green form density that should exist in provided sintered samples. Note the expected decreasing porosity with increasing green form density.

Porosities were measured using the methods described previously, and are shown in Table 7. 3. The results, together with those shown in Table 7.2 and Figure 7.3, are compared in Figure 7.4:

**Table 7. 3 Table of measurements and results for both the standard weigh and measure porosity analysis and also the ISO 2738 open porosity analysis. The table shows results for all samples produced for this study.**

		Weigh and Measure Method						ISO 2738 Determination of Density and Open Porosity				
Nominal Density (g cm <sup>-3</sup> )	ID	Weight (g)	Diameter (mm)	Thickness (mm)	Density (g cm <sup>-3</sup> )	Porosity (%)	Porosity (cm <sup>3</sup> )	Coated Weight in Air (g)	Coated Weight in Water (g)	Density (g cm <sup>-3</sup> )	Porosity (%)	Porosity (cm <sup>3</sup> )
4.2	8	4.2138	14.24	6.282	4.212	47	0.470	4.4738	3.4824	4.25	47	0.466
	6	4.0820	14.23	6.081	4.221	47	0.454	4.3920	3.4225	4.21	47	0.455
	9	4.1783	14.22	6.227	4.225	47	0.463	4.4583	3.4635	4.20	47	0.466
	10	4.0888	14.24	6.065	4.233	47	0.452	4.4188	3.4499	4.22	47	0.453
	16	3.9662	14.23	5.890	4.234	47	0.438	4.2162	3.2697	4.19	47	0.443
4.7	5	3.8414	14.23	5.089	4.746	40	0.326	4.2014	3.3927	4.75	40	0.326
	18	4.0160	14.23	5.318	4.748	40	0.341	4.3260	3.4859	4.78	40	0.337
	24	3.8579	14.23	5.098	4.758	40	0.326	4.1479	3.3306	4.72	41	0.329
	17	3.9049	14.23	5.159	4.759	40	0.329	4.2049	3.3759	4.71	41	0.334
	21	4.0055	14.23	5.286	4.765	40	0.337	4.2655	3.4223	4.75	40	0.338
5.1	19	4.0416	14.23	4.948	5.136	35	0.279	4.3716	3.5823	5.12	36	0.280
	20	4.0523	14.23	4.958	5.139	35	0.279	4.2523	3.4670	5.16	35	0.277
	4	3.7953	14.23	4.643	5.140	35	0.261	4.0553	3.3112	5.10	36	0.265
	11	3.9997	14.23	4.889	5.144	35	0.274	4.2597	3.4891	5.19	35	0.270
	25	3.7573	14.23	4.577	5.162	35	0.255	3.9973	3.2621	5.11	36	0.260
5.4	7	3.8979	14.24	4.489	5.452	31	0.225	4.1879	3.4661	5.40	32	0.229
	13	4.0087	14.23	4.619	5.457	31	0.230	4.3487	3.6150	5.46	31	0.230
	23	4.1090	14.23	4.734	5.458	31	0.236	4.4490	3.6992	5.48	31	0.234
	3	3.8490	14.23	4.424	5.471	31	0.219	4.1090	3.4054	5.47	31	0.219
	12	4.0241	14.23	4.625	5.471	31	0.229	4.3041	3.5631	5.43	32	0.233
	1	3.9232	14.23	4.508	5.472	31	0.223	4.1932	3.4799	5.50	31	0.221
5.7	2	3.9945	14.23	4.438	5.659	29	0.203	4.3045	3.6025	5.69	28	0.201
	22	3.9428	14.23	4.377	5.664	29	0.200	4.2028	3.5000	5.61	29	0.205
	27	3.9512	14.23	4.385	5.666	29	0.200	4.2412	3.5394	5.63	29	0.204
	15	4.0180	14.23	4.450	5.677	29	0.202	4.2380	3.5294	5.67	29	0.203
5.9	26	3.9176	14.23	4.222	5.834	27	0.179	4.1476	3.4836	5.90	26	0.173
	30	3.9778	14.23	4.285	5.837	27	0.181	4.2378	3.5590	5.86	26	0.179
	14	3.9234	14.23	4.221	5.845	26	0.178	4.1934	3.5216	5.84	27	0.178
	28	3.9276	14.23	4.223	5.848	26	0.178	4.2076	3.5316	5.81	27	0.181
	29	4.0010	14.23	4.299	5.852	26	0.180	4.2310	3.5412	5.80	27	0.185



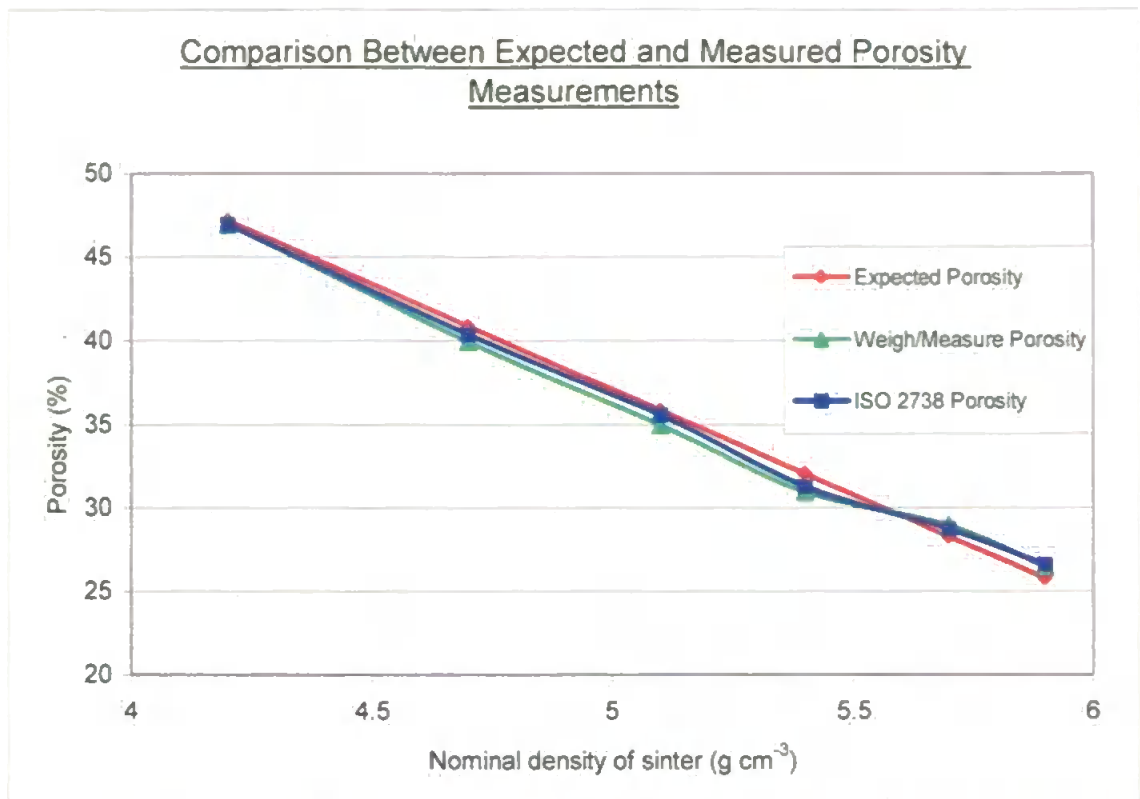


Figure 7.4 Comparison of expected porosity with true measured porosity by way of the weigh/measure technique and the ISO 2738 open porosity method.

It can be seen that the porosities of the samples are not found to differ significantly from their expected values as calculated from the initial green form densities. The small discrepancies differ in direction above and below  $5.5 \text{ g cm}^{-3}$ . However it is possible that concealed porosity could be hidden from all three of these methods of porosity determination.

Therefore to determine and quantify the presence of closed pore occurrence within the samples, mercury intrusion porosimetry was undertaken. As mercury intrusion can only penetrate interconnected pore space, so any reduction in the returned porosity value obtained by this method would indicate a presence of un-connected or closed pore space within the sample.

Porosimetry results are shown here as raw intrusion curves (Figure 7.5) uncorrected for compression effects which are exhibited as gradual pseudo intrusion effects in the high pressure extremities of the analysis. Due to the logarithmic representation of porosimetry data making the observation of these small pseudo intrusion effects difficult, the last few data points taken from an analysis of a nominal density =  $5.9 \text{ g cm}^{-3}$  sample plug are shown in Figure 7.6 as a screen shot representation of high pressure analysis data in the Pore-Comp correction stage, so the effect may be visualised.

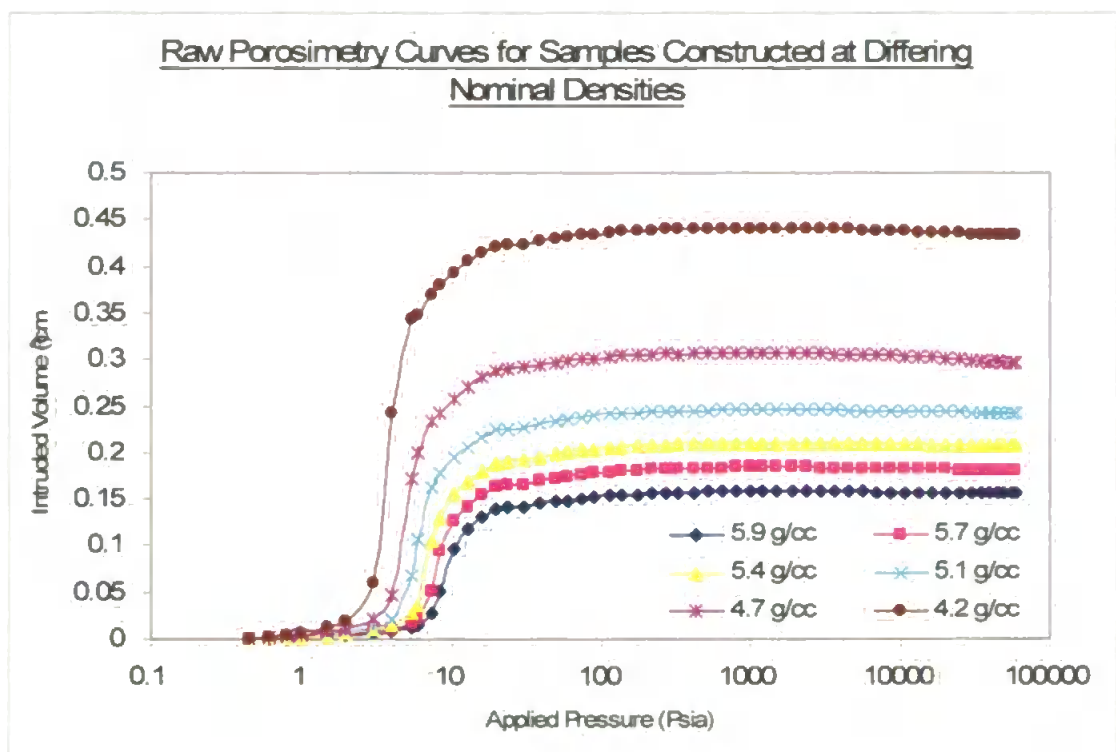


Figure 7.5 Raw porosimetry curves for all nominal densities of sample sinters tested in the compression study. Nominal densities are highlighted in the legend as grams per cubic centimetre (g/cc) and cover the analysed sample range.

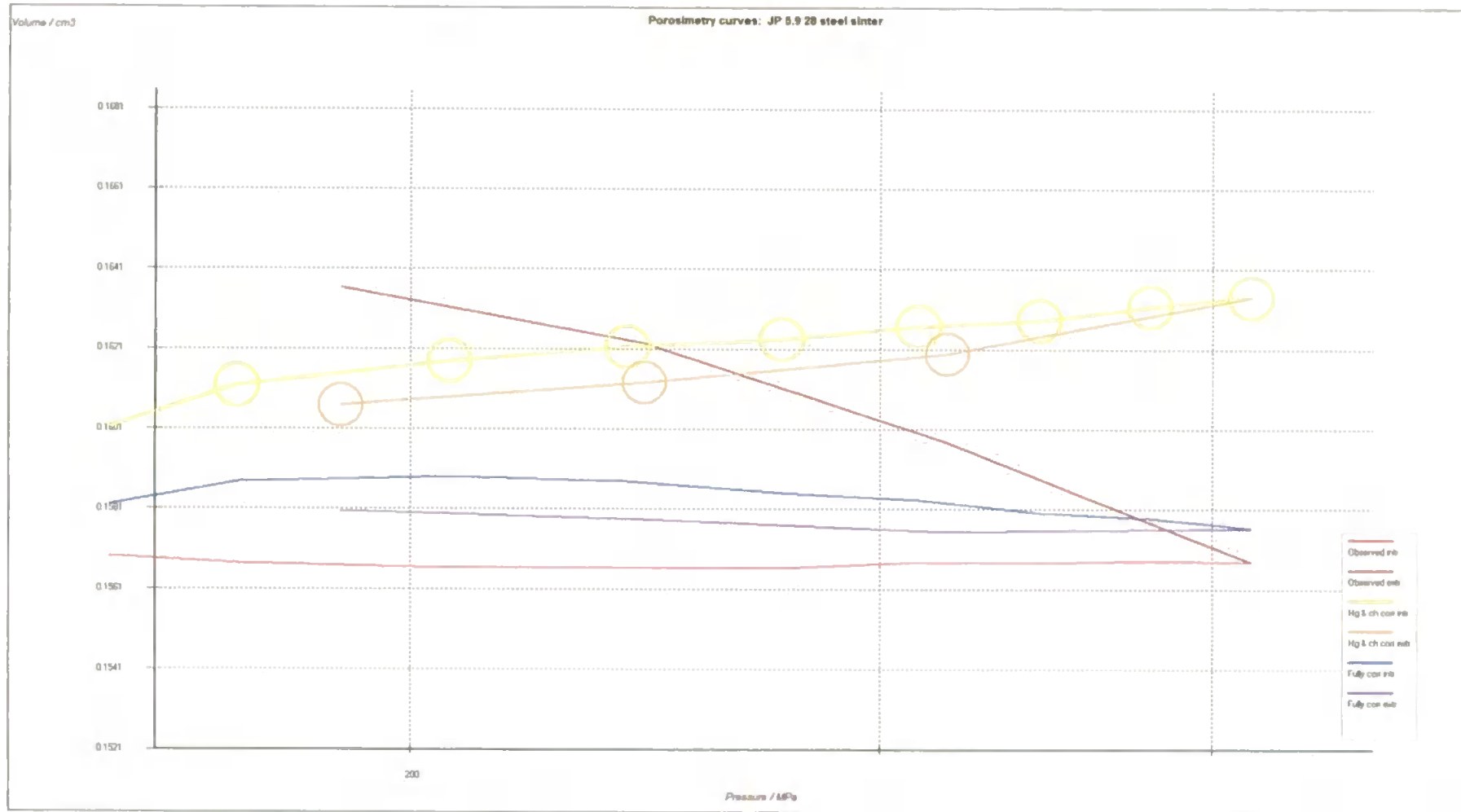


Figure 7.6 Screen shot of the Pore-Comp compression correction on high pressure data points in analysis of a nominal density =  $5.9 \text{ g cm}^{-3}$  sample plug. This shows the presence of the pseudo intrusion effects that are used in the calculation of sample bulk modulus. They are represented by the rising values of the intrusion and extrusion data points (those represented by the circled series). The lower un-circled data series are those that are corrected for mercury and penetrometer compression effects (blue), and additionally for sample compression effects (red) to leave a true intrusion curve (Section 1.3.5.3).

Obtaining corrected results for true sample porosity involves the compressibility correction and trimming of porosimetry curves to include only true intrusion data. This process was undertaken according to the previously described method (Section 3.1) so that curves could be realistically modelled in the Pore-Cor environment. Corrected intrusion curves are shown in Figure 7.7, expressed as intruded volume per unit weight of sample ( $\text{cm}^3 \text{g}^{-1}$ ) against pore diameter ( $\mu\text{m}$ ) as derived by conversion of applied pressure through the Washburn equation (Equation 2.1). These corrected curves were then modelled in the Pore-Cor environment to obtain unit-cell representations, as previously described in Chapter 3, and also porosity values for each of the analysed samples. The porosities found via this analysis are tabulated in comparison to the previous results in Table 7.4, and compared graphically in Figure 7.8. As can be seen porosity values were 2 – 3 % lower than those from the previous methods.

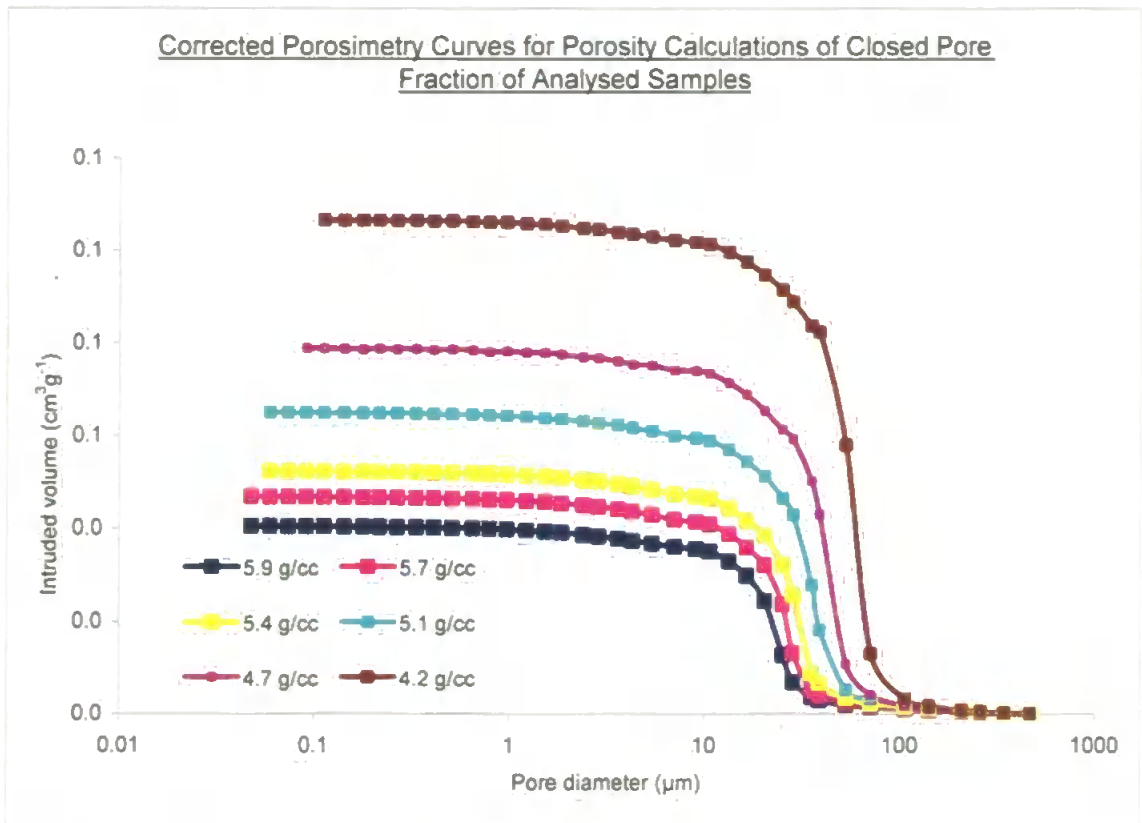


Figure 7.7 Corrected porosimetry curves after compressibility correction and corrective trimming process as described in Section 3.1.

Table 7.4 Comparison of sample porosities derived by all analysis methods.

Nominal Green Form Density (g cm <sup>-3</sup> )	Expected Porosity (%)	Porosity via Weigh and Measure Method (%)	Porosity via ISO 2738 Analysis (%)	Porosity via Porosimetry Analysis (%)
4.2	47.2	47.0	47.0	44.4
4.7	40.9	40.0	40.4	38.4
5.1	35.9	35.0	35.6	33.7
5.4	32.1	31.0	31.3	29.1
5.7	28.3	29.0	28.8	26.8
5.9	25.8	26.5	26.6	24.0

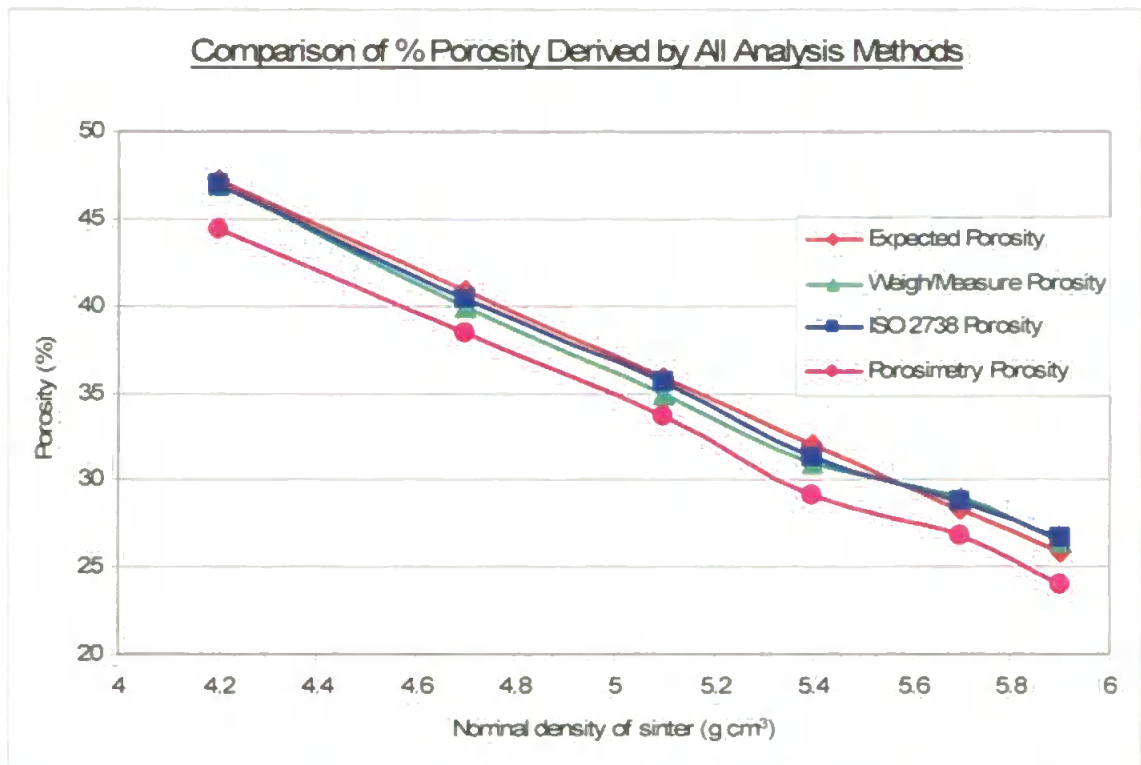
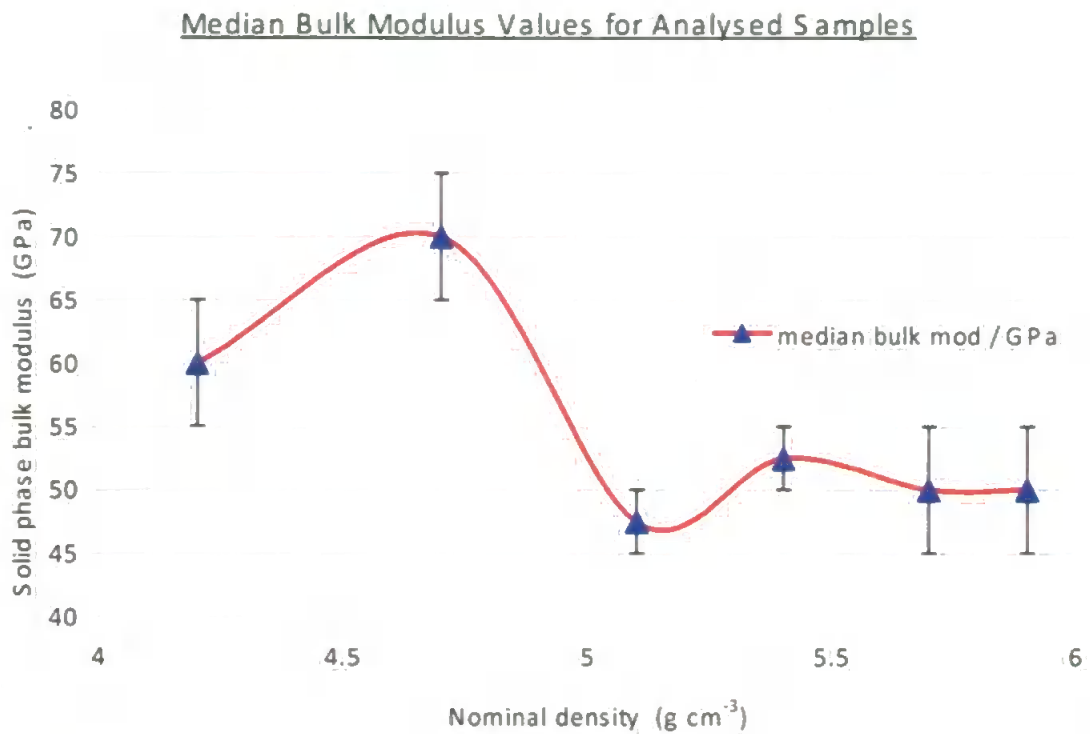


Figure 7.8 Comparison of the returned % porosity values for all nominal densities of samples tested via all analysis methods.

The derived bulk modulus values are presented graphically in Figure 7.9 as median values of bulk modulus at each nominal density with error bars giving estimates of the range of uncertainty of the measurement, determined by observing the changes caused in figures such as Figure 7.6 by manually changing the bulk modulus.



**Figure 7.9** Bulk modulus values from compressibility corrections of porosimetry curves. Results are reported as the median value of the acceptable range as determined by manual processing of the compressibility correction.

It can be seen in Figure 7.9 that the sample media are exhibiting a reduced bulk modulus and enhanced compressibility compared to the mean value found for 316L base powder of 135 GPa. The bulk moduli of the solid phase of the sinters is therefore around half to a third of that expected for solid stainless steel. This large reduction in bulk modulus, and increase in compressibility, could not be explained by the 2 – 3 % porosity discrepancy seen in Figure 7.8.

To further determine the sample characteristics and any sample anomalies, the porosimetry data were modelled with Pore-Cor to check for 'ink bottle pore' pores and any other anomalies in the pore and throat size distributions. Ink bottle, or blind, pores are pores within a structure that contain only one connecting throat and are therefore a dead end for fluid flow. A sample media exhibiting a high number of blind pores could also suggest the presence of entirely closed pore space. This process has been used previously in the structural elucidation and differences between high performance and standard concretes (Matthews, 2008 b). It must be noted however that the software does not explicitly deduce whether these ink bottle pores exist in a sample, only whether the respective mercury intrusion curve is compatible with their existence.

With respect to pore and throat size distributions, a porous sample made by sintering mono-sized particles might be expected to possess a Gaussian distribution of pore and throat sizes around a mean value. A sample containing a high level of closed pores might be expected to have a non Gaussian pore and throat size distribution.

Results of the 'ink bottle pore' analysis are presented in Figures 7.10 – 7.13. The results shown are for  $4.2 \text{ g cm}^{-3}$  and a  $5.9 \text{ g cm}^{-3}$  sinters respectively to show the extremities of the tested range. All other samples were found to exhibit similar results. Results are presented in the first instance as a connectivity analysis, where a connectivity of 1 = ink bottle pore. The results of this analysis are initially reported (Figure 7.10 and Figure 7.12) as a percentage fraction of the total pore number of each sample at each connectivity, with connectivity ranging from 1 – 6 due to the constraints of the model discussed in Section 1.3.5. The second reported result (Figure 7.11 and Figure 7.13) is a percentage fraction of a samples 'ink bottle pores' (those having connectivity = 1) at each size of a representative range of sizes.

**Connectivity of Pores for a  $4.2 \text{ g cm}^{-3}$  Sinter Sample**  
(ink bottles have connectivity = 1)

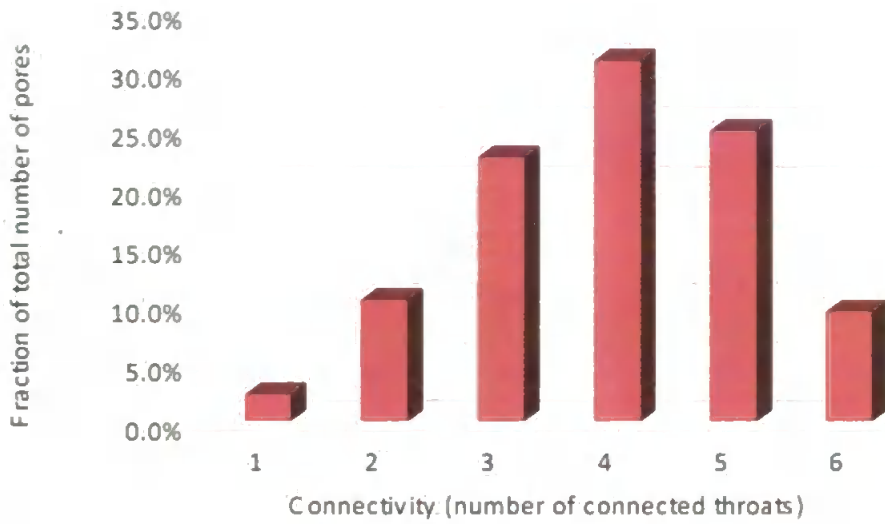


**Figure 7.10** Connectivity analysis for a sinter of nominal density  $4.2 \text{ g cm}^{-3}$ . Results show that the percentage fraction of ink bottle pores, those where connectivity = 1, is ca. 2%. This indicates a low inclusion of the ink bottle phenomena in the tested sinter.

**Frequency and Sizes of Ink Bottle Pores in a  $4.2 \text{ g cm}^{-3}$  Sinter**

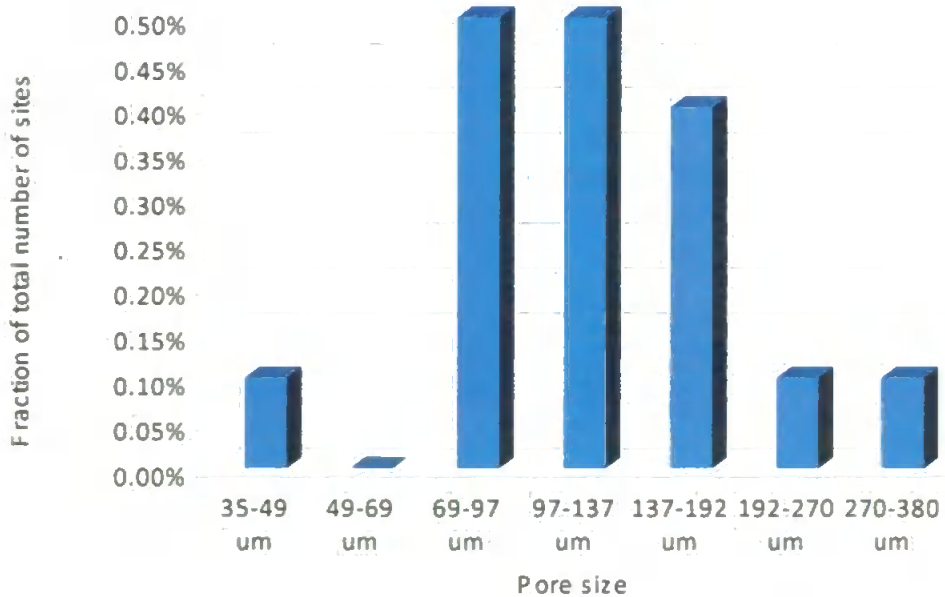


**Figure 7.11** Size distribution of ink bottle pores within the tested  $4.2 \text{ g cm}^{-3}$  nominal density sample plug. Results are expressed as a percentage fraction of total pore number within the sample.



**Connectivity of Pores for a  $5.9 \text{ g cm}^{-3}$  Sinter Sample**  
(ink bottles have connectivity = 1)

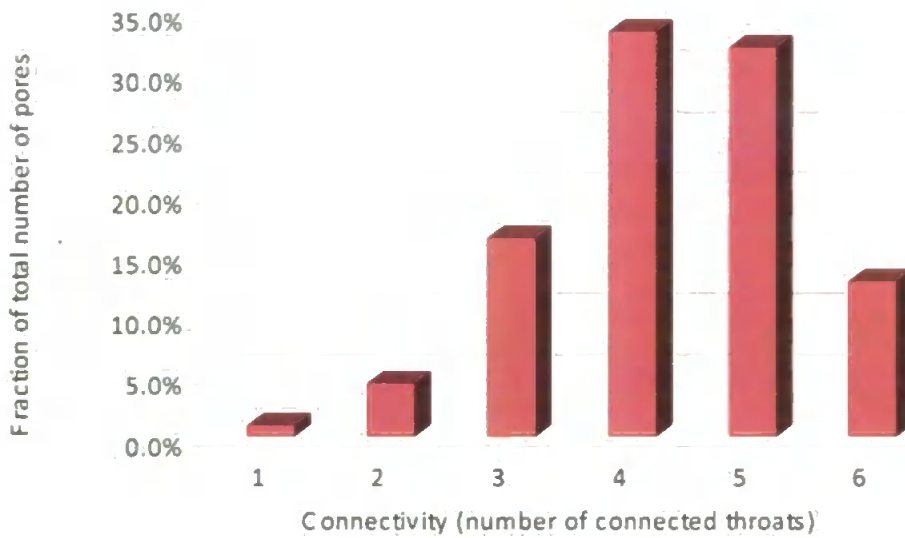


**Figure 7.12** Connectivity analysis for a sinter of nominal density  $5.9 \text{ g cm}^{-3}$ . Results show that the percentage fraction of ink bottle pores, those where connectivity = 1, is ca. 2%. This indicates a low inclusion of the ink bottle phenomena in the tested sinter.

**Frequency and Sizes of Ink Bottle Pores in a  $5.9 \text{ g cm}^{-3}$  Sinter**

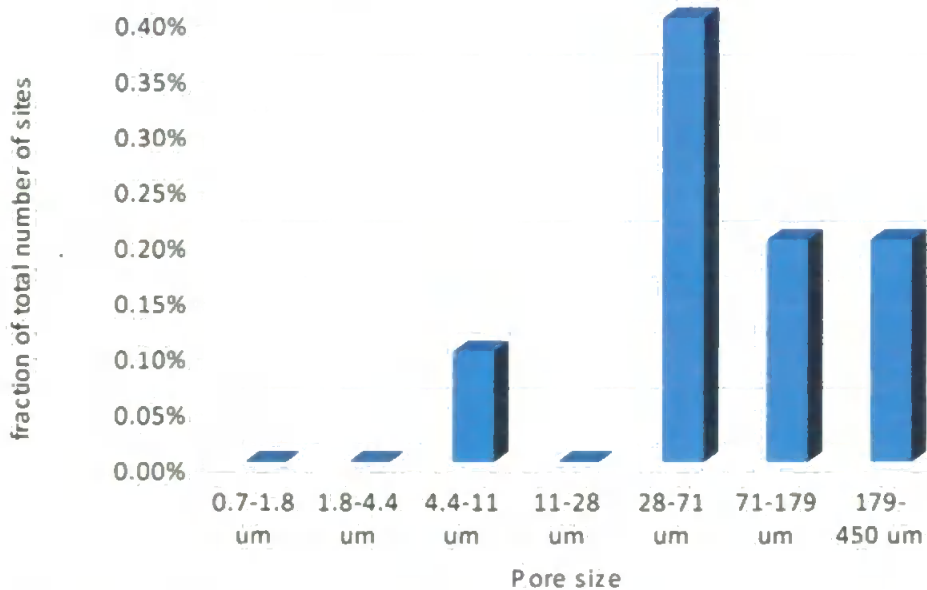


**Figure 7.13** Size distribution of ink bottle pores within the tested  $5.9 \text{ g cm}^{-3}$  nominal density sample plug. Results are expressed as a percentage fraction of total pore number within the sample.

The pore and throat size distributions are shown in Figure 7.14 and Figure 7.15, for the highest and lowest nominal densities tested, 4.2 and 5.9 g cm<sup>-3</sup> respectively. The results show Gaussian type behaviour that is expected for such samples. The 4.2 g cm<sup>-3</sup> sample has a Gaussian throat size distribution centred on a mean value ca. 30 μm, and the 5.9 g cm<sup>-3</sup> sample has a flatter distribution centred on a mean value ca. 3 μm. This flattening and centring on smaller pore sizes of the throat size distribution exhibited by the 5.9 g cm<sup>-3</sup> nominal density sample is expected due to its lower porosity and increased packing efficiency. The modelling of the mercury intrusion results therefore showed no evidence of lost porosity.

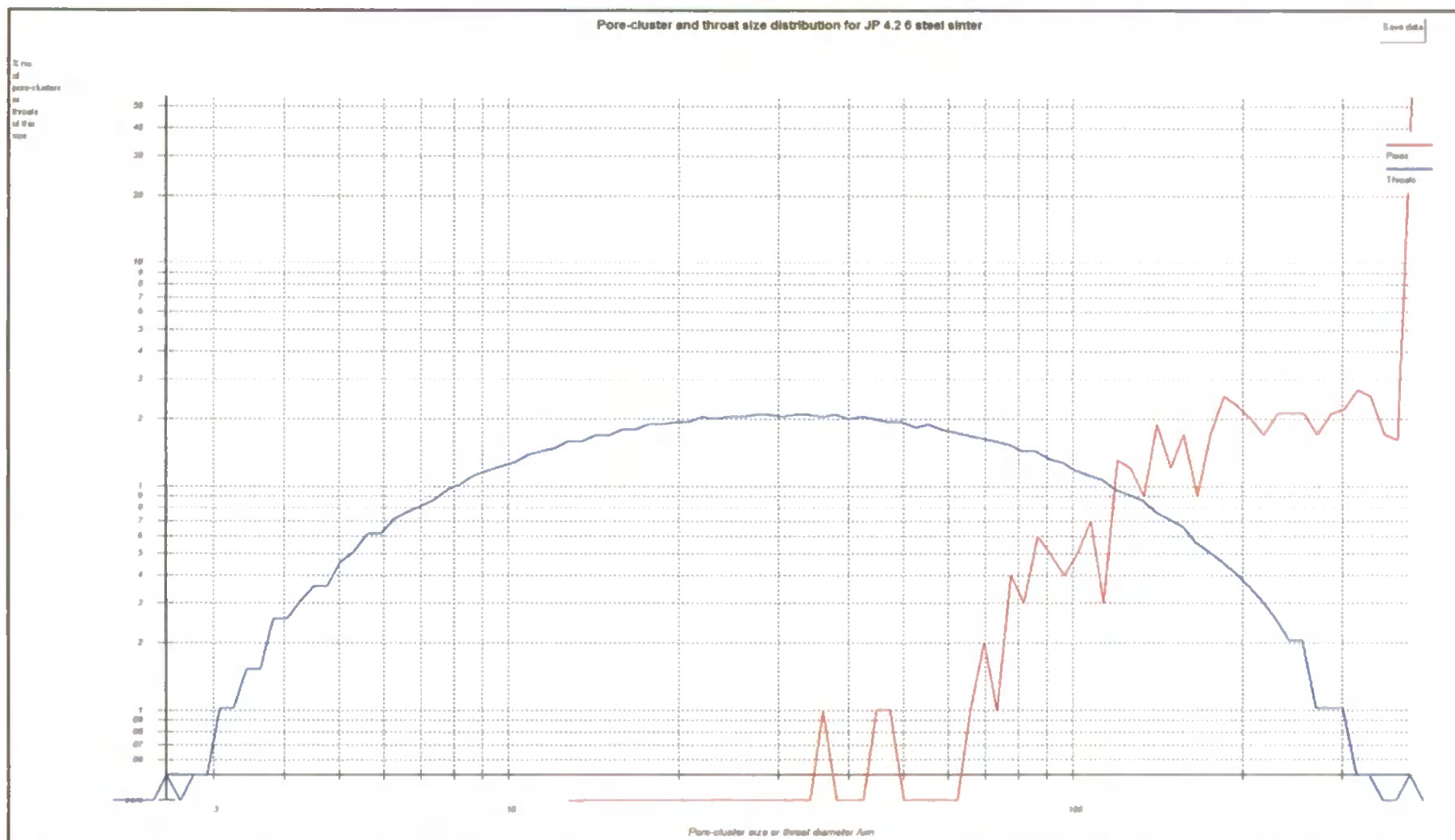


Figure 7.14 Screen shot of PTSD analysis for a  $4.2 \text{ g cm}^{-3}$  nominal density Sinterflo® sample plug. Note centre of the Gaussian throat size distribution ca.  $30 \text{ }\mu\text{m}$ .

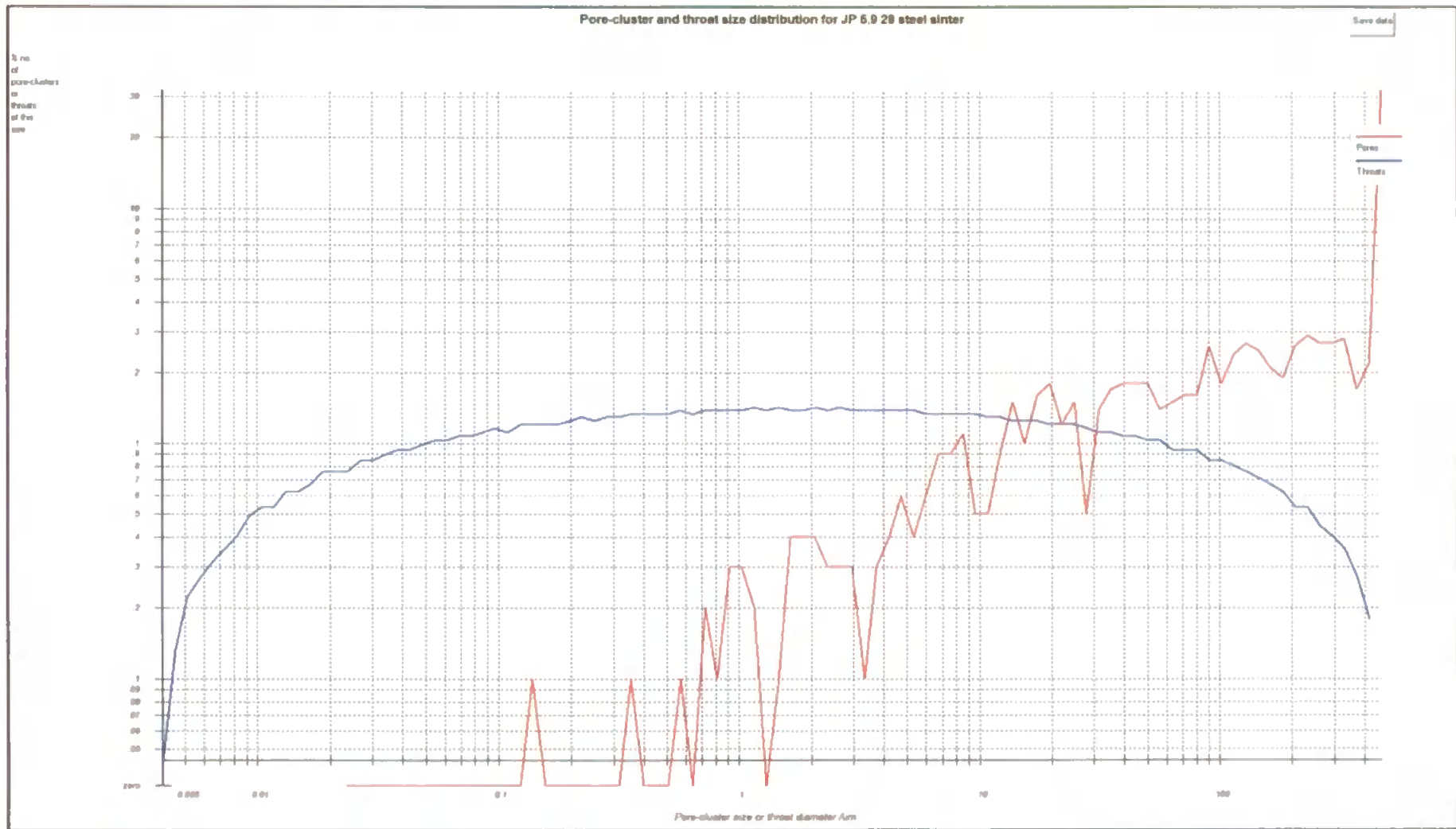


Figure 7.15 Screen shot of PTSD analysis for a  $5.9 \text{ g cm}^{-3}$  nominal density Sinterflo® sample plug. Note centre of the Gaussian throat size distribution ca.  $3 \mu\text{m}$ .

In a further attempt to explain the low bulk moduli of the solid phase of the sinters, the sinters were uni-axially compressed at loads up to 10,000 N. From Equation 7.1, it follows that,

$$\int_{V_0}^V \frac{dV}{V} = \int_{P_0}^P \frac{dP}{M} \quad \text{Equation 7.3}$$

where  $V_0$  is the initial sample volume, and  $P_0 = 0$ , the initial pressure. Then if  $M$  is independent of pressure:

$$\ln V = -\frac{P}{M} + \ln V_0 \quad \text{Equation 7.4}$$

so that a graph of  $\ln V$  against  $P$  should have a slope of  $-1/M$ . Results of the tests on the samples, and a disc of solid stainless steel of similar size, are shown in Figure 7.16 It can be seen that all the samples behave in the same way initially, but then the slope becomes steeper, and hence the bulk modulus less, at a particular threshold pressure for each sinter. Measurements of the extent of barrel deformation in the samples showed that most or all of the slope change could be explained by correcting for the apparent reduction in height of the sample caused by the shear. These tests therefore shed little further light on the anomalously low bulk moduli of the samples' solid phases

Finally mercury porosimetry carried out on the stainless steel powder was re-visited, in particular a different batch of the base powder material. Analysing this different batch of the material yielded a bulk modulus of 35 GPa, i.e. a value similar to that of the analysed sinters. It was therefore finally concluded that the anomalously low bulk moduli of the sinters were due to the material itself, which can vary in property from batch to batch, and which is made by the previously described water atomization process.

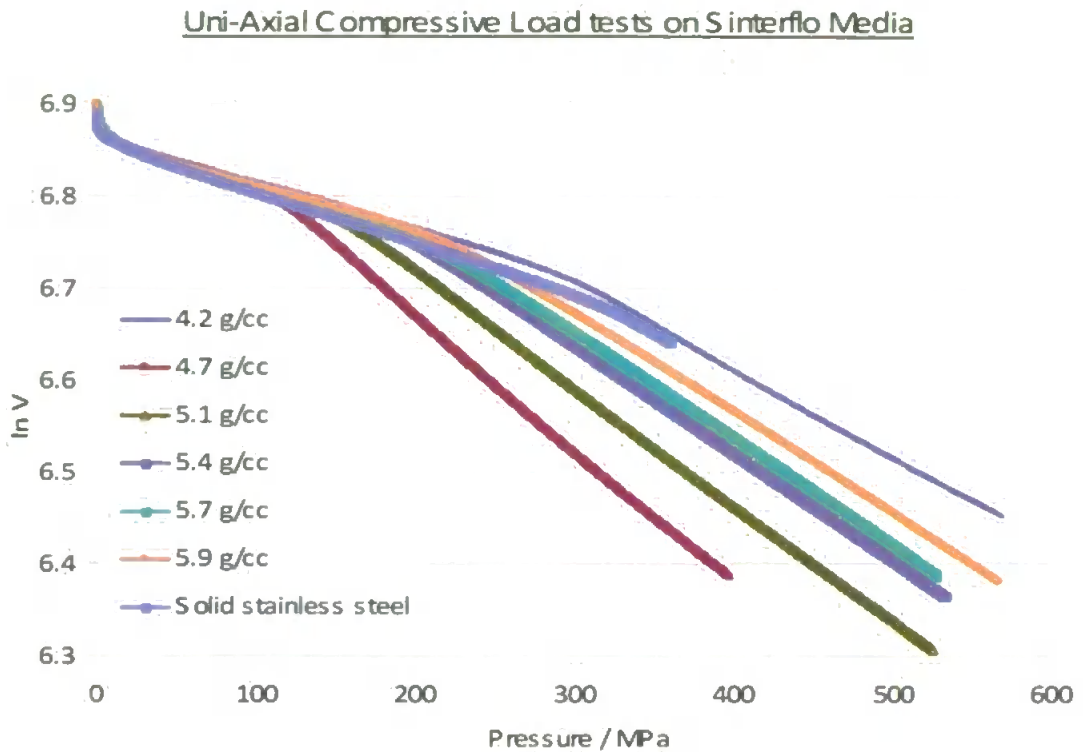


**Figure 7.16** Compressive load test results for the stainless steel Sinterflo® media. Samples 4.2 – 5.9 g cm<sup>-3</sup> nominal densities and solid stainless steel were all run under the same conditions of analysis.

This water atomisation process could provide reason for the compression found in sintered samples and the new tested batch powder. An investigation of the way in which this anomaly occurs was outside of the scope of this work, but is likely to be similar to the previously observed hollow sphere phenomena observed in bronze media previously.

## **8. Overview**

The aim of this final chapter is to give a brief overview of the whole research project in the context of the aims and objectives that were set out in Section 1.2. The thesis has evolved around three main study areas. These areas may be divided into the development of the filtration model which is applicable at a desk-top level, the study of wicking performance in enhanced hydrophilic polymeric sinters and the study of anomalous material compressibility in the stainless steel Sinterflo® media. Each of these areas shall be discussed separately, and areas for future consideration considered in the final section.

### **8.1. Development of a working filtration model**

The main aim of this research has been to investigate and develop a filtration model that may be applied at desk top level to reduce, to some degree, the high financial demand of filter media characterisation. This model was to be based upon the already successful Pore-Cor void network simulator. Although simple in its approximation of void geometries as cylindrical throats and cubic pores, the software had previously shown good correlation with structural properties of many materials from sandstone to concrete, and as consequence offered a good starting point upon which to base the research.

In Chapter 3 the mercury porosimetry data from the analysis of the stainless steel Sinterflo® media was modelled using the Pore-Cor software. The resulting void network structures were validated against previously measured physical property data provided by Porvair Filtration Group Ltd. (PFG) and found to offer good agreement. Validation was undertaken through a number of modelling applications including comparison of the break-through pore size of modelled structure against the maximum

physical pore size (as measured by PFG) and also by the application of a non-dynamic formation damage simulations. The observed trends between the physical property data and the modelled porosimetry data show good correlation, and the use of porosimetry data for the characterisation of filtration media was shown to be a valid technique, as has also been found previously (Caronia et al., 1986). The work was therefore of a solid foundation upon which to develop a filtration model.

In Chapter 4, it was shown that following a stepwise process, computational algorithms could be applied to the simplistic void networks to offer calculations of net flow, particle transport, particle capture and permeability decline. These algorithms were tested on highly correlated network representations. At present only straining processes have been included into the final working model, although a process of critical velocity deposition was manually input to the test networks with a view to their inclusion in future versions of the software. Critical velocity type capture processes have been considered previously (Rege & Fogler, 1987, 1988), but the phenomenon was applied to their final model through a retro-fitting of empirical data to achieve calibration of a fitting parameter. Other considerations of such capture mechanisms, based on trajectory analysis approaches, have also been undertaken in similar models to the one presented in this research (Imdakm & Sahimi, 1991), but even in these more advanced considerations of media-particle-fluid interactions the models have required a degree of data manipulation to fit realistic empirical results. These studies also suggest that one of the most critical parameters that control a realistic approximation of pressure drop and permeability decline in modelled networks is connectivity. In the presented 3-dimensional Pore-Cor networks the connectivity is directly linked to the experimentally derived percolation of mercury through the studied media. It is therefore a true



representation of the media connectivity rather than an applied connectivity adjustment parameter to fit a network constructed from a random pore size distribution.

Application of straining mechanisms applied to the networks has been shown to generate filtration and pore-level redirections of flow that are consistent with previous experimental observations (Ison & Ives, 1961; Tien, 1989). This has been demonstrated via observation of the developed flow tracking using a “Colour Flow” algorithm. The trials suggested that the applied combination of particle input, capture mechanism, flow calculation and permeability algorithms was suitable to simulate particle transport and straining phenomena in the studied Sinterflo® media.

In Chapter 5 the new model was used to undertake filtration simulations on the validated networks for Sinterflo® media produced in Chapter 3. Simulations were directly compared to experimental ‘wet bench’ results obtained from single pass test analysis of the Sinterflo® media. The application of the filtration simulation to the model networks was a totally *a priori* and uncalibrated process.

Results of the simulations were shown usefully to model the filtration process as a function of pressure drop, and the consequential re-routing of fluid flow through the networks due to straining events was evident. The observation of secondary effects was also apparent in model simulations such as the straining induced re-routing of fluid flows sometimes leading to the channelling of flow through singular preferential paths. At present the model simulations do not take account of filtration by particle deposition other than straining, and concertive effects of particles forming aggregates. In the case of Sinterflo® media, its pore size distributions, and the contaminant particle sizes considered in this study, it is known that straining would be the dominant capture

mechanism (Yao et al.,1971; Tien, 1989). However in application of the simulations to smaller particles it is believed that consideration will have to be given to inclusion of other mechanisms of particle capture such as the critical velocity process and fines build up within throat features.

Current simulations only consider a small number of particles and small unit volume of media when compared to a full scale filter unit. Due to this consideration, the results of the simulation have been based on cumulative averages over the whole history of a simulation. This method of calculation leads to the possibility of the reported final efficiency being dragged down by initial low efficiencies of particle capture. It has been observed that in the experimental pass tests this is not the case as capture efficiency is based on independent measurement at each pressure drop. This reasoning suggests that a possible upscaling of the simulation may need to be considered. However a balance must be addressed between the increase in representative elementary volume (REV), computational demand and the ability of the model to be implemented on a desk top computer. High resolution computational models of filtration are already in existence such as that developed by the Fraunhofer Institute (Fraunhofer ITWM, Germany). However these require near supercomputer levels of computational power and long simulation times (ca. 24 hours) to produce usefully long analyses of the filtration process. Even with the current high level of computational capability available in the desk top environment there is still no true “golden Box” filtration model that can provide quick total media characterisation with minimal empirical input. It is therefore felt that the research and model development undertaken within this study has been a successful exercise, and that with further development it could offer a suitable alternative to wet bench testing in some cases.

Also presented in Chapter 5 was a new mode of calculation for determining filtration efficiency, namely alpha efficiency. The calculation has been shown to provide a sensible representation of filtration data obtained from the new model and also from experimental pass test results. Previous modes of data handling have been shown to over- or under-estimate true levels of a filtration medium's capture efficiency depending on the individual particle size ranges considered. The inclusion of the newly proposed alpha efficiency into the model is currently being undertaken and, subject to successful testing against sample data sets, will be presented as a quantitative output function of the model.

## **8.2. Investigation of hydrophilic i-Vyon® media**

In Chapter 6 an investigation is presented whereby the wicking efficiency of a series of polymeric i-Vyon® samples is calculated from the analysis of capillary rise measurements. Analysis of the experimental data was undertaken using an improved method of data manipulation and the results were presented. Initial samples were found to exhibit degradation of the plasma treatment and as consequence an improved method of plasma treatment was utilised to provide a second batch of better prepared samples.

The polymeric i-Vyon® material derives its hydrophilicity through the activation of the pore surfaces using an oxidative plasma process to attach a number of polar functional groups such as C=O (carbonyl), -COOH (carboxyl) and -OH (hydroxyl) groups. When the wicking efficiency of water in these hydrophilic samples was compared with the same process, but using hexane (fully wetting), it was found that the hydrophobic nature of the tested samples exhibited a high variance. The magnitude of this variance was

also found to have an inverse correlation with the empirically derived representative pore size of the media.

It was concluded from the investigation that the degree of variance,  $\sum_{i=1}^N \text{Var}(h_i)$ , was reduced from the first to the second batch of samples. Further to this it has been shown that the variance of such samples may be quantified in future and the analysis process used as a quality control parameter for the optimisation of the oxidative plasma treatment. To achieve a useable protocol a full investigation into different plasma conditions over a series of representative pore sizes must be undertaken for a range of the manufactured polymeric materials.

### **8.3. Investigation of anomalous material compressibility in Sinterflo® media**

In Chapter 7 an investigation was undertaken after initial porosimetry of the stainless steel Sinterflo® media highlighted anomalous compressibility behaviour within the sample sinters. These anomalies were lower than expected bulk moduli values in the Pore-Comp corrections of the porosimetry data. Initial hypotheses of the investigation were tested by further porosimetry on samples of 316L stainless steel base powder. These investigations showed that the base powder behaved as solid stainless steel, highlighted by a returned bulk modulus value of 135 GPa over 2 replicates.

As consequence of the initial investigations it was decided to investigate a “closed pore” hypothesis. This led to the production of a number of sintered samples at differing green form densities that were characterised by porosimetry and further modelling within the Pore-Comp environment to establish any trends in compressibility behaviour

and hypothesised lost porosity. Results indicated that all sintered samples lost ca. 2 - 3 % of their total porosity through the sintering processes when compared with total porosity measurements. It was felt that this reduction in sample porosity was insufficient to induce the reduced values of bulk modulus exhibited by all samples. A further investigation was therefore undertaken that utilised the Pore-Cor software to determine pore and throat size distributions and the number of 'ink bottle' pores. Both these investigations suggested that all tested samples behaved ideally in terms of their structural characteristics although they continued to deliver the anomalous compressibility values. One further investigation using a compressive load test also showed that the samples all behaved similarly with respect to each other and also with respect to a solid stainless steel reference sample. Any differences within the results of this analysis were attributable to the barrel deformation of the samples.

The re-visiting of porosimetry to again investigate the 316L base powder has indicated that batch dependant differences may exist. The high compressibility may arise from formations of closed micro-porosity in the base material generated during to its water-atomised manufacturing process. Another possibility is micro fracturing of the stainless steel caused by increased grain size development under sintering conditions, as previously observed (Yoon et al., 2003)

#### **8.4. Future work**

As mentioned in Chapters 4 and 5 the current model developed throughout the course of this research has proved to be a useful tool in the characterisation of the Sinterflo® media, used as sample sets. However as stated, presently the model only considers straining and concertive particle effects leading to aggregate formation. The model needs to be extended to incorporate the critical velocity deposition mechanisms

highlighted in Chapter 4. The addition of such advanced particle deposition mechanisms would aid the modelling of smaller particles, further media types and different fluids. Whether the further deposition mechanisms are modelled as described in Section 4.3, or by approximations based on particle trajectories, is yet to be decided. The quantification of such interactions is highly complex, but nevertheless necessary for a realistic and versatile model.

The current model offers a useful tool to estimate filter efficiency, permeability decline and ripening effects found in filtration systems dominated by straining. It is suggested that it is tested against varied media types to deduce whether it has *a priori* capability or whether it requires training with calibrated data sets.

In Chapter 6, the study of the wicking characteristics of treated Vyon® samples has provided a novel means of optimising the characteristics of porous wicking systems. Such systems are of great interest for biomedical and emanation applications. It is suggested that the variance-based quality control method developed in this work is applied to a wider sample range, specifically samples covering smaller graduations in pore size, differing conditions of applied plasma oxidation, and different wetting fluids. An investigation of this type would deliver optimal structural and treatment conditions, and provide an efficient and simple method of quality control.

The work presented in Chapter 7 failed to elucidate the exact cause of the anomalously high compressibilities of the stainless steel Sinterflo® media, although it did demonstrate the ability of mercury porosimetry and the Pore-Cor model to establish the absence of anomalies within pore network structure. A metallurgical investigation of the phenomenon is suggested.

## **8.5. Conclusion**

The work presented within this thesis has provided coupled experimental and modelling techniques to characterise and elucidate the properties of filters and wicks. The work is based on complex fundamental principles. Methods have been presented in which these complexities are reduced by approximation and automation of the calculations, in order to make the work easily transferable to the industrial sector, a factor which according to Purchase (2004) is required in the modern climate.

## REFERENCES

- Adamczyk, Z. and van de Ven, T.G.M. (1981) Deposition of particles under external forces in laminar flow through parallel-plate and cylindrical channels. *Journal of Colloid and Interface Science*. **80**, 340 – 356.
- Ahuja, R. K., Kodialam, M., Mishra, A. K. and Orlin, J. B. (1997) Computational investigations of maximum flow algorithms, *European Journal Of Operational Research*, **97**, 509-542.
- Berg, C.R. (1995) A simple, effective-medium model for water saturation in porous rocks, *Geophysics*, **60**, 1070-1080.
- Bodurtha, P.A. (2003) Novel techniques for investigating the permeation properties of environmentally friendly paper coatings: The influence of structural anisotropy on fluid permeation in porous media. *PhD Thesis*, University of Plymouth, Plymouth, U.K.
- Bodurtha, P., Matthews, G. P., Kettle, J. P. and Roy, I. M. (2005) Influence of anisotropy on the dynamic wetting and permeation of paper coatings, *Journal of Colloid and Interface Science*, **283**, 171-189.
- De Boer, R. (2003) Reflections on the development of the theory of porous media. *Applied Mechanics Reviews*, **56**, 6.
- Borhan, A. and Rungta, K.K. (1993) Lucas-Washburn kinetics for capillary penetration between periodically corrugated plates, *Journal of Colloid and Interface Science*. **155**, 438.
- Bosanquet, C. H. (1923) On the flow of liquids into capillary tubes, *Philosophical Magazine, Series 6*, **45**, 525-531.



Bowen, B.D., Levine, S. and Epstein, N. (1976) Fine particle deposition in laminar flow through parallel-plate and cylindrical channels. *Journal of Colloid and Interface Science*, **54**, 375 – 390.

BS EN ISO 2738:1999 Sintered metal materials, excluding hardmetals – Permeable sintered metal materials – Determination of density, oil content and open porosity.

Burganos V.N., Skouras E.D., Paraskeva C.A. and Payatakes A.C. (2001) Simulation of the dynamics of depth filtration of non-Brownian particles. *A.I.Ch.E. Journal*, **47**, 4. 880.

Butters, G.L., Jury, W.A. and Ernst, F.F.. (1989) Field scale transport of bromide in an unsaturated soil. *Water Resources Research*, **25**, 1583.

Carmen, P.C. (1939) Permeability of saturated sands, soils and clays. *Journal of Agricultural Science*, **29**, 262.

Caronia, A.J., McNeil, R.L. and Rucinski, K.J. (1986) Filter media characterisation by mercury intrusion. *Fluid Filtration: Liquid*, **2**, ASTM STP 975. Johnston, P.R. and Schroeder, H.G. Editors, American Society for Testing and Materials. Philadelphia, U.S.A.

Cheremisinoff, N.P., Azbel, D.S. (1983) *Liquid Filtration*, Ann Arbor Science, Butterworths Ltd, Kent, England.

Childs, E.C. and Collis-George, N. (1950) Proceedings of The Royal Society Of London, *Series A – Mathematical Physical and Engineering Sciences*, **A20**, 392.

Constantinides, G.N. and Payatakes, A.C. (1989) A three dimensional network model for consolidated porous media. Basic studies. *Chemical Engineering Communications*, **81**, 55-81.

Coulson, J.M. (1949) The flow of fluids through granular beds: effect of particle shape and voids in streamline flow. *Transactions of the Institute of Chemical Engineers*. **27**, 237.

- Dickenson, T.C. (1997) *Filters and Filtration Handbook*, 4<sup>th</sup> Edition. Elsevier Advanced Technology, Oxford, UK.
- Dodson, C.T.J. and Sampson, W.W. (2000) Flow simulation in stochastic media. *Simulation*, **74**, 6, 351 – 358.
- Dullien, F.A.L. and Batra, V.K. (1970) Determination of the structure of porous media. *Industrial and Engineering Chemistry*, **62**, 25.
- Elimelech M. and O'Melia C.R. (1990) Kinetics of deposition of colloidal particles in porous media. *Environmental Science and Technology*, **24** , 1528.
- Elimelech, M.; Gregory, J.; Jia, X. and Williams, R.A. (1995) *Particle Deposition and Aggregation: Measurement, Modelling and Simulation*. Butterworth Heinemann, U.K.
- Fatt, I. (1956) The network model of porous media. I, II, III. *Pet. Trans.*, **207**, 144.
- Flannery, W.H., Teukolsky, S.A. and Vetterling, W.T. (1986) *Evaluation of Functions in Numerical Recipes – The Art of Scientific Computing*, 1<sup>st</sup> Edition. Cambridge University Press, Cambridge, pp. 145 – 146.
- Free, M. L., Zhu, J. S. and Moudgil, B. M. (1998) Use of a new particle contact probability filtration rate model to determine the effect of particle size distribution in filtration. *Separation Science & Technology*. **33**, 57-66.
- Frey, J.M., Schmitz, P., Dufreche, J. and Pinheiro, I.G. (1999) Particle deposition in porous media: analysis of hydrodynamic and weak inertial effects. *Transport in Porous Media*. **37**, 25-54.
- Gane, P.A.C., Kettle, J.P., Matthews, G.P. and Ridgway, C.J. (1996) Void space structure of compressible polymer spheres and consolidated calcium carbonate paper-coating formulations. *Industrial Engineering Chemistry Research*, **35**, 1753.

- German, R.M. (1998) *Powder Metallurgy of Iron and Steel*, Wiley, New York, NY.
- Gray, D.E., Ed., (1972) *American Institute of Physics Handbook*, 3<sup>rd</sup> Edition, Mc Graw Hill, New York.
- Grundke, K., Nitschke, M., Minko, S., Stamm, M., Froeck, C., Simon, F., Uhlmann, S., Poschel, K. and Motornov, M. (2003) Merging two concepts: Ultrahydrophobic polymer surfaces and switchable wettability. *Contact Angle, Wettability and Adhesion*. **3**, 267 – 291.
- Guo, J., Wang, Y., Liu, R. and Tang, H. (2002) Calculation model of uniform media filtration capacity. *Colloids and Surfaces A: Physicochemical and Engineering Aspects*. **201**, 237 – 245.
- Gupta, V. and Jena, A.K. (1999) Advances in filtration and separation technology. *American Filtration & Separation Society*. **13b**, 833.
- Hallet, P.D., Nunan, N., Douglas, J.T. and Young, I.M. (2004) Millimeter-scale spatial variability in soil water sorptivity: scale, surface elevation and subcritical repellency effects. *Soil Science Society of America Journal*, **68**, 352.
- Heertjes, P.M. and Lerk, F.F. (1967) The function of deep bed filters. *Transactions of the Institute of Chemical Engineers*, **45**, 76.
- Herzig, J.P., Leclerc, D.M. and Le Goff, P. (1970) Flow of suspensions through porous media – Application to deep filtration. *Industrial and Engineering Chemistry*. **62**, 9 – 35.
- Holtham, D.A.L. (2006) Enhanced soil structuring beneath white clover and its impact on nutrient transport. *PhD Thesis, University of Plymouth, U.K.*
- Houi, D. and Lenormand, R. (1986) Particle accumulation at the surface of a filter. *Filtration Separation*, **23**, 238.

- Hsu, E.H. and Fan, L.T. (1984) Experimental study of deep bed filtration: A stochastic treatment. *A.I.Ch.E. Journal*, **30**, 267.
- Imdakm, A.O. and Sahimi, M. (1987) Transport of large particles in flow through porous media. *Physical Review A*, **36**, 5304-5309.
- Imdakm, A.O. and Sahimi, M. (1991) Computer simulation of particle transport processes in flow through porous media. *Chemical Engineering Science*, **46**, 1977.
- Ison, C.R. and Ives, K.J. (1969) Removal mechanisms in deep bed filtration. *Chemical Engineering Science*, **24**, 717.
- Ives, K.J. (1960) Rational design of filters. *Proceedings of the Institute of Civil Engineers*, **20**, 189.
- Johnson, A., Roy, I.M., Matthews, G.P. and Patel, D. (2003) An improved simulation of void structure, water retention and hydraulic conductivity in soil with the Pore-Cor three-dimensional network. *European Journal of Soil Science*, **54**, 477.
- Laudone G.M. (2005) *Environmentally friendly technology: The behaviour of natural and synthetic binder systems within paper coatings*. PhD Thesis, University of Plymouth, U.K..
- Le Coq, L. and Silvy, J. (1999) Fibrous media plugging modelling for liquid filtration. *Chemical Engineering Communications*, **174**, 145 – 166.
- Lee, J. and Koplik, J. (1996) Simple model for deep bed filtration. *Physical Review E*. **54**, 4, 4011 – 4020.
- Lee, J. and Koplik, J. (2001) Network model for deep bed filtration. *Physics of Fluids*. **13**, 1076 – 1086.

- Lin, C.L. and Miller, J.D. (2004) Pore structure analysis of particle beds for fluid transport simulation during filtration. *International Journal of Mineral Processing*, **73**, 281 – 294.
- Lucas, R. (1918) Ueber das zeitgesetz des kapillaren aufstiegs von fluessigkeiten, *Kolloid Z*, **23**, 15
- Mathews, T.J. (1999) Void structure, colloid and tracer transport properties of stratified porous media. *PhD Thesis*, University of Plymouth, U.K.
- Matthews, G.P., Ridgway, C.J. and Small, J.S. (1996) Modelling of simulated clay precipitation within reservoir sandstones. *Marine Petroleum Geology*, **13**, 581.
- Matthews, G.P., Bodurtha, P.A., Price, J.C., Ridgway, C.J., Johnson, A., Roy, I.M. and Laudone, G.M. (2004) Pore-Cor Research Suite User's Guide. *University of Plymouth Enterprise Ltd*.
- Matthews, G.P., Canonville, C.G. and Moss, A.K. (2006) Use of a void network model to correlate porosity, mercury porosimetry, thin section, absolute permeability and NMR relaxation time data for sandstone rocks. *Physical Review E*, **73**, 031370.
- Matthews, G.P., Watts, C.W., Price J.C., Powlson, D.S. and Whalley, W.R. (2008) Wetting of agricultural soil measured by a simplified capillary rise technique. *European Journal of Soil Science*, **59**, 4, 817.
- Matthews, G.P., Grible, C., Luarelli, L., Schreiber, A. and Adolphs, A. (2008 b) Analysis of ink bottle pores with the Pore-Cor model. Presentation at, *Characterisation of Porous Solids Conference*, 22 October, Edinburgh, U.K.
- Moshinskii, A.I. (1997) Consideration of inertial force in capillary rise of a newtonian liquid in a cylindrical tube. *Colloid Journal* **59**, 62.

Ochi, J. and Vernoux, J. (1999) A two-dimensional network model to simulate permeability decrease under hydrodynamic effect of particle release and capture. *Transport in Porous Media*, **37**, 303-325.

Ojha, C.S.P. and Graham, N.J.D. (1992) Computer-aided solutions of filtration equations. *Water Research*, **26**, 2, 145 – 150.

Osmak, S., Gosak, D. and Glasnovic, A. Dynamic mathematical model of deep bed filtration processes. *Computers and Chemical Engineering*, 1997, **21**, S763 – S768.

Payatakes, A.C., Tien, C. and Turian, R.M. (1973) A new model for granular porous media. I: Model formulation. *AIChE Journal*, **19**, 58.

Peat, D.M.W., Matthews, G.P., Worsfold, P.J. and Jarvis, S.C. (2000) Simulation of water retention and hydraulic conductivity in soil using a three-dimensional network. *European Journal of Soil Science*, **51**, 65.

Petersen, L.W., Moldrup, P., Jacobson, O.H. and Rolston, D.E. (1996) Relations between specific surface area and soil physical and chemical properties. *Soil Science*, **161**, 9 – 21.

Polyakov, Y. S., Kazenin, D. A., Maksimov, E. D. and Polyakov, S. V. (2003) Kinetic model of depth filtration with reversible adsorption. *Theoretical Foundations of Chemical Engineering*, **37**, 439 – 446.

Porvair data sheet 1, *Sintered Porous Metals*. Porvair Filtration Group product information sheets, web based format available 05/11/08 at: [www.porvairfiltration.com](http://www.porvairfiltration.com).

Porvair data sheet 2, *Sintered porous polymers*. Porvair Filtration Group product information sheets, web based format available 05/11/08 at: [www.porvairfiltration.com](http://www.porvairfiltration.com).

Porvair data sheet 3. *Developments in porous polymeric materials*. Povair Filtration Group press release, September 2005. Available at: [www.porvairfiltration.com](http://www.porvairfiltration.com)

Porvair data sheet 4. *Filtration Efficiency testing of Flat Sheet Media Samples*. Porvair Filtration Group, testing protocol. Company confidential document.

Press, W.H. and Teukolsky, S.A. (1991) Simulated annealing optimization over continuous control spaces. *Computers in Physics*, **5**, 426

Purchas, D.B. (2004), A practical view of filtration theory. *Filtration (Special issue)*.

Rajagopalan, R. and Tien, C. (1979) The theory of deep bed filtration. *Progress in Filtration and Separation*. **1**, 179 – 269.

Rege,S.D. and Fogler,H.S. (1987) Network model for straining dominated particle entrapment in porous media. *Chemical Engineering Science*, **42**, 1553.

Rege,S.D. and Fogler,H.S. (1988) A network model for deep bed filtration of solid particles and emulsion drops. *A.I.Ch.E. Journal*, **34**(11): 1761-1772.

Ridgway, C.J., Schoelkopf, J., Mathews, G.P., Gane, P.A.C. and James, P.W. (2001) the effects of void geometry and contact angle on the absorption of liquids into porous CaCO<sub>3</sub> structures. *Journal of Colloid and Interface Science*, **239**, 417.

Rouquerol, J.; Anvir, D., Fairbridge, C.W., Everett, D.H., Haynes, J.H., Pernicone, N., Ramsay, J.D.F., Sing, K.S.W. and Unger, K.K. (1994) Recommendations for the characterisation of porous solids. *Pure Applied Chemistry*, **66**, 1739.

Sahimi, M., Davis, H.T. and Scriven, L.E. (1983) Dispersion in disordered porous media. *Chemical Engineering Communications*, **23**, 329 – 341.

Sahimi, M., Heiba, A.A., Davis, H.T. and Scriven, L.E. (1986 a) Dispersion in flow through porous media - II. Two phase flow. *Chemical Engineering Science*, **41**, 2123 – 2136.

- Sahimi, M., Huges, B.D., Scriven, L.E. and Davis, H.T. (1986 b) Dispersion in flow through porous media – I. One phase flow. *Chemical Engineering Science*, **41**, 2103 – 2122.
- Sahimi, M. and Imdakm, A.O. (1988) The effect of morphological disorder on hydrodynamic dispersion in flow through porous media. *Journal of Physics A*, **21**, 3833 – 3870.
- Sahimi, M.; Gavalas, G.R. and Tsotsis, T.T. (1990) Statistical and continuum models of fluid-solid reactions in porous media. *Chemical Engineering Science*, **45**, 1443 – 1502.
- Scheidegger, A.E. (1974) *The Physics of Flow Through Porous Media*. University of Toronto Press, Toronto.
- Schoelkopf, J., Ridgway, C.J., Gane, P.A.C., Matthews, G.P. and Spielmann, D.C. (2000) Measurement and network modelling of liquid permeation into compacted mineral blocks, *Journal of Colloid and Interface Science*, **227**, 119-131.
- Schoelkopf, J. (2002) Observation and modeling of fluid transport into porous paper coating structures, *PhD Thesis*, University of Plymouth, Plymouth, U.K.
- Siebold, A., Walliser, A., Nardin, M., Oppliger M. and Schultz, J. (1997) Capillary rise for thermodynamic characterization of solid particle surface. *Journal of Colloid and Interface Science*, **186**, 60-70.
- Slattery, J.C. (1967) Flow of viscoelastic fluids through porous media. *A.I.Ch.E. Journal*, **13**, 1066 – 1071.
- Sjollema, J. and Busscher, H.J. (1989) Deposition of polystyrene latex particles toward polymethylmethacrylate in parallel-plate flow cell. *Journal of Colloid and Interface Science*. **132**, 382 – 394.



Sjollema, J. and Busscher, H.J. (1990) Deposition of polystyrene particles in a parallel-plate flow cell. 1. The influence of collector surface properties on the experimental deposition rate. *Colloids and Surfaces*. **47**, 323 - 336.

Sutherland, K. (2004), *Profile of the International Filtration & Separation Industry*, 5<sup>th</sup> Edition – Market Prospects to 2009, Elsevier Advanced Technology, Kidlington, U.K.

Tien C. and Payatakes A.C. (1979) Advances in deep bed filtration . *A.I.Ch.E. Journal*., **25**, 9, 737.

Tien C. (1989) *Granular filtration of aerosols and hydrosols*. Butterworths series in Chemical Engineering. Boston MA.

Todd, A.C., Somerville, J.E. and Scott, G. (1984) The application of depth of formation damage measurements in predicting water injectivity decline. *Society of Petroleum Engineers*, Report, 12498.

Toivakka, M. And Nyfors, K. (2000) Pore space characterisation of coating layers. *2000 Tappi Coating Conference*, Washington DC, Tappi Press.

Tsiang, R.C., Wang, C. and Tien, C. (1982) Dynamics of particle deposition in model fibre filters. *Chemical Engineering Science*., **37**, 1661 – 1673.

Van Brakel, J., Modry, S. and Svata, M. (1981) Mercury porosimetry : state of the art. *Powder Technology*, **29**, 1 - 12.

Wakeman, R. (2007) Testing filter media for liquid filtration. *Filtration*, **7**, 138 – 147.

Washburn, E. W. (1921) The dynamics of fluid flow, *Physical Review*, **17**, 273

Webb, P.A. and Orr, C. (1997) *Analytical Methods in Fine Particle Technology*, 1<sup>st</sup> Edition., Micromeritics, Norcross,GA, U.S.A.

Wenrong, M., Shihong, S., Tianhua, L., Wenzhong, L. and Guoheng, H. (1996) Pore and throat network model and its application to the optimal selection of temporary plugging particles. *Society of Petroleum Engineers*, Report 31099, 293 – 300.

Whitaker, S. (1967) Diffusion and dispersion in porous media. *A.I.Ch.E. Journal*, **13**, 420 - 427.

Xonics Data Sheet. *Xonics Porometer 3<sup>G</sup>*. Web based pdf. format available 05/11/08 at: [www.porometer.com/PorometerIII.pdf](http://www.porometer.com/PorometerIII.pdf)

Yao K.M., Habibian M.T. and O'Melia C.R. (1971) Water and waste water filtration: Concepts and applications. *Environmental Science and Technology*, **5**, 1105.

Yao, J., Thovert, J.F., Adler, P.M., Tsakiroglou, C.D., Burganos, V.N., Payatakes, A.C., Moulu, J.C. and Kalaydjian, F. (1997) Characterisation, reconstruction and transport properties of Vosges sandstones. *Revue de L'Institute Francais du Petrole*. **52**, 3 – 21.

Yoon, T.S., Lee, Y.H., Ahn, S.H., Lee, J.H. and Lee, C.S. (2003) Effects of sintering conditions on the mechanical properties of metal injection moulded 316L stainless steel. *The Iron and Steel Institute of Japan International*, **43**, 119 – 126.